UNIVERSITY OF CAMERINO

SCHOOL OF ADVANCED STUDIES

Chemical and Pharmaceutical Sciences and Biotechnologies Area

Ph.D. Curriculum in Chemical Science

XXXV Cycle

Doctoral Thesis

Sustainable Electrodes and Cell Configurations for Li-ion and Na-ion Batteries

Ph.D. Candidate
Leonardo Sbrascini

Supervisor
Prof. Francesco Nobili

Academic Year 2019/2020 – 2022/2023

UNIVERSITY OF CAMERINO

SCHOOL OF ADVANCED STUDIES

Chemical and Pharmaceutical Sciences and Biotechnologies Area

Ph.D. Curriculum in Chemical Science

XXXV Cycle

Doctoral Thesis

Sustainable Electrodes and Cell Configurations for Li-ion and Na-ion Batteries

Ph.D. Candidate
Leonardo Sbrascini

Supervisor
Prof. Francesco Nobili

Academic Year 2019/2020 – 2022/2023

"There's two wolves battling us all right now

One's good, the other one's evil

If you're wondering which wolf inside will succeed

Simple, it's the one that you feed"

PREFACE

The present doctoral thesis reports the results obtained during the three-year PhD course with curriculum in Chemical Sciences at the University of Camerino (Italy), under the supervision of Prof. Francesco Nobili. It also reports the results obtained during a five-month period in collaboration with the Karlsruhe Institute of Technology – KIT (Germany), under the supervision of Dr. Sonia Dsoke. The research work reported in this thesis is the subject of some of the scientific publications and conference proceedings listed below.

Scientific Publications:

- H. Darjazi, A. Staffolani, **L. Sbrascini**, L. Bottoni, R. Tossici, F. Nobili. *Sustainable Anodes for Lithium- and Sodium-ion Batteries Based on Coffee Ground-derived Hard Carbon and Green Binders*, Energies (2020), 13(23), 6216, https://doi.org/10.3390/en13236216.
- V. Ferrone, P. Bruni, V. Canale, **L. Sbrascini**, F. Nobili, G. Carlucci, S. Ferrari. *Simple Synthesis of Fe_3O_4@-Activated Carbon from Wastepaper for Dispersive Magnetic Solid-Phase Extraction of Non-Steroidal Anti-Inflammatory Drugs and Their UHPLC–PDA Determination in Human Plasma*, Fibers (2022), 10(7), 58, https://doi.org/10.3390/fib10070058.
- **L. Sbrascini**, A. Staffolani, L. Bottoni, H. Darjazi, L. Minnetti, M. Minicucci, F. Nobili. *Structural and Interfacial Characterization of a Sustainable Si/Hard Carbon Composite Anode for Lithium-Ion Batteries*, ACS Applied Materials & Interfaces (2022), 14, 29, 33257-33273, https://doi.org/10.1021/acsami.2c07888.
- H. Darjazi, L. Bottoni, H.R. Moazami, S.J. Rezvani, L. Balducci, **L. Sbrascini**, A. Staffolani, A. Tombesi, F. Nobili. *From Waste to Resources: Transforming Olive Leaves to Hard Carbon as Sustainable and Versatile Electrode Material for Li/Na-ion Batteries and Supercapacitors*, Materials Today Sustainability (2023), 21, 100313, https://doi.org/10.1016/j.mtsust.2022.100313.
- V. Ferrone, G. Carlucci, P. Bruni, L. Marinelli, P. Avino, E. Milanetti, S. Pilato, **L. Sbrascini**, P. Di Profio, S. Ferrari. *Synthesis and Characterization of Electrospun Sorbent for the Solid-Phase Extraction of Fluoroquinolones in Human Plasma and Their UHPLC-PDA Determination*, Separations (2023), 10(2), 104, https://doi.org/10.3390/separations10020104.
- L. Bottoni, H. Darjazi, **L. Sbrascini**, A. Staffolani, S. Gabrielli, G. Pastore, A. Tombesi, F. Nobili. *Electrochemical Characterization of Charge Storage at Anodes for Sodium-Ion Batteries based on Corncob Waste-derived Hard Carbon and Binder*, ChemElectroChem (2023), e202201117, https://doi.org/10.1002/celc.202201117.

- **L. Sbrascini**, A. Sarapulova, C. Gauckler, L. Gehrlein, F. Jeschull, T. Akcay, M. Marinaro, F. Nobili, S. Dsoke. *Effect of Presodiation Additive on Structural and Interfacial Stability of* $Na_{0.66}Mn_{0.75}Ni_{0.2}Mg_{0.05}O_2$*/Hard Carbon Full Cell*, ChemSusChem (2023), **In preparation.**

Conference Proceedings:

- **L. Sbrascini**, A. Staffolani, F. Nobili. *SnO_2-based Composite Anodes for High Energy Density LIBs*, Enerchem 2, University of Padova, Italy, 12-14/02/2020 - **Poster**.
- **L. Sbrascini**, L. Bottoni, A. Staffolani, H. Darjazi, F. Nobili. *Enhanced Performance of a Sustainable Si/C Anode for High Energy Density Lithium-ion Batteries*, XXVII Congresso della Società Chimica Italiana (SCI 2021), 14-23/09/2021 – **Oral Communication (accepted speaker)**.
- **L. Sbrascini**, L. Bottoni, A. Staffolani, H. Darjazi, F. Nobili. *Sustainable Conversion and Alloying Composite Anodes for Li- and Na-ion Batteries*, NanoInnovation 2021, Sapienza University of Rome, Italy, 21-24/09/2021 – **Oral Communication (invited speaker)**.
- **L. Sbrascini**, A. Staffolani, L. Bottoni, H. Darjazi, F. Nobili. *A Silicon/Hard Carbon Composite Anode Towards Sustainable High-Energy Density Lithium-ion Batteries*, XIII Convegno INSTM sulla Scienza e Tecnologia dei Materiali, Sestriere, Italy, 23-26/01/2022 – **Oral Communication (accepted speaker)**.
- D. Triller, A. Sarapulova, **L. Sbrascini**, J. Anhalt, K. Pfeifer, S. Dsoke. *The Effect of Pre-sodiation in a Sodium-ion Full Cell*, 7th ICNaB 2022, Ulm, Germany, 5-8/12/2022 – **Participant**.
- **L. Sbrascini**, F. Nobili, S. Dsoke, A. Sarapulova. *Compatibility Study of a Pre-sodiation Additive for Application in Sodium-ion Full Cells Based on P2-Layered Cathode and Hard Carbon Anode*, 2nd Italian Workshop on Energy Storage (IWES 2023), Bressanone, Italy, 25-27/01/2023 – **Oral Communication (accepted speaker)**.

ABSTRACT

In the present thesis work, two types of electrochemical energy storage systems have been studied, focusing on the sustainability of materials and applicability in practical applications: a Si-based composite anode for Lithium-ion batteries and a Na-ion full cell employing a green presodiation additive.

In order to face the ever-rising greenhouse gases emissions associated with the use of fossil fuels for energy production, transport electrification and renewable energy sources are rapidly starting to grow. In this context, the use of new materials for powering electric vehicles while still granting a high driving range per single charge is required to achieve desirable energy densities from next-generation Li-ion batteries. Moreover, the use of Na-ion batteries for stationary storage, coupled to the intermittent renewable energy sources, will be the key systems for production and storage of greener and cheaper energy. These goals towards a low-carbon society can however be achieved only by focusing on several practical aspects, considering either performance or sustainability of the materials employed in the final system. Concerning Li-ion batteries, the state-of-the-art graphite serving as the anode material is likely to be replaced in next-generation batteries, due to its relatively low theoretical specific capacity (372 mAh g^{-1}), which is unable to meet the required densities for efficiently powering electric vehicles, and due to its introduction in the list of critical raw materials by the European Union in recent years, although its simple preparation and low cost are still desirable properties for battery manufacturing. Silicon is considered the best candidate anode for its replacement, as it is able to deliver a specific capacity almost ten times higher than graphite (3579 mAh g^{-1}), hence being suitable for high-energy density applications. In addition, it is environmentally friendly and abundant all over the Earth's crust. However, it suffers from fast capacity fade due to the large volume changes upon cycling. In this regard, a hard carbon from waste corn-cobs was synthesized and employed in combination with commercial Si to act as a buffering matrix for volume changes, also using a crosslinked chitosan-based binder to provide better electrode integrity compared to commercial PVdF. The composite anode was deeply characterized in terms of performance and interfacial and structural properties. As a result, the studied Si/Hard Carbon anode offers promising performance in terms of specific capacity, rate capability, and structural and interfacial stability upon cycling, with a good energy efficiency when coupled to a commercial $LiFePO_4$ cathode in full cell configuration. Concerning Na-ion batteries, a layered cathode $Na_{0.66}Mn_{0.75}Ni_{0.2}Mg_{0.05}O_2$ was used in combination with the same hard carbon employed as the buffering matrix for Si in a full cell configuration, and the compatibility of the two materials has been evaluated. A green sacrificial salt (sodium squarate) was synthesized and used as a cathode additive to provide an appropriate amount of additional Na and address the SEI formation at the anode side, in order to make the full cell more viable for practical applications. As a result, the

two materials display good compatibility in full cell configuration, with performance decreasing due to the irreversible SEI formation. The sacrificial additive is found to provide additional sodium during the first charge, hence being suitable to address the abovementioned issue, but it also affects the structural and interfacial stability upon cycling. An in-depth study of interfaces and structural evolution reveals that the phase transitions and SEI composition and thickness are indeed affected by the decomposition of sodium squarate, highlighting the necessity to further optimize the system.

TABLE OF CONTENTS

FIGURES INDEX

TABLES INDEX

1 Introduction

Nowadays, the problem of global climate change is progressively becoming more and more concerning, greatly impacting ecosystems all over the Earth. Many severe effects can already be observed as a consequence of this phenomenon, including shrinkage of ice sheets and glaciers, sea levels rising, shifts in plants blooming times, expansion of deserts, relocation or extinction of animal species, extreme weather, and scarcity of water and food for human beings [1]. According to data from NASA's Goddard Institute for Space Studies (GISS) and the National Centers for Environmental Information (NCEI), the Earth's long-term warming trend reached an average 0.85°C temperature increase in 2021 as compared to a baseline period from 1951 to 1980 (**Figure 1-1**), with an increase rate of 0.08°C/decade and the past eight years being the consecutive warmest ones since 1880 [2,3].

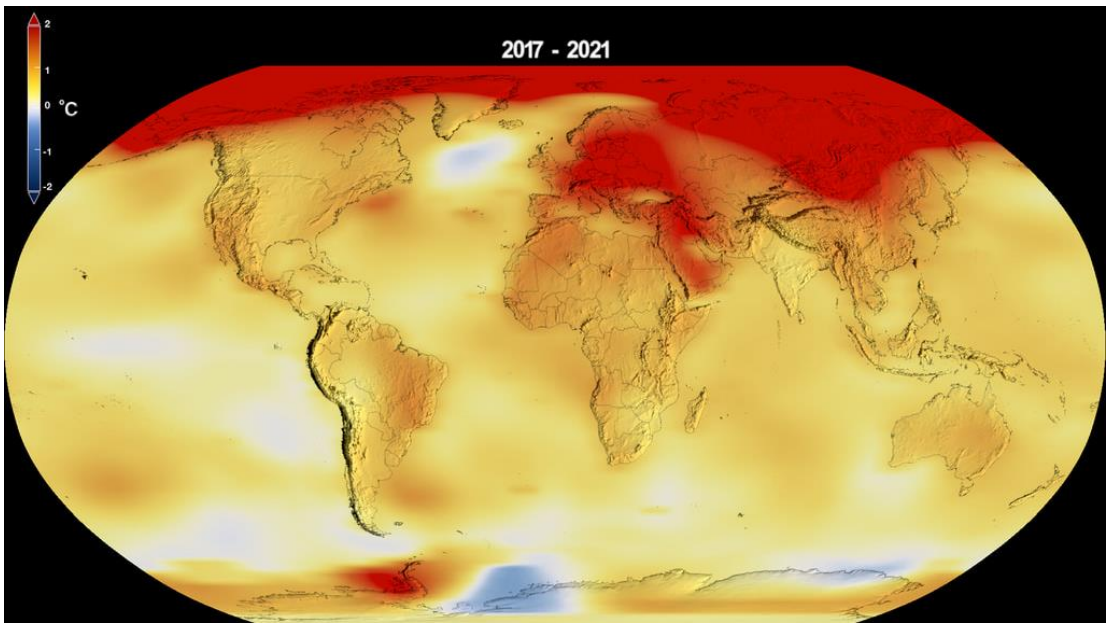

Figure 1-1. Five-year global temperature anomalies from 2017 to 2021. Normal temperatures are shown in white, higher-than-normal temperatures are shown in red and lower-than-normal temperatures are shown in blue. Image taken from NASA's website.

Such changes in the global climate were never observed before in human history, and some of them will be irreversible over hundreds or thousands of years. The global temperature is foreseen to continue to rise for many decades, with the main driver being the emission in the Earth's atmosphere of greenhouse gases such as methane, and in particular CO_2, as a direct result of human activities. In fact, during the COP26 summit, the Intergovernmental Panel on Climate Change (IPCC) assessed that human emissions already caused an increase of 1.1°C since 1750, and that it will exceed the threshold limit of 1.5°C in the next few decades, after which the catastrophic effects of global warming

will become irreversible [1,4]. Indeed, the concentration of CO_2 in the atmosphere is still steadily increasing since pre-industrial levels, with a record increment higher than 50% in 2021 (Figure 1-2).

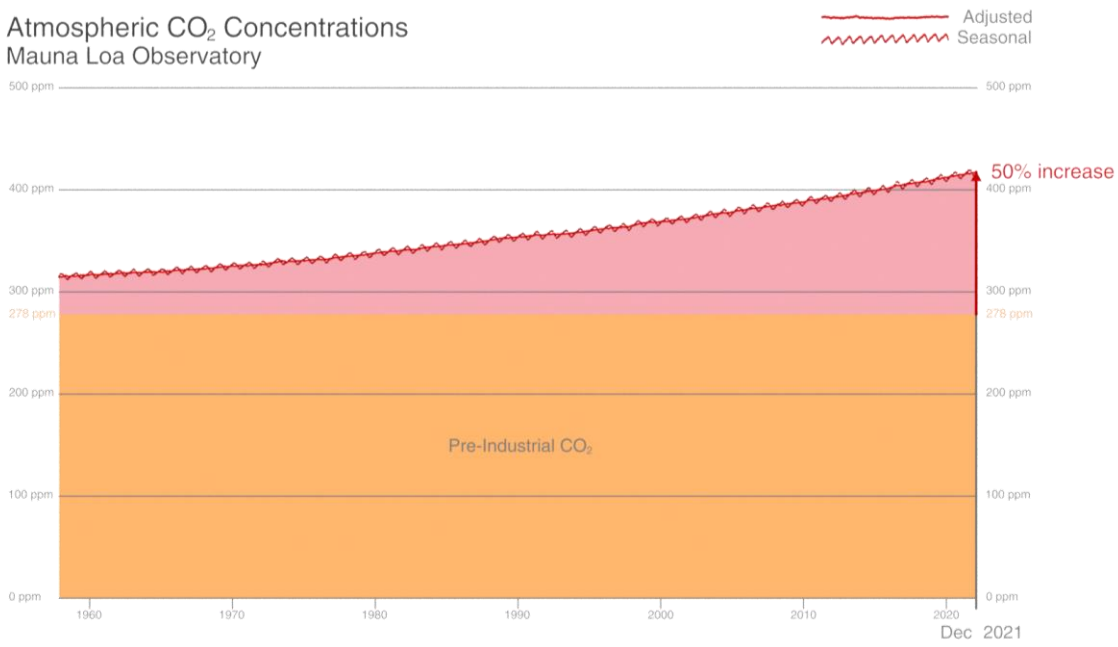

Figure 1-2. Timeplot (1958-2021) of atmospheric CO_2 concentration increase relative to pre-industrial CO_2 mean value of 278 ppm. Image taken from NASA's website.

In order to meet the targets stated in the Paris Agreement, a fast reduction in CO_2 emissions towards a Net-Zero Scenario by 2050 is imperative, and this would require a broad range of initiatives and policy approaches, taking into account key factors such as energy efficiency, electrification, renewables and carbon capture/storage [5,6].

Overall, about 50 billion tonnes of CO_2eq are produced every year globally [7] due to fossil fuels consumption; by breaking down the total emissions, it is clear that the global power sector (electricity and heat production for buildings and industry), as well as the transport sector (especially road vehicles), are those mostly contributing to CO_2 production (Figure 1-3), accounting for the 73.2% of the total emissions [8,9]. In 2021, the strong increase in coal-fired electricity generation caused an all-time high CO_2 emission from the power sector, with an increment of almost 700 Mt CO_2 [10]; moreover, as COVID-19 pandemic restrictions began to lift, CO_2 emissions from the transport sector in 2021 started to rise back with the previous growth trend, increasing by 8% as compared to 2020, when most countries still had a limited mobility and international commercial traffic [11].

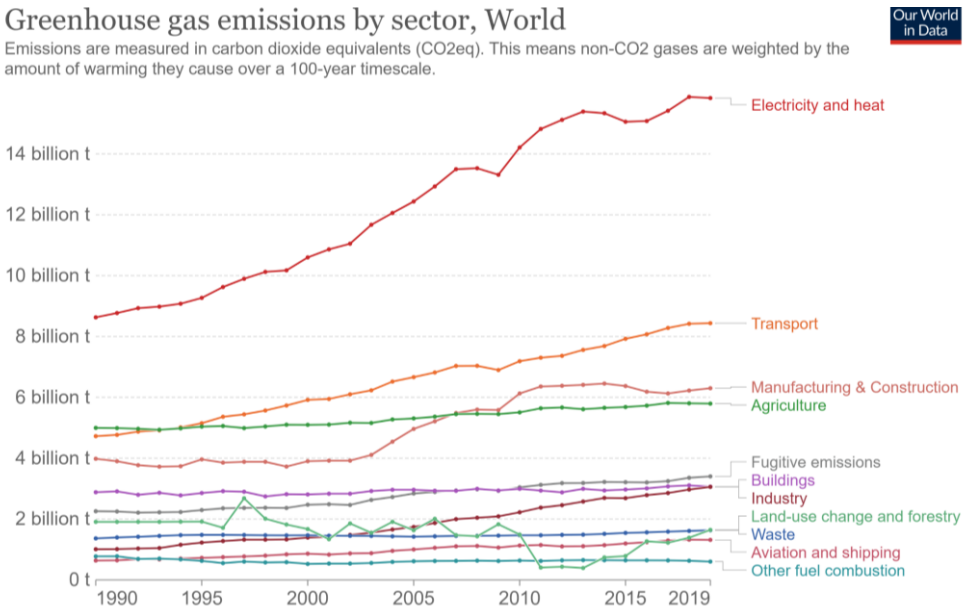

Figure 1-3. Global GHGs emissions by sector, measured in CO_2eq. Image taken from ourworldindata.org website.

All these data clearly show the necessity to change the way energy is produced, shifting from the usage of limited and polluting sources like fossil fuels (and their derivatives such as oil, coal and natural gas), towards more sustainable and renewable sources like solar, wind, hydroelectric or geothermal.

1.1 Electrochemical Energy Storage for the Grid

In order to promote a sustainable infrastructure to address energetic, economic and environmental problems related to the use of fossil fuels, electricity is progressively becoming the main energy source due to the increased usage of renewables on a large scale. Renewable sources would in fact offer a potential greener alternative to fossil fuels, but the intrinsic intermittent nature of these systems makes them unsuitable for widespread adoption and integration in the energy grid: the supply of electrical energy from variable resources like sun or wind might not be able to match the ever-increasing energy demand in the long run [12]. In addition, the use of fossil fuels for transportation still poses a major issue that must be addressed in terms of CO_2 emissions, making the electrification process essential in order to improve air quality especially in densely populated cities. In both cases, decarbonization can only be achieved by moving away from fossil energy production, meaning that hydrocarbons can no longer be the first choice for energy storage. This implies that a continuous supply of renewable energy is mandatory and can only be ensured by the presence of an appropriate energy storage system (ESS).

Being electricity the preferential way energy is going to be stored, the importance of electrochemical energy storage systems (EESSs) in this regard becomes highly relevant, especially for the transition towards a low-carbon society. These systems include all the devices able to store and release electrical

energy by exploiting redox reactions, and can be divided into several classes, as displayed in Figure 1-4.

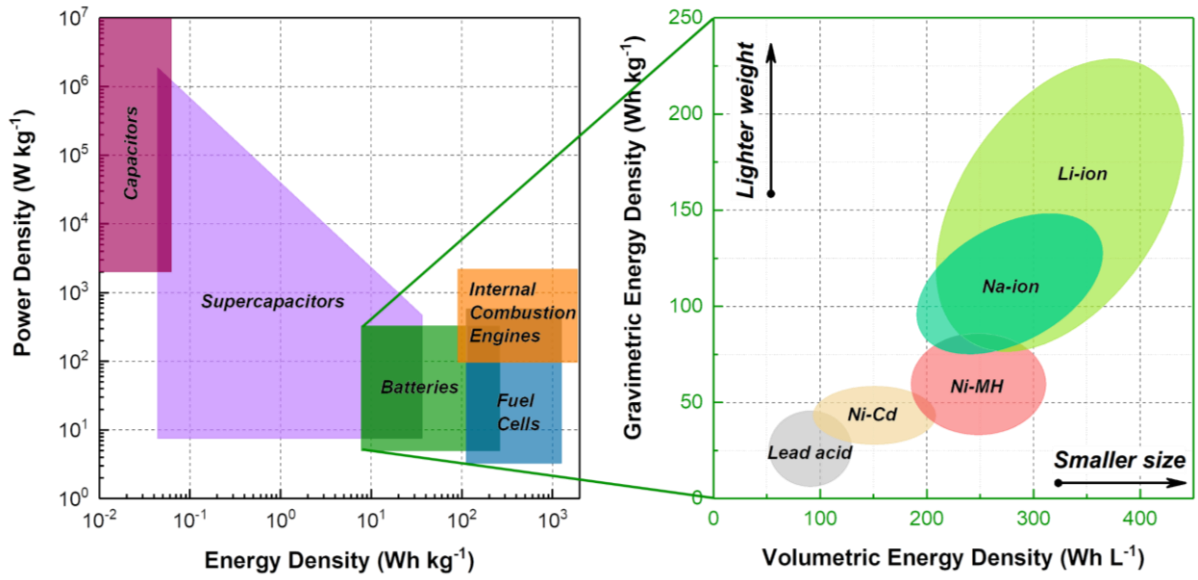

Figure 1-4. Ragone plot showing different EESSs in comparison to internal combustion engines, with emphasis on the different types of batteries.

All these systems can be mainly divided into capacitors, batteries and fuel cells, the latter possessing the highest energy density but still requiring a continuous input of reactants and a backup system to store the produced energy. Capacitors (and to a certain extent also supercapacitors) are devices which mainly exploit capacitive surface charge processes to store electrical energy; by contrast, the main drivers for energy storage in batteries are bulk redox reactions occurring within the electrode structure via charge transfer processes. When it comes to energy demanding applications, secondary rechargeable batteries are the devices possessing the highest energy density, together with an acceptable power density, hence they represent the devices of choice for the grid and the most promising devices to substitute internal combustion engines. However, most of the parameters such as nominal voltage, cycle life, stability, energy and power densities, largely depend on the cell chemistry comprising the battery [13,14].

Among the different types of batteries, two technologies are expected to be dominating starting from the next years to come:

-The first one is the already established Li-ion technology, which became the most employed one since its commercialization by SONY Corporation in 1991 [15] and took over the battery market for portable electronic devices and large-scale stationary storage applications thanks to its superior volumetric and gravimetric energy densities as compared to other battery types (i.e. Lead acid, Ni-Cd and Ni-MH), hence resulting in a higher output while maintaining a smaller size and weight for the device.

-The second one is the soon-to-be-commercialized Na-ion technology (e.g. by Faradion, Natron and CATL)[16–18], which was initially studied as a parallel research line to that of lithium; this type of device was recently brought back, and is expected to compete with the Li-ion battery market, providing a more environmentally sustainable and cheaper alternative at the expenses of some energy density.

1.2 Lithium-ion Batteries (LIBs)

Li-ion batteries (LIBs) are nowadays the power sources of choice for portable electronic devices and large-scale applications such as hybrid (HEVs) or electric (EVs) vehicles and stationary energy storage, providing power and energy densities much greater than any other battery type; rapidly becoming part of everyone's daily life, these systems have been constantly improved over the last three decades. Thanks to suitable properties such as low atomic mass (6.941 a.m.u.), low density (0.535 g cm^{-3}), low standard electrode potential (-3.04 V vs. SHE) and high theoretical specific capacity (3860 mAh g^{-1}), metal Li has always been a very attractive choice as a possible anode material in batteries. Its use in primary batteries was one of the research hotspots even before the discovery of lithium-ion intercalation into host materials. Since the 1960's nonaqueous 3 V primary lithium batteries employing metal Li as the anode have been commercially available in the market coupled with a variety of different cathodes [19–22]. In the 1970's, the first conceptualization for the fabrication of a lithium-ion battery came from M. Armand, with a system based on two different intercalation materials for both the anode and cathode [23]; the concept of lithium ions being transferred from one electrode to the other during the charge/discharge processes was later demonstrated in 1980 by Lazzari and Scrosati [24], and the battery was named "rocking-chair battery" after the peculiar shuttling mechanism of Li^+ ions. The chemical intercalation of lithium into a variety of layered transition dichalcogenides (sulfides and selenides) had previously been demonstrated by Wittingham in 1975, via a wet route employing n-butyl lithium [25]. Among the different studied compounds, TiS_2 emerged as the preferential one because of its low molecular weight, low cost, and good electronic conductivity, demonstrating the ability to intercalate lithium at a one mole ratio with an intercalation potential of about 2 V vs. Li^+/Li and a theoretical capacity of 240 mAh g^{-1} [26].This idea was then chosen by EXXON in an attempt to produce secondary lithium-ion batteries in nonaqueous liquid electrolytes employing TiS_2 and Li metal as electrodes [27]. However, synthetic and storage difficulties posed a major drawback for TiS_2, as the material is highly moisture-sensitive and must be kept under inert conditions to prevent its decomposition in TiO_2 and H_2S upon exposure to water. Moreover, the formation of a surface layer called Solid Electrolyte Interphase (SEI) had been observed when combining liquid nonaqueous electrolytes with alkali metals [28]. Being electrically insulating but ionically conductive, this layer is in principle beneficial as it passivates the surface of lithium making it stable in the electrolyte; however, the SEI itself was found to be unstable upon prolonged cycling, producing cracks and exposing further

lithium to the electrolyte, thus leading to a consumption of electrolyte and active lithium for the continuous reformation of the passivation layer. This effect led to the necessity of designing secondary cells with an excess lithium metal to offset the low coulombic efficiency [29]. However, the uneven deposition of lithium onto the cracked SEI still posed a problem in terms of safety, as it leads to the formation of dendrites and islands of highly reactive lithium metal, which causes a lowering in the thermal stability of the battery. This eventually led to the first attempts to lower the dendritic growth rate by employing Li/Al or Li/Mg alloys at the anode side [30,31], at the expenses of capacity and electrode potential, making the combination with TiS_2 much less appealing due to the low cell voltage. In 1976, the first studies by Besenhard and Eichinger regarding intercalation of Li^+ ions into graphite showed an intercalation potential close to the thermodynamic potential of Li metal, demonstrating a reversible intercalation up to LiC_6 [29,32,33]. However, lithiated graphite was not yet used as a cathode material due to the lack of suitable electrolytes to prevent solvent co-intercalation into the lamellar structure of graphite, leading to exfoliation and fast capacity fading [34–36]. In 1978 the group of Armand was able to demonstrate the suitability of graphite as an intercalated negative electrode, solving the co-intercalation problem by using a polymer electrolyte [37,38]. Due to the feasibility of using graphite instead of lithium as the anode, in 1979 the group of Basu developed a synthetic method for LiC_6 by employing molten lithium [39], eventually leading to a reversible intercalation battery combining LiC_6 and TiS_2 in a molten electrolyte system, patented by the Bell labs [36], although the use of this battery was limited by the high operating temperatures ranging from 375 to 500 °C.

Together with the abovementioned concept of rocking-chair battery, the high-voltage layered $LiCoO_2$ (LCO) cathode was eventually developed by Goodenough in 1980 [40], from which lithium could be safely and reversibly removed to an upper cut-off voltage of 4.2 V vs. Li^+/Li. Finally, in 1990 a decisive study by Dahn demonstrated the stability of graphite anodes in nonaqueous electrolyte solutions, showing that a combination of ethylene carbonate (EC) and propylene carbonate (PC) as the solvents allowed the reversible intercalation of lithium with little capacity fading, thanks to the formation of a stable SEI at 0.8 V vs. Li^+/Li [41]. Indeed, solvent mixtures of cyclic esters (EC or PC) and linear esters (dimethyl carbonate (DMC) or diethyl carbonate (DEC)) with $LiPF_6$ as the salt, are the commonly employed electrolytes in today's LIBs [42]. With all the pieces in place, the commercialization of the first Li-ion battery based on a LCO cathode, a disordered carbon anode and a nonaqueous electrolyte solution of $LiPF_6$ in PC:DEC eventually happened in 1991, and it became widely successful ever since [15]. The disordered carbon was then substituted with the more suitable graphite from 1993 on, allowing for the formation of a stable SEI before the actual intercalation of lithium took place (Li^+ intercalation for graphite is at $E < 0.25$ V vs. Li^+/Li, while for hard carbons it starts at $E < 1.5$ V vs. Li^+/Li) [43,44].

Despite a progressive optimization during the years, lithium-ion batteries still rely on the same basic design as three decades ago, with the main components being the cathode, anode, electrolyte, separator and the current collectors (Figure 1-5).

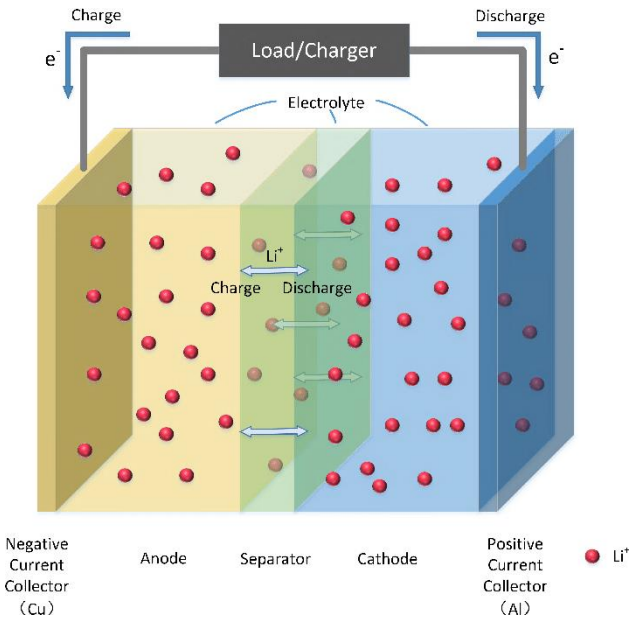

Figure 1-5. Schematic illustration of a Lithium-ion battery [45].

The cathode is the electrode at the higher potential, which is oxidized during the charge process of the cell; on the contrary, the anode is the electrode at the lower potential, which in turn gets reduced during the charge process. When discharging, the two processes are reversed. Upon charge/discharge, the electrons flow from one side to the other through an external electrical circuit connecting the two electrodes. On the other hand, Li^+ ions shuttle from one electrode to the other through the electrolyte solution to provide the flow of ionic current and guarantee the charge balance between the electrodes. A microporous polymeric separator, generally made of polyethylene or polypropylene, is immersed into the electrolyte and between the two electrodes in order to ensure permeability of the former, physically separate the latter preventing any short circuit from direct contact. Finally, the current collectors (Cu for anodes and Al for cathodes) act as a rigid and electronically support for the active materials, which are coated and attached to them by means of a polymeric binder able to provide adhesion and flexibility to the electrode film.

The charge/discharge reaction mechanism for the state-of-the-art LIBs comprising a graphite anode and a $LiCoO_2$ cathode is summarized as follows (Equation 1-6).

Charge process

Cathode $$LiCoO_2 \rightarrow Li_{1-x}CoO_2 + xLi^+ + xe^- \quad \text{Eq. 1}$$

Anode $$6C_{(graphite)} + xLi^+ + xe^- \rightarrow Li_xC_6 \quad \text{Eq. 2}$$

Overall $LiCoO_2 + 6C_{(graphite)} \rightarrow Li_{1-x}CoO_2 + Li_xC_6$ **Eq. 3**

Discharge process

Cathode $Li_{1-x}CoO_2 + xLi^+ + xe^- \rightarrow LiCoO_2$ **Eq. 4**

Anode $Li_xC_6 \rightarrow 6C_{(graphite)} + xLi^+ + xe^-$ **Eq. 5**

Overall $Li_{1-x}CoO_2 + Li_xC_6 \rightarrow LiCoO_2 + 6C_{(graphite)}$ **Eq. 6**

Upon charge, Co is oxidized from +3 to +4 oxidation state, releasing Li^+ ions which move to the anode side through the electrolyte solution, and electrons which move to the same direction but through the external circuit. On the anode side, graphite is in turn reduced with the insertion of Li^+ ions within the graphene layers composing the structure.

As previously mentioned, during the first cycle the anode (and, to a minor extent, the cathode) can react with the electrolyte solution and form a solid passivation layer on the electrode-electrolyte interface, called Solid Electrolyte Interphase, or SEI (Figure 1-6); this layer is generated due to the decomposition of the electrolyte at the lower (or higher) potential cut-off, where it becomes unstable. It generally behaves as an ionic conductor and an electronic insulator, and once formed it protects the electrodes from further reactions with the electrolyte, however its formation is irreversible and causes an initial loss of efficiency. The extent of its formation and stability are determined by the nature of the electrolyte and its solvents, since some solutions may be favorable while others may not [46,47].

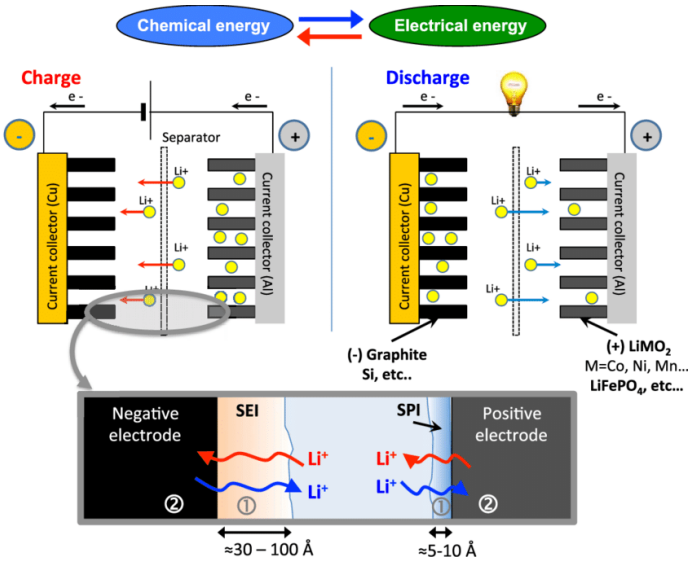

Figure 1-6. Formation of Solid Electrolyte Interphase (SEI) and Cathode Electrolyte Interphase (CEI) [48].

Despite the optimizations carried on in the last 30 years of research, lithium-ion batteries still suffer from some drawbacks, such as higher initial costs with respect to other types of batteries, possibility of permanent damage of the cell out of the recommended temperature ranges, and irreversible

degradation due to overcharge of the cell or excessive lowering of the potential. Moreover, the currently employed materials struggle when it comes to reaching the proper energy density for powering EVs while guaranteeing a suitable driving range per single charge [49].

1.3 Sodium-ion Batteries (SIBs)

The history of sodium-ion batteries (SIBs) goes back to the early studies on LIBs, but it was hindered after the commercialization of the latter. When the ability of TiS_2 to reversibly undergo electrochemical intercalation reactions was first reported, Li and Na were found to be equally capable of being inserted into the layered structure [50], despite no functional devices could be developed due to the low cathode operating voltage. The discovery of layered metal oxides of the $NaMO_2$ family was pioneered by Delmas in the early 1980s, parallel to the proposal by Goodenough to employ $LiMO_2$ compounds as cathodes for LIBs [51,52], but the lithium-based compounds resulted more attractive due to their superior electrochemical properties. As for the anode side, after the "rocking chair" concept was proposed by Scrosati [24] and after the discovery that carbonaceous materials could intercalate lithium at a desirably low potential [53], the first LIB was successfully commercialized [15]. The sharp rise in the popularity of the lithium-ion battery, combined to the fact that the use of soft carbons or graphite as anodes for SIBs resulted into a capacity almost tenfold lower than LIBs, set the start of the decline for research in sodium-ion systems [54,55]. Intensive developments were carried out only in high-temperature sodium batteries like the sodium-sulfur system (Na-S) or the ZEBRA cell, operating between 250 and 350 °C [56,57], which were employed for stationary grid energy storage and space missions [58]. Despite the problems associated with the use of high operating temperatures such as corrosion and low energy efficiency, these systems proved the feasibility of sodium-based energy storage on a large scale. A first rejuvenated interest in room-temperature SIBs came in 2000 with the discovery of Na intercalation into hard carbons (HC) by Stevens and Dahn, with performance close to those of graphite in LIBs [59,60]. From the year 2000 on, published research on SIBs started to increase, with the number of related publications slowly rising until 2008 and eventually rising exponentially up to becoming even higher than that related to LIBs (**Figure 1-7**).

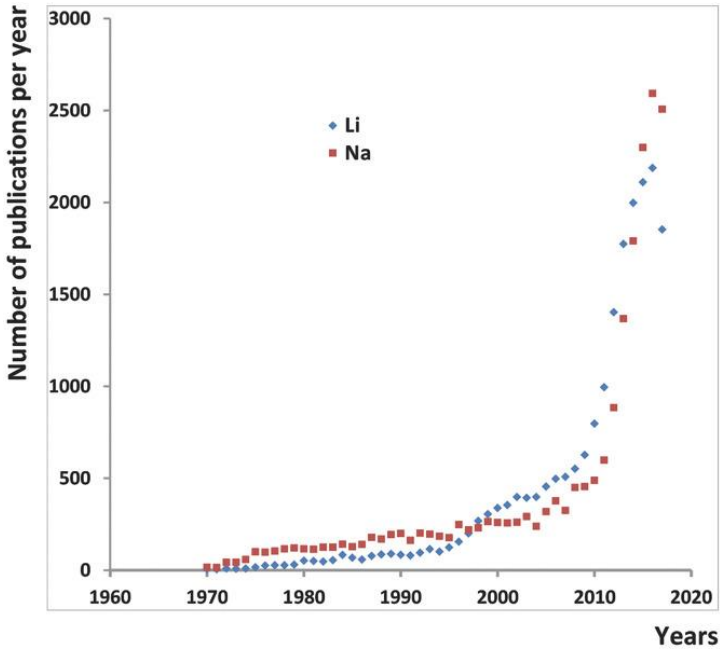

Figure 1-7. Comparative evolution of the number of publications per year for both LIBs and SIBs [61].

As already mentioned, with the development of portable electronic devices such as laptops and mobile phones, the production of LIBs became more and more relevant over the past years. However, with the recent development of EVs to offset emissions from internal combustion engines, and the need for higher gravimetric and volumetric energy densities, a greater number of large battery factories is needed to meet the demand for LIBs production and the optimization of capacity, lifetime, safety and price required by car producers. Although these requirements are already on the way to be addressed, the limited availability of Li on the Earth's crust is becoming an increasingly concerning topic, both because of the price increase of raw materials (e.g. the price of battery-grade Li_2CO_3 increased of nearly three times in 2015 due to demand from e-mobility sector), and their uneven geographical distribution in few countries [61,62], which could result in supply shortage and overexploitation of the sources.

With the transition towards climate neutrality, LIBs are also expected to play a critical role in the stationary storage sector for renewable energy sources, with big installations of the gigawatt-hour scale already being anticipated [63,64]. However, whether energy density is the primary metric for mobile applications like portable electronics and EVs, the main parameters to be considered for stationary applications for the grid are price and power. For this reason, the application of SIBs for stationary purposes is now considered an equally viable technology as LIBs, with the ability to partly release the huge pressure on the already congested value chain of lithium-ion batteries. Given the characteristic of Na as compared to Li (**Table 1-1**), research interest on SIBs recently gained momentum, since they are the devices which hold the greatest potential to match the performance of LIBs [65].

Table 1-1. Main differences between LIBs and SIBs in terms of cation properties, cost of materials and abundance.

	Li-ion battery	Sodium-ion battery
Cation radius	0.76 Å	1.06 Å
Atomic weight	6.9 g mol^{-1}	23 g mol^{-1}
E^0 (vs. SHE)	Li^+/Li, - 3.04 V	Na^+/Na, - 2.71 V
Cost (carbonates) [352]	78.00 $ / kg (april 2022)	0.40 $ / kg (april 2022)
Cost (collector at anode)	Cu, 7000-8500 $ / ton	Al, 2000-2500 $ / ton
Abundance on Earth's crust	20 mg kg^{-1}	23.6 x 10^3 mg kg^{-1}

Being Li and Na neighboring alkali metals, they share most of their chemistry, hence the working principles of SIBs is basically the same as LIBs, with Na^+ ions reversibly shuttling between the two electrode materials through an electrolyte solution upon charge/discharge processes. However, Li^+ and Na^+ present some important differences as electrochemical carriers which must be considered for practical applications: by looking at the two systems, Na possesses a larger ionic radius, a higher atomic weight and a slightly higher redox potential vs. SHE as compared to Li. All these factors contribute to a slower ion transport and diffusion, a less stable formation of interphases, larger volume variations, and inevitably to an energy penalty to pay with respect to LIBs. However, the strength of SIBs relies in the higher availability of raw materials and the possibility to have lower costs of production for the whole battery, including the possibility to employ the cheaper Al current collector also on the anode side (Na does not alloy with Al even at low potentials).

Same as in lithium-ion batteries, the formation of an interphase at both electrodes during the first cycles also happens in SIBs; however, due to the high reactivity of the sodiated compounds, this is a much more crucial phenomenon, since the electrolyte decomposes into oxygen-rich compounds such as sodium carbonates and alkoxides. The passivation layer, especially at the anode, is partially soluble in carbonate electrolytes, often resulting in a dynamic formation-dissolution process upon cycling and progressive depletion of active Na from the electrolyte [66]. The formation and characteristics of the solid electrolyte interphase in Na-ion batteries is one of the most important parameters, and it is believed that it could have a fundamental role towards the economic success of this technology.

Rechargeable batteries based on sodium are indeed very promising for EES applications and for the creation of an interplay between renewable energy generation, energy storage and energy supply [67–69], and in this regard companies like CATL, Faradion or Natron recently announced the commercialization of the first SIBs for large scale applications [16–18].

1.4 Cell components

All the main components comprising the final cell have a critical influence over its performance. The anode and cathode materials are of primary importance, since they are the ones mainly influencing the

characteristics of the cell. Several materials that could properly work as electrodes have already been studied along with strategies to improve their performance, but a plethora of other materials with intriguing characteristics are still the focus of intense research. The development of new binders is also a research hotspot since they are also responsible, to some extent, for the performance of the cell. Environmentally friendly binder materials with desirable mechanical characteristics have been studied for the development of greener electrodes. Finally, another key component is the electrolyte solution, since it determines the formation and stability of the SEI/CEI and the ionic conductivity of the system. Therefore, an ideal combination of salt and solvent must be researched, together with possible additives that could improve the stability of the passivation layers.

An overview of the abovementioned components in Li- and Na-ion batteries is provided in **Subsections 1.4.1**, **1.4.2**, **1.4.3** and **1.4.4**.

1.4.1 Anode materials

Anode materials are compounds able to accept Li^+ or Na^+ ions during charge, and release them during discharge, granting the cyclic working of the cell. Desirable anode materials should be able to react with lithium at a low working potential with respect to the Li^+/Li or Na^+/Na redox couples. According to the type of interaction they have with the positive ions, anode materials can be generally divided into different classes: intercalation, conversion and alloying mechanism. Each type of anode possesses advantages and drawbacks over the others, and their characteristics are summarized in the following subsections.

Intercalation materials – Carbon-based

In metal-ion batteries, the negative electrode can be composed of intercalation carbonaceous materials, whose characteristics are influenced by the surface area, crystallinity, morphology and spatial orientation of atoms, since different degrees of graphitization and order of the layers can exist [70]. The success behind the use of carbon and its allotropes in rechargeable batteries lies in their low cost, large abundance, excellent reversibility shown during cycling and uniquely tunable electronic and structural properties.

In the case of LIBs, the anode material of choice is graphite, the most stable among the allotropic forms of carbon. Graphite structure is composed of stacked sp^2-hybridized graphene layers linked together by weak van der Waals forces and π-π interactions between the delocalized electron orbitals [71]. The layers are mostly stacked in the thermodynamically stable ABAB fashion with hexagonal symmetry (**Figure 1-8a**), with a small contribution from the less stable ABCABC sequence with rhombohedral symmetry [72]. The weakness of the van der Waals interactions between graphene layers

enable the intercalation of ionic species, since they allow for expansion of the interplanar distances with re-stacking of the layers [73], making it a suitable host material for Li^+ ions in LIBs.

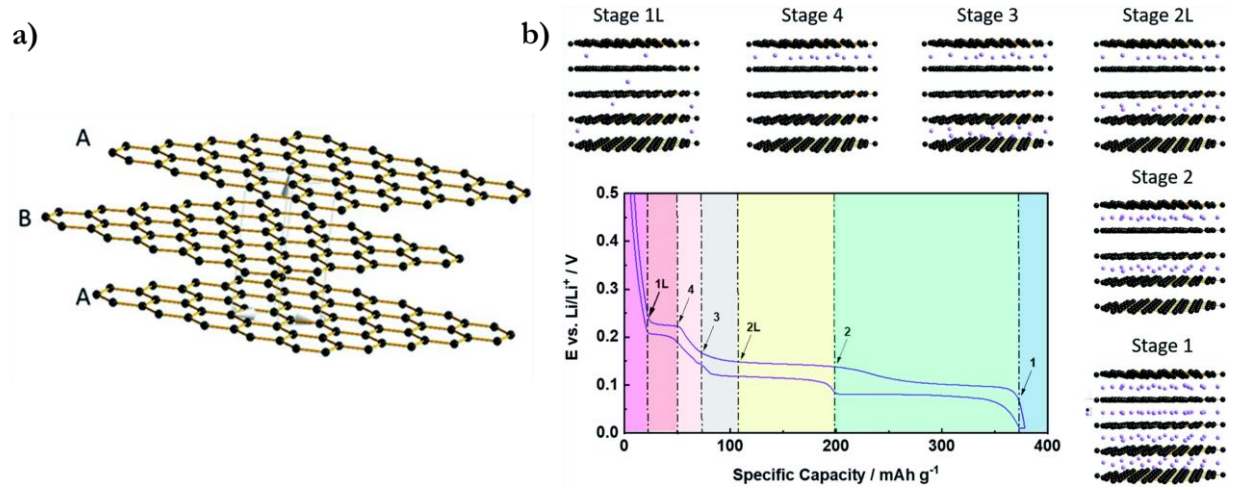

Figure 1-8. a) Schematic representation of ABAB-stacked graphene layers with hexagonal structure; b) Illustration of the staging mechanism for electrochemical (de)intercalation of Li^+ ions into graphite [74].

The intercalation of Li^+ ions in graphite occurs via a concentration-dependent process called "staging mechanism" [75,76], as illustrated in **Figure 1-8b**. According to this model, each n^{th} stage compound is characterized by a periodic sequence of layers incorporating the intercalant species separated by layers without any intercalant species, in which n defines the number of graphene planes between two intercalated layers, with Stage 1 as the highest lithiated state of graphite at ambient conditions. By electrochemically intercalating lithium ions into graphite, the different stages can be identified as plateaus (or sloping regions) in the galvanostatic profiles. The staging process occurs through the formation of a first random solid-solution-type intercalation, with Li^+ ions organized in a liquid-like manner (Stage 1L). Subsequently, a phase transition occurs from Stage 1L to Stage 4 and then Stage 3. The transition to Stage 2L is temperature-dependent, and its structure is not yet completely understood. An increasing lithium content leads to the formation of Stage 2 accompanied by an increase in the in-plane ordering. Finally, a first-order transition to Stage 1, accompanied by a sliding of the single planes with respect to each other and an increase of the interlayer distance to 3.70 Å (lithium-free graphite is 3.35 Å), leads to a stoichiometry of LiC_6 providing a theoretical capacity of 372 mAh g^{-1} [77–80]. The whole process of lithium intercalation is summarized in **Equation 7**:

Intercalation $$6C_{(graphite)} + xLi^+ + xe^- \leftrightarrow Li_xC_6$$ **Eq. 7**

Despite the high stability and reversibility of graphite as the anode in LIBs, its relatively low theoretical specific capacity is not suitable for high-energy-density applications such as transport electrification, and other types of anode materials have been progressively studied, considering performance as well as sustainability, stability, cost and safety.

The inability of Na^+ ions to be reversibly intercalated and form graphite intercalation compounds (GICs) inhibited so far the use of graphite as the anode material for SIBs. The higher ionic radius of sodium as compared to lithium is not the main obstacle for intercalation, since larger alkali metal ions (i.e. K^+, Rb^+ and Cs^+) have been reported to form GICs [81–83]. Rather, Na-GICs were found to have the lowest energetic stability and formation potentials, below that of metal Na [81,84,85], due to the very weak chemical binding ability of sodium towards a given substrate as compared to all other alkali metals. Attempts to promote electrochemical activity of graphite as the anode in SIBs involved the use of glyme-based electrolytes enabling the co-intercalation of solvated Na^+ ions, although only a limited capacity has been achieved so far [86,87].

For these reasons, the anode of choice for SIBs is a disordered, non-graphitizable carbon called hard carbon [69,88,89], which represents the most promising negative electrode due to its high storage capacity, low working potential and cycling stability. Moreover, hard carbons can be produced by several sources including waste biomass, which represents a great advantage regarding costs, sustainability and large-scale production [90–92]. Differently from the non-porous graphitizable soft carbons, which are generally produced by gas or liquid phase carbonization of aromatic compounds or polymers [93], the synthesis of hard carbons is generally performed by solid-phase carbonization at temperatures near 1000 °C [94], giving rise to a mechanically hard and porous type of carbon, with an interlayer spacing of 3.7-4.0 Å able to facilitate the access of Na^+ ions into energetically stable sites near defects [93,95,96].

Depending on the employed precursor, the presence of folded graphenic domains, local random stacking, interlayer crosslinking, pores, voids and interstitial heteroatoms (e.g. N, O, S, P), hard carbons generally have quite complex turbostratic structures [97–101], making it difficult to properly describe a unique model. Indeed, several structural models have been already proposed over the years, each of them emphasizing the different properties of hard carbons (**Figure 1-9**). Although porosity is a common key property of all these models, the definition of a structural model able to take into account the complex nature of porosity in hard carbons has not yet been defined, and it is still one of the main controversial topics in this regard.

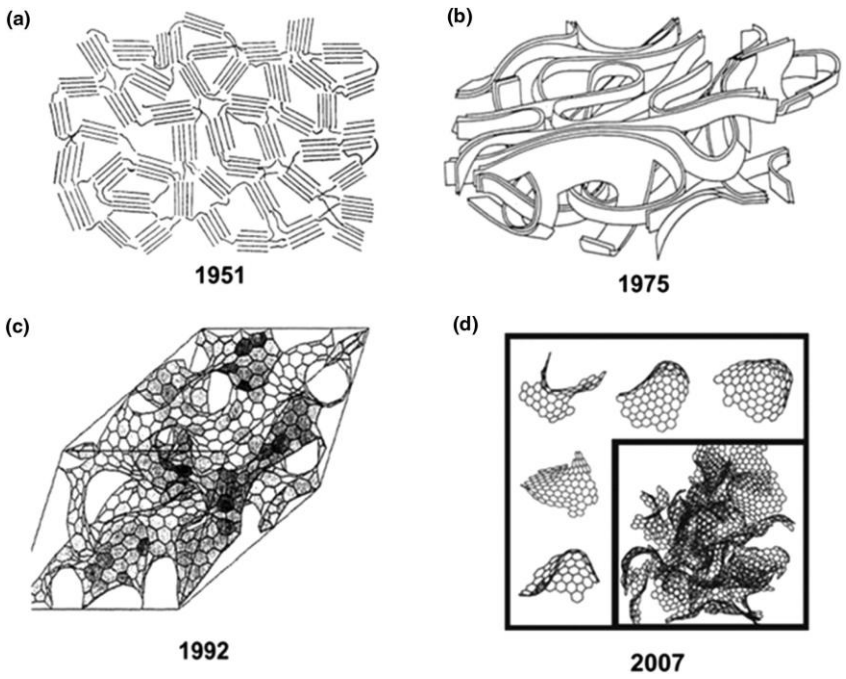

Figure 1-9. Schematic representation of the main models for the structural representation of hard carbons [98,102–104].

Despite the different attempts to describe the structures of hard carbons, the "house of cards" model proposed by Dahn [93] is still the most employed one when trying to link between porosity and structure, with the assumption that hard carbons are composed of a combination of pseudo-graphitic micro-crystallites (sp^2-hybridized turbostratic stacked graphene planes) and amorphous regions (sp^3-hybridized edges and defects in the graphene planes).

Regarding the electrochemical behavior of hard carbons as anodes in SIBs, many improvements in terms of performance have been achieved thanks to the contributions from several research groups, with specific capacities reaching values close to those of graphite in LIBs. However, given the lack of a unique structural model, the sodium storage mechanism still remains a controversial topic, with debates over the sloping or plateau regions of the typical galvanostatic (dis)charge profile of the material. Basically, three different kinds of occurring processes can be summarized:

- Na-ion adsorption/chemisorption at defects in the graphene planes, mainly influenced by the presence of heteroatoms serving as reactive sites and increasing the achievable capacity (and initial irreversibility) [60,95,97,105].
- Na-ion inter-lamellae intercalation, mainly influenced by the interlayer spacing and the presence of defects or heteroatoms in the graphene planes [106,107].
- Nanopore filling from pseudo-adsorption or clustering of sodium on the micropore walls, mainly influenced by the bulk internal closed microporosity and accounting for the diffusive contribution in the storage mechanism [105,108–110].

According to the different processes, the sodium storage mechanism can be summarized into four main proposed models (Figure 1-10).

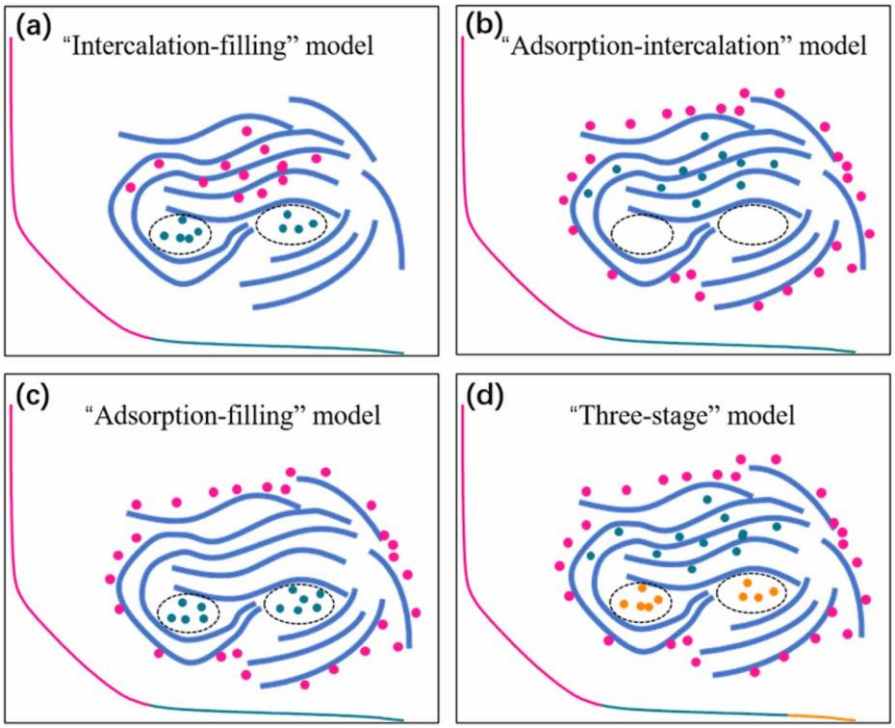

Figure 1-10. Schematic representation of the sodium storage models. a) intercalation-filling model; b) adsorption-intercalation model; c) adsorption-filling model; d) three-stage model [111].

The first model (intercalation-filling) assumes the sloping region of the galvanostatic profile to be related to Na^+ ions intercalation within graphene planes, while the plateau region is associated to nanopore filling between the randomly stacked planes [59,60].

In the second model (adsorption-intercalation) the sloping region is associated with Na^+ ions adsorbing at the surface of defect sites and later intercalating into the graphene planes in the plateau region [112,113].

As for the third model (adsorption-filling), the Na^+ ions are adsorbed at the defect sites in the sloping region as well, while the plateau region is related to nanopore filling [114,115].

Finally, the fourth model (three-stage) addresses the sloping region to the Na^+ ions adsorption at the defects, while in the plateau region both the ion intercalation and eventually the nanopore filling are accounted for [107].

Although the sodium storage models differ from each other, they are a useful tool for the design of optimized hard carbons for SIBs: combining the use of cheap and widely available waste biomass as the carbon precursor with the possibility to tune the formation of structural defects, heteroatom doping, interlayer spacing and porosity upon synthesis, would indeed provide a great opportunity towards commercialization of low-cost and sustainable SIBs with high performance.

Conversion materials

Because of the limited number of intercalated ions in the crystal structure, carbonaceous intercalation compounds generally yield relatively low theoretical capacities. Researched as a parallel line to alloying and intercalation materials, conversion-type compounds have been attracting much interest as possible ideal anodes for alkali-ion batteries. A wide range of transition metal oxides, sulfides, phosphides and similar compounds of p-block metalloids have been explored as conversion-type anodes thanks to their interesting electrochemical properties, greatly broadening the material selection for high-performance batteries [116–121]. Considering that many conversion-type materials can be found in their natural form (e.g. magnetite, pyrite, pyrolusite, etc.), they could indeed provide low-cost compared to other materials. When compared to intercalation anodes, conversion anodes display a broader range of working potentials vs. Li^+/Li and Na^+/Na (generally between 0.5 and 1.5 V) and higher theoretical capacities, depending on the strength of the ionic bond between the transition metal cations and the counter-anion employed (Figure 1-11) [117,122,123]. Moreover, they can ensure better safety than carbon-based anodes thanks to the slightly higher operating potential, reducing the risk of dendrite formation [124], and as a result they have been studied as promising candidates for next-generation LIBs and for SIBs.

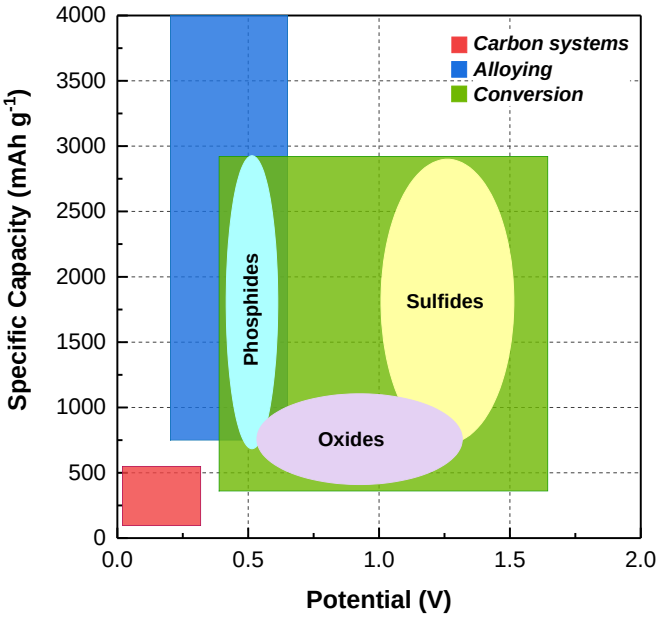

Figure 1-11. Different Li- and Na-ion battery anode systems listed on the basis of reaction potential and specific theoretical capacities. Different types of conversion anodes are also highlighted.

This category of materials includes all the compounds able to store ions through a reversible replacement redox reaction between the alkali metal ion and the transition metal, ultimately resulting in the formation of a metallic phase and an alkali oxide/sulfide/phosphide [125–127] according to the general reaction in Equation 8:

Conversion $$M_bX_c + (c \cdot n)A^+ + (c \cdot n)e^- \leftrightarrow bM^0 + cA_nX$$ **Eq. 8**

where A = Li, Na; M = TM; X = O, S, P, N, Se, F, H

The lithiation and sodiation processes inevitably involve breakdown of the single-crystalline parent material to polycrystalline metal nanoclusters dispersed in an amorphous alkali metal oxide matrix. Hence, the reaction can only occur via bond breaking and formation of new bonds with a complete structural rearrangement (**Figure 1-12**), formation of multiple intermediate phases and loss of long-range crystalline ordering [128–130].

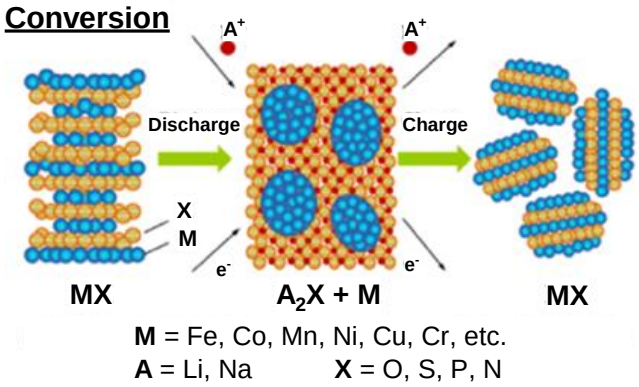

Figure 1-12. Schematic illustration of the conversion reaction mechanism and structural rearrangements for Li^+ and Na^+ ions storage [131].

Although these materials offer the possibility to tune the working potential by accordingly choosing the most appropriate combination of TM and counter-anion, while achieving high specific capacities and energy densities thanks to the exploitation of multiple oxidation states and multiple electrons per single process, their practical application has been hindered by some intrinsic shortcomings.

The formation of the A_nX species is thermodynamically feasible, but due to the electrochemical inactivity of these species, their decomposition by bulk M powder is hard, but reversibility is in principle ensured by the formation of highly electroactive metal nanoparticles able to decompose the A_nX matrix [132,133]. However, M nanoparticles may nucleate and aggregate after their formation and gradually increase in size upon cycling, resulting in the gradual loss of reversibility of the process and leading to inconsistent cycling stability [134]. Another drawback for industrial applications is the fact that the incomplete reduction, the formation of metastable phases and the ion diffusion within the material generally originate the characteristic sloping plateaus in the potential profiles of conversion anodes, implying that the (dis)charge process occurs over a range of different potentials rather than one fixed voltage (flat plateau), which would be more desirable in order to have less voltage fluctuations in a full cell configuration [135]. Moreover, the substantial structural rearrangement upon (de)lithiation or (de)sodiation generally cause low coulombic efficiency at the first cycle, [126], pulverization issues upon repeated cycling [136] and a high voltage hysteresis between the charge and discharge processes, which

leads to a low energy efficiency and internal heat evolution [133]. The voltage hysteresis appears to be highly dependent on the nature of the anionic species in the order of fluorides > oxides > sulfides > phosphides [126,133], but although different explanations have been proposed for this phenomenon [137,138], the origin of the voltage hysteresis in conversion anodes is still not clearly understood. In general, improving the performance of these materials requires a proper control over the particle size and morphology [139,140] in order to mediate faster ionic transport and minimize the effects of sluggish kinetics. The use of carbon materials to form composite anodes in combination with conversion materials also showed to enhance the electrochemical performance of the active component, providing high conductivity, surface area and mechanical strength [141–143]. Finally, composition control is also important to reduce the voltage hysteresis and improve the overall performance of the material, as several transition metals can be combined to different anionic species to achieve suitable performance.

Among the different conversion anodes, binary and ternary oxides of 3d transition metals (e.g. Cr, Mn, Fe, Co, Ni and Cu) are the most explored for both LIBs and SIBs [144,145]. In particular, due to its high capacity of 1011 mAh g^{-1}, abundance and stability, Fe_2O_3 is one of the mostly studied systems in this category, and several efforts have been studied in terms of morphology, size, precursors and synthetic procedures [146]. Mixed oxides with more than one electrochemically active metal with formula AB_2O_4 have also been studied as hosts for Li-/Na-ion batteries [147,148], displaying transition from spinel to cubic phases upon conversion, but a somehow restricted back conversion due to the lesser tendency of one of the constituent metals to change between oxidation states.

In addition to oxides, transition metal chalcogenides, phosphides, nitrides and hydrides have also been explored for LIBs and SIBs, with sulfides displaying particularly interesting properties [149,150]. Compared to oxides, sulfide species possess better electrical conductivity but suffer from dissolution of the discharge product leading to low coulombic efficiency and poor cycle life.

Alloying materials

Anode materials based on alloying mechanism generally exhibit very high specific capacities approximately 1-3 times higher than those of conversion-type materials and up to 10 times higher than those of carbon intercalation materials, with formation of Li- or Na-rich alloys forming upon reaction with the alkali metals (**Figure 1-13**). Many metals and metalloids, in particular those of groups IV and V, are active towards alloy formation with Li or Na even at room temperature [151–154], and thanks to their relatively good electronic conductivities, suitable discharge plateaus and operating voltage, they are among the most promising anode materials for high-energy density batteries.

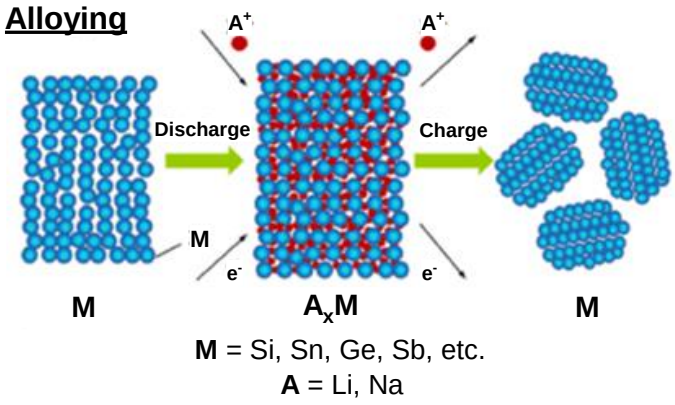

Figure 1-13. Schematic illustration of the alloying reaction mechanism and A_xM-type alloy formation for Li^+ and Na^+ ions storage [131].

The alloying process generally occurs through formation of Li_xM-type (or Na_xM) alloy phases with progressively increasing Li/Na content upon uptake of the alkali metal, and the general reaction is described by **Equation 9**:

Alloying $$M + xA^+ + xe^- \leftrightarrow A_xM$$ **Eq. 9**

where A = Li, Na; M = Si, Sn, Ge, Sb, P

Alloying-type anodes are able to work at a relatively low potential versus Li^+/Li or Na^+/Na, with specific capacities and energy densities largely exceeding that of the state-of-the-art graphite [155]. This advantage, combined to the abundance, safety, environmental benignity and low cost of elements such as Si and Sn raised an increasing interest on alloying-type materials as suitable anodes for next-generation LIBs and for SIBs. Nevertheless, there are still big challenges to be overcome for the full implementation and commercialization of these materials: the alloying process involves huge volumetric expansion (up to 300% for Si) and contraction, leading to pulverization of the electrode, loss of contact from the current collector (**Figure 1-14**) and instability of the SEI, resulting in poor cycling stability and fast performance decay [131,152,156,157]. Moreover, the radius of the alkali metal has a strong influence on the alloying reaction, resulting in higher deformation and lower capacities for Na-alloys as compared to Li-alloys [158,159]. Alloying anodes in SIBs are therefore expected to deliver lower specific capacities at higher potentials, providing a lower gravimetric and volumetric energy density than in LIBs [160]. However, the less reductive Na^+/Na potential in Na-alloys should provide a lower electrolyte reduction and degradation at the electrode surface [161].

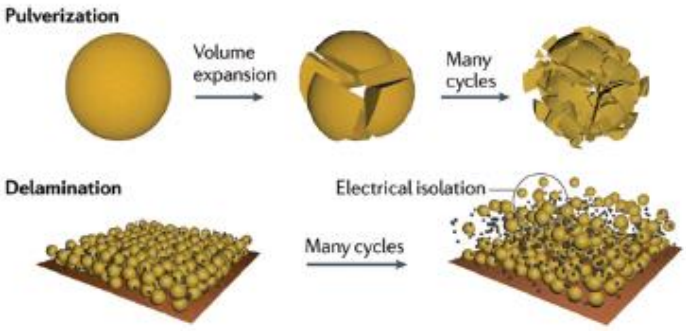

Figure 1-14. Schematic illustration of the pulverization process of the active material particles and their detachment from the current collector during the alloying reaction [156].

More generally, a number of phenomena can occur when the alloying reaction takes place [152]: 1) the loss of active material due to the volume expansion and subsequent pulverization leads to the isolation of particles and inactivation of the electrode, which translates into a lower conductivity; 2) the formation of an unstable SEI onto alloying anodes and its breaking due to the continuous volume changes upon cycling leads to a loss of both reversible and irreversible capacity; 3) the trapping of ions into the host alloy due to a slow kinetics of release, the formation of stable lithiated/sodiated compounds, or the formation of strong bonds with less coordinated atoms in defects of the structure, is an irreversible process, thus affecting the irreversible capacity; 4) the reaction of ions with the oxide layer on the surface of metal particles, formed during preparation of the electrode or naturally present, leads to further Li^+ or Na^+ depletion, since they can irreversibly react to form insulating Li_2O and Na_2O; 5) the aggregation of particles due to the heating induced by the pressure generated upon volume expansion constitutes another irreversible process.

In order to mitigate these phenomena, different strategies have been developed to reduce the effects of the volume changes. A good approach is to disperse the particles of active material in a matrix, in order to buffer the volume changes and preserve the integrity of the electrode. The matrix must favor a fast ion exchange and maintain the structural stability of the whole electrode; moreover, it must prevent particle aggregation by working as a spacer. Materials suitable for use as matrices can be divided into four main categories [152]:

1. Inactive matrix compounds, when the matrix is electrochemically inert.
2. Active matrix compounds, when the matrix is electrochemically active.
3. Electrodes with 3D porous structures.
4. Carbon-based compounds (e.g. graphene).

Another approach is the reduction of particle size: different studies have proven that a reduction of size at the nanometer scale can significantly improve the performance of the cell when alloying anodes

are used. This is because nanoparticles can better sustain a mechanical stress without fracturing; moreover, they can shorten the electronic and ionic transport distances, providing faster diffusion paths [152,156].

Among the most studied alloying compounds for LIBs, silicon is surely the most interesting one, owing much of its popularity among researchers to the very high theoretical specific capacity of 3579 mAh g^{-1} and the suitably low charge-discharge potential (< 0.4 V vs. Li^+/Li) [162]. The reaction of alloying with lithium produces a compound with a stoichiometry up to $Li_{15}Si_4$ at room temperature, according to the process described in **Equation 10**:

$$4Si + 15Li^+ + 15e^- \leftrightarrow Li_{15}Si_4 \qquad \textbf{Eq. 10}$$

At higher temperatures, further lithiation can be promoted, reaching the highest achievable stoichiometry of $Li_{22}Si_5$ (**Equation 11**) corresponding to a theoretical capacity of 4200 mAh g^{-1} [163].

$$5Si + 22Li^+ + 22e^- \leftrightarrow Li_{22}Si_5 \qquad \textbf{Eq. 11}$$

Other than the very high theoretical capacity, silicon possesses desirable qualities such as high relative abundance (Si is the 2nd most abundant element on the Earth's crust), low cost and environmental sustainability [164]. However, it also suffers from a huge volume expansion, and given the high amount of Li stored, this effect is even greater than other materials following the same lithiation mechanism (up to 400%), easily leading to repeated SEI formation and breaking, irreversible capacity losses, and detachment of the electrode from the collector [165].

Although silicon has triggered a great attention for LIBs, its use in SIBs has not received the same success, since it has been demonstrated that, although the formation of an alloy with NaSi stoichiometry is indeed possible, no reversible cycling can be obtained [160,166]. For this reason, Sn has received a much greater focus as a possible alloying anode in SIBs. Indeed, Sn can electrochemically react with both Li and Na to form various alloys, hence it has been extensively studied for both systems. According to **Equations 12** and **13**, the formation of alkali-rich phases can reach stoichiometries as high as $Li_{22}Sn_5$ in LIBs and $Na_{15}Sn_4$ in SIBs, corresponding to theoretical capacities of 994 mAh g^{-1} and 847 mAh g^{-1}, respectively [167].

$$5Sn + 22Li^+ + 22e^- \leftrightarrow Li_{22}Sn_5 \qquad \textbf{Eq. 12}$$

$$4Sn + 15Na^+ + 15e^- \leftrightarrow Na_{15}Sn_4 \qquad \textbf{Eq. 13}$$

The volume changes of Sn upon cycling are lower than those of Si, but it can still reach expansions up to 259 % for LIBs and 423 % for SIBs [168], hence this drawback has been the core point of investigations for Sn-based anodes in both systems since their first studies.

1.4.2 Cathode materials

Cathodes are all those materials able to accept Li^+ or Na^+ ions during discharge and release them during charge. In commercial LIBs, the cathode is the key component limiting the performance of the battery, and it is generally also the most expensive part. Continuous efforts have been devoted to the study of transition metal compounds which crystallize in stable structures favoring a high Li^+ ion mobility avoiding big volume changes. Suitable compounds should display specific properties such as high capacity, chemical stability, low toxicity and safety, and a high working potential vs. Li^+/Li or Na^+/Na redox couples. In commercial LIBs, the most used cathode materials are transition metal oxides and phosphates, which can be oxidized to higher oxidation states while maintaining a neutral charge upon ion release. According to their crystal structure, they can be divided into three main classes of compounds: layered oxides, spinel oxides and olivine phosphates [169]. As for SIBs, given the greater dimensions of Na^+ ions, volume changes are more critical than in LIBs, and ion diffusion into the host is slower; therefore, it is necessary to focus on structures able to keep the volume changes as small as possible, with favorable sites for a fast ion exchange. The most viable cathode families for SIBs can be divided into layered oxides, prussian blue analogues and polyanionic compounds [170,171].

Layered oxides - LIBs

The most employed cathode material for lithium-ion batteries, $LiCoO_2$ (LCO), belongs to this class of compounds, but all oxides of general formula $LiMO_2$ (M = Co, Mn, Ni, Al or a mixture of them) possess a layered structure. These compounds are isostructural to α-$NaFeO_2$, a natural salt with a distorted structure, and have a distribution of Li and M ions in octahedral sites separated by layers of cubic close-packed (ccp) oxygen array, with an ABCABC stacking sequence defined as O3-type structure (**Figure 1-15**); such ionic disposition in the crystal lattice corresponds to an $R\bar{3}m$ trigonal structure, which allows reversible insertion and de-insertion of the alkali metal through a two-dimensional framework [169]. During cycling, Li^+ ions are reversibly removed from the framework and inserted back, generating or annihilating vacancies within the planes.

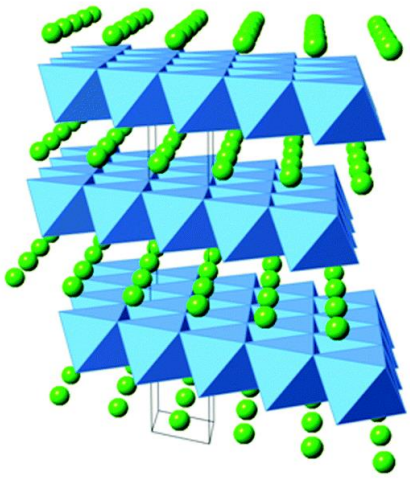

Figure 1-15. Crystal structure of layered $LiMO_2$ cathodes, where Li^+ ions move through the 2D framework [169].

However, the vacancies forming upon Li removal from LCO can indirectly drive electronic transitions or promote a structural change. In Li_xCoO_2, for $1.0 \geq x > 0.5$, the charge compensation upon Li extraction occurs through removal of d-electrons with oxidation of Co^{3+} to Co^{4+}, maintaining the valence band mainly unchanged [172]. At $x = 0.5$, an interplanar stacking leading to an equivalent environment for all Co ions is preferred, leading to an intermediate oxidation state of +3.5, and eventually inducing a transition to a monoclinic structure [173]. Upon further Li removal, for $x < 0.5$ the (CoO_6)-slab distances tend to decrease, with the charge compensation for delithiation leading to partial oxidation of the O^{2-} ions and subsequent release of oxygen, leading to a poor capacity retention [174,175]. In order to avoid the progressive breakdown of the cathode, different strategies such as surface modifications by coating with metal oxides (e.g. ZrO_2, Al_2O_3 or TiO_2) have proven to be effective in stabilizing the whole structure [176,177].

Among the layered oxides for LIBs, the family of $LiNi_xMn_{1-x-y}Co_yO_2$ (NMC) compounds received great attention as possible replacements for LCO, providing a better structural stability over cycling and an improved reversible capacity [178], together with a lower Co content (hence resulting in cheaper and more sustainable cathode materials). The main problem affecting this family of layered oxides is the possible cation mixing between Ni^{2+} and Li^+ due to their similar ionic radii (0.69 Å and 0.76 Å, respectively), which may cause a deterioration of the electrochemical performance of the material [179].

Layered oxides - SIBs

Analogous to LIBs, layered oxides with general formula Na_xMO_2 are composed of stacked layers of edge-sharing MO_6 octahedra with Na^+ ions being sandwiched in between. Depending on the surrounding Na environment and the number of unique oxide layer packings, Na layered oxides can be classified as O3- or P2-phases, with the letter indexing the site where Na^+ ions are located (i.e. O = octahedral; P = prismatic) and the number indicating how many unique interlayers are surrounded

by the different oxide layers (**Figure 1-16**). When a distorted phase is present, the notation (') is used (e.g. O'3 or P'2) [180]. Generally, the sodium stoichiometry in the oxide largely influences the formation of a structure over the others. The O3-phase belongs to $R\bar{3}m$ space group and it is known to mainly occur when $1.0 \geq x > 0.7$, with edge-sharing NaO_6 and MO_6 octahedra ordered into alternated layers and forming NaO_2 and MO_2 slabs with an ABCABC pattern; the Na^+ ions are accommodated in octahedral sites between the MO_2 layers.

Though consisting of MO_2 layers, the P2-phase has a different sodium environment compared to the O3-phase: given the larger ionic radius of Na^+ with respect to Li^+, sodium can also be accommodated in prismatic sites. When the sodium stoichiometry in Na_xMO_2 is $0.7 > x > 0.6$, a P2-type phase belonging to the $P6_3/mmc$ space group and consisting of oxide layers stacked in an ABBA fashion, is structurally stabilized.

Generally, sodium extraction from O3- and P2-type structures is known to induce phase transitions. In the O3-type phase, Na-ions are stabilized at edge-shared octahedral sites; however, upon partial sodium removal, vacancies are generated and Na-ions at prismatic sites become energetically stable by gliding the MO_2 layerswithout M-O bonds breaking [51,180]. As a result, a new phase with oxide layers stacked in an ABBCCA fashion, classified as P3-type, is formed. This phase can also be synthetically obtained through direct crystallization by solid-state reaction [181]. Phase transition from P3/O3- to P2-type structure requires M-O bond breaking and reformation, hence it is a forbidden transition at room temperature. In the P2-type phase, the large prismatic sites are energetically stabilized by Na-ions; upon sodium removal, MO2 slabs glide to form octahedral sites [182,183]. This leads to the formation of a new O2-type phase with oxide layers stacked in an ABACAB fashion. Differently from the O3-type structure, which is locally composed of a cubic close-packed (ccp) array based on the oxygen packing, the O2-type phase is classified as an intergrowth structure between cubic and hexagonal close-packed (hcp) array. This often induces the formation of stacking faults after Na extraction from the P2-type structure [182].

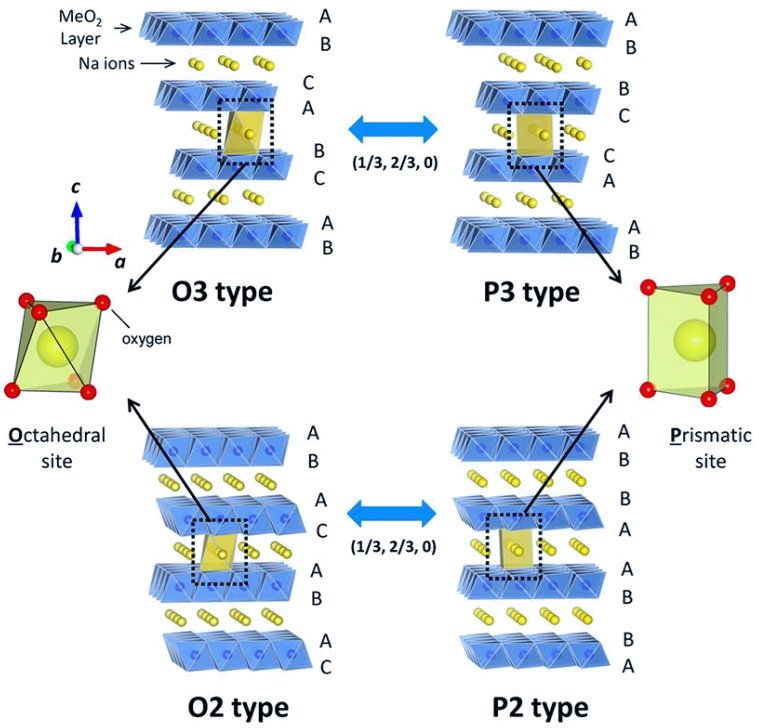

Figure 1-16. Classification of Na_xMO_2 layered structures and phase transition processes upon Na extraction [89].

Single-metal systems of the type Na_xMO_2, analogous to $LiCoO_2$, are generally studied as the basis of other more complex binary systems, since each transition metal shows quite unique electrochemical performance in terms of specific capacity, capacity retention and working potential, given that the kinetics for the electrochemical processes are heavily influenced by crystal phase and structural stability. Indeed, the cooperative effect of binary $Na_xMM'O_2$ systems with different electrochemically active transition metals (i.e. Ni, Fe, Mn) allowed to obtain some of the best performance like high reversible capacity, fairly flat potential profile and high operating voltage [184–186].

Generally, the P2-phase displays better overall electrochemistry than the O3-phase because of its low diffusion barrier and high ionic conductivity, and it is considered to be structurally more stable [187–189]. The sodium deficiency due to the lower Na stoichiometry makes their application in full cells quite difficult, as the practical capacity is limited by the cathode being unable to provide its full capacity. In this regard, the use of sacrificial additives has proven to be effective in compensating the deficiency at the cathode side, making it possible to exploit its full capacity in SIBs [190,191].

Layered oxides have attracted much attention at the industrial level, and the application of O3-type and mixed O3/P2-type in high-energy SIBs has already been patented by Faradion for commercial applications [16].

Spinel oxides - LIBs

$LiMn_2O_4$ (LMO) is among the most employed cathode materials for LIBs and one of the first to be studied alongside layered oxides. Belonging to the more general LiM_2O_4 spinel-type family, it

crystallizes in the *Fd3m* space group [192]. Its structure is composed of a 3D framework of edge-sharing MnO_6 octahedra, with Mn ions occupying half of the octahedral sites and an oxygen array forming a nearly ideal ccp sublattice. Li^+ ions are located at the tetrahedral sites sharing faces with four neighboring empty octahedral sites (**Figure 1-17**). The 3D network of this type of lattice can offer suitable transport paths for Li^+ ions to diffuse during insertion/extraction [193,194].

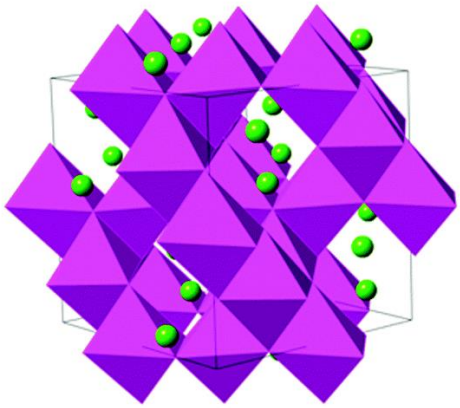

Figure 1-17. Crystal structure of spinel LiM_2O_4 cathodes, where Li^+ ions move through the 3D framework [169].

Surely, $LiMn_2O_4$ has some advantages over $LiCoO_2$, since manganese is much cheaper and abundant than Co, and it shows an excellent rate capability. However, despite its strong edge-shared $[Mn_2]O_4$ octahedral lattice and structural robustness, $LiMn_2O_4$ spinels display a performance decay upon cycling and an irreversible loss of capacity becoming rapid at high temperatures [195]. When Li^+ ions are extracted from the tetrahedral sites of the $Li_xMn_2O_4$ spinel, a two-stage process occurs due to ordering of Li-ions on half of the tetrahedral sites. Generally, in LMO the Li^+ ions move from tetrahedral sites to vacant octahedral sites, with the 3D network providing energetically favorable pathways for lithium diffusion during (dis)charge: since octahedral sites share faces with the tetrahedral ones, electrostatic interactions between Li^+ ions into these sites arise after insertion and cause the displacement of ions from the tetrahedral interstices into octahedral ones. This reaction results in a first-order transition to $Li_2Mn_2O_4$ with a stoichiometric rock-salt composition at the surface of the particles. As a result of the increased concentration of Mn^{3+} ions in the spinel lattice, a severe Jahn-Teller distortion is generally observed, reducing the crystal symmetry from cubic to tetragonal [196]. At the end of discharge, especially at high current densities (under dynamic, non-equilibrium conditions), the Jahn-Teller distortion has been observed to cause some crystallites to be more lithiated than others, driving the composition of the electrode surface into a Mn^{3+}-rich $Li_{1-x}Mn_2O_4$ region [197,198]. This poses a major drawback regarding the capacity fade for LMO, as Mn^{3+} species at the particle surface can easily disproportionate into Mn^{2+} and Mn^{4+} in the presence of trace amounts of acidic H^+ from decomposition of $LiPF_6$ and the organic solvents, according to **Equation 14**:

$$2Mn^{3+}_{(solid)} \rightarrow Mn^{4+}_{(solid)} + Mn^{2+}_{(solution)} \qquad \text{Eq. 14}$$

Since Mn^{2+} species are soluble in the electrolyte, this disproportion results in a leaching of Mn from the structure of the cathode, resulting in a progressive capacity loss [199,200].

The partial substitution of Mn with other metal cations forming $LiM_xMn_{2-x}O_4$ solid solutions (M = Ni, Cu, Cr, etc.) has proven to be an effective strategy to improve the cycling of LMO, at the expense of a decrease in the initial capacity. In particular, the substitution of 25 % Mn with Ni in LMO spinel provides an effective composition for Mn to stay in the 4+ valence state, thus reducing the Jahn-Teller distortion associated to the presence of Mn^{3+} ions, while still possessing a high capacity associated to a high-voltage plateau at 4.7 V [201]. The electrochemical activity for $LiNi_{0.5}Mn_{1.5}O_4$ (LNMO) spinel is mostly due to the oxidation/reduction of Ni^{2+}/Ni^{4+} couple, with an overall $2e^-$ transferred per single half-cycle. According to the cationic sublattice, the LNMO spinel can crystallize in two different structures, namely the face-centered "disordered" spinel with space group *Fd3m*, and the simple cubic "ordered" spinel with space group $P4_332$, the latter possessing a reduced unit cell volume thanks to a more optimized space occupation. However, phase-pure LNMO is hard to synthesize due to the coexistence of impurities like NiO and $Li_xNi_{1-x}O$ [202].

As for SIBs, due to their structural instability upon cycling, leading to the conversion into layered oxides, spinel NaM_2O_4 oxides have not yet been implemented [203].

Olivine phosphates - LIBs

The crystal structure of $LiMPO_4$-type olivine phosphates (M = Fe, Mn, Ni, Co) has been extensively studied over the years [204,205], leading to practical application of $LiFePO_4$ (LFP) in some commercial batteries. LFP belongs to the orthorhombic system with space group *Pnma*, and it consists of a distorted hcp oxygen array with Li and Fe in half of the octahedral sites and P ions in one-eighth of the tetrahedral sites, generating FeO_6 octahedra with a distorted geometry. The tetrahedral PO_4 groups share a common edge with one FeO_6 octahedron and two edges with LiO_6 octahedra. In such a structure, Fe^{2+} ions occupy the center of the FeO_6 units and are therefore distributed to form FeO_6 octahedra isolated from each other. Built by layers of FeO_6 octahedra sharing corners and mixed layers of LiO_6/PO_4 octahedra, the lattice displays a strong two-dimensional character, with Li^+ ions able to be inserted and removed in the 1D tunnel-like structure as displayed in **Figure 1-18**.

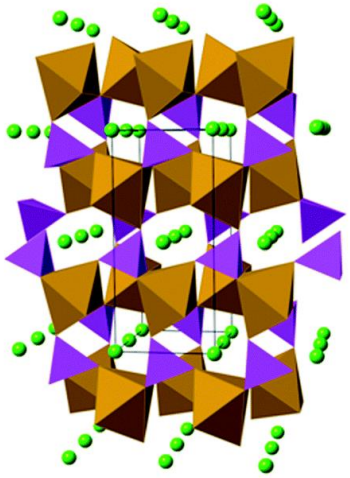

Figure 1-18. Crystal structure of olivine $LiMPO_4$ cathodes, where Li^+ ions move through the 1D framework [169].

This class of compounds have a high theoretical capacity of about 170 mAh g^{-1} and a working potential which depends on the transition metal employed [206], the latter being advantageously constant during the redox processes associated with Li^+ (de)insertion [207,208]. The olivine-type family displays rather interesting properties such as a low toxicity and a high structural and thermal stability [209]. The release of oxygen typical of layered oxides is indeed suppressed for these systems, as oxygen can form strong covalent bonds with phosphorous in the PO_4 tetrahedra [210]. However, the most important limitation of olivine-type materials is given by their low electronic and ionic conductivity [211], which can be overcome by using thin carbon coatings on the surface of the material's particles [212]. Given the commercial success of LFP, other olivine materials with different transition metals have been studied, since they possess higher energy densities, higher operating voltages, comparable specific capacities and similar thermal stabilities [213–218], as highlighted in **Table 1-2**.

Table 1-2. Summary of working potential, theoretical specific capacity and theoretical energy density for different $LiMPO_4$ systems (M = Fe, Mn, Co, Ni).

M	Olivine	Working potential vs. Li^+/Li	Theoretical specific capacity	Theoretical energy density
Fe	$LiFePO_4$	3.4 V	170 mAh g^{-1}	578 Wh kg^{-1}
Mn	$LiMnPO_4$	4.1 V	168 mAh g^{-1}	689 Wh kg^{-1}
Co	$LiCoPO_4$	4.8 V	167 mAh g^{-1}	802 Wh kg^{-1}
Ni	$LiNiPO_4$	5.1 V	166 mAh g^{-1}	847 Wh kg^{-1}

Despite the better theoretical performance, olivine-type materials other than LFP still have problems that hinder their commercial application. The $LiMnPO_4$ displays local Jahn-Teller distortions associated with the formation of Mn^{3+} during cycling, in a similar way to the spinel oxide cathodes [219]. As for $LiCoPO_4$, it has a relatively high working potential, suitable for applications in LIBs, but the electrochemical performance shows specific capacities lower than the theoretical ones and a significant

capacity loss upon cycling [215]. Finally, $LiNiPO_4$ possesses the highest working potential, but it is out of the electrochemical stability window of conventional electrolytes, thus requiring the development of alternative electrolyte solutions [214]. An effective strategy to improve the performance of olivine-type materials is the combination of different transition metals in a mixed $LiMM'PO_4$-type compound [220]. As an example, $LiFe_{1-x}Mn_xPO_4$ displays improved ionic and electronic conductivities, and reduced Jahn-Teller deformation thanks to the presence of Fe in the structure [221,222].

Olivine phosphates and NASICON-type compounds - SIBs

As for SIBs, the olivine-type material with the highest theoretical capacity (154 mAh g^{-1}) is $NaFePO_4$. However, this material has not been deeply studied due to the difficulty to be synthesized by standard routes. Among the different sodium-based polymorphs, the electrochemically active triphylite $NaFePO_4$ possesses an analogous structure to LFP with a one-dimensional Na^+ diffusion channel; however, it cannot be obtained by direct synthesis, as it would produce the more thermodynamically stable, but electrochemically inactive, maricite $NaFePO_4$, which does not possess cationic channels for Na^+ movement [223]. The only way to obtain triphylite $NaFePO_4$ is by chemical or electrochemical sodiation of heterosite $FePO_4$, which is not suitable at an industrial scale.

By contrast, polyanionic compounds of the NASICON-type (Na Super Ionic CONductor) family present a distinctive robust structure for Na migration channels and a superior ionic conductivity, which make them suitable as cathodes for SIBs. These compounds can be described by the general formula $Na_xM_2(XO_4)_3$, with $4 \geq x \geq 1$ (M = V, Fe, Ni, Mn, Ti, Cr, Zr; X = P, S, Si, Se, Mo). The general structure presents MO_6 octahedra connected to three XO_4 tetrahedral units each, forming a "lantern" unit further composing a 3D framework with large interstices (**Figure 1-19**). Both the cation M and the anion X can be tuned in this type of structure, hence offering quite a great versatility of synthesis [224,225]. Indeed, several NASICON materials have demonstrated satisfactory rate capability and cyclic stability.

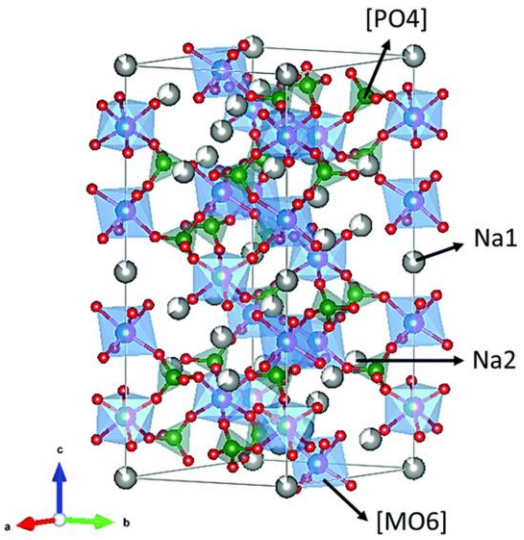

Figure 1-19. Crystal lattice of the NASICON-type structure, depicting MO_6 octahedra, XO_4 tetrahedra and Na atoms [226].

Among the most promising NASICON-type compounds, $Na_3V_2(PO_4)_3$ (NVP) was found to possess great sodium storage capabilities under different voltage ranges. It crystallizes in a rhombohedral structure belonging to the $R\bar{3}c$ space group, with interlinked VO_6 octahedra and PO_4 tetrahedra sharing corners in a 3D framework where Na^+ ions occupy two different crystallographic sites [227,228]. Only two Na^+ ions per formula unit can be extracted contributing to a theoretical capacity of 117 mAh g^{-1} and a flat voltage plateau, while the last Na^+ ion helps providing stability upon sodium extraction without any noticeable structural changes [227,229]. However, as with many other phosphate compounds, the main drawback for this cathode material is the poor electronic conductivity leading to low specific capacities. Reducing the particle size to provide shorter Na^+ ion diffusion paths and using a conductive network to enable fast electron transport are generally successful strategies to overcome these issues [230].

Given the lower output voltage and capacity with respect to other classes of cathode materials, much effort has been devoted to increasing their energy density by introducing highly electronegative anions able to increase the redox potential of polyanionic materials. Among these, F^- is the most widely explored anion, especially when coupled to NVP. Indeed, the fluorinated $Na_3V_2(PO_4)_2F_3$ (NVPF), which crystallizes in the tetragonal structure with space group *Amam* where three different sites pointing towards the tunnel directions are present for Na^+ ions [231], has proven to be able to deliver a theoretical capacity up to 130 mAh g^{-1} with a suitably high operating voltage of 3.9 V, thus attracting much attention as a possible candidate to be used in SIBs.

Prussian blue analogues - SIBs

Thanks to their excellent redox activity, low cost and highly reversible phase transitions during insertion/extraction of alkali metal ions, prussian blue analogues (PBAs) have been widely studied as

promising materials especially for SIBs [232]. They are described by the general formula $Na_xM[M'(CN)_6]_y\square_{1-y}\cdot zH_2O$, where M and M' represent transition metals bonded by C≡N− bonds in a 3D open structure able to host Na^+ ions, while □ represents the vacancy caused by the removal of an $M'(CN)_6$ group and the occupation by coordination or interstitial water. According to the different possible species and ratios of Na/M/M', presence of defects, crystal water, guest ion content and external factors such as temperature, the structure of PBAs can vary between a number of different crystal phases, including monoclinic [233], rhombohedral [234], cubic [235], tetragonal [236] and hexagonal [237], as summarized in **Figure 1-20**.

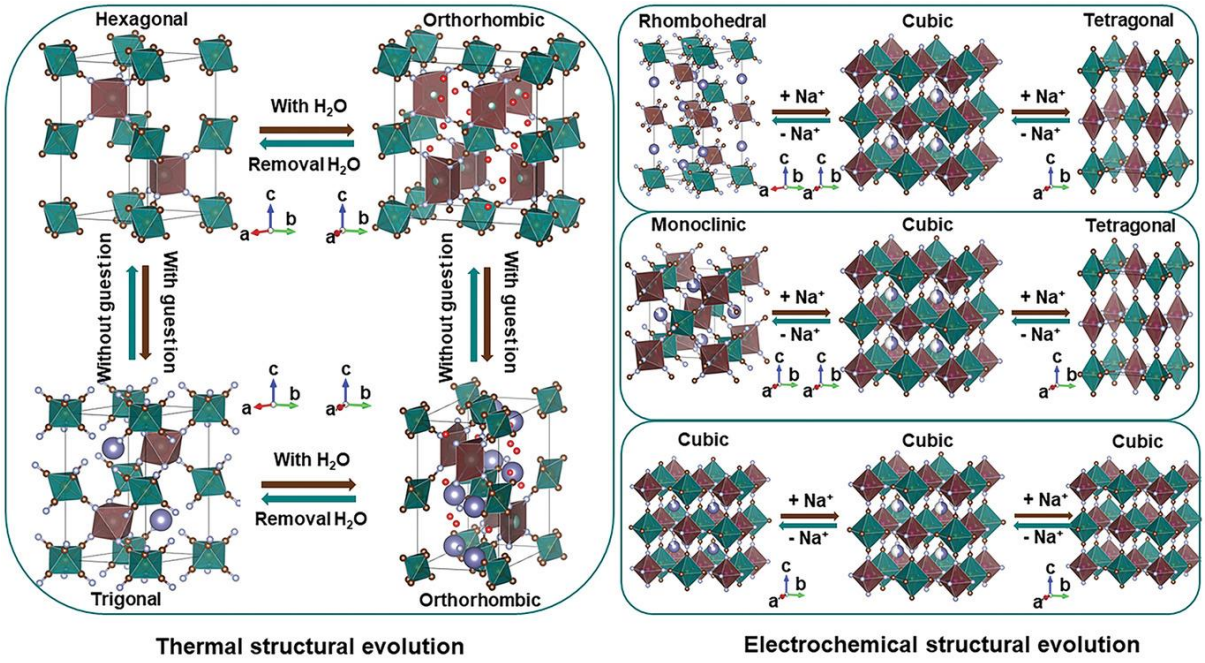

Figure 1-20. Schematic illustration of thermal and electrochemical structural evolutions of PBAs [232].

The redox mechanism of PBAs is quite complex and greatly depends on two main key factors: the crystallite size and the morphological evolution can affect both the ion diffusion dynamics and the structural evolution mechanism of PBAs; in general, well-crystallized PBA particles with small dimensions and high specific surface area promote a faster diffusion and a greater depth [238]. However, simultaneously obtaining PBAs with both intact crystal structure and small particle size is rather impractical, since highly crystallized PBAs tend to show large particle sizes with a solid cubic shape. The use of chemical etching, self-assembly and a careful composition design are generally required to produce a nano-hierarchical morphology with large surface area and short diffusion distance to generate more redox sites [239,240]. As already mentioned, the structural evolution of PBAs during charge/discharge process is quite complicated; although it has been extensively studied in SIBs, the defined mechanism has not been conclusively established yet, being the structures of PBAs sensitive to inner configuration, temperature and electrochemical cycling conditions.

When it comes to energy density, increasing the average voltage and specific capacity of the electrode requires the overcoming of several challenges at the material level. The interstitial water content of most PBAs can be as high as 15 % inside the crystal lattice. These water molecules don't provide any contribution to the capacity, and promote negative effects such as deterioration due to hindered Na^+ migration, side-reactions with the electrolyte and structural collapse [241]. Improving the energy density is typically achieved by increasing the crystallization through an optimized synthesis [242,243] or removing the crystal water by heating under vacuum [244]. An increased crystallinity is also a key factor to enhance the power density of PBAs and their stability under high current densities, since the suppression of side reactions and the reduction of vacancies would result in an improved ionic/electronic conductivity [241,245]. For batteries based on PBA cathodes, their cycling stability is generally poor and capacity fading is generally correlated to a crystal structure collapse [246,247], which leads to a progressive dissolution of $M'(CN)_6$ groups in the electrolyte [241]. Indeed, large amounts of crystal vacancies and structural water can be caused by fast nucleation and grain growth speed, irreversible structural evolution during Na^+ insertion/extraction and side reactions with the electrolyte, and a series of optimizations are required to address all these issues. Increasing the crystallinity of PBAs with preferable stoichiometry is regarded as an effective strategy to achieve increased capacity, rate performance and prolonged cycle life [241].

Encouragingly, like the layered oxide family, PBAs are also on the way to commercial application in SIBs, as both CATL and Natron have already announced its first-generation SIBs based on PBA at the cathode [17,18].

1.4.3 Binders

Among the main components in an electrode for batteries, the binder is a polymeric material accounting for the proper adhesion of the active material and the conductive agent to the current collector, while granting interparticle cohesion. Although it is generally employed in small percentages (generally < 5 %) and its cost is less than 2 % over the entire cost of the battery, the binder plays a crucial role for the functioning of the device; without the binder, the active materials will inevitably lose physical and electrical contact with the current collector upon prolonged cycling [248]. When speaking of conversion and alloying materials, the binder is of particular importance, as it must also be able to sustain the volume variations during (dis)charge cycles [249]. Hence, much research is devoted to the study of binders, aiming to find the best combinations of performance, cost and environmental friendliness.

Among the possible different polymers, polyvinylidene fluoride (PVdF) is the binder of choice for commercial LIBs; it is able to provide a good adhesion with the current collector, and it is chemically inert towards the commonly employed solvents of the electrolyte (EC, DEC, DMC). It belongs to the

poly-fluorinated olefins family, a group of macromolecular compounds possessing high stability due to the presence of C-F bonds, which are stronger than C-H bonds (Figure 1-21). PVdF shows a good mechanical resistance, a high solubility in polar solvents, and a thermal stability in the range of temperatures between –40°C and +150°C.

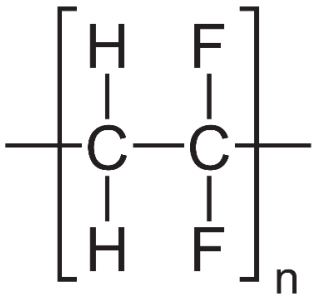

Figure 1-21. Chemical structure of PVdF.

However, there are undesirable characteristics for this binder, such as the high industrial costs and the necessity to use toxic and volatile solvents, such as N-methyl-2-pyrrolidone (NMP), as well as the difficulty associated with their recycling. Due to these problems, new types of binders have been proposed in the last years, aiming to lower toxicity and environmental impact [250].

One of the alternatives to PVdF which received a huge attention as the binder for both LIBs and SIBs, especially for the anode side, is the sodium salt of carboxymethyl cellulose (NaCMC). This polymer is water-processable, allowing for the possibility to avoid the use of NMP and to promote an easier and effective recycling; moreover, it can be produced starting from the naturally abundant cellulose, granting a lower cost with respect to PVdF. Its application in Li-ion batteries showed promising characteristics, including an improvement of electrochemical performance, good stability upon cycling and a low environmental impact [251]. NaCMC is a linear polymer derived from cellulose, which can possess different degrees of substitution with carboxymethyl groups -OCH_2COO^- Na^+ (Figure 1-22).

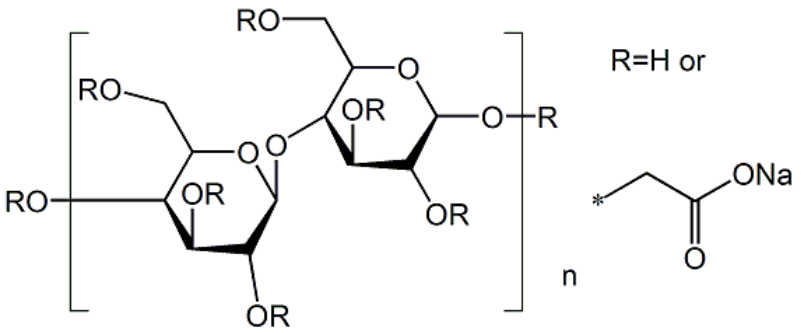

Figure 1-22. Chemical structure of NaCMC.

The OH groups present on the glucopyranosyl ring do not participate to reactions with lithium or sodium, therefore they do not contribute to the irreversible capacity. Moreover, both carboxylic and

hydroxyl functional groups allow the formation of much stronger hydrogen bonding with respect to PVdF, granting the solubility of the polymer in water thanks to their polarity. To further enhance its mechanical properties, NaCMC is often used in combination with low-viscosity styrene butadiene rubber (SBR) as a thickening agent [251]. From an electrochemical point of view, by increasing the degree of substitution and decreasing the molecular weight, there are advantages with respect to PVdF, such as a higher ionic conductivity, a low resistance to charge transfer and a certain permeability of the electrolyte. NaCMC also shows a good adhesion to the current collector and a good resistance to volume changes [252].

Like NaCMC, polyacrylic acid (PAA) and its salts have also been recently considered as promising binders as well, because of their appealing characteristics. Similarly to the family of polyvinyl acids, PAA has a good solubility not only in water but also in a series of organic solvents with low environmental impact and low cost, such as ethanol. Binders based on PAA are able to form strong hydrogen bonding with either the active material or the current collector, thanks to the presence of carboxylic groups (**Figure 1-23**). Therefore, they can provide a very good interface between the two components, with a better adhesion with respect to PVdF [253].

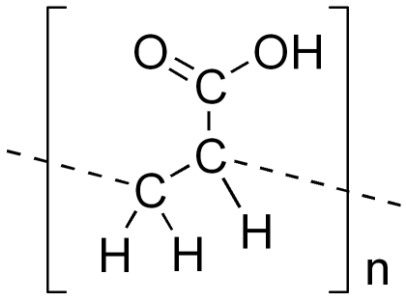

Figure 1-23. Chemical structure of PAA.

From both a mechanical and electrochemical point of view, PAA shows better results than PVdF, such as a higher resistance to volume changes upon charge/discharge processes and better performance. However, one of the disadvantages of PAA is the high hygroscopicity, which can lead to a volume expansion due to water adsorption, compromising the proper working of the electrode; hence, a more careful drying the electrodes prior to usage is needed [253].

The sodium salt of alginic acid (NaAlg) is a less widely studied binder, but still displaying interesting properties. It is a water-soluble biopolymer which can be extracted from brown algae, composed of 1,4-linked β-D-mannurate and α-L-guluronate rings arranged to form a copolymer, in a similar fashion to NaCMC (**Figure 1-24**) [254].

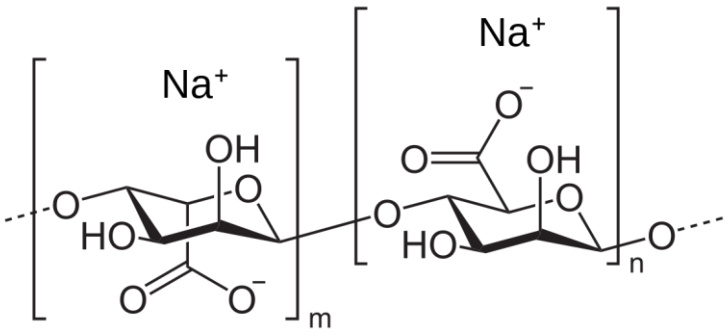

Figure 1-24. Chemical structure of NaAlg.

Because of the presence of hydroxyl and carboxyl functional moieties, NaAlg is also able to form hydrogen bonding with the active material, granting a better adhesion. It is also suggested that the more homogeneous distribution of functionalities with respect to NaCMC promotes a Li-ion hopping between neighboring carboxylic groups, leading to a higher Li^+ ion conduction. In addition, the high polarity of NaAlg results in a higher viscosity of the slurry, making it possible to employ a lower amount of binder in the electrode formulation [255].

Among the natural polymers, chitin is the second most abundant one after cellulose, available in large quantities in the shells of shrimps, lobsters and crabs, which make a cheap and readily available source for its extraction. Through a deacetylation process, the derivative chitosan (CS) can easily be obtained. Chitosan is a linear polysaccharide composed of randomly distributed β-(1-4)-linked N-acetyl-D-glucosamine and D-glucosamine units (**Figure 1-25**), whose degree of deacetylation can be tuned by adjusting the reaction conditions [256]. It can be dissolved in water in the presence of diluted acetic acid (i.e. 1% solution).

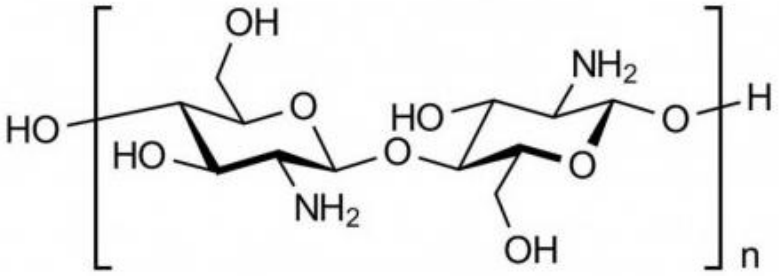

Figure 1-25. Chemical structure of CS.

The presence of NH_2 and OH groups makes this binder quite attractive to promote H-bonding with the active material, but also opens the possibility to have crosslinking reactions with carboxylic acids. Molecules such as PAA or citric acid (CA), can lead to a crosslinked chitosan-based binder with improved mechanical properties, effectively enhancing the cycling stability of the cell for both anodes and cathodes [257].

1.4.4 Electrolytes

The electrolyte is another major key component of a battery; the choice of the electrolyte is crucial for the performance of the cell, since it is the medium through which Li^+ and Na^+ ions can migrate from one electrode to the other. For both LIBs and SIBs, several types of electrolytes have been studied over the years, such as liquid- and glyme-based [258], gel and solid polymers [259,260], or solid ceramics [261], although the most widely studied and commercially employed are liquid solutions containing an inorganic salt dissolved in organic solvents.

In both LIBs and SIBs, it is generally not possible to use aqueous electrolytes, since the working potentials of cathode and anode go beyond their electrochemical stability window (ESW), hence they would decompose upon cycling; therefore, organic electrolytes with a wide ESW, a low melting point and high boiling point are generally preferred over the water-based ones [262]. As for the salts, there are only few appropriate species, and they must possess a very hindered negative counter-ion, so that its contribution to the ion diffusion is negligible with respect to that of Li^+ or Na^+. In order to provide good performance, an optimal electrolyte solution should possess a high ionic conductivity, a high chemical stability, safety and low cost [263].

Different organic solvents (**Figure 1-26**) are available for both LIBs and SIBs, each one with its own dielectric constant and viscosity, making the choice for the most appropriate combinations extremely crucial in order to favor a high ionic conductivity and cyclability, as the SEI/CEI formation and composition depends on the employed system.

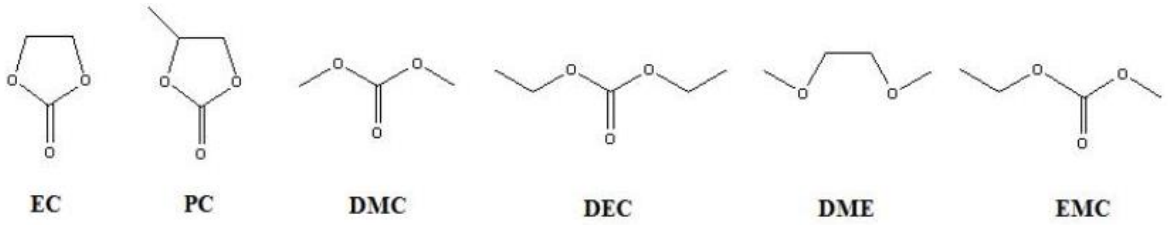

Figure 1-26. Chemical structures of the most employed carbonate solvents for LIBs and SIBs.

Generally, a mixture of organic solvents can guarantee a better performance, by increasing the conductivity and the range of accessible temperatures of the single components; in the same way, more than one salt can be dissolved, in order to avoid gas production and improve cyclability at high temperatures. For Li-ion batteries, the most widely used electrolyte is 1M $LiPF_6$ dissolved in a 1:1 v/v mixture of EC:DMC, commercially known as LP30, while for Na-ion batteries, better performance and have been observed with 1M $NaClO_4$ dissolved in 1:1 v/v mixture of EC:PC or EC:DEC [264], although recently there is a rising tendency to replace the salt with $NaPF_6$ due to safety concerns regarding the stability of perchlorate salts [265].

Organic solvents display a tendency to decompose at the negative electrode, causing problems to the electrochemical performance of the cell. In this regard, the SEI formation on the surface of the anode material is particularly important; the SEI is an electronically insulating layer whose formation is irreversible, but it offers a good ionic conductivity, and its protective action avoids further reactions between the anode and the electrolyte. The nature of the passivation layer depends on the composition of the electrolyte: for example, electrolytes based on ethylene carbonate tend to form a compact SEI, so that commercial batteries have a combination of EC with other organic solvents; by contrast, the use of propylene carbonate has proven to be detrimental in LIBs, since it tends to be co-intercalated between graphene layers and cause exfoliation, while it is required in SIBs to provide the most favorable solvation energy and charge transfer [47,266], although the SEI itself in sodium-ion systems is generally less stable and partially soluble in carbonate solvents [267].

In order to control SEI formation and avoid an excessive growth that could act as a barrier blocking the interactions with the anode, an effective strategy is the use of additives. They are compounds whose purpose is to be consumed during the formation of the passivation layer, providing a composition with higher stability. Among the different additives, the most employed ones for both LIBs and SIBs are vinylene carbonate (VC) and fluoroethylene carbonate (FEC) (**Figure 1-27**) [266,268]. Moreover, especially when running tests with sodium-ion half-cells, one has to take into account that the use of additives is often necessary to provide stabilization of the metal Na used as the reference and counter-electrode, favoring a proper monitoring of the potential and a more homogeneous plating/stripping onto/from the counter-electrode [269].

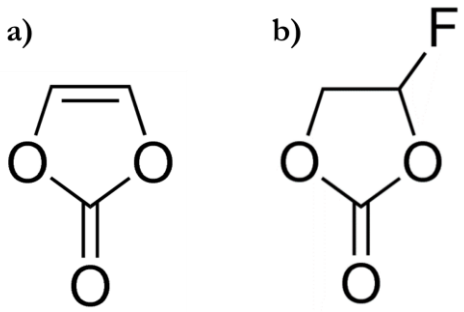

Figure 1-27. Chemical structures of a) VC and b) FEC.

1.5 Aim of the thesis

In the present thesis work, the aim of sustainability is pursued by studying both systems (LIBs and SIBs) from the point of view of anode and cathode materials, in order to achieve suitable performance, by maintaining the environmental benignity of the proposed cells. Although the optimization of cells and materials tested is out of the aim of this work – hence it has not been fully explored –, the key point of the developed research is to propose materials, electrodes and methodologies aimed at

enhancing sustainability of the battery value chain. In particular, this common approach is translated into specific objectives such as: (i) the study of green and abundant materials such as Si and Chitosan; (ii) the re-purpose of waste biomass to produce hard carbons to be used either as pure active material or mixed in a composite electrode; (iii) the use of low-cost Co-free cathodes such as LFP and Ni,Mn-based layered oxides; (iv) the use of cheap additives such as sodium squarate for practical application in SIBs. The feasibility of combining these materials in a full Li-ion or Na-ion cell configuration is evaluated, also taking into account the mass loadings of the electrodes, with considerations on the achieved performance and energy densities regarding possible optimizations and scalability of the systems.

2 Investigation of Structural and Interfacial Properties of Si/Hard Carbon Composite Anode for Li-ion Batteries

The sector of automotive industry is growing at an increasing rate, focusing on the production of electric vehicles (EVs) in order to lower the environmental impact caused, among other factors, by internal combustion engines [270,271]. The low specific capacity of the state-of-the-art graphite anode employed in commercial batteries is becoming a limiting factor in the development of high-energy density devices, thus a progressive substitution of this material at the anode is expected, promoting the use of composite materials that could ensure higher energy densities and specific capacities, with the aim to obtain a suitable driving range per single charge [272,273]. Moreover, in a circular economy perspective, the valorization of waste materials through second-life applications is imperative for reducing the environmental footprint that would otherwise be generated from their immediate disposal [274–276].

Alternative materials that could ensure high performance while being in line with a low environmental impact are now being studied at an increasing rate. As highlighted in **Subsection 1.4.1**, among these, alloying anodes based on silicon (Si) are the most promising ones because of their high specific capacity at room temperature of 3579 mAh g^{-1} ($Li_{15}Si_4$), low working potential vs. Li^+/Li and relative abundance on Earth's crust, resulting as the best candidates for application in next-generation batteries [152,277,278]. In spite of its excellent electrochemical characteristics, Si is subjected to huge volume changes upon charge/discharge cycles, which lead to unstable interfaces, electrode pulverization, loss of electrical contact and fast performance decay [131,156,157]. The use of carbon materials as buffering matrices for the volume expansion of alloying materials is very attractive in order to overcome these issues [279,280]. In particular, the application of Hard Carbons in composite electrodes allows to combine the desirable physical-chemical characteristics of carbon materials, such as good conductivity, porosity and surface area, with the high gravimetric and volumetric energy densities of alloying materials [281,282]. Hard Carbons are also attractive because they can be obtained from waste biomass and, if properly optimized, their synthesis can provide a lower impact with respect to other complex carbon-based matrices such as graphene, both in terms of production cost and energy efficiency [283].

It is also well known that the use of green binders with a high content of polar functional groups such as carboxyl group (-COOH), hydroxyl group (-OH) and amino group ($-NH_2$), can help improving both performance and stability in alloying materials, not only thanks to better elastic and adhesive properties of the polymers, but also to a better interaction between binder and active material [284,285]. The possibility to exploit inter- and intra-molecular polar interactions makes the choice of the binder particularly important for alloying materials [256,286].

It is therefore clear that the implementation of next-generation anode materials requires an in-depth study of the interfacial and structural behavior upon cycling to fully understand the mechanisms of Li^+ ions storage, especially for composite anodes containing a carbon matrix which yields both a stabilizing effect and a non-negligible electrochemical activity. In this regard, ex-situ and in-situ spectroscopic techniques are fundamental to evaluate the evolution of structural, electrochemical and kinetic properties of electrode materials [287–290].

In this chapter, the preparation and characterization of a Si/Hard Carbon composite anode from waste biomass (Corn Cobs) via a simple route and without the use of activating agents, combined with the use of a sustainable crosslinked Chitosan-based binder, is reported. The composite electrode is prepared by employing a relatively high Si content, with a Si:HC ratio of 3:5 (i.e. 37.5 % Si in the active material) in order to provide a good balancing between structural stability and electrochemical performance, especially when considering that commercial Si/Graphite anodes still cannot go beyond a Si mass content of 10-15 % to maintain electrode integrity [291,292]. The crosslinked chitosan-based binder is prepared according to a method reported in literature [256] and employed as a greener alternative to commercial polyvinylidene fluoride (PVdF). An extensive structural, interfacial and electrochemical characterization of the material is also reported, which includes ex-situ Raman spectroscopy, impedance measurements and calculation of the distribution of relaxation times (DRT), performed during both lithiation and de-lithiation processes. Finally, a preliminary study for the applicability of the material in a full cell configuration is also studied as a proof-of-concept evaluation, by employing a commercial $LiFePO_4$ (LFP) as a sustainable cathode electrode.

2.1 Experimental Section

In this section, the details about synthetic procedures, electrode processing, structural, chemical, morphological and electrochemical characterizations are summarized.

2.1.1 Synthesis of Corn Cobs-Derived Hard Carbon

The hard carbon from Corn Cobs biowaste (labeled as CCDHC) was prepared via a simple and easy-to-perform carbonization route under inert gas flow, without any acid/base pretreatment step. The adopted procedure can be summarized as follows: the precursor was preliminarily ground, sieved (dimensions < 1mm) and annealed in a tubular furnace at 950 °C for 3 h under argon atmosphere, with a heating ramp of 5 °C min^{-1}. The as-obtained carbon was then finely ground through a planetary ball-mill for 30 min at 300 rpm in clockwise/counterclockwise mode, to reduce the particle size of the final CCDHC (50 mL steel jar with 3 steel balls of 20 mm diameter and ball-to-powder weight ratio of 15:1).

2.1.2 Electrode processing

The slurry for the preparation of Si/CCDHC and Si/Graphite (Si/Gr) composite electrodes, and for bare Si electrodes, were obtained by mixing all the components in the formulation of 80:15:5 (active material : binder : conductive carbon Super C-65), with a 3:5 w/w ratio between Si and CCDHC. The chitosan/citric acid (CS/CA) binder solution was firstly prepared by dissolving chitosan in a 1 % acetic acid solution, and separately adding a proper amount of citric acid solution to obtain a 9:1 w/w ratio (Chitosan : Citric acid) between the two components. Polyacrylic acid (PAA), sodium carboxymethyl cellulose (CMC) and sodium alginate (Alg) were dissolved in ultrapure water and used to assess the influence of the binder on the Si/CCDHC composite. The active material (Si/CCDHC, Si/Gr or bare Si) and the carbon additive were ground and mixed through a planetary ball-mill for 30 min at 200 rpm in clockwise/counterclockwise mode, added to the binder solution and left stirring overnight through a magnetic stirrer. The as-obtained slurries were casted onto copper foil (10 μm thickness) through doctor blading technique with a wet thickness of 150 μm. Finally, the electrode layers with the CS/CA binder were dried at 150 °C for 2 h in order to thermally induce condensation between the binder components, while those containing the other binders were dried at 70 °C for 2 h. Circular electrodes of Ø = 9 mm and Ø = 16 mm were cut by using electrode punchers (EL-CELL) with the proper diameter, pressed at 7.86 ton cm^{-2} through a hydraulic press, weighed and eventually vacuum-dried at 120 °C overnight. The mass loadings of the active material ranged 1.0 to 1.2 mg cm^{-2} for all the tested electrodes.

The slurry for the preparation of LFP electrodes for full cell application was obtained by mixing the components in the formulation 90:5:5 (active material : PVdF : conductive carbon Super C-65). The binder solution was prepared by first dissolving PVdF in N-methyl-2-pyrrolidone (NMP). The active material and the carbon additive were mixed through an agate mortar, added to the binder solution and left stirring for 1 h. The obtained slurry was casted onto Al foil (20 μm thickness) through doctor blading technique with a wet thickness of 300 μm and left drying at 70 °C for 3 h. Finally, circular electrodes of Ø = 9 mm were cut by using an electrode puncher (EL-CELL) and vacuum-dried at 120 °C overnight.

2.1.3 Structural, chemical and morphological characterization

Infrared spectroscopy (Perkin-Elmer Frontier FTIR) was employed on two films of the sole binder (casted and dried at 60 °C and 150 °C respectively) to confirm the presence of the amide functional group resulting from the condensation. For the measurement, mixtures only containing chitosan and citric acid in a 9:1 w/w ratio were prepared in a 1 % acetic acid solution and left stirring for 12 h; afterwards, both solutions were casted onto polytetrafluoroethylene (PTFE) foil and dried at the target temperatures for comparison. The morphologies of CCDHC, of the Si/CCDHC composite, and of

electrodes prepared with different binders (pristine and after cycling) were studied using scanning electron microscopy (Zeiss Sigma 300 FE-SEM equipped with Bruker QUANTAX EDX detector). The structure of the obtained materials was characterized by means of Raman spectroscopy (Horiba IHR 320, λ = 532 nm) and powder X-ray diffraction (Philips diffractometer equipped with a Cu-Kα source, λ = 1.540 Å). A thermogravimetric analysis (Perkin-Elmer STA6000 TGA-DTA) was performed on the Si/CCDHC composite under oxidative conditions to confirm the 3:5 ratio between Si and CCDHC after ball-mill.

2.1.4 Electrochemical measurements

Most of the electrochemical measurements for the Si/CCDHC anode were carried out by using three-electrode Swagelok-type polypropylene cells, with lithium metal serving both as counter and reference electrode. For the impedance measurements of electrodes with different binders, the Swagelok-type polypropylene cells were employed in a two-electrode configuration, since the contribution of Li metal to the total resistance at the fully de-lithiated state is expected to be negligible. Two-electrode CR2032 coin-type cells were employed for the impedance measurements performed through a "staircase" protocol, in order to avoid the presence of inductive loops, especially at low potentials. Whatman GF/A fiberglass separators were used for all the measurements. All cells tested were assembled in a high-purity Argon-filled glovebox (Jacomex GP-Campus) with O_2 and H_2O content < 0.8 ppm. The electrolyte employed was 1M $LiPF_6$ dissolved in a 1:1 v/v mixture of ethylene carbonate and dimethyl carbonate (EC:DMC) with 5 % VC (w/w) additive. All electrochemical measurements were performed using a VMP-3 multichannel electrochemical workstation with an integrated frequency response analyzer by Bio-Logic. Prior to any electrochemical characterization, a 12-hour OCV period was used. Cyclic voltammetries (CV) were acquired at a scan rate of 0.1 mV s^{-1}. The composite's charge-discharge performance was evaluated by galvanostatic cycling with a constant current of 1 A g^{-1} for 100 cycles, applying a constant-voltage step at the end of each lithiation. The composite electrode employing commercial graphite (KS15) as the buffering matrix and the CS/CA binder, as well as the bare Si electrode, were tested in the same cycling conditions. A rate capability test was performed by galvanostatic cycling the material with specific currents ranging from 0.1 A g^{-1} up to 4.0 A g^{-1}. All the cycling tests were performed within the voltage window 0.01 V < E < 1.50 V. Electrochemical impedance spectroscopy (EIS) measurements were acquired upon cycling in potentiostatic mode during 1st cycle and every 10th cycle at a fixed bias potential E = 0.4 V. Moreover, impedance measurements were also carried out on electrodes with different binders at OCV and at a bias potential of E = 1.5 V after 1 and 10 charge/discharge cycles. "Staircase" impedance measurements were carried out within a single cycle (10th cycle) at different states of charge (SoC) during both lithiation and de-lithiation, with a sampling interval of 0.02 V. For all the EIS

measurements, a sinusoidal perturbation of $\Delta E = \pm 5$ mV was applied over the frequency range 10 mHz < f < 199 kHz, with 10 points per decade and logarithmic spacing. For the "staircase" impedance measurements, the low-frequency diffusion region was subtracted from the obtained Nyquist plots in order to calculate the function of distribution of relaxation times (DRT). The fitting procedures by Equivalent Circuit Method (ECM) and the calculation of the DRT function (Tikhonov regularization, $\lambda = 10^{-4}$) were performed by using the software RelaxIS3. All the potential values are referred to the Li^+/Li redox couple ($E° = -3.04$ V vs. RHE).

For full cell measurements, the cycling was performed in three-electrode Swagelok-type cells by controlling the anode and applying a specific current of 1.0 A g^{-1}_{anode} within the working potential window of the controlled electrode, while monitoring the cathode and cell potentials.

Ex-situ Raman measurements were performed on samples charged/discharged to different states of charge during the first cycle. The cells were galvanostatically cycled at a specific current of 1 A g^{-1} until a certain state of charge and then equilibrated by applying a constant voltage for 6 h. The cells were subsequently disassembled in the glovebox under Ar atmosphere, and each electrode was washed three times in dimethyl carbonate (anhydrous, Sigma Aldrich) to remove any electrolyte residues which could generate interferences in the Raman measurements. The electrodes were eventually sealed by epoxy resin between two microscope slides to prevent unwanted reactions with air and moisture during the analysis.

2.2 Results and discussion

2.2.1 Chemical and structural analysis of the binder

Prior to cell assembly, a chemical and structural analysis was carried out on two films of the sole binder dried at different temperatures (i.e. 60 °C and 150 °C), to verify the crosslinking reaction between chitosan and citric acid. The FTIR spectra of the two films are shown in **Figure 2-1**.

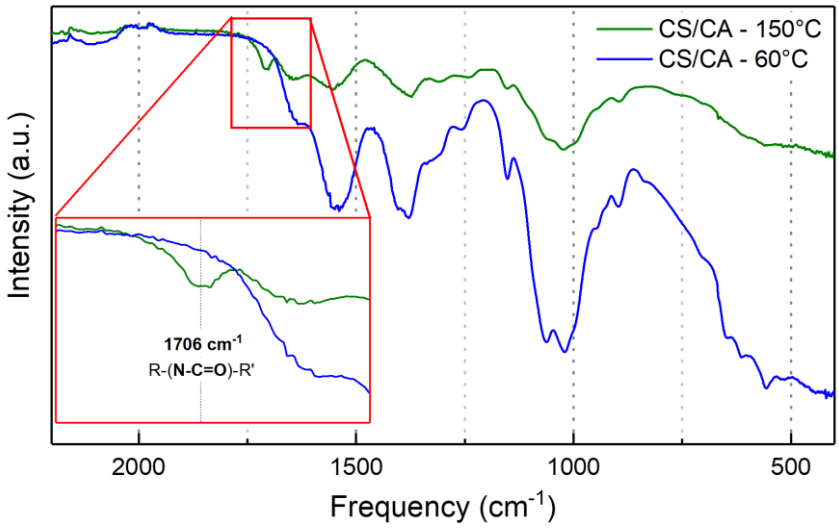

Figure 2-1. FTIR spectra of the binder polymeric film heated at 60 °C (blue) and 150 °C (green). The inset shows the peak related to the formation of the amide bond from condensation.

The FTIR spectra recorded for both samples are consistent with other results reported in literature [256], and the main signals are summarized in **Table 2-1**. In particular, both samples display the characteristic signals corresponding to the deformation vibrations of primary and secondary amines between 1500 and 1600 cm^{-1} arising from chitosan. However, after heat-treating the sample at 150 °C, an additional feature at about 1706 cm^{-1} appears (see inset in **Figure 2-1**), clearly indicating the formation of the N-C=O amide bond. The presence of a proper covalent bonding between the free deacetylated amine of chitosan and the carboxyl groups of citric acid indicates that the thermally induced condensation reaction successfully occurred, resulting in the interconnection of chitosan chains through bridging citric acid.

Table 2-1. Summary of the FTIR main signals and associated bonds of the polymeric binder films.

Peak position	Associated bond
894 cm^{-1}	Primary **N-H**
1022 cm^{-1}	**C-O-C**
1062 cm^{-1}	Secondary **C-O**H
1152 cm^{-1}	**C-O-C**
1254 cm^{-1}	Secondary R_2C**O-H**
1300-1450 cm^{-1}	**C-H**
1500-1600 cm^{-1}	Primary RH**N-H** and secondary R_2**N-H**
1649 cm^{-1}	**C-N**
1706 cm^{-1}	R(**N-C=O**)R’

2.2.2 Structural and morphological characterization of Si/CCDHC

The structure, morphology, and composition of the synthesized carbon (CCDHC) and of the composite Si/CCDHC were investigated by means of Raman spectroscopy, X-ray diffraction (XRD),

scanning electron microscopy (SEM) and EDX analysis, as reported in **Figure 2-2** and **Figure 2-3**, respectively.

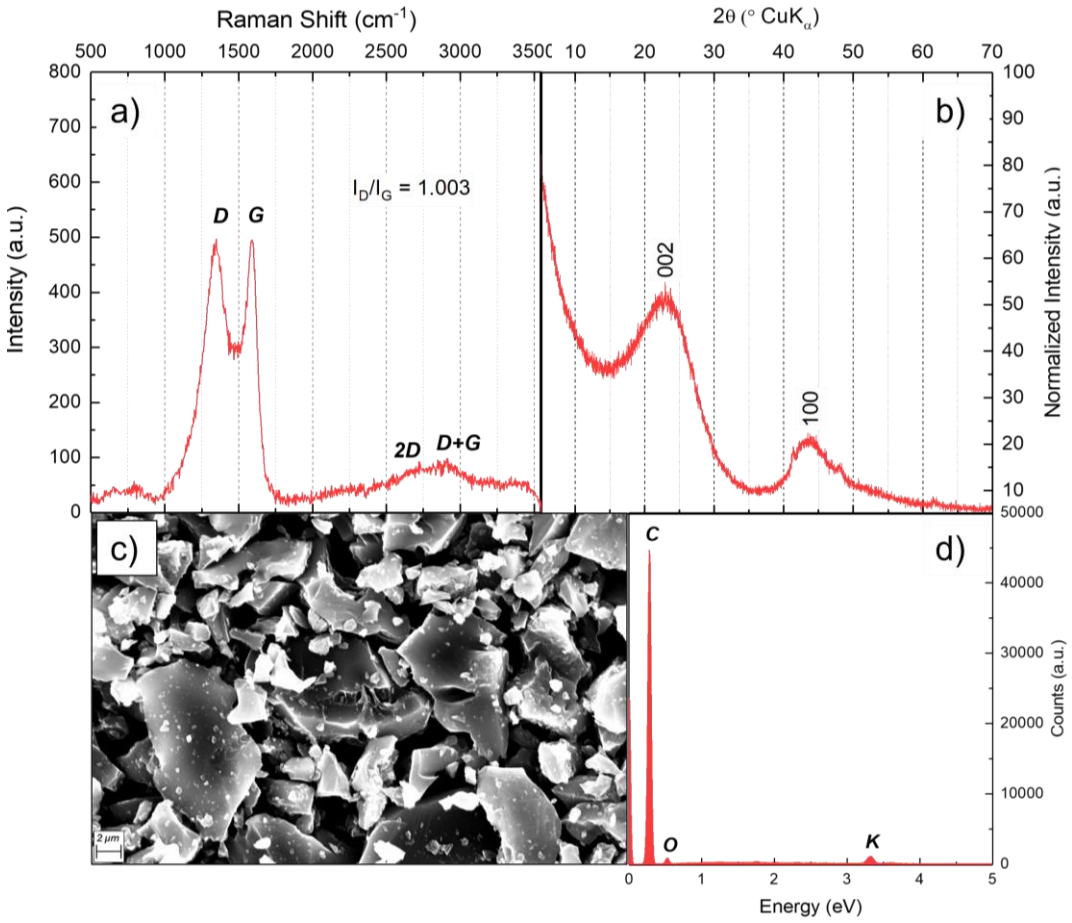

Figure 2-2. a) Raman spectrum of CCDHC; b) Experimental diffraction pattern of CCDHC; c) SEM micrograph of CCDHC at 5000x magnification; d) EDX analysis of CCDHC.

The Raman spectrum of CCDHC (**Figure 2-2a**) displays the presence of the two characteristic bands of disordered carbons: the D band at 1337 cm^{-1} and the G band at 1587 cm^{-1}, associated with the breathing mode of A_{1g} symmetry and with the in-plane bond-stretching motion of pairs of C sp^2 atoms of E_{2g} symmetry, respectively. The former mode is not active in pure graphite and only becomes active in the presence of structural defects, while the latter is typical of ordered graphitic sites. Hence the intensity ratio ID/IG can provide an indication of the degree of disorder of the hard carbon [293,294]. For CCDHC this ratio was calculated to be 1.003, suggesting a highly disordered structure with the presence of defects. Additionally, in the region 2500-3200 cm^{-1}, the second order bands associated to 2D (characteristic of graphitic domains) and D+G (characteristic of defect-activated scattering) bands are visible [295]. The XRD pattern in **Figure 2-2b** shows the presence of a clear signal at $2\theta \approx 24°$ corresponding to the (002) plane, and a weaker signal at $2\theta \approx 43°$ corresponding to the (100) plane, both related to graphitic-like domains. The (002) band indicates the spacing between graphene layers in the graphitic domains, and the broadening of the signal is consistent with the presence of short-

range structures composed of a random layer lattice with defective sites and crystalline graphitic domains [296]. The graphitic domain size (L_a) for the hard carbon sample was calculated from the Raman spectrum according to **Equation 15**:

$$L_a = (2.4E^{-10})\lambda^4 (I_D/I_G)^{-1} \qquad \textbf{Eq. 15}$$

where λ = 532 nm

From the XRD pattern, the diffraction peak in the plane (002) was used to calculate the interlayer spacing (d_{002}) and the stacking height (L_c), by using Bragg's Law (**Equation 16**) and Scherrer's equation (**Equation 17**), respectively:

$$d_{002} = \lambda/2\sin(\theta_{002}) \qquad \textbf{Eq. 16}$$

$$L_c = 0.9\lambda/\beta_{002}\cos(\theta_{002}) \qquad \textbf{Eq. 17}$$

where λ = 0.154 nm, and β_{002} = Full Width at Half Maximum (FWHM) of the peak associated to the (002) reflection plane.

Finally, an estimation of the number of graphene stacking layers (n) was obtained by dividing the stacking height L_c by the interlayer spacing d_{002}. All the values obtained by Raman spectroscopy and X-ray diffraction are summarized in **Table 2-2**, and are in line with the literature data of hard carbons possessing amorphous regions mixed with graphitic domains [294,296].

Table 2-2. Summary of the crystallographic parameters obtained by Raman spectroscopy and X-Ray diffraction.

Sample	I_D/I_G	L_a (nm)	d_{002}	L_c (nm)	n
CCDHC	1.003	19.17	0.387	0.89	2.30

The SEM micrographs of the hard carbon powder (**Figure 2-2c**) show the presence of large, aggregated clusters with a block-like morphology, composed of smaller nanoparticles. A certain degree of graphitization can be visually discerned by the presence of some lamellar-like structures composing the graphene stacking sheets. The EDX analysis in **Figure 2-2d** finally shows that despite the absence of acid leaching, the only observable impurity from the starting biomass after annealing is traces of K, probably in the form of K_2O. The low intensity of the signal from O atoms indicates a very low surface functionalization of the obtained hard carbon.

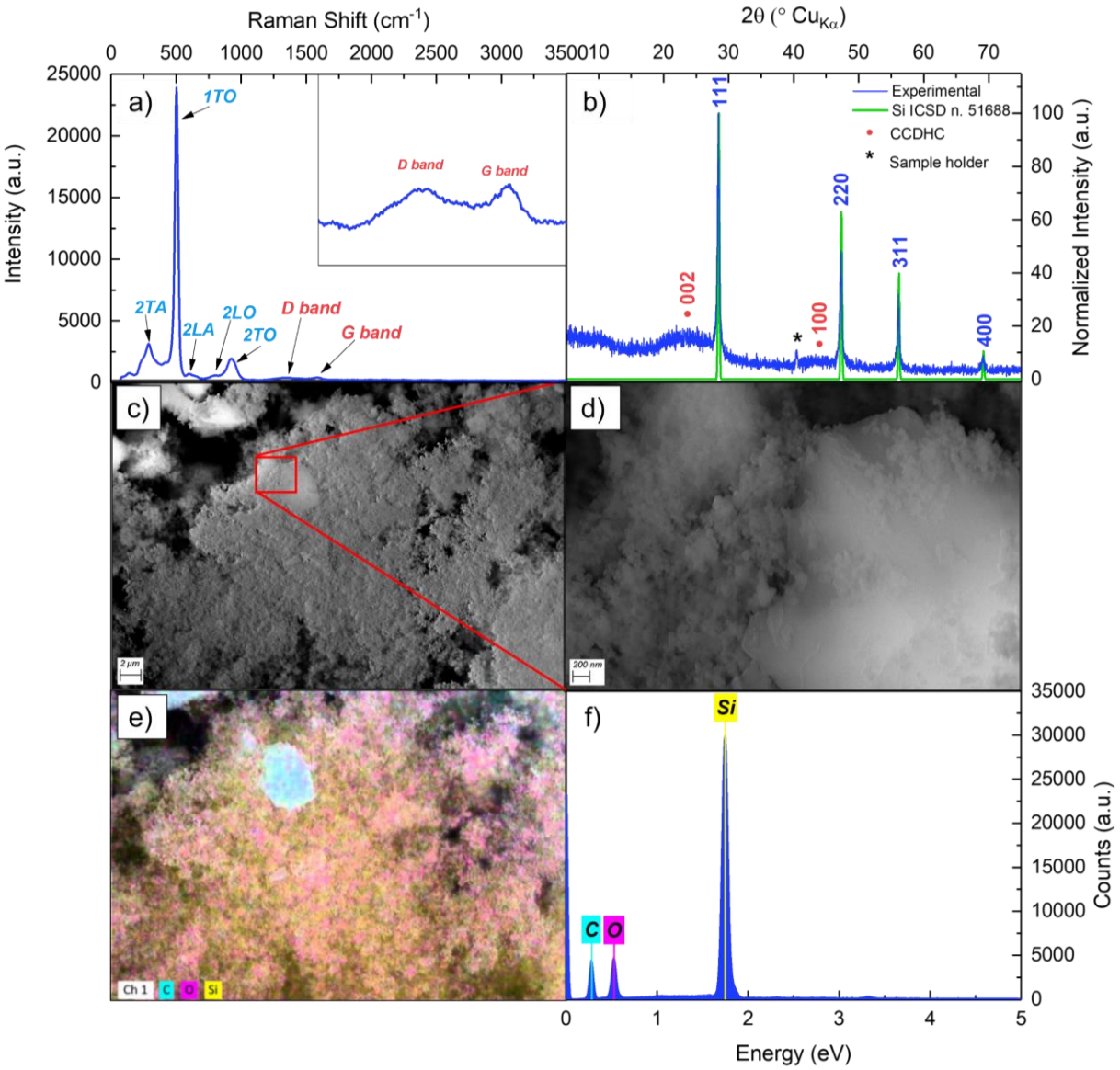

Figure 2-3. a) Raman spectrum of Si/CCDHC, with magnification on the D and G bands (inset); b) Experimental diffraction pattern of Si/CCDHC (blue) and reference diffractogram of Si (green); SEM micrographs of Si/CCDHC at c) 5000x and d) 40000x magnifications; e) Elemental mapping of Si/CCDHC for Si, C and O; f) EDX analysis of Si/CCDHC.

The Raman spectrum of the Si/CCDHC powder after ball-mill (**Figure 2-3a**), is consistent with literature findings for Si and hard carbon matrix. Specifically, the peak at 520 cm^{-1} can be ascribed to the first order transverse optical mode (1TO) typical of c-Si; the bands at 300 cm^{-1}, 609 cm^{-1}, 808 cm^{-1} and 930 cm^{-1} are consistent with the second order transverse acoustic (2TA), longitudinal acoustic (2LA), longitudinal optic (2LO) and transverse optical (2TO) modes of Si, respectively [297]; the D and G bands of CCDHC are also slightly visible at 1339 cm^{-1} and 1589 cm^{-1}, while the second order 2D and D+G fall within the background due to the very high intensity of Si-related peaks. The crystallinity of Si is confirmed by calculating the value of the integrated intensity ratio between the second and first order transverse modes (I_{2TO}/I_{1TO}), which is reported to be close to 0.25 for a-Si and decreases to

0.1 for bulk c-Si: the obtained ratio of 0.083, indicates a crystallinity similar to that reported for bulk c-Si. However, the positions of the 2TO and 2LO modes (here 808 and 930 cm^{-1}) are found to be slightly shifted to lower wavenumbers with respect to those reported for the bulk c-Si (namely 825 and 940 cm^{-1}), consistently with the presence of some nanocrystals with dimensions in the range of 5-7 nm [298–300]. The experimental diffraction pattern of Si/CCDHC, reported in **Figure 2-3b**, is consistent with the presence of cubic Si with space group *Fd3m* (ICSD n. 51688). A crystallite size of ≈ 109 nm was calculated by applying **Equation 17** (Scherrer's equation). This value is in line with the particle dimensions declared by the supplier. The peaks at 2θ ≈ 24° and 2θ ≈ 43° are consistent with the diffraction pattern shown in **Figure 2-2b** for the bare CCDHC powder. The small peak at 2θ ≈ 40 ° labeled as (*) is attributed to the brass sample holder used for the analysis. **Figure 2-3c-e** shows the SEM micrographs of the Si/CCDHC composite at different magnifications and the elemental mapping of Si, C and O performed on the same spot. At higher magnifications (**Figure 2-3d**), it is possible to observe that the Si nanoparticles visually possess a spherical morphology with a particle size of about 100 nm, which is consistent with the calculated crystallite size from the structural characterization. By comparing the micrographs obtained at low and high magnification (**Figure 2-3c-d**) with the elemental mapping (**Figure 2-3e**), Si and CCDHC can be properly distinguished, as the small Si particles seem to be lying either onto the rough surface of the larger clusters of hard carbon or between chunks. From the SEM micrograph in **Figure 2-2c**, the lamellar-like structures and the big cavities on the rough surface of CCDHC may act as sites where most of the Si can be accommodated, being Si particles much smaller than those of the Hard Carbon; this could provide a reasonable buffering activity for Si volume expansion upon cycling. Moreover, if compared to **Figure 2-2d**, the presence of homogeneously distributed O atoms throughout the whole sample suggests that Si particles do possess a slight degree of surface oxidation. This is also confirmed by the more pronounced intensity of the related EDX peak in **Figure 2-3f**, suggesting a higher O content than bare CCDHC (O peak becomes comparable to the C one). For the sake of clarity, from **Figure 2-3f** one could argue that the intensity of Si peak seems to be much higher than that of C, thus indicating a much higher amount of Si related to C. However, in the absence of a flat- and highly polished-surface standard, a proper quantification of Si and C cannot be performed: lighter elements (i.e. O and C) generally yield low-energy photons which are susceptible to self-absorption phenomena when an energy beam E_0 > 3 keV is employed for the measurement. This phenomenon can lead to a lowering of the intensity of the C peak relative to that of Si, thus underestimating the amount of C when considering relative intensities [301]. Hence, in order to provide a more accurate measurement, a TGA analysis was performed on the composite powder to assess the Si/C composition after ball-milling (**Figure 2-4**).

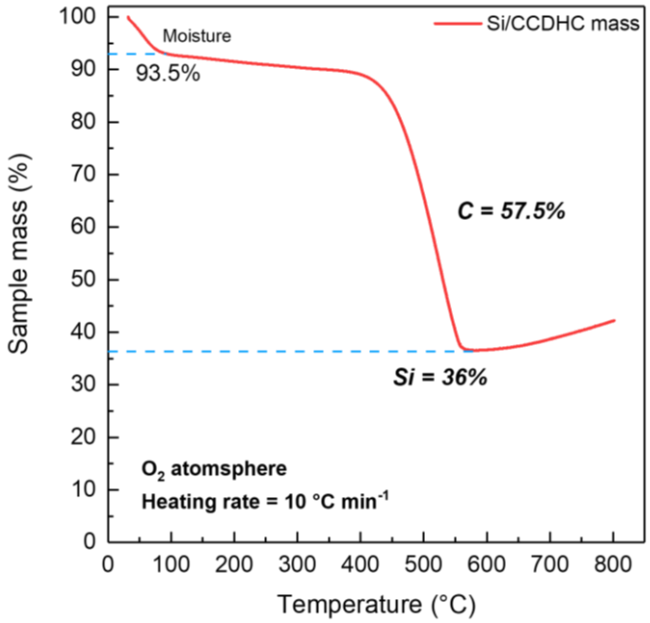

Figure 2-4. TGA of the Si/CCDHC composite after ball-mill in O_2 atmosphere (heating rate = 10 °C min^{-1}; temperature scan range = 30-800 °C).

The results from TGA indicate a small initial weight loss of about 6.5 % in the range 30-100 °C, which can be attributed to the moisture from the atmosphere. The subsequent pronounced mass loss of about 57.5 % in the range 400-600 °C is consistent with the oxidation of CCDHC to CO_2, while the remaining 36% mass is attributed to Si. This result provides confirmation of the 3:5 w/w ratio between Si and C and indicates a homogeneous mixing of the components after ball-milling. The small weight increase from 600 °C can be addressed to partial oxidation of Si forming SiO_x.

2.2.3 Electrochemical characterization

In order to investigate the redox processes occurring during Li storage and assess the effect of the carbon matrix upon cycling, electrodes of Si/CCDHC were subjected to cyclic voltammetry (CV) at a scan rate of 0.1 mV s^{-1} and galvanostatic cycling within the potential window of 0.01-1.50 V in half-cells vs. Li. The electrochemical behavior of the bare hard carbon matrix is shown in **Figure 2-5**, in terms of both cyclic voltammetry and galvanostatic cycling.

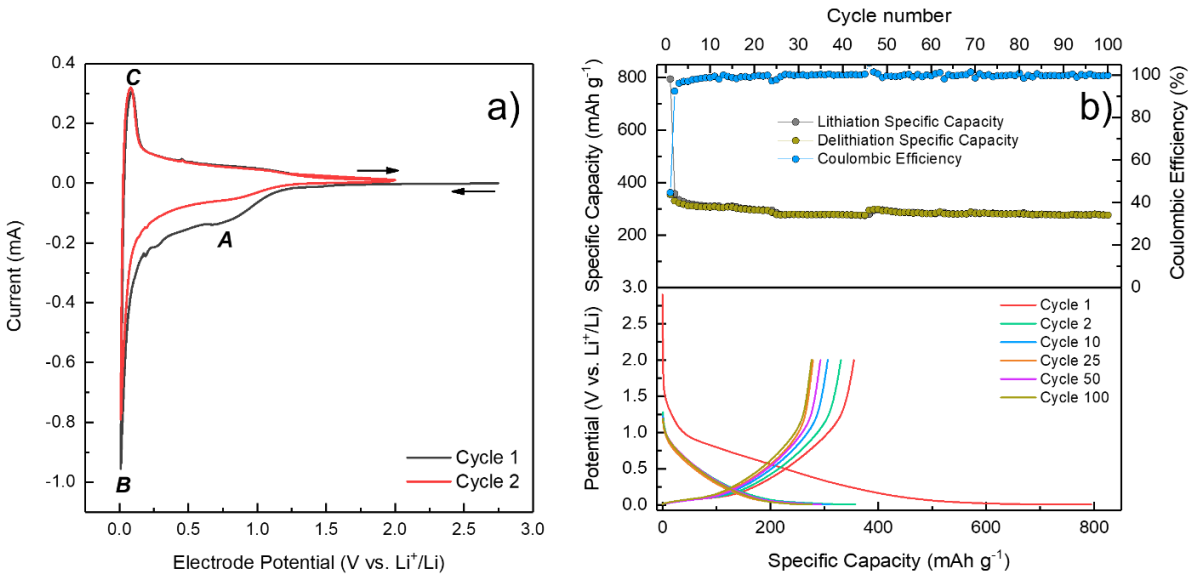

Figure 2-5. a) Cyclic voltammetry of the first two cycles for the bare CCDHC; b) galvanostatic cycles and E vs Q profiles obtained at 0.3 A g^{-1} for the bare CCDHC.

In **Figure 2-5a**, a broad signal is present between 0.8 and 0.6 V during the first cathodic scan (peak A), which is due to the electrolyte decomposition on the electrode surface to form the SEI layer. This process is the main cause for the irreversible capacity displayed in **Figure 2-5b**. In the following cycles, this peak disappears, meaning the SEI is completely formed. At lower potentials, peak B starts appearing at about 0.1 V. This intense signal is attributed to the intercalation of Li^+ ions between graphene planes. During the first anodic scan, the peak centered at 0.1 V (peak C) can be attributed to the process of de-intercalation of Li^+ ions. For both charge and discharge, the broadened regions above 0.2 V can finally be associated to the adsorption/desorption of Li from the surface defects of the hard carbon [302]. From the second scan onwards, the voltammograms are superimposed. Notably, despite the high initial irreversible capacity, the coulombic efficiency rapidly rises to values close to 100 %.

The electrochemical behavior of Si/CCDHC was compared with electrodes of Si/Graphite (Si/Gr) prepared in the same way and with comparable active material mass loading. The voltammograms acquired during the first and second cycle for the two composites are reported in **Figure 2-6a-b**. During the cathodic and anodic scans, the characteristic features of lithium storage by Si can be observed, as well as the signals related to the lithiation of the different carbon matrices and to SEI formation. As for the Si/Gr composite (**Figure 2-6a**), during the first cathodic scan, the small peak at 1.23 V (D1) and the broad peak at 0.75 V (D2) can be attributed to the irreversible decomposition of VC from the electrolyte and formation of the passivation layer, respectively [303,304]; the peak at 0.20 V (G1) is related to the first stage of intercalation of Li^+ ions into graphite, with formation of LiC_{24} phase, while the sharp peak ranging from 0.13 V to 0.01 V (G2+S1) can be assigned to the

superposition of the different lithiation phases of graphite (from LiC_{24} to LiC_{18}, LiC_{12} and finally LiC_6) and the alloying of Si with phase transition to amorphous Li_xSi and crystalline $Li_{15}Si_4$ phases. Upon the first anodic scan, the three close peaks ranging from 0.11 V to 0.27 V are related to the stepwise de-intercalation of Li from graphite, with reformation of the phases LiC_{12} (G3), LiC_{18}/LiC_{24} (G4), and complete delithiation to C_6 (G5); the peaks at 0.34 V (S2) and 0.47 V (S3) can be assigned to the de-alloying of the amorphous Li_xSi phases and dissolution of $Li_{15}Si_4$ phase with amorphization of the resulting Si. From the second cathodic scan Si lithiation proceeds mostly through formation of amorphous Li_xSi phases, which endmember corresponds to $Li_{13}Si_4$ stoichiometry as evidenced by the small hump visible at 0.21 V (S4) [163,304–306]. As for the Si/CCDHC (**Figure 2-6b**), during the first cathodic scan, the peaks related to the irreversible decomposition of VC (D1) and formation of SEI (D2) are also present. The peak ranging from 0.13 V to 0.01 V (C1+S1) can be attributed to both insertion of Li^+ ions between the graphene planes of the disordered carbon [302], and to alloying reaction of Si to Li_xSi and $Li_{15}Si_4$ phases. Upon the first anodic scan, the small hump at 0.08 V (C2) indicates the de-insertion of Li from the hard carbon matrix, while the peaks at 0.35 V (S2) and at 0.47 V (S3) are consistent with the de-alloying process and dissolution of the higher lithiated state, as observed in the Si/Gr composite. From the second cycle, the electrochemical signal related to Si lithiation processes, already evidenced in **Figure 2-6a**, are confirmed. All the carbon-related peaks are consistent with the cyclic voltammetry reported in **Figure 2-5a**. No additional processes are evidenced after the second cycle for both composites.

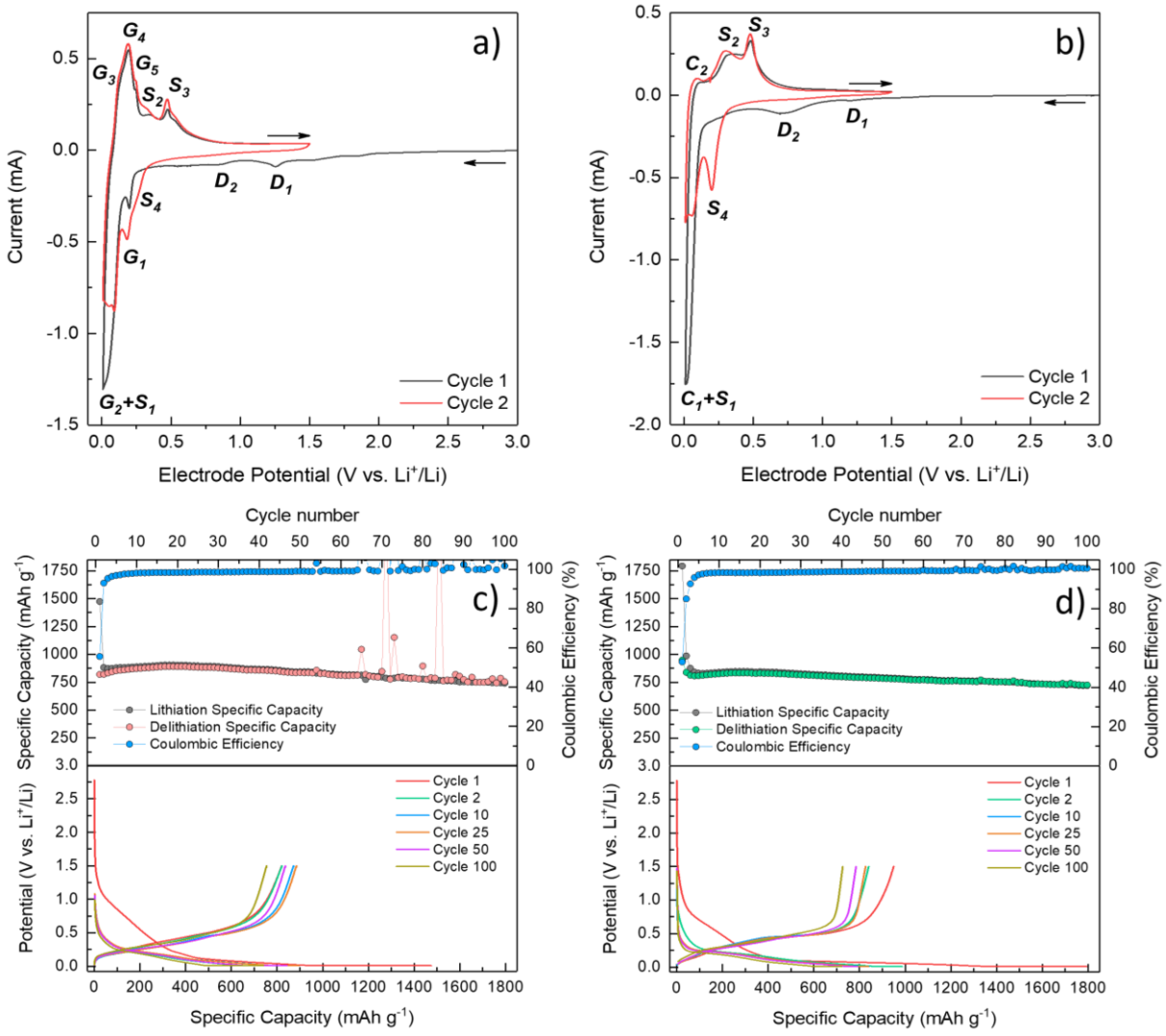

Figure 2-6. Cyclic voltammetry of the first two cycles for a) Si/Gr and b) Si/CCDHC; galvanostatic cycles and E vs. Q profiles obtained at 1 A g^{-1} current density for c) Si/Gr and d) Si/CCDHC. Both composite electrodes employ the CS/CA binder.

The charge/discharge performance over 100 cycles and the stability of the Si/CCDHC composite have been evaluated by galvanostatic cycling at 1.0 A g^{-1} in the 0.01 V < E < 1.5 V potential window, and compared to the benchmark Si/Gr composite cycled in the same conditions. The specific capacities obtained for both electrodes are reported in **Figure 2-6c-d**, as well as the related coulombic efficiencies. Both composites show a high initial capacity decay mainly due to two irreversible processes: the formation of the solid electrolyte interphase and the amorphization of the initial crystalline silicon. As it can be visualized from both potential profiles and galvanostatic cycles, these processes mainly occur during the first cycle, leading to poor initial coulombic efficiency of 55.94 % and 53.24 % for Si/Gr and Si/CCDHC, respectively, with a progressive increase in reversibility starting from the 5th cycle on, after which the specific capacity tends to stabilize at about 800 mAh g^{-1} for both materials. Despite the slightly lower initial coulombic efficiency of Si/CCDHC with respect to the benchmark Si/Gr electrode, the average coulombic efficiency of the latter stabilizes at about

98.8 %, while that of Si/CCDHC can reach values up to 99.4 %, thus indicating a better reversibility of the processes after the first cycles. Moreover, after 64 cycles the benchmark Si/Gr electrode starts experiencing high spikes in the delivered capacity during the oxidation process, suggesting breakage and reformation of SEI as a result of the structural shrinkage of Si particles upon de-alloying [307]. This behavior is not encountered with the Si/CCDHC composite during the entire test, indicating that the hard carbon matrix is able to mitigate the effects of the volume changes upon cycling and to maintain a good structural integrity of the electrode.

The electrochemical performance of bare Si employing the CS/CA binder is also given for comparison in **Figure 2-7**, in order to assess the superiority of the Si/CCDHC composite.

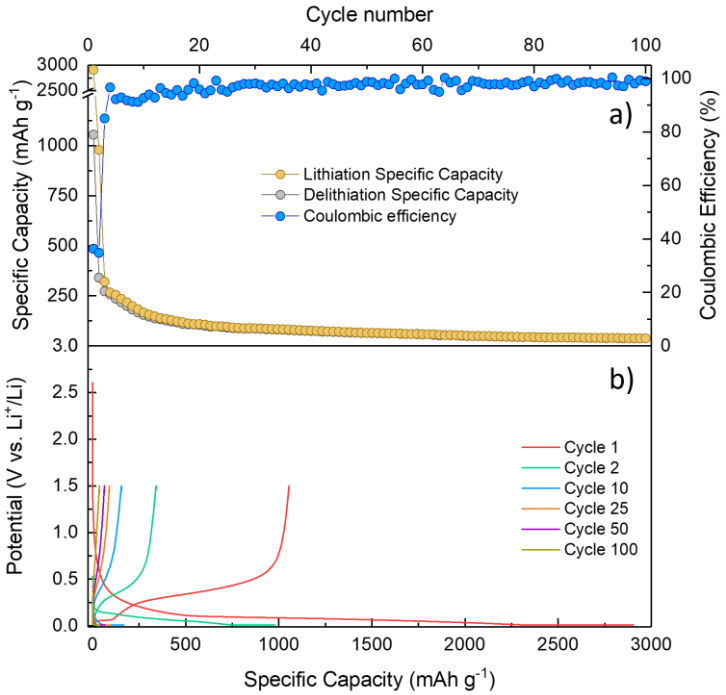

Figure 2-7. a) Galvanostatic cycles and b) E vs Q profiles obtained at 1.0 A g^{-1} for bare Si nanoparticles with the CS/CA binder.

Indeed, the bare Si electrode displays the characteristic decay of capacity due to repeated volume changes upon cycling, starting with a first lithiation yielding a capacity of almost 3000 mAh g^{-1} but falling to very low values after just few cycles, as a result of delamination and loss of electrical contact in the absence of a buffering matrix. This result further provides confirmation of the beneficial effect of CCDHC when coupled to bare Si.

The effect of the crosslinked binder was also studied by comparing the cycling performance of Si/CCDHC electrodes fabricated with different binders, maintaining the same electrode formulation and cycling conditions (**Figure 2-8**).

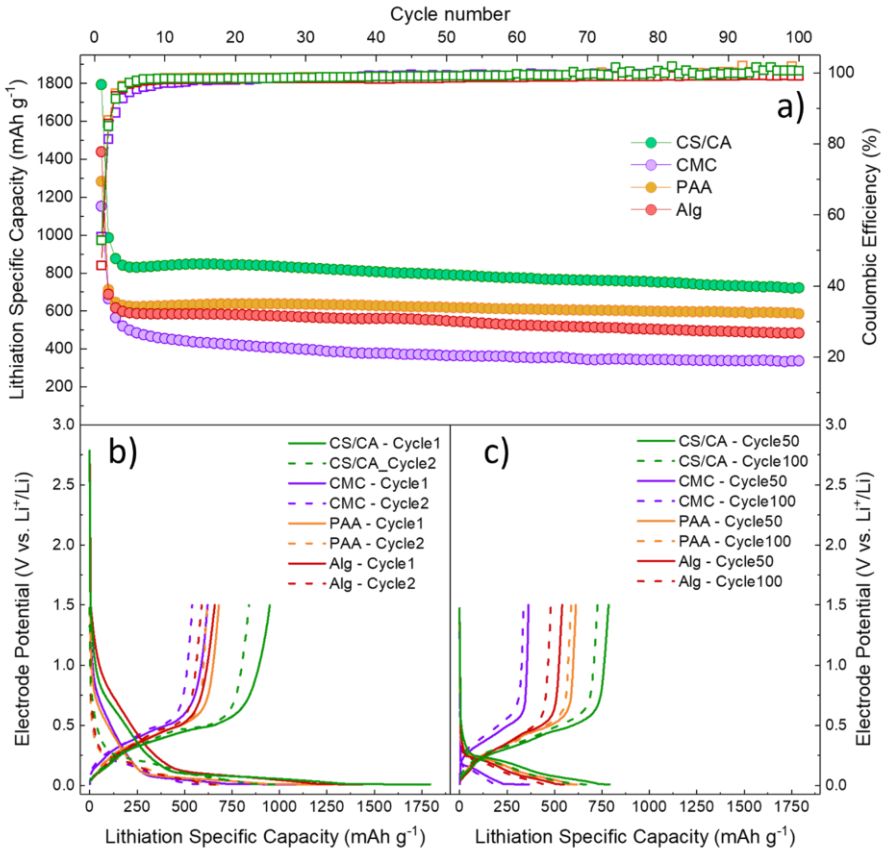

Figure 2-8. a) Comparison of galvanostatic cycling of Si/CCDHC employing different binders at 1.0 A g^{-1} (CS/CA = green, CMC = violet, PAA = orange, Alg = red); E vs Q profiles at b) 1st and 2nd cycle, and c) 50th and 100th cycle, for each binder employed.

Notably, from the data reported in **Figure 2-8a**, the crosslinked CS/CA binder shows improved performance and stability with respect to all other binders studied for the comparison (i.e. PAA, CMC and Alg). The results obtained clearly demonstrate the beneficial effects from the combination of the hard carbon matrix and the crosslinked binder in promoting a higher stability with respect to conventionally studied components, resulting in better performance and slower capacity decay, as evidenced in the potential profiles in **Figure 2-8b-c**.

A morphological investigation by SEM was also carried out on pristine (**Figure 2-9a-d**) and cycled electrodes (**Figure 2-9e-h**) in order to obtain additional information about the electrode integrity after repeated cycling. Impedance measurements were also performed at OCV, after 1 cycle and after 10 cycles for all electrodes, to further prove the ability of the CS/CA binder to improve the electrode stability upon cycling (**Figure 2-9i-k**).

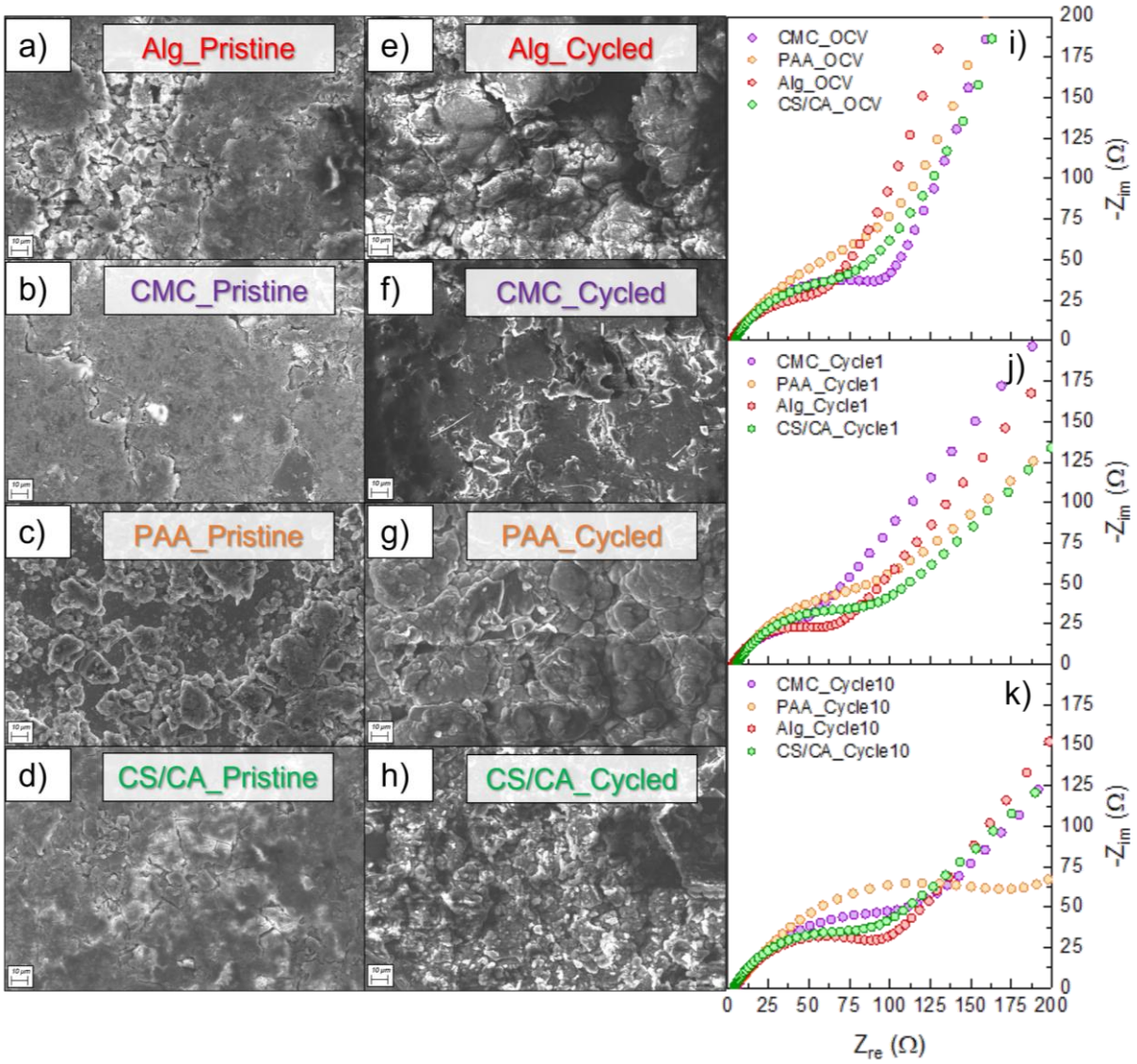

Figure 2-9. SEM micrographs at 1000x magnification of pristine Si/CCDHC electrodes employing a) Alg, b) CMC, c) PAA and d) CS/CA binders; SEM micrographs at 1000x of Si/CCDHC electrodes after 100 cycles employing e) Alg, f) CMC, g) PAA and h) CS/CA binders; EIS performed on all electrodes at i) OCV, j) cycle 1 and k) cycle 10.

The morphologies of the pristine electrodes in **Figure 2-9a-d** show different textures according to the binder employed: in particular, the PAA-based electrode displays a very rough surface and higher inhomogeneity in the spatial distribution of particles compared to the other electrodes, which have a more homogeneous distribution and a flat surface. Moreover, the Alginate-based electrode visually displays a higher number of cracks with respect to the CMC- and the Chitosan-based ones, which possess a relatively flat surface. After 100 cycles (**Figure 2-9e-h**) all electrodes show some degree of agglomeration: the electrodes based on Alginate, CMC and PAA all show a very high particle agglomeration after cycling, with the formation of big clusters; in turn, the Chitosan-based electrode displays a less pronounced agglomeration, with smaller clusters and a more homogeneous particle distribution. This indicates that the CS/CA binder is able to favor a better adhesion with the current collector and cohesion between Si particles, which are more homogeneously kept close to each other

avoiding the formation of isolated clusters. This evidence is further supported by the impedance measurements in **Figure 2-9i-k**, which show the tendency of the CS/CA binder to favor a more stable total impedance (diameter of semicircle) upon cycling, with values remaining almost constant.

The rate capability was evaluated in order to assess low- and high-current tolerance of the Si/CCDHC composite anode. In detail, specific currents of 0.1, 0.2, 0.5, 1.0, 2.0 and 4.0 A g^{-1} have been applied, with current rate changing every 5th cycle; subsequently, a specific current of 1.0 A g^{-1} was restored and kept for 150 cycles in order to verify the capacity retention of the material. No constant voltage step was applied at the end of the lithiation. The results of the rate capability test are shown in **Figure 2-10**.

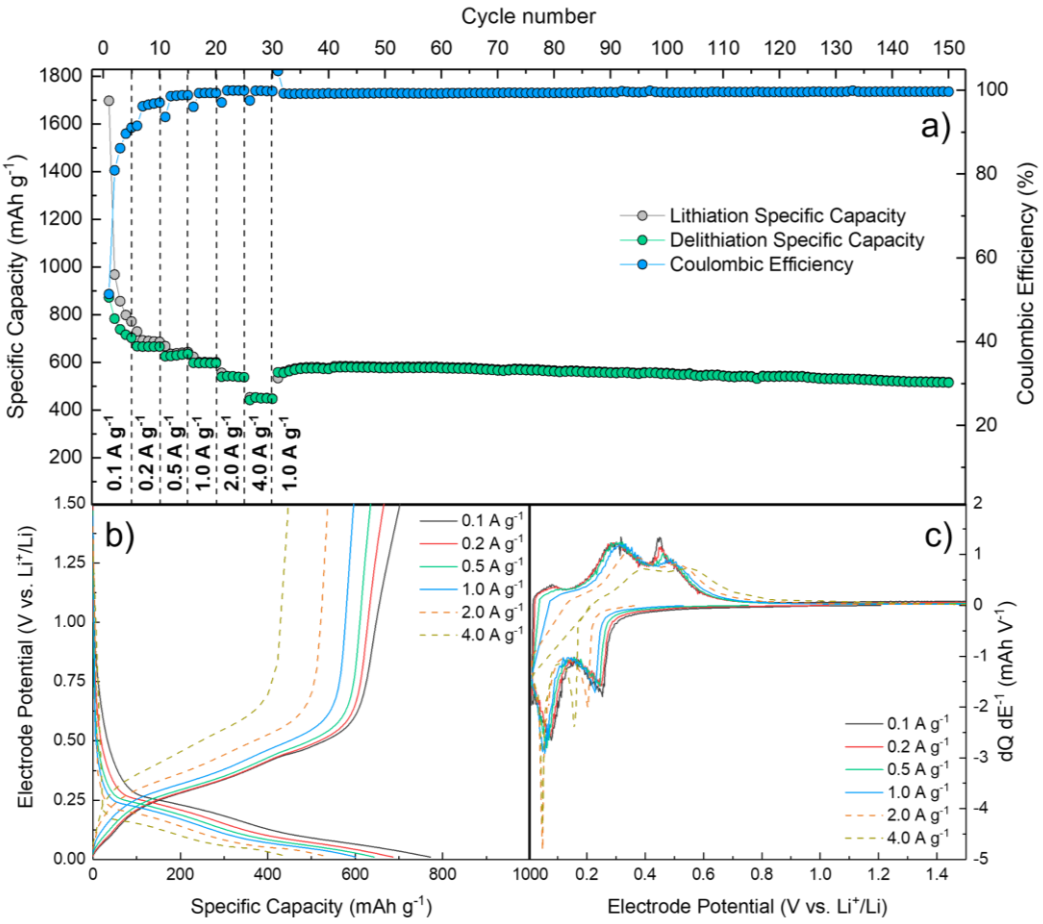

Figure 2-10. Rate capability of Si/CCDHC with CS/CA binder: a) Cycle number vs. Specific capacity/Coulombic efficiency; b) E vs. Q potential profiles for each specific current applied; c) Differential dQ dE^{-1} vs. E profiles for each specific current applied.

The specific capacity of the material only slightly decreases with increasing current rate up to 1.0 A g^{-1}, and the decrease becomes more pronounced for the higher rates. However, from the 6th cycle on, by progressively increasing the specific current applied up to 10 and 20 times (i.e. from 0.2 to 2.0 and 4.0 A g^{-1}) the capacity retention displayed by the composite is still of 77 % and 63 %, respectively. Moreover, the capacity retention of the material at the highest current rate tested is as high as 75 %

when considering the standard cycling conditions at 1.0 A g^{-1} as the reference current rate, confirming the ability of the material to sustain high specific currents. When the current of 1.0 A g^{-1} is restored, the specific capacity is recovered and maintained for 120 cycles at values comparable to those previously obtained at the same rate, thus further demonstrating an excellent capacity retention. Notably, the coulombic efficiencies are lower at slow currents (i.e. 0.1 A g^{-1}), but progressively increase at higher specific currents up to nearly 100 % when 4.0 A g^{-1} is applied. This result suggests that, on one side lower currents facilitate the kinetics of irreversible interfacial processes, while on the other side the kinetics of the reversible (de)alloying process is favored at higher currents. In **Table 2-3**, the main characteristics of the electrodes tested in terms of mass loading, composition, rate capability performance, capacity retention at high specific currents and production of the C buffering matrix, are compared to some Si/C composites recently published [308–317]. It is worth to notice that, despite the lower performance with respect to some works present in literature, the Si/CCDHC composite displays a higher capacity retention when going from slow to high current rates, while maintaining a higher active material mass loading and percentage in the electrode composition than many other materials considered hereby. In addition, the preparation of the CCDHC is kept as simple and sustainable as possible, thus offering promising scale-up opportunities.

Table 2-3. Comparison of electrode characteristics and rate performance of some Si/C composite anodes.

Si-based composite	Loading (mg cm^{-2}) Composition	Current rates (A g^{-1})	Specific cap. (mAh g^{-1}) Cap. retention	Buffering agent	Ref. (year)
Hierarchically C-coated Si	0.5 70:20:10	0.4 – 4.0	2900 – 1500 52 %	Resorcinol/Formaldehyde coating and annealing in Ar	[308] (2018)
Core-shell Si@Ni-NP@GNS	Not specified 60:20:20	0.2 – 1.0	1930 – 1107 57 %	GO coating and annealing in N_2 to obtain rGO	[309] (2018)
Si@void@C nanocomposite	0.24 – 0.44 60:20:20	0.2 – 4.0	1800 – 960 53 %	Resorcinol/Formaldehyde coating and annealing in Ar	[310] (2019)
Mesocarbon microbeads/nano-Si/amorphous C	2.0 80:10:10	0.2 – 1.0	≈720 – ≈350 ≈ 49%	Functionalization of C in HNO_3/H_2SO_4 solution; Annealing in Ar	[311] (2019)
Nanoporous Si@Graphitized C	1.0 70:20:10	0.2 – 2.0	698 – 294 42 %	Magnesiothermic reduction in CO_2 flow	[312] (2021)
Si/C/Graphite	1.0 – 3.0 50:25:25	0.2 – 2.0	697 – 487 70 %	Hydrothermal reaction at 160 °C Annealing in N_2	[313] (2021)
N-doped C-coated hierarchically porous Si	1.5 70:20:10	0.2 – 2.0	925 – 435 47 %	Dopamine polymerization in HCl/Tris-buffer solution and annealing in Ar	[314] (2021)

Si-based composite	Loading (mg cm^{-2}) Composition	Current rates (A g^{-1})	Specific cap. (mAh g^{-1}) Cap. retention	Buffering agent	Ref. (year)
Si@RF@MP	1.0 80:10:10	0.2 – 2.0	≈610 – 421 ≈69 %	Resorcinol/Formaldehyde coating and heating at 370 °C in reactor Annealing in oxidative atmosphere and then Ar	[315] (2022)
Si@C	Not specified 50:30:20	0.2 – 2.0	3019 – 2310 77 %	Annealing in N_2 with C_3H_6	[316] (2022)
Si@GNCC	1.0 80:10:10	0.2 – 2.0	≈1750 – ≈1250 ≈ 71 %	C deposition via CVD from acetonitrile in Ar	[317] (2022)
Si/CCDHC	**1.0 – 1.2** **80:15:5**	**0.2 – 1.0** **0.2 – 2.0** **0.2 – 4.0**	**690 – 600** **87 %** **690 – 535** **77%** **690 – 440** **63 %**	**Annealing of waste corn-cobs in Ar**	**This work**

Finally, from the E vs. Q potential profiles in **Figure 2-10b** it is possible to observe that a low polarization is displayed by the material for all currents up to 1.0 A g^{-1}, indicated by the plateaus only slightly shifting to lower/higher potentials. This effect is even more clearly visualized in the calculated dQ dE^{-1} vs. E differential plots in **Figure 2-10c**, where the peaks related to the redox processes are almost completely superimposed with the exception of the highest current rates.

2.2.4 Characterization of structural evolution and interfacial properties

The structural stability and interfacial behavior of the material were investigated by means of ex-situ Raman spectroscopy and potentiostatic electrochemical impedance spectroscopy.

In order to verify the structural evolution of both Si and CCDHC matrix upon Li uptake/release, the first discharge/charge cycle has been studied through ex-situ Raman spectroscopy performed at selected electrode potentials. The potential values of interest correspond to the electrode being in the following conditions during lithiation (**Figure 2-11a**) and de-lithiation (**Figure 2-11c**) processes: (A) fresh electrode before SEI formation and alloying process (E = 1.0 V); (B) SEI formation (E = 0.7 V); (C) initial stages of Li-Si alloying and lithiation of the hard carbon matrix (E = 0.25 V); (D) complete formation of $Li_{15}Si_4$ alloy and full lithiation of the hard carbon matrix (E = 0.01 V); (E) de-lithiation of the hard carbon matrix (E = 0.085 V); (F) de-alloying of amorphous Si phases (E = 0.35 V); (G) dissolution of crystalline $Li_{15}Si_4$ phase (E = 0.48 V); (H) fully discharged and de-lithiated electrode (E = 1.5 V).

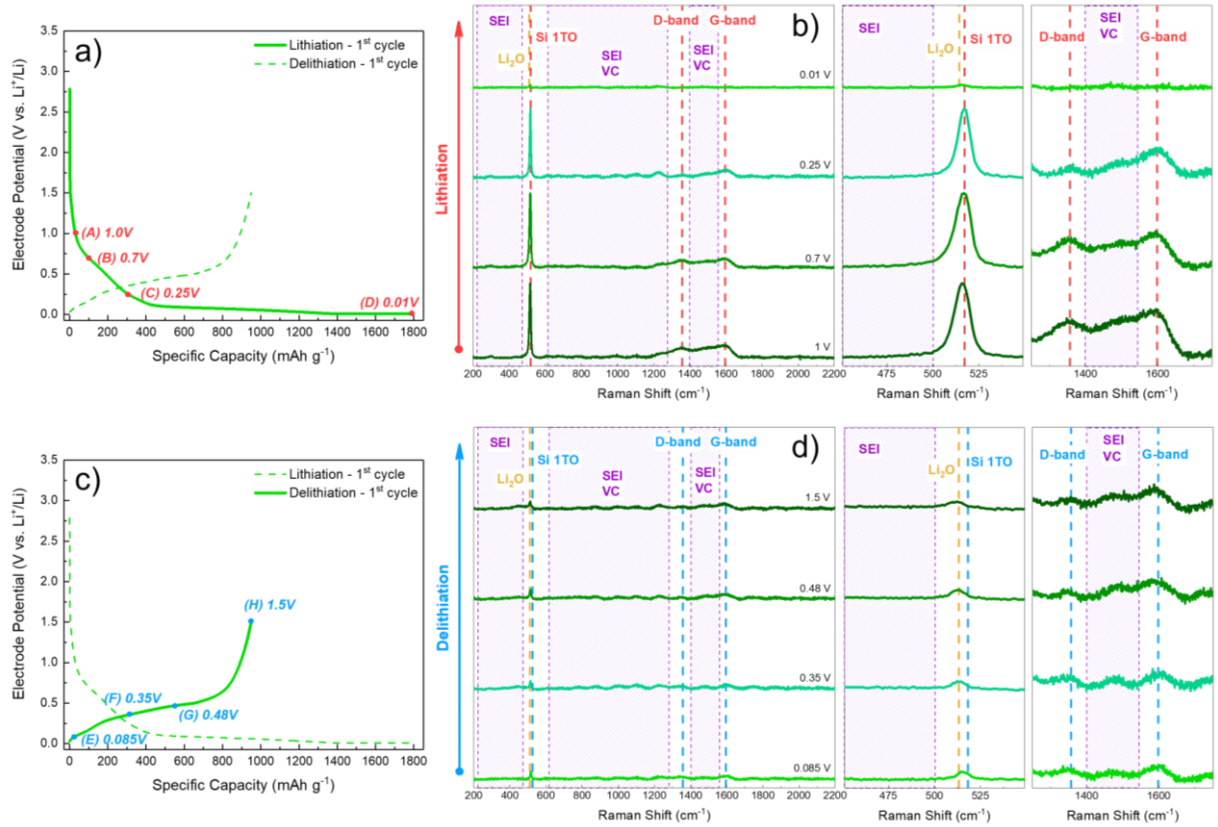

Figure 2-11. Ex-situ Raman characterization of Si/CCDHC electrodes with CS/CA binder: galvanostatic profiles with highlighted acquisition points during a) lithiation and c) de-lithiation; Raman spectra acquired during b) lithiation and d) de-lithiation, with magnifications on the Si 1TO and Li_2O peaks, and D/G bands of hard carbon.

During lithiation (**Figure 2-11b**), the spectra show the characteristic 1TO peak of crystalline Si at 920 cm^{-1} and the typical D and G bands from the hard carbon matrix and Super C-65 additive, located at 1357 cm^{-1} and 1598 cm^{-1}, respectively. Upon discharge, the intensity of the Si-related 1TO peak remains almost unchanged until very low potential values, and only at the lower cut-off (0.01 V) it is possible to observe the disappearance of the signal, indicating the conversion of crystalline Si to the $Li_{15}Si_4$ phase, which is Raman inactive. This phenomenon is in line with other findings in literature, and is addressed to the formation of Li-Si bonds upon lithiation (which disrupts the crystalline order of Si lattice) [318]. Generally, lithiation of Si is often accompanied by peak shift or broadening for the Si 1TO mode due to the stress induced in the crystal structure [319]; in this case, none of these features is encountered at low potentials upon lithiation, indicating a good buffering activity from the hard carbon matrix and/or the crosslinked binder. In the last phase of the discharge, i.e. 0.01 V, a small peak is present at 515 cm^{-1}. At a first approximation this peak could be argued as a shift to lower wavenumbers of the 1TO mode of unreacted c-Si due to an induced stress from the lattice expansion of neighboring alloyed Si particles; however, since this peak is still present in the whole subsequent charge (**Figure 2-11d**), and no peak shift to higher wavenumbers is encountered until full de-lithiation (i.e. upon contraction and restoration of the Si crystal lattice), this possibility seems unlikely. Rather,

this signal might be the result of Li reacting with the partially oxidized surface of Si particles (evidenced from the elemental mapping in **Figure 2-3e**) upon the first discharge, resulting in the irreversible formation of Li_2O [320]. Although the background is too high to observe any evidence of amorphous Si at 480 cm^{-1} [298] upon the charge process, the absence of Si-related peaks suggests amorphization of the resulting Si after the first cycle. In the 200-500 cm^{-1}, 600-1350 cm^{-1} and 1450-1500 cm^{-1} regions of the spectra, very low and enlarged signals can be observed, which are related with decomposition compounds from the electrolyte forming the passivation layer, mostly Li_2CO_3 from the carbonate solvents [319]. Interestingly, the SEI-related signals and the two peaks located at about 1000 cm^{-1} and 1475 cm^{-1} are already present at potentials higher than that of SEI formation upon discharge, and no obvious differences can be observed between 1.0 V and 0.7 V. Therefore, these features at 1.0 V can originate either from the binder [321] or more likely from the decomposition of VC [322], the latter occurring at potentials higher than 1.0 V. In **Figure 2-12** a Raman spectrum performed on a pristine electrode is reported: in the absence of electrolyte and of its related decomposition products, the Raman spectrum clearly shows the peaks related to Si 1TO and all the second-order vibrational modes as well as the carbon-related D and G band, and neither SEI-related humps nor peaks at 1000 cm^{-1} and 1475 cm^{-1} can be observed in this case. Hence, the signals cannot be attributed to the binder.

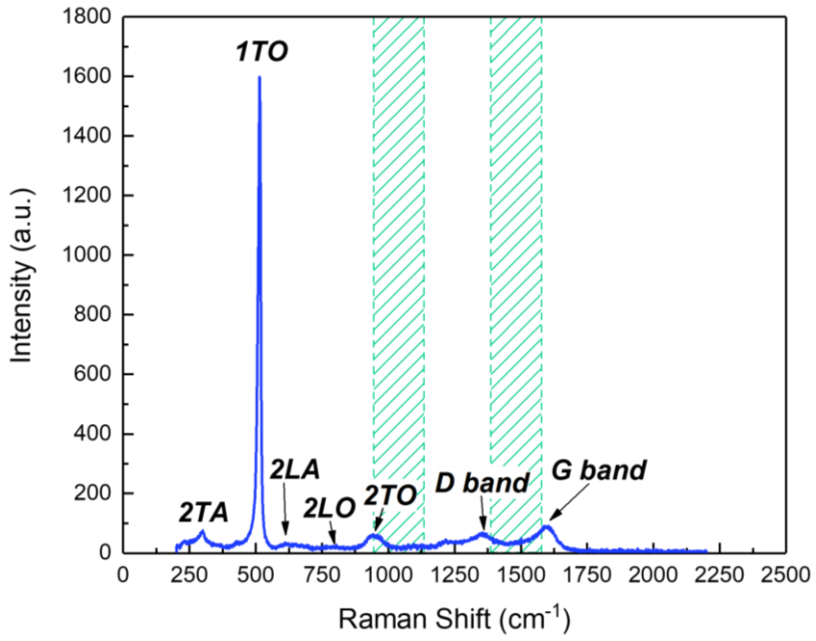

Figure 2-12. Raman spectrum acquired on the pristine Si/CCDHC electrode evidencing the regions where Chitosan signals are expected.

In particular, the peak at 1000 cm^{-1} in **Figure 2-11** is indeed assigned to a specific feature of VC-containing electrolytes, i.e. the R-O and C-C stretching modes of polycarbonates related to a radical polymerization of VC, as reported in another study [322]. The peak at 1475 cm^{-1} can be associated to one of the vibration modes of CO_3^{2-}, which may also be related to a ring opening reaction and a subsequent

radical polymerization encountered in carbonate species [319,322–324]. As for the D and G bands, upon lithiation it is possible to observe a progressive decrease in intensity for both signals, which starts before the disappearance of the 1TO mode of Si, as the lithiation of C starts at slightly higher potentials. The decrease of the D band can be explained from the occupancy of defective sites of the hard carbon by Li^+ ions limiting the breathing mode of sp^2 C atoms in the rings. The decrease of the G band is instead explained by the weakening of resonance caused by intercalation of Li^+ ions between graphene planes. At the lower cut-off voltage (i.e. 0.01 V), the intensity of the D and G bands becomes so low that the signals fall within the background generated by the presence of the SEI components on the electrode surface, and cannot be distinguished properly. The progressive decrease of intensity by increasing the lithiation degree is already reported in literature for carbonaceous materials, and it provides confirmation of the mixed adsorption-intercalation mechanism typical of hard carbons [319,325,326]. During de-lithiation, the D and G peaks start increasing again, and can be distinguished even at 0.085 V; however, the intensity ratio between D and G band is slightly lower than the initial one, suggesting a decrease of the D band after Li extraction. This indicates that some defective sites of the carbon matrix remain occupied after the first discharge, contributing to the initial irreversible capacity of the material. However, this partially lithiated state of the hard carbon may act as a Li scaffold, increasing the conductivity of the whole composite and gradually improving the charge transfer kinetics for the subsequent cycles.

In order to further investigate the interfacial properties of the material, impedance spectra were recorded at the bias potential of 0.4 V during the 1st cycle and then every 10th cycle upon lithiation (**Figure 2-13**), using a three-electrode cell configuration. All the Nyquist plots obtained (**Figure 2-13b**) are characterized by four main features: (I) an intercept with the real axis in the high frequency region; (II) a small semicircle in the medium frequency region; (III) a bigger semicircle in the medium-to-low frequency region; (IV) a straight line in the low frequency region. The obtained Nyquist plots have been modeled by the Equivalent Circuit method [327], and the related parameters have been calculated through a NLLS fitting protocol by using the RelaxIS3 software (rhd instruments). The intercept (I) at high frequencies represents the migration of Li^+ ions through the electrolyte solution, hence it was modeled as a pure resistive element (R_{el}). The semicircle (II) at medium frequencies is related to the migration of Li^+ ions through the passivation layer with charges accumulating onto its surface, and was modeled as a resistive element (R_{SEI}) in parallel with a capacitor element (C_{SEI}). The bigger semicircle (III) at medium-to-low frequencies can be ascribed to the faradaic charge transfer process with electrical double layer formation onto the surface of the active material particles, modeled as a resistive element (R_{ct}) in parallel with a capacitor element (C_{dl}). Finally, the line (IV) at low frequency describes a semi-infinite diffusion to a blocking electrode, which was modeled with a Warburg impedance (W) in series with a capacitor element (C_i) indicating the differential intercalation

capacitance. The resulting equivalent circuit, written according to Boukamp's notation [328,329], is $R_{el}(R_{SEI}C_{SEI})(R_{ct}C_{dl})WC_i$. For the fitting procedure, the pure capacitive elements were substituted by constant phase elements (Q), in order to consider the non-ideal, capacitive behavior given by electrode inhomogeneity and surface roughness [327].

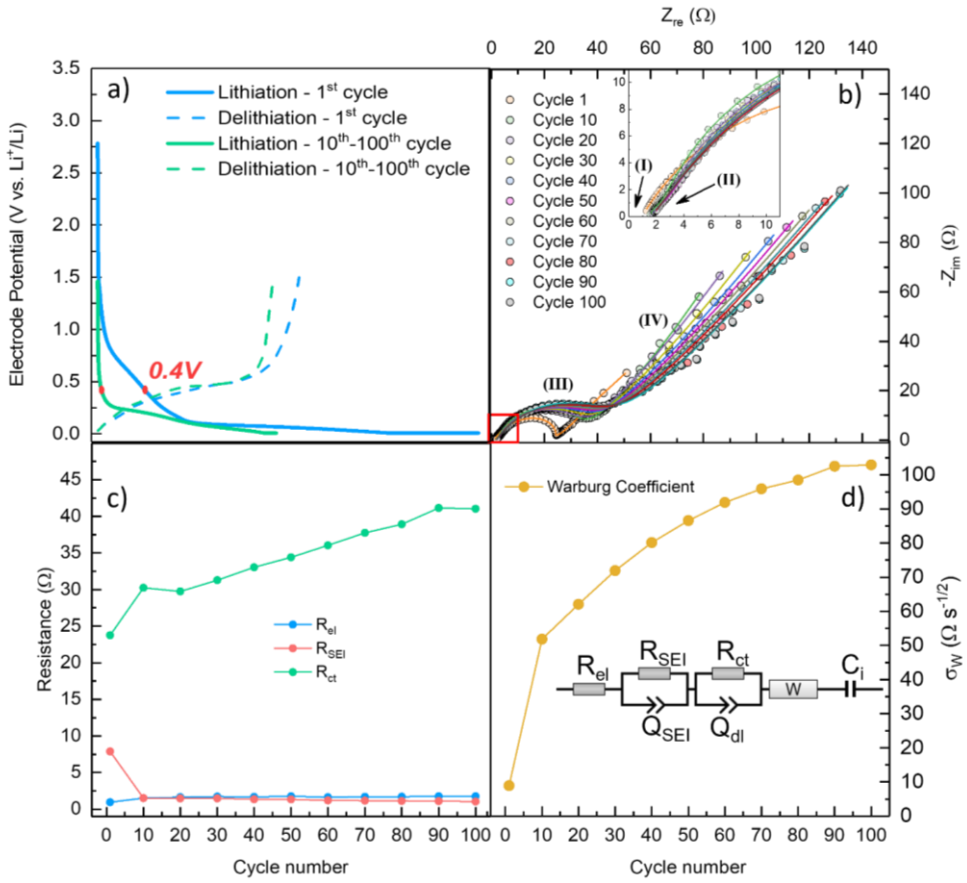

Figure 2-13. Electrochemical impedance spectroscopy analysis of Si/CCDHC electrode with CS/CA binder: a) Galvanostatic profiles with highlighted acquisition potential during 1st and every 10th cycles; b) Nyquist plots obtained and related fits, with magnification on the high-frequency region (inset); c) Trend of resistances upon cycling; d) Trend of Warburg coefficient upon cycling. The fit results have been obtained by using the equivalent circuit model reported in panel d).

In **Figure 2-13c-d** the values of R_{el}, R_{SEI}, R_{ct} and σ_W, calculated by using the previously described model for fitting, are reported as a function of the number of cycles, in order to evidence the behavior of the interfaces upon cycling. The resistance of the electrolyte, R_{el}, basically remains constant upon cycling until 100 cycles. The resistance of the passivation layer, R_{SEI}, displays a higher value in the first cycle due to the formation of the SEI, and then decreases to very low values remaining constant upon cycling. These results suggest the formation of a thin passivation layer during the first discharge, which then remains stable in the subsequent cycles, hence preventing further electrolyte decomposition. This trend is consistent with the results obtained by the galvanostatic cycling in **Figure 2-6d**, which did not show any obvious charge capacity spikes ascribable to SEI breakage and subsequent reformation.

As for the resistance to charge transfer, R_{ct}, a sharp increase is observed from the 1st to the 10th cycle, after which the resistance increment becomes less pronounced; eventually, stabilization is reached between 90 and 100 cycles. The initial sharper increase is consistent with the observations from ex-situ Raman (**Figure 2-11**), which revealed the presence of insulating Li_2O at the surface of the active material after the first discharge, thus increasing the electrode polarization in the subsequent cycles. Finally, the Warburg coefficient, σ_W, has an increasing trend upon cycling, which translates in progressively more hindered solid-state diffusion of Li^+ and decreasing of diffusion coefficient. However, the sharpest increment is encountered on going from the 1st to the 10th cycle due to the irreversible formation of the passivation layer making the diffusion slower [330]; in the following cycles, the increase bends towards a plateau, indicating a progressive stabilization of diffusion upon cycling.

The interfacial and kinetic properties of the material were also studied within a single cycle at different states of charge, by performing impedance measurements with a sampling interval of 0.02 V upon full lithiation and subsequent de-lithiation during cycle 10, to minimize any bias coming from possible modification of SEI and thickness (**Figure 2-14a-b**), using a two-electrode cell configuration to avoid inductive contributions at low potentials. For the sake of clarity, only selected diagrams are displayed to give a general trend upon decreasing/increasing potential. A quite large low-frequency semicircle can be observed at high potentials, which progressively tends to split in two contributions upon lithiation. When charging, the opposite behavior is displayed, with the two semicircles progressively merging into one larger feature. The additional semicircle in the medium-to-low frequency range was attributed to the contribution of the metal Li counter-electrode to the cell impedance, which cannot be approximated to zero in absence of a reference electrode (i.e. in two-electrode configuration here adopted). In order to deconvolute working and counter electrode contributions, the DRT analysis method was applied, by calculating the DRT function γ according to Tikhonov regularization [331]. For the DRT calculation to be valid, the boundary conditions require the convergence of the impedance towards the real axis when ω tends to 0; the typical impedance spectra in LIBs generally do not possess this requirement, as the low-frequency Warburg diffusion diverges from the real axis. For this reason, a pre-processing fit by the Nyquist plot by the equivalent circuit method is required prior to DRT determination [332,333]. Specifically, the raw spectra have been modeled, as a first approximation, according to the equivalent circuit $R_{el}(R_{SEI}C_{SEI})(R_{Li}C_{Li})(R_{ct}C_{dl})WC_i$, taking into account also the contribution from the counter-electrode. For the fitting procedure, the pure capacitive elements were substituted by constant phase element (Q) [328,329]. Then, the low frequency points, as simulated by WC_i elements, were subtracted from the overall impedance.

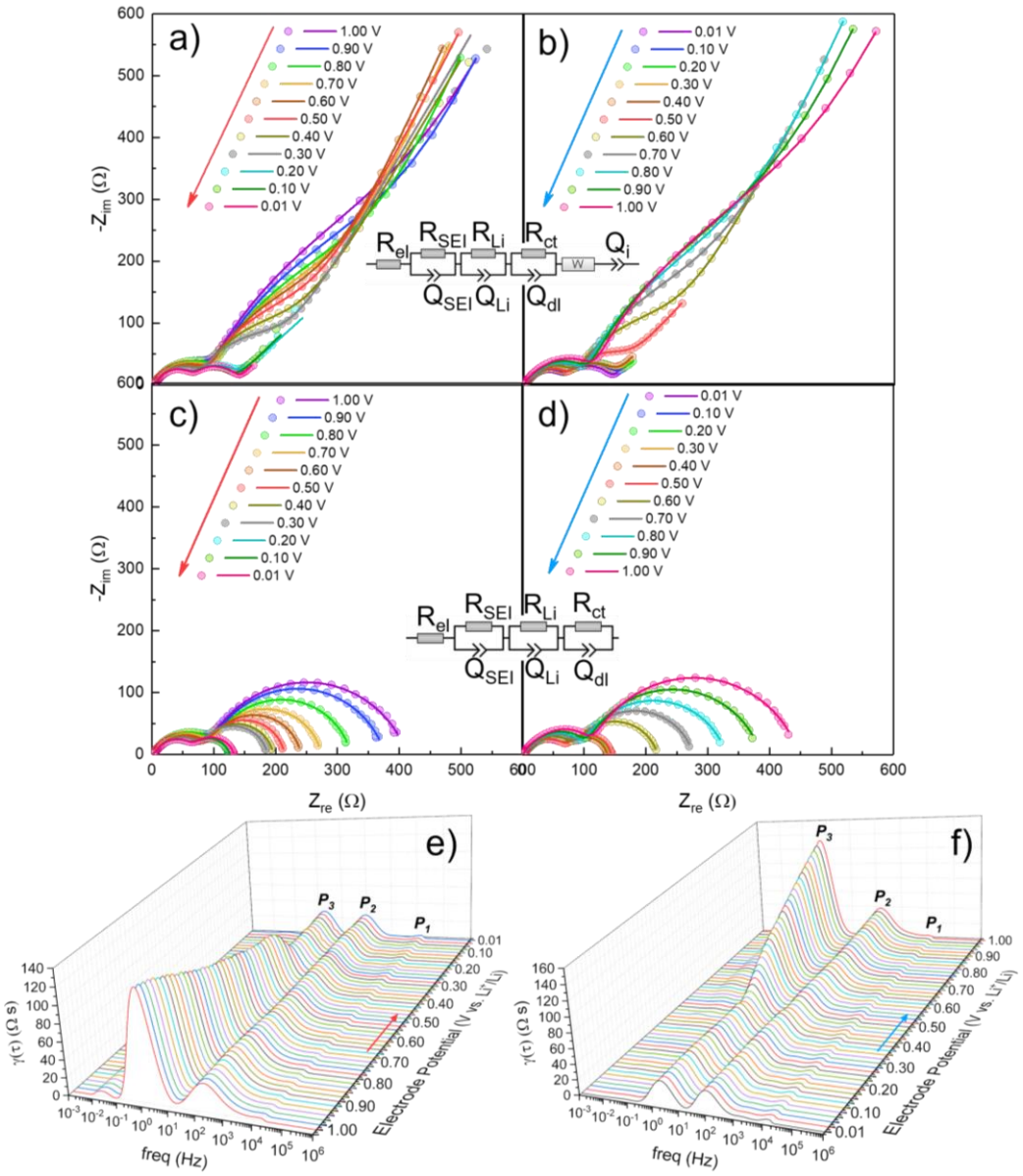

Figure 2-14. "Staircase" electrochemical impedance spectroscopy analysis of Si/CCDHC electrode with CS/CA binder, performed at the 10th cycle: Nyquist plots obtained during a) lithiation and b) de-lithiation, with related fits and equivalent circuit employed; Nyquist plots after subtraction of the diffusive part displayed for c) lithiation and d) de-lithiation, with related fits and equivalent circuit employed; Distribution of relaxation times for e) lithiation and f) de-lithiation.

The Nyquist plots obtained after subtraction are shown in **Figure 2-14c-d**. By observing the resulting diagrams, the previously overlapped semicircles are now well split into two contributions at all potentials. In particular, the medium-to-low frequency semicircle appears to remain almost constant upon discharge and the subsequent charge. The presence of this additional semicircle confirms the contribution of Li counter-electrode to the overall impedance. From the calculation of the DRT (**Figure 2-14e-f**), the various polarizations and the associated processes can be deconvoluted according to their different time constants, resulting in different characteristic frequencies. By calculating the DRT as a function of potential, it was possible to clearly define three main peaks (the small hump at low frequencies is an artifact due to the removal of Warburg diffusion) having different

behaviors: P1 is in a high frequency range, consistent with the resistance of the passivation layer (R_{SEI}); P2 remains basically constant and can be related to the contribution of the metal Li counter electrode (R_{Li}); finally, P3 at low frequencies has a strong dependency on the electrode potential, thus suggesting its association with the resistance of charge-transfer (R_{ct}) of the Si/CCDHC electrode. Interestingly, P3 progressively decreases by increasing degree of lithiation, with a sudden drop at about 0.25 V; upon de-lithiation, the opposite behavior is observed, with a sudden increase in peak intensity at about 0.50 V.

Based on the DRT findings, the fits of the impedance dispersions have been repeated on the Nyquist plots obtained after subtraction of the low frequency region (shown in **Figure 2-14c-d**), by using the equivalent circuit $R_{el}(R_{SEI}C_{SEI})(R_{Li}C_{Li})(R_{ct}C_{dl})$. The calculated values of the circuital elements are reported as a function of electrode potential for the lithiation and de-lithiation processes in **Figure 2-15a-b**.

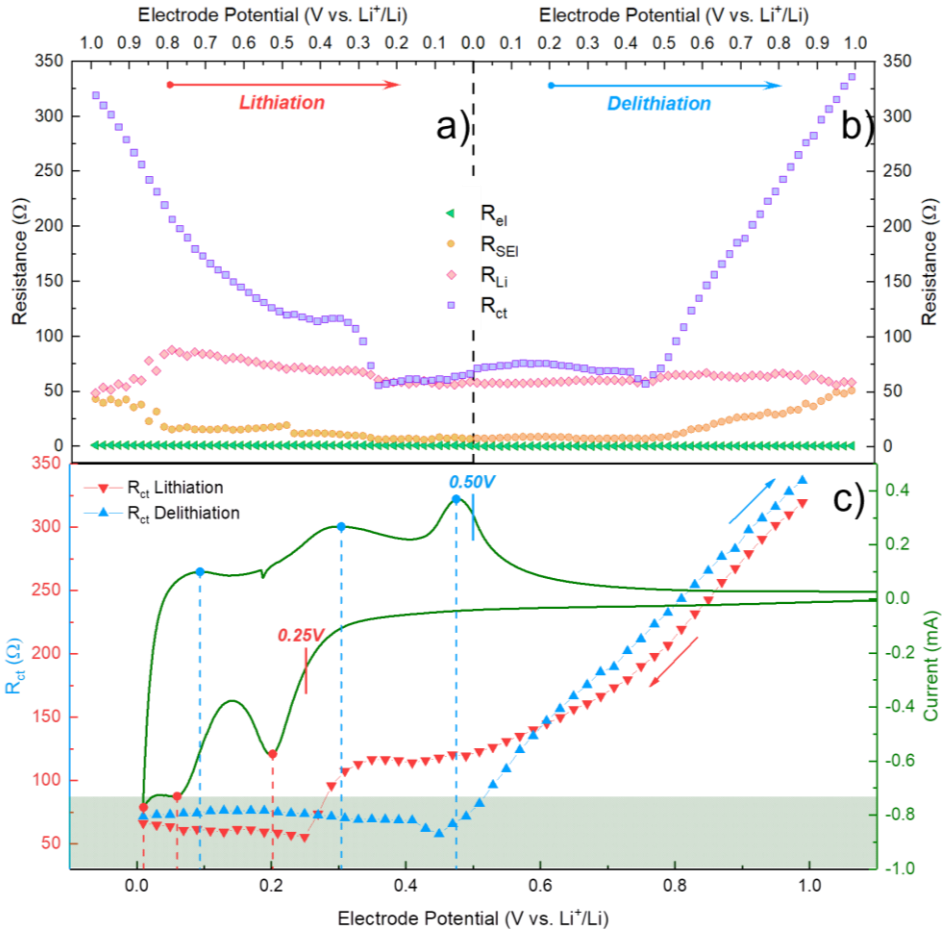

Figure 2-15. Trend of R_{el}, R_{SEI}, R_{Li} and R_{ct} as a function of potential during a) lithiation and b) de-lithiation; c) Trend of R_{ct} as a function of electrode potential, with correlation to cyclic voltammetry.

The resistance of the electrolyte, R_{el}, always remains constant and very low, as expected. The resistance of the passivation layer, R_{SEI}, displays a higher value at high potential, and progressively decreases

when approaching full lithiation; the opposite trend is displayed upon de-lithiation. This result suggests that upon lithiation, the SEI is stretched due to volume expansion of Si particles, becoming thinner but without cracking, thus providing a lower resistance and confirming the observations from ex-situ Raman (**Figure 2-11**) and from impedance measurements upon cycling (**Figure 2-13**). The resistance associated to Li metal counter-electrode, R_{Li}, is basically constant throughout the whole cycle, as previously described. As for the resistance associated with charge transfer, R_{ct}, it progressively decreases upon lithiation, and reversibly increases upon de-lithiation. The trend of R_{ct} as a function of potential was correlated to the cyclic voltammetry of the material (**Figure 2-15c**): the polarization due to charge-transfer reactions drops at 0.25 V upon discharge and sharply increases after 0.50 V upon charge, as observed from **Figure 2-14e-f**. These values are consistent with the starting and ending of redox activities in the cyclic voltammetry, respectively, and confirm the reversibility of the (de)alloying process within the single cycle.

2.2.5 Proof of concept Si/CCDHC||LFP full cell

In order to have a preliminary evaluation for the compatibility of the Si/CCDHC composite anode in a full cell with LFP cathode, the cell was galvanostatically cycled by applying a constant specific current of 1.0 A g^{-1}_{anode} (**Figure 2-16**). A cathode excess was here employed, with Si/CCDHC serving as the working electrode to prevent any plating issues.

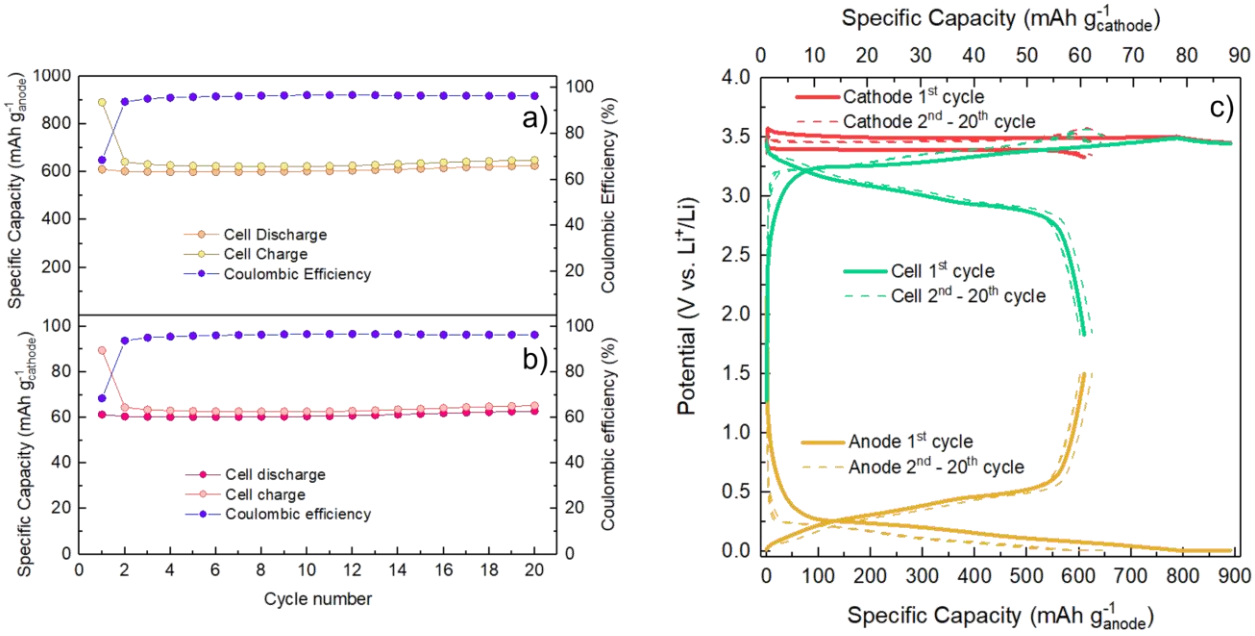

Figure 2-16. Galvanostatic cycles obtained at 1.0 A g^{-1} with normalization according to a) anode and b) cathode active material masses, respectively; c) E vs Q profiles for Si/CCDHC (yellow), LFP (red) and Si/CCDHC || LFP full cell (green).

In **Figure 2-16a-b** a specific capacity of 890.5 and 610.1 mAh g^{-1}_{anode} (corresponding to 89.5 and 61.3 mAh $g^{-1}_{cathode}$) is observed for the first cell charge and discharge, respectively, with a coulombic

efficiency of 68.5 %. In the following cycles, the full cell displays a stable capacity of about 600 mAh g^{-1}_{anode} (61 mAh $g^{-1}_{cathode}$), with a coulombic efficiency rising up to values > 95 %, and an average cell energy density of about 175.4 Wh kg^{-1}. As a proof of concept, these results suggest the feasibility to use the two materials in a full cell configuration, with quite good values for specific capacity, coulombic efficiency and specific energy density, which can be optimized through a proper balancing between the two components [334]. This compatibility is confirmed by observing the potential profiles in **Figure 2-16c**, where all the plateaus from anode, cathode and full cell basically don't change in shape and are not polarized upon cycling from the 2nd cycle on despite the high current density applied.

In **Figure 2-17**, the potential hysteresis of both the anode and cathode material are graphically displayed as a function of the specific capacity of the cell. The reversible and lost energy were evaluated by considering the 10th galvanostatic cycle, in order to make sure that any contributions from irreversible processes took place and the capacity was stable.

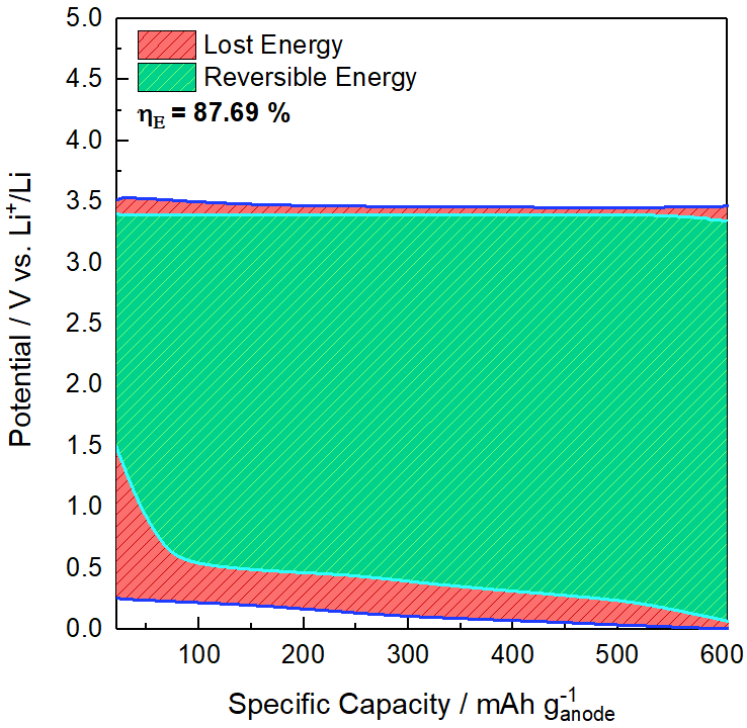

Figure 2-17. Energy efficiency for the Si/CDHC | | LFP full cell, calculated at the 10th cycle, displaying both the reversible energy (green area) and the lost energy (red area).

From the plot it is possible to observe a low voltage hysteresis (red) due to the small gap between the charge and discharge curves of the two materials. The amount of reversible energy released during the discharge step is displayed as the green area, hence from this plot it was possible to calculate the energy efficiency of the cell according to **Equation 18**:

$$\eta_E = \eta_Q \times \eta_U = \eta_Q \frac{\bar{U}_D}{\bar{U}_C} = \frac{\int_0^{Q_{fD}} U(Q)dq}{\int_0^{Q_{fC}} U(Q)dq} \qquad \textbf{Eq. 18}$$

where η_E, η_Q and η_U are the energy, coulombic and voltage efficiencies, respectively; the terms $\bar{U}_D$ and $\bar{U}_C$ refer to the average voltage of discharge and charge, respectively; Q_f refers to the final amount of charge in the half-cycle [335].

Thus, the calculated value for the energy efficiency at the 10th cycle is found to be as high as 87.69 %, which combined to the low voltage hysteresis, provides confirmation of the compatibility of the anode material Si/CCDHC with the employed cathode LFP in a full cell configuration. The reversible energy could be further improved by properly optimizing the balancing of anode and cathode materials, and providing a prelithiation step to account for the Li loss during SEI formation. However, due to time constraints, these strategies have not been studied at present and will be the subject of future works.

2.3 Conclusions

The performance and stability of a composite anode based on Si and a biomass-derived hard carbon employing a green crosslinked binder were evaluated. The standard galvanostatic cycling displayed quite high performance comparable to those of the same material employing commercial graphite as the buffering matrix, but a higher stability was displayed over prolonged cycling and no SEI breakage was observed. Moreover, the crosslinked binder also proved to be more effective in promoting a higher structural stability with respect to the conventionally studied binders. From the rate capability test, the Si/CCDHC composite showed very high capacity retention and reduced polarization even at high current rates. Ex-situ Raman spectroscopy proved to be a powerful technique in determining the structural stability of the material within the first discharge/charge cycle. Si was found to undergo irreversible amorphization during the first cycle, and the hard carbon matrix also underwent a partially irreversible lithiation, consistent with the low coulombic efficiency at first cycle. However, the reversibility of the processes was confirmed by impedance spectroscopy measurements performed firstly upon increasing cycle number, and secondly upon full (de)lithiation within a single cycle, aided by the calculation of DRT function. The results showed that the hard carbon matrix is effective in buffering the volume changes upon cycling; moreover, a stable SEI was formed after the first cycle, providing a limited contribution to the overall impedance and no further electrolyte decomposition in the subsequent cycles. The reversibility of processes was further confirmed by the trend of R_{ct} compared to the redox peaks in cyclic voltammetry, in excellent agreement with the results obtained by ex-situ Raman, impedance measurements and DRT function. Overall, considering the high amount of Si in the formulation, the material still displayed promising characteristics as a next-generation anode for LIBs, and its compatibility with a commercial LFP cathode was assessed in a proof-of-concept full cell measurement. Further optimizations are still needed for practical applications, and they will be the subject of future studies.

3 Investigation of Structural and Interfacial Evolution upon Presodiation in $Na_{0.66}Mn_{0.75}Ni_{0.2}Mg_{0.05}O_2||$Hard Carbon Full Cell

In order to face the ever-rising fossil fuel depletion and advancement of global warming, several renewable energy sources like wind and solar energy are recently being developed with the aim to be used as alternative technologies for electrical energy production [336]. However, the intermittent nature of renewable energies leads to an irregular supply of electricity to the grid, since the electrical energy usage in homes, transportation, industries and offices is periodic in nature [13,337,338]. Large-scale ESSs are indeed fundamental for a proper scale-up utilization of renewables [339–341], and among all the storage technologies, rechargeable batteries are those attracting the highest attention, thanks to their intrinsic characteristics like high round-trip efficiency and long cycle life [342,343]. Since energy storage for stationary applications must meet the renewable energy demands, the ability to store energies of the order of MWh is needed, requiring the production of extremely large batteries for large-scale electricity storage. Hence, for stationary storage, material abundance, cost and safety become the primary issues over the energy density [344,345]. Concerning the most appropriate type of device, as already highlighted in Section 1.3, sodium is well-known for its wide distribution and elemental abundance over the Earth's crust as compared to lithium, with sodium salt supplies being readily available [67,69,346]. As a consequence, sodium-ion batteries pose advantages in terms of costs and resources with respect to the lithium counterpart, and innovations on this field have lately been strongly encouraged [347], with much effort devoted to the development of suitable electrode materials.

When it comes to the cathode materials, layered transition metal oxides are the most successful ones for commercial LIBs, hence this class of compounds is particularly interesting for SIBs because of their high specific capacity, a number of possible redox-active metals, and the possibility to employ established synthetic procedures [348–351]. Although the choice of the best cathode for application in commercial SIBs is still under debate, other classes of cathode materials like Prussian blue analogues and polyanionic compounds [226,232] possess disadvantages like intrinsic water, potential toxicity, lower specific capacity or low capacity retention. In turn, layered oxides suffer from irreversible phase transitions and high reactivity towards moisture, and an evaluation of the chemical composition is fundamental to achieve optimal cathode materials for this class of compounds. In this regard, among the TM cations to be used in the cathode composition, Mn and Fe have the highest abundance and the lowest price, with the former showing the lowest price turbulence because of its wide distribution; moreover, Mn ions can either contribute to capacity as a redox center or work as a structural scaffold when kept in the 4+ oxidation state. When considering the specific transferred electrons by the redox

active species and the average working potential, the $Ni^{4+/2+}$ redox couple possesses the highest average potential and can achieve a high specific energy density, hence also being one of the most favorable active elements to be employed [352]. Phase transformations upon cycling are typical of layered oxides, and can be attributed to electronic structural changes of cations and oxygen leading to anisotropic distortions [353] (e.g. Jahn-Teller-active Mn^{3+}), cation migration [354,355] or unbalancing of electrostatic interactions between the O-O repulsion, O-Na attraction and van der Waals force leading to P-type → O-type phase transitions [183,356] (e.g. Ni^{4+}/Ni^{2+} redox couple). These phase transitions are unlikely to be completely suppressed, but they can be largely mitigated or stabilized by cation substitution [357–360].

As for the anode side, hard carbons are regarded as the best choice thanks to the possibility to produce them starting from waste biomass [294,361,362]. However, due to the intrinsic nature of these carbonaceous materials, a significant first cycle irreversible capacity is generally observed due to SEI formation and Na-ion trapping in the material [363], posing a bottleneck for practical applications, as it results in a loss of cyclable sodium when in full cell configuration. Yet, the highest coulombic efficiencies at first cycle reported for commercial hard carbons is about 85 % [364,365], meaning at least a 15 % cyclable sodium is irreversibly lost in the best-case scenario. Given that the addition of a cathode excess to balance the high irreversible capacity from SEI formation would pose additional costs to the cell manufacture and leave in part of the cathode as a dead weight, presodiation strategies have been studied to favor the applicability of hard carbons in practical full cells, mainly consisting in the direct contact method with Na metal, or electrochemical sodiation method [366]. However, these methods are suitable for lab-scale applications but hard to employ on a larger scale. The use of sacrificial sodium sources as additives in the positive electrode formulation has recently received increasing attention, with a number of compounds studied for this purpose [367–373]. Among these the use of Na-squarate is regarded as a cheap, green and easy-to-prepare solution for presodiation, given the irreversible oxidative decomposition at 3.6 V vs Na^+/Na [191,373–375].

In this chapter, the combination of a layered $Na_{0.66}Mn_{0.75}Ni_{0.2}Mg_{0.05}O_2$ cathode (NaMNMO) and the previously studied corn-cob-derived hard carbon (CCDHC) for application in a sodium-ion full cell is reported, focusing on a compatibility study with a presodiation method employing sodium squarate sacrificial salt ($Na_2C_4O_4$). The electrodes are first characterized singularly by means of CV, GCPL, and Rate Capability tests. An extensive structural, interfacial and electrochemical characterization of the electrodes when used in full cell configuration is also reported, which includes ex-situ SEM, operando XRD, operando XAS, ex-situ XPS, impedance measurements and calculation of the distribution of relaxation times (DRT). A comparison between the system with and without presodiation is provided, together with a tentative explanation of the structural and interfacial evolution in both cases.

The present work was carried out during a 5-month internship at the Institute for Applied Materials – Energy Storage Systems (IAM-ESS) of Karlsruhe Institute of Technology (KIT), in the research group of Dr. Sonia Dsoke.

3.1 Experimental section

In this section, details regarding synthetic procedures, electrode processing, structural, chemical and electrochemical characterization are summarized.

3.1.1 Synthesis of CCDHC and $Na_{0.66}Mn_{0.75}Ni_{0.2}Mg_{0.05}O_2$

The synthetic procedure for the CCDHC anode is the same as reported in **Subsection 2.1.1**.

As for the cathode powder, in a joint collaboration within the Post Lithium Storage (POLiS) Cluster of Excellence, the doped P2 $Na_{0.66}Mn_{0.75}Ni_{0.2}Mg_{0.05}O_2$ layered oxide (labeled as NaMNMO) was synthesized by the research group of Dr. Mario Marinaro at ZSW, according to a method reported in literature which consists in a two-step synthesis [376]. Briefly, $Mn_{0.75}Ni_{0.25}(OH)_2$ was first synthesized by co-precipitation in a continuous stirred tank reactor (V = 1 L) by employing a mixture of $Ni(NO_3)_2 \cdot 4H_2O$, $Mn(NO_3)_2 \cdot 6H_2O$, NaOH and NH_3 solution with the appropriate ratios. The obtained precursor was then subjected to a solid-state synthesis step by mixing via wet impregnation with an aqueous solution containing appropriate amounts of NaOH (7 mol L^{-1}) and $MgCO_3$ (3.7 w/w %). The mixture was dried at 140 °C for 3 h and the obtained powder was calcined at 900°C in a batch furnace for 12 h under air atmosphere followed by cooling to 200 °C. The powder was immediately transferred to a Büchi Glass oven and kept under vacuum at 200 °C overnight. The dried powder was transferred and stored in an Ar-filled glovebox (MBraun) with O_2 and H_2O content < 0.5 ppm.

3.1.2 Synthesis of $Na_2C_4O_4$

The sacrificial additive $Na_2C_4O_4$ (sodium squarate) was synthesized according to the reaction described in **Equation 19**, by starting from the corresponding acid to produce the sodium salt.

$$H_2C_4O_4 + Na_2CO_3 \rightarrow Na_2C_4O_4 + CO_2 + H_2O \qquad \textbf{Eq. 19}$$

Briefly, stoichiometric amounts of 3,4-dihydroxy-3-cyclobutene-1,2-dione (squaric acid) and Na_2CO_3 were dissolved in d.i. H_2O and left stirring overnight at room temperature [191]. A Büchi rotavapor was employed to evaporate water, and the obtained white powder was subsequently dried under vacuum at 100 °C for 12 h and finely ground in an agate mortar prior to any use.

3.1.3 Structural characterization of NaMNMO and $Na_2C_4O_4$

The phase purity of the cathode active material, NaMNMO, and of the synthesized $Na_2C_4O_4$ was verified through powder X-ray diffraction (STOE STADI P diffractometer equipped with a Mo-Kα

radiation source, λ = 0.709 Å, and Debye-Scherrer geometry). All the diffraction patterns were analyzed through Rietveld refinements by using the FullProf software from the WinPLOTR software package.

3.1.4 Electrode processing

The slurry for the preparation of NaMNMO electrodes was obtained by mixing the different components in the formulation of 84 : 8 : 8 (NaMNMO : PVdF : Super C-65). All the components were first ground together in an agate mortar, added to NMP and left stirring for 4 h to form a homogeneous dispersion, with a 40% solid content. The obtained slurry was coated onto Al foil (15 μm thickness) through doctor blading technique and left drying for 2 h at room temperature and then at 100 °C in a vacuum oven. Finally, circular electrodes of Ø = 12 mm and Ø = 18 mm were cut by using an electrode puncher with the proper diameter and pressed at 4.42 ton cm^{-2} through a hydraulic press. Due to the air and moisture sensitivity of the cathode active material, all the abovementioned procedure was performed inside an Ar-filled glovebox (MBraun) with O_2 and H_2O content < 0.5 ppm. The slurries and electrodes for the sole $Na_2C_4O_4$ and for the NaMNMO/$Na_2C_4O_4$ mixture were prepared in the same way as for NaMNMO, with formulations of 65 : 5 : 30 ($Na_2C_4O_4$: PVdF : Super C-65) and 64.6 : 23.28 : 6.06 : 6.06 (NaMNMO : $Na_2C_4O_4$: PVdF : Super C-65), respectively. Electrodes for Operando XRD measurements of NaMNMO and NaMNMO/$Na_2C_4O_4$ were prepared by coating onto carbon paper current collector rather than Al foil, in order to avoid any signals from the current collector.

The slurry for the preparation of CCDHC electrodes was obtained by mixing the components in the formulation 93 : 5.6 : 1.4 (CCDHC : CMC/SBR (1:2) : Super C-65). The powders of CCDHC and Super C-65 were first dry-mixed through a SpeedMixer (DAC 150 FVZ-K) for 15 min at 300 rpm. A 2 % CMC solution in d.i. H_2O was then added to the powders and stirred at 1500 rpm for 45 min. Finally, a 39 % SBR emulsion was also added, together with a proper amount of d.i. H_2O to obtain a final solid content of 43 %, and the dispersion was stirred at 500 rpm for 15 min. The obtained slurry was coated onto Al foil (15 μm thickness) through doctor blading technique and left drying overnight at room temperature. The coating was then calendared by applying a force of 50 kN at 50 °C in order to have a 10 % thickness reduction. Finally, circular electrodes of Ø = 12 mm and Ø = 18 mm were cut by using an electrode puncher with the proper diameter and vacuum-dried at 110 °C overnight.

For full cell measurements, the wet thicknesses of the cathodic and anodic coatings were adjusted to provide charge balancing between positive and negative electrode (without considering SEI contribution), maintaining a slight excess of the latter to prevent plating effects. The mass loadings of the electrodes employed in the full cells ranged from 9 to 11 mg cm^{-2} for NaMNMO and 6 to 7 mg cm^{-2} for CCDHC.

3.1.5 Electrochemical measurements

Most of the electrochemical measurements for NaMNMO, $Na_2C_4O_4$, NaMNMO/$Na_2C_4O_4$, CCDHC half cells, and the related NaMNMO||CCDHC and NaMNMO/$Na_2C_4O_4$||CCDHC full cells, were carried out by using three-electrode Swagelok-type cells, with sodium metal serving as reference (both half and full cells) and counter electrode (only half cells). Modified two-electrode CR2032 coin-type cells were employed for operando XRD and Synchrotron XAS measurements of NaMNMO and NaMNMO/$Na_2C_4O_4$. Three-electrode PAT-Cells (EL-Cell) with pre-assembled sodium metal disk reference electrode were employed for impedance measurements on NaMNMO||CCDHC and NaMNMO/$Na_2C_4O_4$||CCDHC full cells. Whatman GF/D fiberglass separators were used for all the measurements, with the only exception being the cells employed for ex-situ XPS analyses, where a cellulose separator was chosen in order to avoid the presence of residues on the electrode surface after cycling. All cells were assembled in a high-purity Argon-filled glovebox (MBraun) with O_2 and H_2O content < 0.5 ppm. The electrolyte employed was 1M $NaPF_6$ dissolved in a 1:1 mol/mol mixture of ethylene carbonate and propylene carbonate (EC:PC) for all cells tested, with the addition of 5 % w/w fluoroethylene carbonate (FEC) only for half-cell measurements in order to stabilize the sodium metal from the counter electrode [377]. All electrochemical measurements were performed using a VMP-3 multichannel electrochemical workstation with an integrated frequency response analyzed by Bio-Logic. Cyclic voltammetries were acquired at a scan rate of 0.1 mV s^{-1} for all cells. The charge-discharge performance of all materials in both half-cell and full cell configurations were evaluated by galvanostatic cycling the electrodes for 2 formation cycles at 10 mA g^{-1} and then 20 mA g^{-1} for 100 cycles; for full cells, a slight anode excess was kept, and the applied current density was normalized according to the cathode active material mass. Rate capability tests were performed by galvanostatically cycling the materials with specific currents ranging from 10 mA g^{-1} to 2000 mA g^{-1}. The cycling tests for NaMNMO, $Na_2C_4O_4$ and NaMNMO/$Na_2C_4O_4$ half-cells were performed within the voltage window 2.70 V < E < 4.30 V, while those for CCDHC were performed within the window 0.01 V < E < 1.50 V. For the electrochemical tests performed on NaMNMO/$Na_2C_4O_4$, the cells were brought inside the glovebox after one full cycle and opened to remove the CO_2 formed during presodiation, thus avoiding any unwanted polarizations in the following cycles due to the increased pressure from gas evolution. For the full cells, a three-electrode setup was employed to control the cell potential while monitoring the anode and cathode ones, with a voltage window chosen by calculating the difference between the cut-offs of the single electrodes (i.e. 1.20 V < E < 4.29 V). Electrochemical impedance spectroscopy (EIS) measurements were acquired upon cycling in potentiostatic mode during the 1st, 2nd and every 12th cycle at bias potentials E_{cell} = 4.00 V and 4.29 V. For all EIS measurements, a sinusoidal perturbation of $\Delta E = \pm 10$ mV was applied over the frequency range 3 mHz < f < 199 kHz, with 10 points per decade and logarithmic spacing. The low-frequency diffusion

region was subtracted from the obtained Nyquist plots in order to calculate the function of distribution of relaxation times (DRT). The fitting procedure by Equivalent Circuit Method (ECM) and the calculation of the DRT function (Tikhonov regularization, $\lambda = 10^{-2}$) were performed by using the software RelaxIS3. All the potential values are referred to the Na^+/Na redox couple ($E° = -2.71$ V vs. RHE).

3.1.6 Morphological characterization

The evolution of the electrode morphology on electrodes of NaMNMO and NaMNMO/$Na_2C_4O_4$ (both pristine and after one cycle in full cell configuration) were performed through scanning electron microscopy (SEM) from Merlin, Zeiss NTS, in order to check possible surface modifications after sodium squarate decomposition and gas evolution. The full cells were charged by applying a specific current of 10 mA g^{-1}_{cat}, transferred into an Ar-filled glovebox (MBraun) with O_2 and H_2O content < 0.5 ppm, and the electrodes were washed in dimethyl carbonate (DMC) prior to investigation. A vacuum-transfer system (Leica EM VCT100) was used to transfer the electrodes from the glovebox to the microscope avoiding exposure to air.

3.1.7 Ex-situ and Operando measurements

Ex-situ X-ray photoelectron spectroscopy (XPS) measurements on electrodes of NaMNMO, NaMNMO/$Na_2C_4O_4$ and CCDHC (both pristine and after one cycle in full cell configuration) were conducted through a K-alpha spectrometer from Thermo-Fisher Scientific equipped with a micro-focused, monochromated Al-Kα X-ray source with 400 μm spot size. A pass energy of 50 eV was used. Data acquisition and elaboration was performed via the Thermo Advantage software [378], and the obtained spectra were fitted through one or more Voigt profiles. Quantification was performed by applying Scofield sensitivity factors, and all spectra were referenced in binding energy to the hydrocarbon C 1s peak at 285 eV. For the sake of clarity, all spectra were normalized to the maximum intensity (i.e. highest peak and background are normalized to [1,0]). In order to analyze the effect of $Na_2C_4O_4$ on the SEI and CEI composition, the full cells were charged and discharged by applying a specific current of 10 mA g^{-1}_{cat}, and a 1 h constant voltage step was employed at the discharge endpoint potential to ensure SEI/CEI stability. The cells were transferred into an Ar-filled glovebox (MBraun) with O_2 and H_2O content < 1.0 ppm, and the electrodes were recovered and washed by a 1-minute submersion in dimethyl carbonate (DMC). After washing, all electrodes were dried and mounted on a sample holder using a conductive Cu tape. The transfer to the XP spectrometer was performed through a transfer module under inert gas conditions.

In order to evaluate the effect of $Na_2C_4O_4$ on the stability of phase transitions, operando X-ray diffraction was carried out on NaMNMO and NaMNMO/$Na_2C_4O_4$ half-cells during the first two

cycles at 10 mA g^{-1}, through a high-energy and high-angular-resolution STOE diffractometer equipped with Ag-Kα radiation source, λ = 0.559 Å, two Mythen detectors and a dedicated coin cell setup [379], in transmission geometry. The modified coin cells acted as sample containers rotating continuously to improve the crystallite statistics. Diffraction patterns were collected in the scattering range 0 ° < 2θ < 36 ° with 0.005 ° intervals and a dwell time of 20 min.

Operando XAS measurements were performed at synchrotron beamlines P64 at PETRA III (DESY), Hamburg. The Mn and Ni K-edge for NaMNMO and NaMNMO/$Na_2C_4O_4$ were measured, and the energy was calibrated by using a corresponding Mn or Ni foil, as commonly applied in XAS experiments. MnO, Mn_2O_3, MnO_2 and NiO were used as standard materials. All data were collected at room temperature with a Si(111) double crystal monochromator, and all XAS spectra were processed by using the DEMETER software package [380]. A modified CR2032 coin cell setup with Kapton windows (Ø = 6 mm) was used to cycle the cells at 10 mA g^{-1} to investigate the first two cycles.

3.2 Results and discussion

3.2.1 Structural analysis of NaMNMO and $Na_2C_4O_4$

The structure of NaMNMO was investigated by means of X-Ray diffraction (XRD), and the Rietveld refinement of the obtained data is reported in **Figure 3-1**.

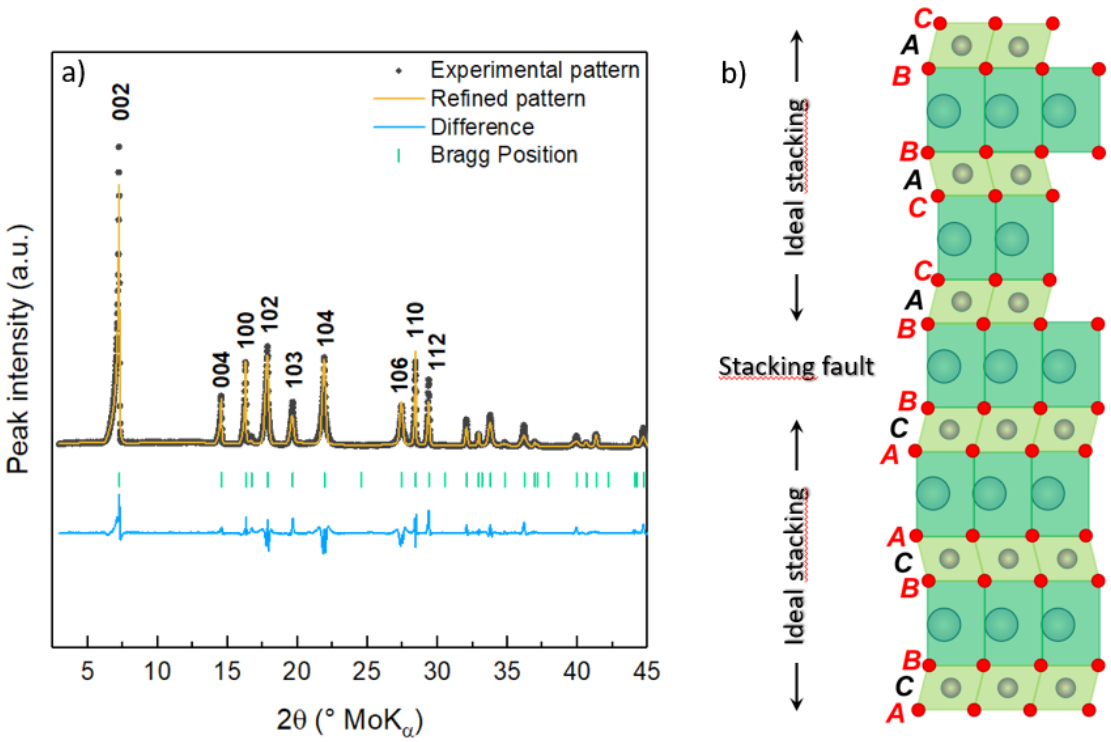

Figure 3-1. a) Diffraction pattern and Rietveld refinement from XRD data for P2-NaMNMO; b) Schematic representation of the stacking fault sequence.

All reflections in the diffraction pattern from **Figure 3-1a** are consistent with ICDD PDF 01-070-3726, and the material can be indexed as a P2-type structure with space group $P6_3/mmc$ possessing lattice parameters a = 2.886 Å and c = 11.183 Å. The 10*l* reflections (i.e. 102, 104, 106, 108) display anisotropic peak broadening, pointing out the presence of stacking faults in the structure. The ideal P2 structure should in fact display transition metals arranged in a CC fashion (stacking of metals on top of each other), with oxygen in a AB BA sequence [381]. The introduction of a stacking fault changes the stacking sequence of the metals from CC to CA, hence resulting in peak broadening of 10*l* reflections (**Figure 3-1b**). In this layer, Na exhibits a prismatic environment sharing edges and faces with the transition metal octahedra, similar to P3-type structures, where the oxygen is stacked in AB BC CA fashion. Although other stacking faults can account for similar anisotropy, they would result in Na^+ ions exhibiting an octahedral environment, which is not consistent with the c lattice parameter observed (octahedral environment usually results in smaller c parameter and additional reflections in the pattern). Hence, these stacking faults were not considered.

Prior to usage, the structure and phase purity of the synthesized $Na_2C_4O_4$ was also investigated by means of XRD, and the Rietveld refinement of the obtained data is reported in **Figure 3-2**.

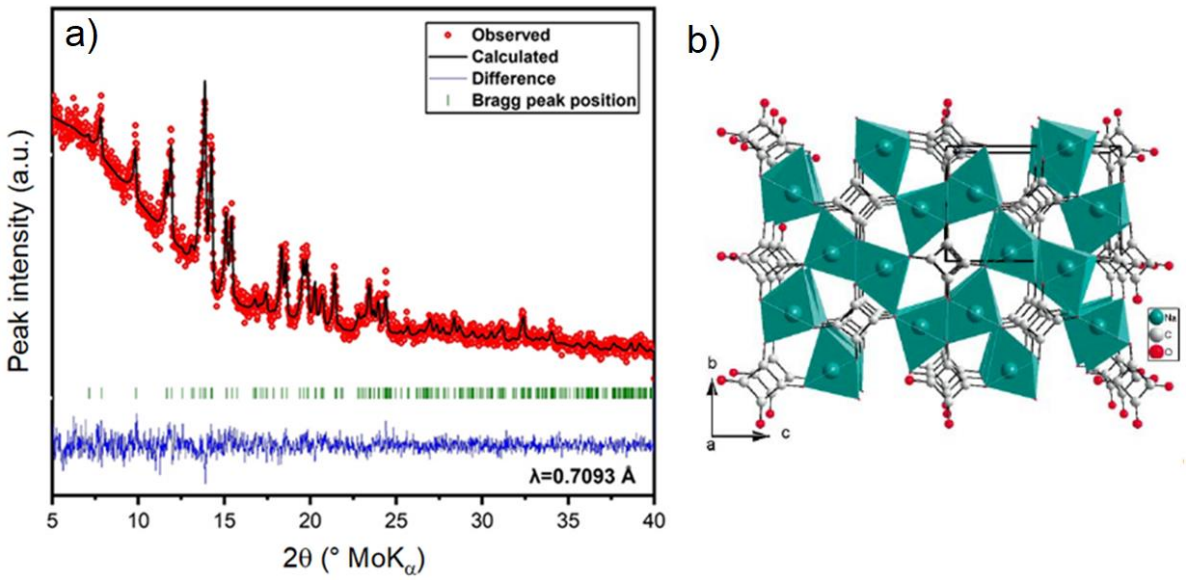

Figure 3-2. a) Diffraction pattern and Rietveld refinement from XRD data for $Na_2C_4O_4$; b) Representation of crystal structure with ion packing scheme [382].

All reflections in the diffraction pattern shown in **Figure 3-2a** are consistent with the as-synthesized $Na_2C_4O_4$ being crystallized with a primitive monoclinic unit cell belonging to the $P2_1/c$ space group [382], with lattice parameters a = 3.493 Å, b = 6.823 Å, c = 10.316 Å and β = 91.484 °. The general packing scheme can be described as an array of Na^+ ions surrounded by oxygen atoms forming distorted octahedra (**Figure 3-2b**). No other phases are detected, indicating absence of impurities for the synthesized salt.

3.2.2 Electrochemical characterization

In order to investigate the redox processes occurring during Na storage and assess the specific capacities of the single cathode and anode materials, electrodes of NaMNMO and CCDHC were subjected to cyclic voltammetry (CV), galvanostatic cycling with potential limitation and rate capability test in half-cells vs. Na. However, several studies in literature pointed out the instability of sodium metal when used as the counter electrode in half cells, suggesting the use of electrolyte additives like fluoroethylene carbonate (FEC) [377]. Hence, prior to the proper electrochemical characterization of the materials, the effect of FEC additive on the counter electrode was investigated at different current rates. Specifically, cathode and anode half cells were assembled by employing standard 1M $NaPF_6$ in EC:PC electrolyte solution (300 µL) and compared to cells employing the same electrolyte with the addition of 5 % w/w FEC, monitoring the Na plating and stripping onto the counter electrode. The obtained E_{CE} vs. t plots are reported in **Figure 3-3**.

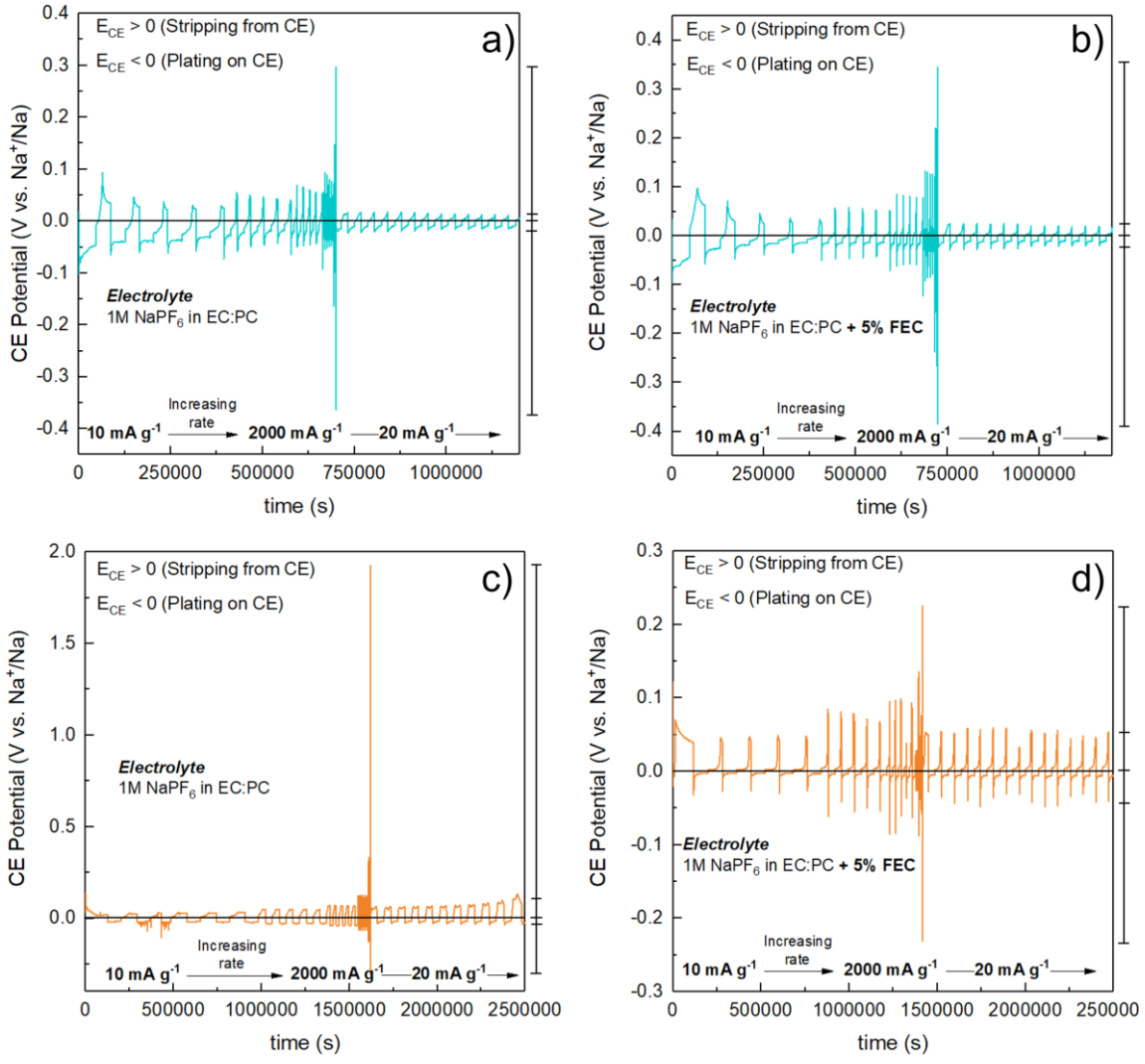

Figure 3-3. E_{CE} vs. t plot at different rates (10, 20, 40, 100, 400, 1000 and 2000 mA g^{-1}) for half cells of NaMNMO a) without FEC and b) with FEC additive in the electrolyte; E_{CE} vs. t plot at different rates (10, 20, 40, 100, 400, 1000 and 2000 mA g^{-1}) for half cells of CCDHC a) without FEC and b) with FEC additive in the electrolyte.

When comparing the counter electrode potential trend upon cycling for cells without FEC (**Figure 3-3a,c**) and those with 5 % FEC in the electrolyte (**Figure 3-3b,d**), it is possible to observe that the sodium metal plating/stripping is not symmetrical in the former case at all current rates. This generally translates in an inhomogeneous deposition/dissolution of Na metal at the counter electrode, which could result in the formation of dendrites. This effect becomes visible from the NaMNMO cells after some cycling even at slow rates (**Figure 3-3a-b**), and it is much more pronounced in the CCDHC cells especially at high current rates (**Figure 3-3c-d**). In order to provide a better stability of sodium metal at the counter electrode and avoid possible issues regarding dendrite formation upon cycling, all half-cell measurements have been performed by employing 5 % FEC additive in the electrolyte.

In order to investigate the redox processes occurring during Na storage, electrodes of NaMNMO were subjected to cyclic voltammetry (CV) at a scan rate of 0.1 mV s^{-1} and galvanostatic cycling in half-cells vs. Na within the potential window of 2.70-4.30 V. **Figure 3-4** shows the results obtained for both measurements.

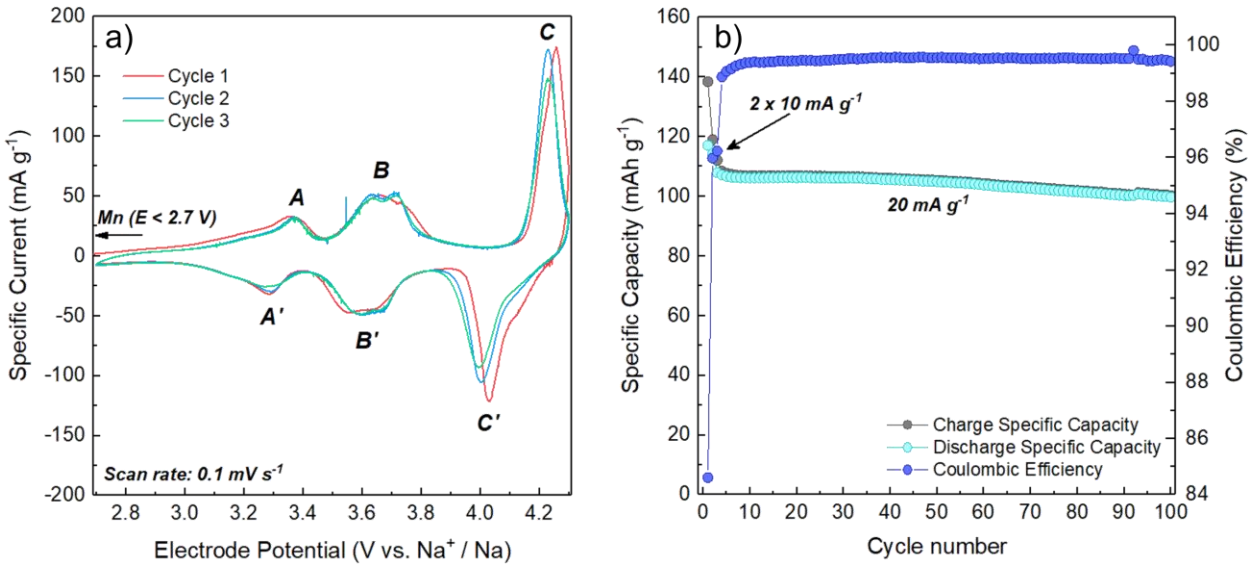

Figure 3-4. a) Cyclic voltammetry of the first three cycles at a scan rate of 0.1 mV s^{-1} and b) galvanostatic cycles obtained at 20 mA g^{-1} current density with two activation cycles at 10 mA g^{-1} for NaMNMO.

From the voltammograms in **Figure 3-4a**, the anodic and cathodic scans display the characteristic features of sodium storage by NaMNMO. The working potential window of the material was purposely chosen to cut out the Mn^{3+}/Mn^{4+} redox couple from the reaction, allowing Mn to stay in 4+ oxidation state and avoiding the presence of Jahn-Teller-active Mn^{3+} ions or dismutation into soluble Mn^{2+} ions [383], with the aim to provide a higher structural stability upon cycling. During the first anodic scan, two peaks in the 3.20-3.90 V potential region can be indexed to Ni redox activity. Specifically, peak A centered at about 3.35 V is attributed to the oxidation of Ni^{2+} to Ni^{3+}, while peak B is attributed to further oxidation from Ni^{3+} to Ni^{4+} [384,385]. An intense peak centered at 4.20 V is also

observed upon charge, which is related to the phase transition from P2 towards a fully desodiated O2 structure [386]. However, the presence of electrochemically inactive Mg as a dopant in the structure prevents the complete P2-O2 phase transition, which is one of the main causes of capacity fading for P2 layered oxides, while it favors and stabilizes the formation of an intermediate phase between the two structures, called OP4 phase, as demonstrated in a previous study [376]. During the cathodic scan, the presence of peak C' in the high voltage region (E = 4.00 V) is related to the transition from OP4 back to the P2 phase [387], confirming the reversibility of the process upon sodiation. Finally, the two peaks B' (E = 3.60 V) and A' (E = 3.30 V) are associated with the reduction of Ni^{4+}, first to Ni^{3+} and then to Ni^{2+}, respectively [384,385]. From the second cycle onwards, all processes are repeated and superimposed, indicating a high reversibility of the redox processes upon cycling.

The charge/discharge performance over 100 cycles and the stability of NaMNMO have been evaluated by galvanostatic cycling at 20 mA g^{-1} within the 2.70 V < E < 4.30 V potential window; two activation cycles at 10 mA g^{-1} have been performed at the beginning of the measurement, to stabilize the electrode-electrolyte interface. The specific capacity obtained for the cathode material is reported in **Figure 3-4b**, as well as the related coulombic efficiencies.

Despite only the Ni^{2+}/Ni^{4+} redox couples being exploited, the NaMNMO cathode material displays an initial capacity of about 138 mAh g^{-1}, with an irreversible capacity at first cycle of about 20 mAh g^{-1} and an initial coulombic efficiency > 84 %. After two activation cycles at slower rate, the coulombic efficiency rapidly rises to values higher than 99.5 %, with a specific capacity of 110 mAh g^{-1}. After 100 cycles, the material still exhibits capacities as high as 100 mAh g^{-1}, consisting in a capacity retention of 91 % as compared to the third cycle. These results suggest a high reversibility of processes, as highlighted in the CV measurements, together with a very high stability of the material upon cycling and almost no capacity fading after 100 cycles.

The rate capability of the material was evaluated in order to assess low- and high-current tolerance of the NaMNMO cathode. In detail, specific currents of 10, 20, 40, 100, 400, 1000 and 2000 mA g^{-1} have been applied, with current rate changing every 5^{th} cycle; subsequently, a specific current of 20 mA g^{-1} was restored in order to verify the capacity retention of the material. The results of the rate capability test are shown in **Figure 3-5**.

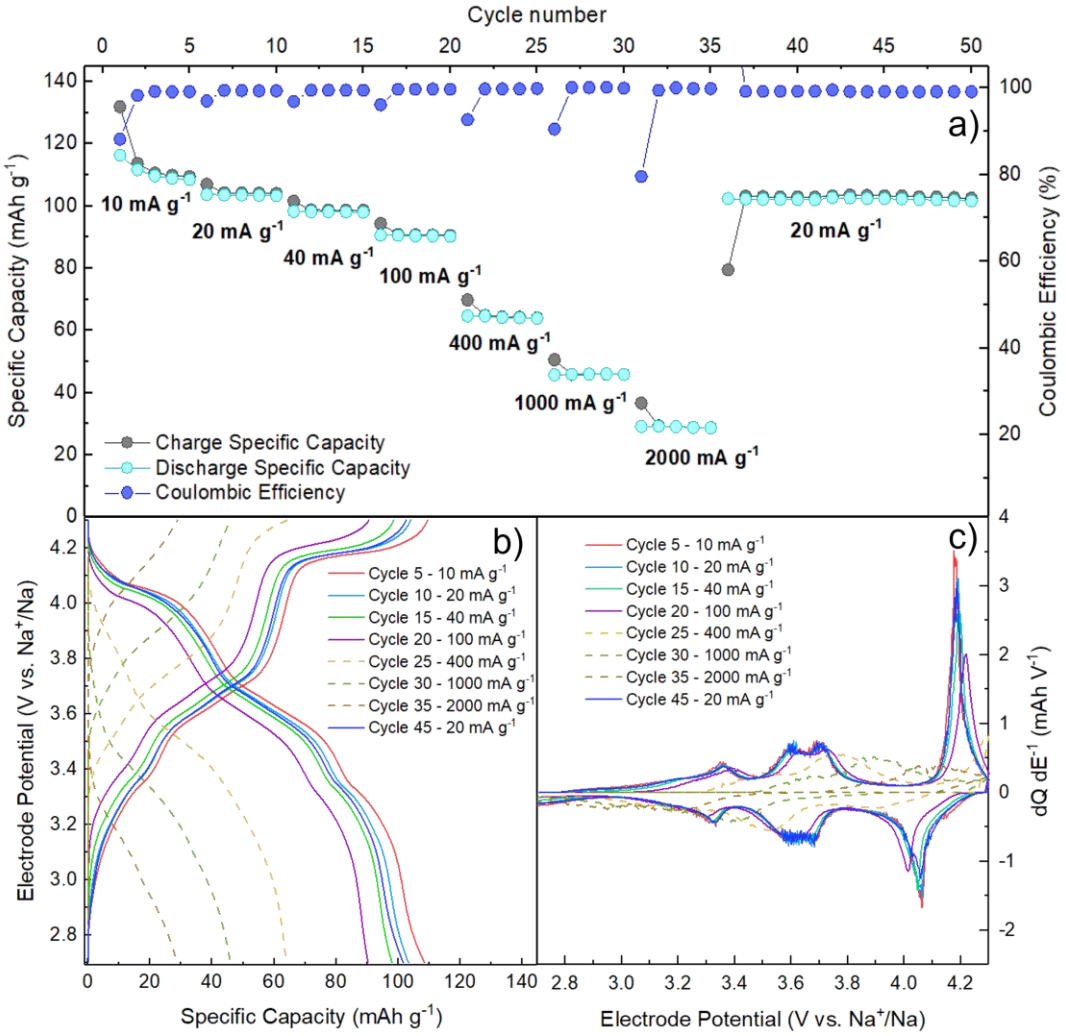

Figure 3-5. Rate capability of NaMNMO: a) Cycle number vs. Specific capacity/Coulombic efficiency; b) E vs. Q potential profiles for each specific current applied; c) Differential dQ dE^{-1} vs. E profiles for each specific current applied.

The specific capacity of the material only slightly decreases with increasing current rate up to 100 mA g^{-1}, with the decrease becoming more pronounced for the higher rates (**Figure 3-5a**). From the 6th cycle on, by progressively increasing the specific current applied up to 5 times (i.e. from 20 to 100 mA g^{-1}) the capacity retention displayed by the layered oxide is as high as 88 %. Moreover, the material is able to still display a reversible capacity of 29 mAh g^{-1} at 2000 mA g^{-1} current rate, confirming the ability of the material to sustain high specific currents. When the specific current of 20 mA g^{-1} is restored, the specific capacity is fully recovered and maintained at the same values as those previously obtained at the same rate, thus further demonstrating an excellent capacity retention. Notably, the coulombic efficiencies after the first activation cycles are higher than 99.3 % for all current rates tested. From the E vs. Q potential profiles in **Figure 3-5b**, it is possible to observe that a low polarization is displayed by the material for all currents up to 100 mA g^{-1}, indicated by the sloping plateaus only slightly shifting to lower/higher potentials. This effect is even more clearly visualized in the calculated

dQ dE^{-1} vs. E differential plots in **Figure 3-5c**, where the peaks related to the redox processes are almost completely superimposed with the exception of the highest current rates.

To investigate the redox processes occurring at the anode, electrodes of CCDHC were also subjected to cyclic voltammetry (CV) at a scan rate of 0.1 mV s^{-1} and galvanostatic cycling in half-cells vs. Na within the potential window of 0.01-1.50 V. **Figure 3-6** shows the results obtained for both measurements.

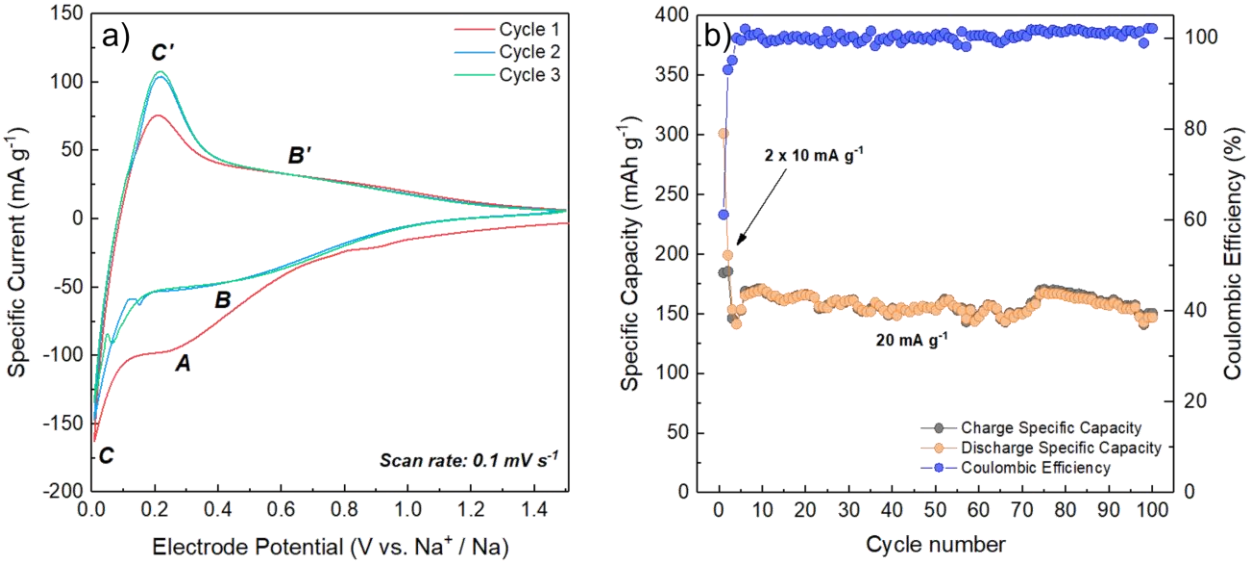

Figure 3-6. a) Cyclic voltammetry of the first three cycles at a scan rate of 0.1 mV s^{-1} and b) galvanostatic cycles obtained at 20 mA g^{-1} current density with two activation cycles at 10 mA g^{-1} for CCDHC.

The voltammograms in **Figure 3-6a** show the characteristic features of sodium storage into hard carbons. In particular, the broad peak A upon sodiation, starting at about 0.7 V and centered at 0.35 V, is attributed to the electrolyte decomposition (together with FEC additive) on the anode surface forming the SEI layer. This process is addressed as the main cause for the initial irreversible capacity of the material displayed during the first cycle in **Figure 3-6b**. The disappearance of this process in the following cycles indicates that the SEI is completely formed after the first cycle. As for peaks B and C, they represent the adsorption-intercalation processes typical of hard carbons. Since the sodiation/desodiation mechanism in hard carbons is still poorly understood, and several models can be found in literature [111], the attribution of the signals to the correct process is not an easy task. However, in a recently published work [362], we carried out an extensive characterization of the charge storage mechanism in CCDHC when used as anode material for Na-ion batteries, evidencing that the high-potential region (0.15 V < E < 0.75 V), related to peak B in the CV measurement, is mainly controlled by surface adsorption phenomena, while for the low potential region (E < 0.15 V), corresponding to peak A, diffusion processes are the dominant ones, hence being consistent with Na-ion intercalation into the carbon framework. Upon desodiation, peak C' centered at 0.25 V and peak

B' at E > 0.25 V represent Na^+ ion deintercalation and desorption from the carbon matrix, respectively. All processes after the first cycle, with the exception of the SEI formation, are repeated and superimposed, suggesting a high reversibility.

The charge/discharge performance over 100 cycles and the stability of CCDHC has been evaluated by galvanostatic cycling at 20 mA g^{-1} within the 0.01 V < E < 1.50 V potential window; also in this case, two activation cycles at 10 mA g^{-1} have been performed at the beginning of the measurement to stabilize the electrode-electrolyte interface. The specific capacity obtained for the anode material is reported in **Figure 3-6b**, as well as the related coulombic efficiencies.
The CCDHC anode material displays an initial discharge capacity of about 301 mAh g^{-1}, with a quite high irreversible capacity at first cycle of 116 mAh g^{-1} due to SEI formation, resulting in an initial coulombic efficiency of 61 %. After the two activation cycles, the coulombic efficiency rises to values close to 100 %, with an average specific capacity of about 165 mAh g^{-1}. Despite some fluctuations in the trend of capacity upon cycling, after 100 cycles the material is still able to deliver a specific capacity of about 150 mAh g^{-1}, consisting in a capacity retention of 88 % as compared to the third cycle.

The rate capability of the material was evaluated to assess the tolerance of the CCDHC anode towards low and high current densities applied. The protocol used is the same as for NaMNMO, with applied specific currents of 10, 20, 40, 100, 400, 1000 and 2000 mA g^{-1}, and current rate changing every 5^{th} cycle; subsequently, a specific current of 20 mA g^{-1} was restored in order to verify the capacity retention of the material. The results of the rate capability test are shown in **Figure 3-7**.

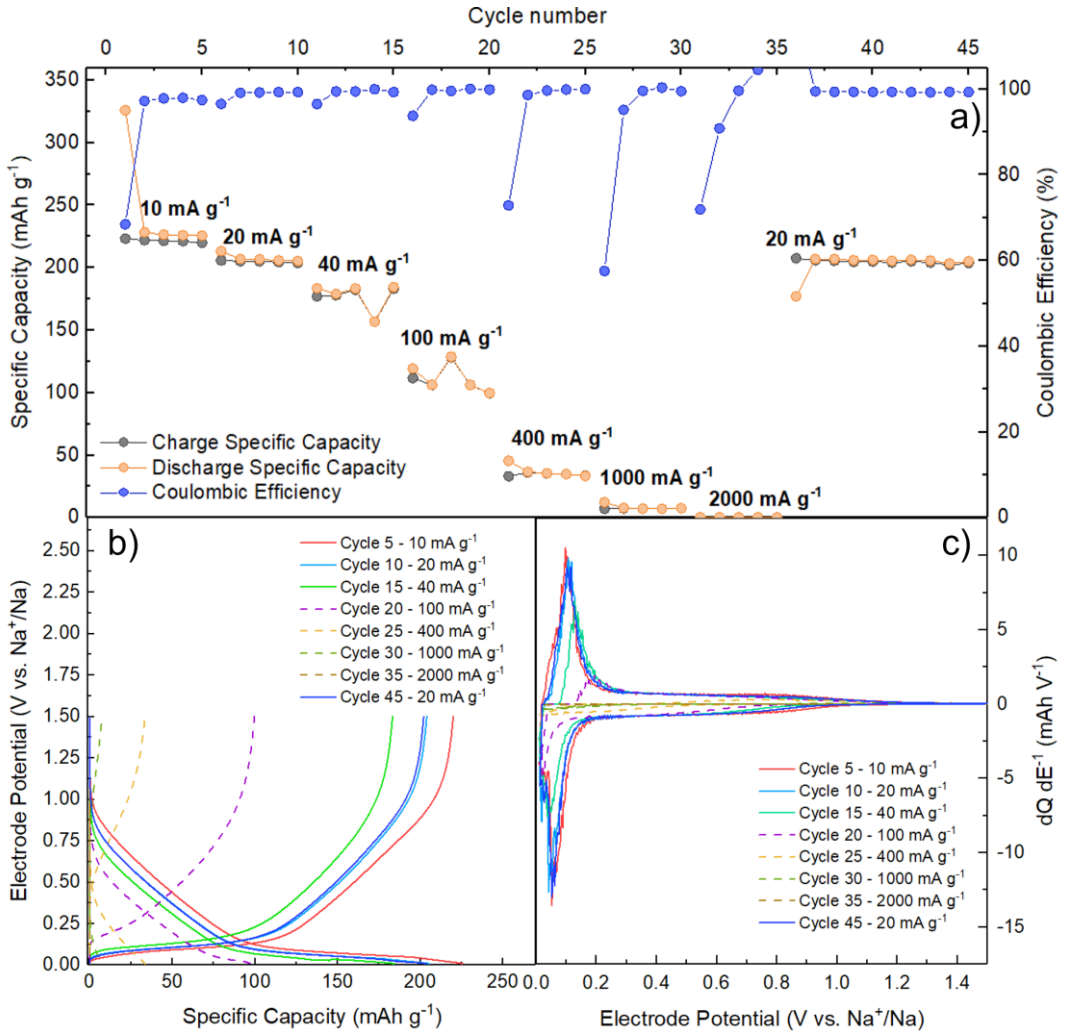

Figure 3-7. Rate capability of CCDHC: a) Cycle number vs. Specific capacity/Coulombic efficiency; b) E vs. Q potential profiles for each specific current applied; c) Differential dQ dE^{-1} vs. E profiles for each specific current applied.

The specific capacity of the material only slightly decreases at slow current rates up to 40 mA g^{-1}, also becoming less stable at the higher rates (**Figure 3-7a**). In particular, when cycling at 1000 and 2000 mA g^{-1}, the capacity drops to values close to zero, with a lower reversibility of the processes as indicated by the related coulombic efficiencies. Hence the material displays a limited ability to sustain high specific currents. However, when the specific current of 20 mA g^{-1} is restored, the specific capacity is fully recovered and maintained with values comparable to those previously observed for the same current rate, demonstrating a good capacity retention. From the E vs. Q potential profiles in **Figure 3-7b**, a low polarization is displayed for all current densities up to 40 mA g-1, as indicated by the sloping plateaus only slightly shifting. This effect is more clearly visualized in the dQ dE^{-1} differential plots in **Figure 3-7c**, where the peaks related to each process are almost completely superimposed apart from the higher current rates.

After testing the two materials separately in half-cells vs. Na metal, their compatibility in full cell setup was evaluated. The electrodes were balanced by first considering the reversible specific capacities of

the single anode and cathode at a given specific current and then adjusting the loadings of the electrode coatings to have a negative-to-positive (N/P) charge ratio of 1.05-1.10, in order to prevent any plating effect at the anode side. For the sake of clarity, the cell balancing was calculated without taking into account the contribution of the SEI formation at the first cycle, which will be addressed by the $Na_2C_4O_4$ presodiation additive. Prior to the long cycling measurement, two full cells were compared in order to assess the influence of the FEC-containing electrolyte in absence of Na metal, and the results are displayed in **Figure 3-8**.

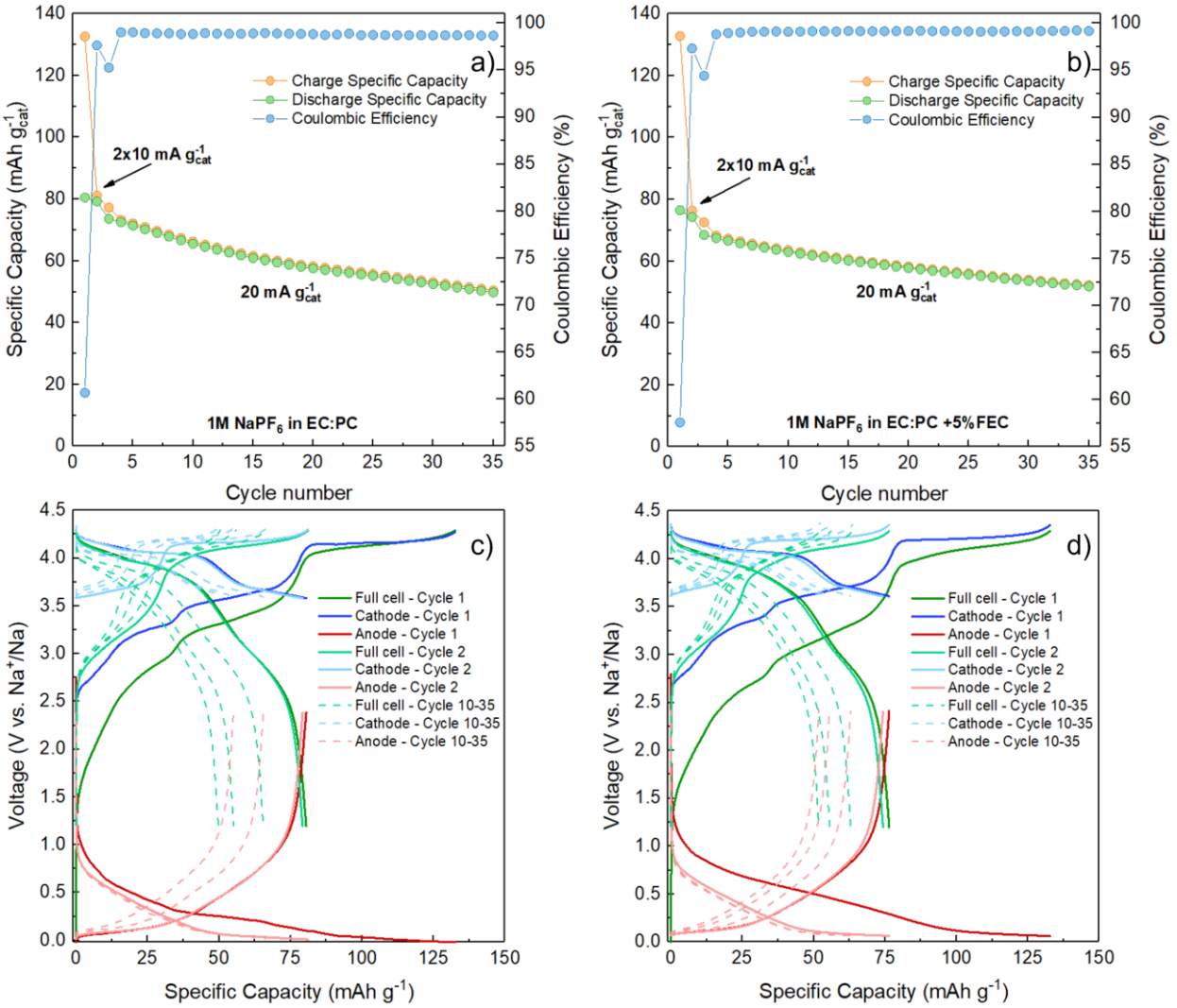

Figure 3-8. a) Galvanostatic cycles and c) E vs. Q potential profiles for the full cell employing standard $NaPF_6$ in EC:PC electrolyte; b) Galvanostatic cycles and d) E vs. Q potential profiles for the full cell employing $NaPF_6$ in EC:PC with 5% FEC electrolyte. The applied current densities (20 mA g^{-1} with two activation cycles at 10 mA g^{-1}) and specific capacities are normalized according to the mass of the cathode active material.

As shown in **Figure 3-8a-b**, both cells basically display the same performance in terms of specific capacity, indicating that the use of FEC in a full cell configuration (i.e. in the absence of metal Na at the counter electrode) does not provide additional benefits upon cycling. This is also confirmed by the potential profiles in **Figure 3-8c-d**, where no significant differences can be observed between the

two cells apart from the first charge; the slight difference of the first charge plateaus in **Figure 3-8d** as compared to **Figure 3-8c** is ascribed to the additional decomposition of FEC from the electrolyte during the SEI formation at the anode side, which results in a slightly lower initial coulombic efficiency due to the increased irreversible consumption of sodium. Hence, given the costly nature of the electrolyte solution when considering possible applications on a larger scale, and given that no improvement was observed in this system, the use of expensive FEC for all the tested full cells was hereby avoided.

The behavior of the NaMNMO||CCDHC full cell upon long cycling was thus more extensively studied by galvanostatic cycling at 20 mA g^{-1}_{cat} for 120 cycles, with two slower activation cycles at 10 mA g^{-1}_{cat}. The working potential window for the full cell (1.20 V < E < 4.29 V) was chosen by calculating the difference between the potential limits employed for the single half-cells. The specific capacity upon cycling and the related E vs. Q profiles are shown in **Figure 3-9**.

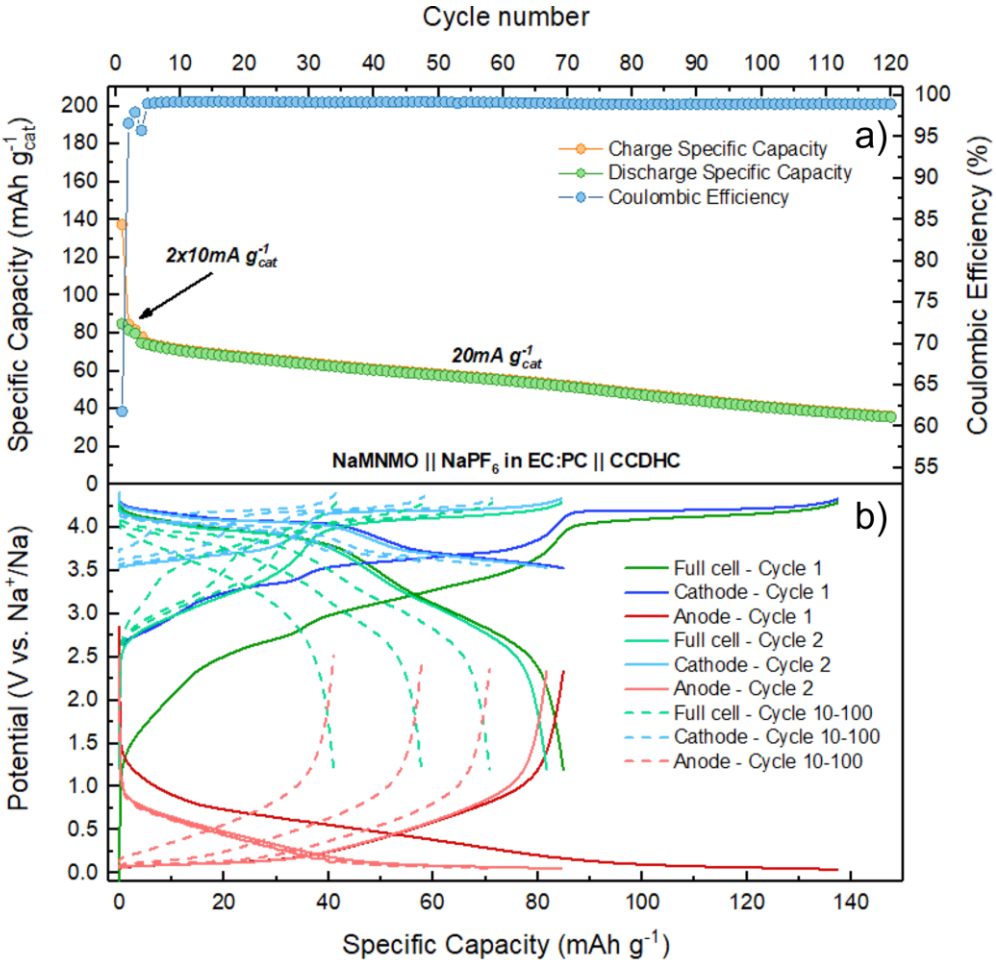

Figure 3-9. a) Galvanostatic cycles and b) E vs. Q potential profiles obtained at 20 mA g^{-1} current density with two activation cycles at 10 mA g^{-1} for the full cell NaMNMO||$NaPF_6$ in EC:PC||CCDHC. The applied current densities and specific capacities are normalized according to the mass of the cathode active material.

From **Figure 3-9a**, the NaMNMO||CCDHC full cell displays an initial charge capacity of about 138 mAh g^{-1}, which is in line with the first charge capacity of the cathode in half-cell configuration, being it the limiting electrode. During the first discharge, a high irreversible capacity of 53 mAh g^{-1} is observed due to SEI formation at the anode side, resulting in an initial coulombic efficiency of about 60 %, which is also in line with the coulombic efficiency displayed by the anode in half-cell configuration. As expected, the lack of an "infinite" source of sodium results in the unbalancing of charges after the irreversible SEI formation during the first charge, and the cathode is only partly sodiated during the following discharge. This is more clearly evident by considering the E vs. Q plot in **Figure 3-9b**, where the cathode profile upon discharge is not able to reach its lower voltage cut-off. As a result of the abovementioned phenomena, after the first cycle the cell is only able to deliver about 80 mAh g^{-1} specific capacity. The coulombic efficiency in the following cycles quickly stabilizes at about 99.5 % for all the duration of the test, meaning a quite stable SEI is formed during the first cycles, with the capacity slowly decreasing up to 36 mAh g^{-1} at the 120th cycle and only a 46 % capacity retention with respect to the third cycle, making the cell performance and energy density (about 70 Wh kg^{-1}) poorly suitable for practical applications.

To address the issues associated with the irreversible SEI formation and increase the practical achievable capacity and energy density of the cell, sodium squarate ($Na_2C_4O_4$) was chosen as a cheap and green sacrificial additive. Indeed, $Na_2C_4O_4$ is decomposed during oxidation according to the reaction described by **Equation 20**, with a theoretical capacity of 339 mAh g^{-1}.

$$Na_2C_4O_4 \rightarrow 2Na^+ + 2e^- + 2CO_2 + 2C \qquad \textbf{Eq. 20}$$

Hence, a coating only employing $Na_2C_4O_4$ as the active material was prepared, in order to calculate the amount of salt needed to address the sodium loss during the first charge of the full cell. In order to verify the irreversibility of the process and the specific capacity provided upon oxidation, the salt oxidative decomposition was studied by means of CV at a scan rate of 0.1 mV s^{-1} and galvanostatic cycling at a C-rate of C/10 (**Figure 3-10**).

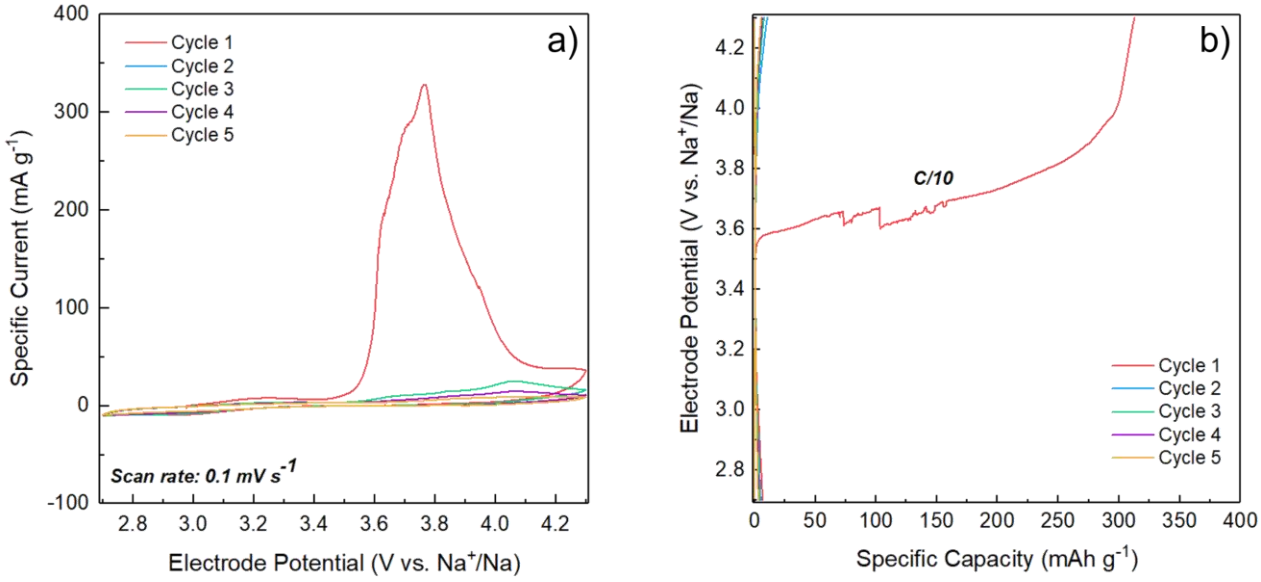

Figure 3-10. a) Cyclic voltammetry of five cycles at a scan rate of 0.1 mV s^{-1} and b) E vs. Q potential profiles of five galvanostatic cycles obtained at C/10 C-rate (Q_{th} = 339 mAh g^{-1}) for $Na_2C_4O_4$.

The voltammogram in **Figure 3-10a** show a single oxidation peak centered at about 3.75 V, which is related to the squarate decomposition. After the first oxidation, no other process is displayed in the subsequent cathodic or in the anodic scans, indicating that the salt decomposition is completely irreversible. This can also be observed in the potential profiles displayed in **Figure 3-10b**, where a plateau starts appearing during the first oxidation at about 3.6 V until 4.0 V (here the sharp oscillations in voltage profile upon decomposition can be attributed to the CO_2 evolution), in accordance with the results obtained from CV. The specific capacity normalized to the amount of $Na_2C_4O_4$ in the electrode is calculated to be 315 mAh g^{-1}, which is very close to the theoretical capacity of the salt (Qth = 339 mAh g^{-1}). Also during the galvanostatic cycling, no further process can be observed after the first charge, confirming the irreversibility of the salt decomposition.

By knowing the amount of charge provided by $Na_2C_2O_4$ and the charge needed to address the SEI formation at the anode during the first charge, electrodes of NaMNMO/$Na_2C_2O_4$ with a proper amount of sodium squarate in the formulation (23.28 %) were fabricated and tested in half-cell configuration. To investigate the effect of $Na_2C_4O_4$ on the cyclability of the cathode material and on the reversibility of the redox processes, a preliminary characterization was performed by means of CV on electrodes of NaMNMO/$Na_2C_4O_4$, as shown in **Figure 3-11**.

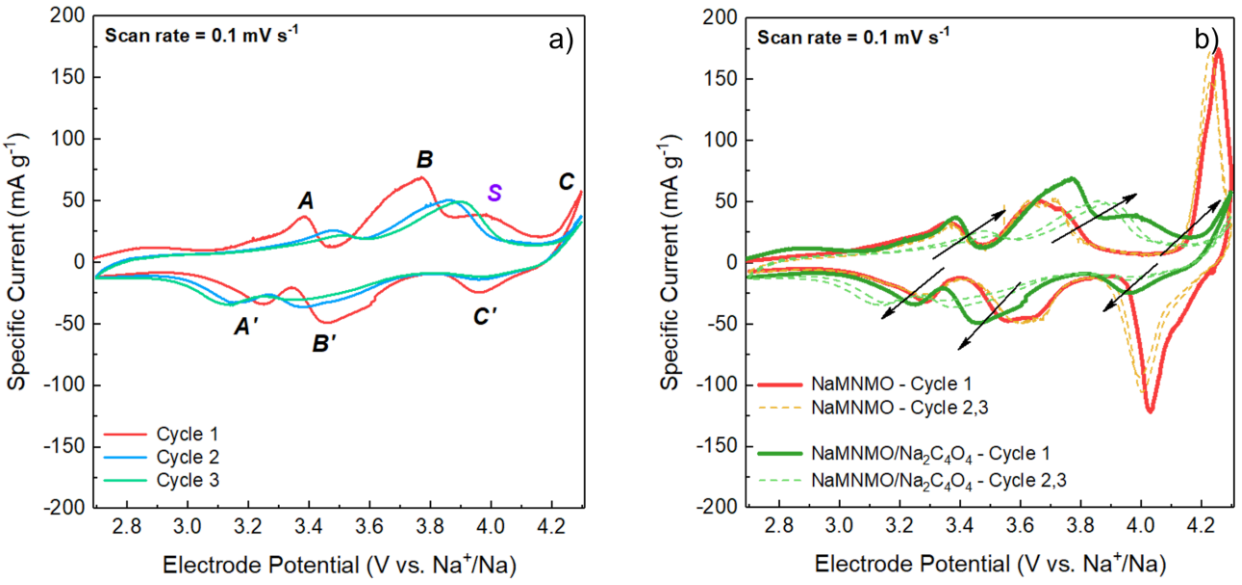

Figure 3-11. a) Cyclic voltammetry of the first three cycles at a scan rate of 0.1 mV s^{-1} for NaMNMO/$Na_2C_4O_4$ and b) Comparison between the redox peaks in NaMNMO and in NaMNMO/$Na_2C_4O_4$ half-cells at the same scan rate.

The voltammograms in **Figure 3-11a** show the typical NaMNMO redox processes associated to the Ni^{2+}/Ni^{3+} and Ni^{3+}/Ni^{4+} oxidations (peaks A and B) together with an additional feature between 3.6 V and 4.1 V which is not repeated in the following cycles, hence being consistent with the irreversible squarate decomposition (peak S); indeed, during the cathodic scan, no reduction peak for the process associated with peak S is observed, while the reductions from Ni^{4+} to Ni^{3+} and finally back to Ni^{2+} are clearly visible (peaks B' and A'). However, the signal related to the P2-to-OP4 phase transition during the anodic scan (peak C) is barely visible, as well as the signal associated to the inverse process during the cathodic scan (peak C'), suggesting that the phase transition is not started. In general, all the signals in the CV seem to be highly polarized especially after the irreversible decomposition of $Na_2C_4O_4$. In particular, when comparing the CV of the bare NaMNMO with that of NaMNMO/$Na_2C_4O_4$ (**Figure 3-11b**), a superposition of processes is encountered only until 3.65 V upon the first charge. As the decomposition of sodium squarate is started, all the following redox processes seemingly become polarized for both the anodic and cathodic scans; moreover, after the first cycle, all peaks change in shape and become broader as compared to those of NaMNMO, indicating a change in the redox activity of the cathode material, with peaks C/C' completely disappearing after the first cycle.

To further investigate the effect of sodium squarate on the cathode's charge/discharge performance and stability, NaMNMO/$Na_2C_4O_4$ half-cells vs. Na were galvanostatically cycled within the potential window 2.70 V < E < 4.30 V at an applied specific current of 20 mA g^{-1}, with two activation cycles at 10 mA g^{-1}. The specific capacity and coulombic efficiency upon cycling is reported in **Figure 3-12**.

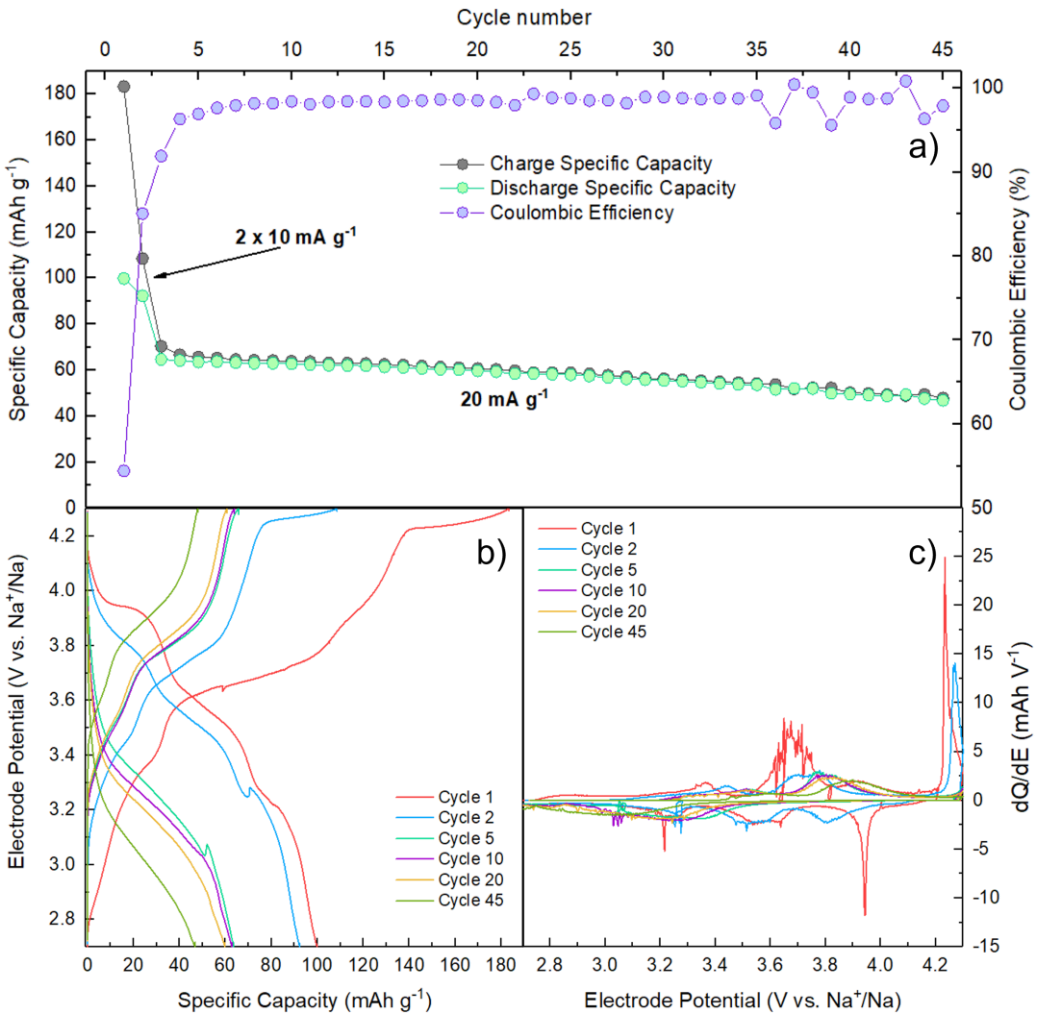

Figure 3-12. Galvanostatic cycles obtained at 20 mA g^{-1} current density with two activation cycles at 10 mA g^{-1} for NaMNMO/$Na_2C_4O_4$: a) Cycle number vs. Specific capacity/Coulombic efficiency; b) E vs. Q potential profiles; c) Differential dQ dE^{-1} vs. E profiles.

From the galvanostatic cycling (**Figure 3-12a**), the material displays an initial charge capacity higher than 180 mAh g^{-1}, indicating that the $Na_2C_4O_4$ additive successfully provided additional sodium upon oxidation, which can be potentially exploited to address the SEI formation at the anode side when in full cell configuration. However, after the slow activation cycles, the specific capacity drops to 60 mAh g^{-1}, which is lower than the reversible capacity of bare NaMNMO when used in full cell with CCDHC. The capacity retention upon cycling is 75 % after just 45 cycles (third cycle considered as reference), with a coulombic efficiency slowly rising to values higher than 95 %, but eventually stabilizing at values close to 99 %. The potential profiles and the related differential plot in **Figure 3-12b-c** provide confirmation of what observed from the CV analysis in **Figure 3-11**, with the irreversible squarate decomposition taking place at the first cycle, and a very high polarization of all processes in the following cycles, with the phase transition plateaus/peaks quickly disappearing, hence causing a decrease in the specific capacity. Also in this case, the oscillations in voltage profiles, displayed especially in the initial cycles, can be attributed to polarizations due to CO_2 evolution.

The behavior of the NaMNMO cathode mixed with the presodiation additive was also evaluated in full cell configuration, cycling the cell at 20 mA g^{-1} current density for 120 cycles with two activation cycles at 10 mA g^{-1} (**Figure 3-13**).

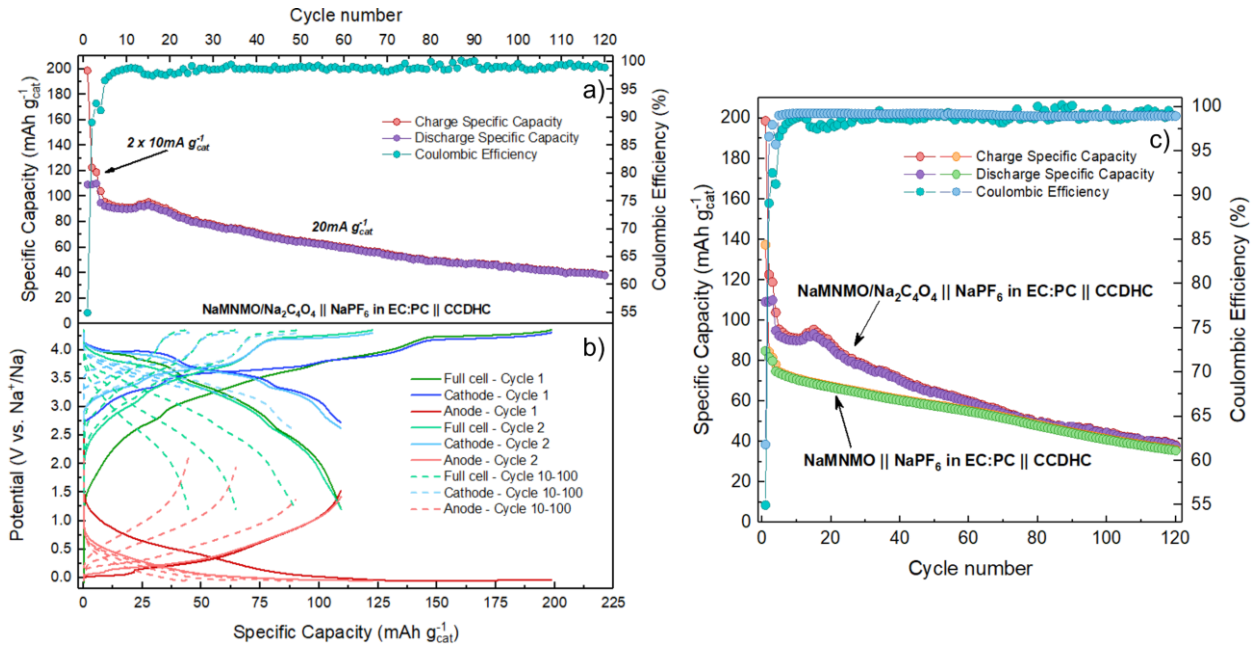

Figure 3-13. a) Galvanostatic cycles and b) E vs. Q potential profiles obtained at 20 mA g^{-1} current density with two activation cycles at 10 mA g^{-1} for the full cell NaMNMO/$Na_2C_4O_4$||$NaPF_6$ in EC:PC||CCDHC; c) Comparison between full cells long cycling performance with and without presodiation additive. The applied current densities and specific capacities are normalized according to the mass of the cathode active material.

From **Figure 3-13a**, the NaMNMO/$Na_2C_4O_4$||CCDHC full cell displays an initial charge capacity of about 200 mAh g^{-1}, which is in line with the first charge capacity of the presodiated cathode in half-cell configuration. During the first discharge, a high irreversible capacity of 60 mAh g^{-1} is observed due to SEI formation at the anode side, resulting in an initial coulombic efficiency of about 55 %. In the following cycles, the specific capacity stabilizes at values close to 90-95 mAh g^{-1}, with an average cell energy density as high as 150 Wh kg^{-1}, thus demonstrating an improvement as compared to the full cell without presodiation shown in **Figure 3-9**. However, within 15 cycles the capacity starts to rapidly decrease, with a progressive charge unbalancing upon cycling, as indicated by the potential profiles decreasing along the x-axis, with those of the anode and cathode progressively ending at higher potentials upon desodiation and sodiation, respectively (**Figure 3-13b**). The redox processes associated to the cathode, especially at high voltage, are also affected becoming more and more polarized. During the long cycling, the coulombic efficiency slowly stabilizes to average values of about 99 %, with the specific capacity approaching the values of the NaMNMO||CCDHC full cell after 70 cycles (**Figure 3-13c**), and then maintaining a similar descending trend up to 120 cycles, with a final capacity of 40 mAh g^{-1} and a capacity retention of 44 % with respect to the third cycle. The cell energy density calculated at the 120th cycle also decreases to about 66.7 Wh kg^{-1}. Moreover, when

comparing the coulombic efficiencies, some fluctuations are encountered in the presodiated full cell upon long-term cycling.

3.2.3 Morphological, structural and interfacial evolution

Given the electrochemical performance of both full cells, in particular for the presodiated one, a more extensive analysis was carried out in order to better investigate the morphological, structural and interfacial evolution of the materials upon cycling, by means of ex-situ SEM, operando XRD, synchrotron XAS, ex-situ XPS and impedance spectroscopy.

In **Figure 3-14** and **Figure 3-15**, the change in surface morphology of NaMNMO and NaMNMO/$Na_2C_4O_4$ upon the first charge in full cell have been evaluated, respectively.

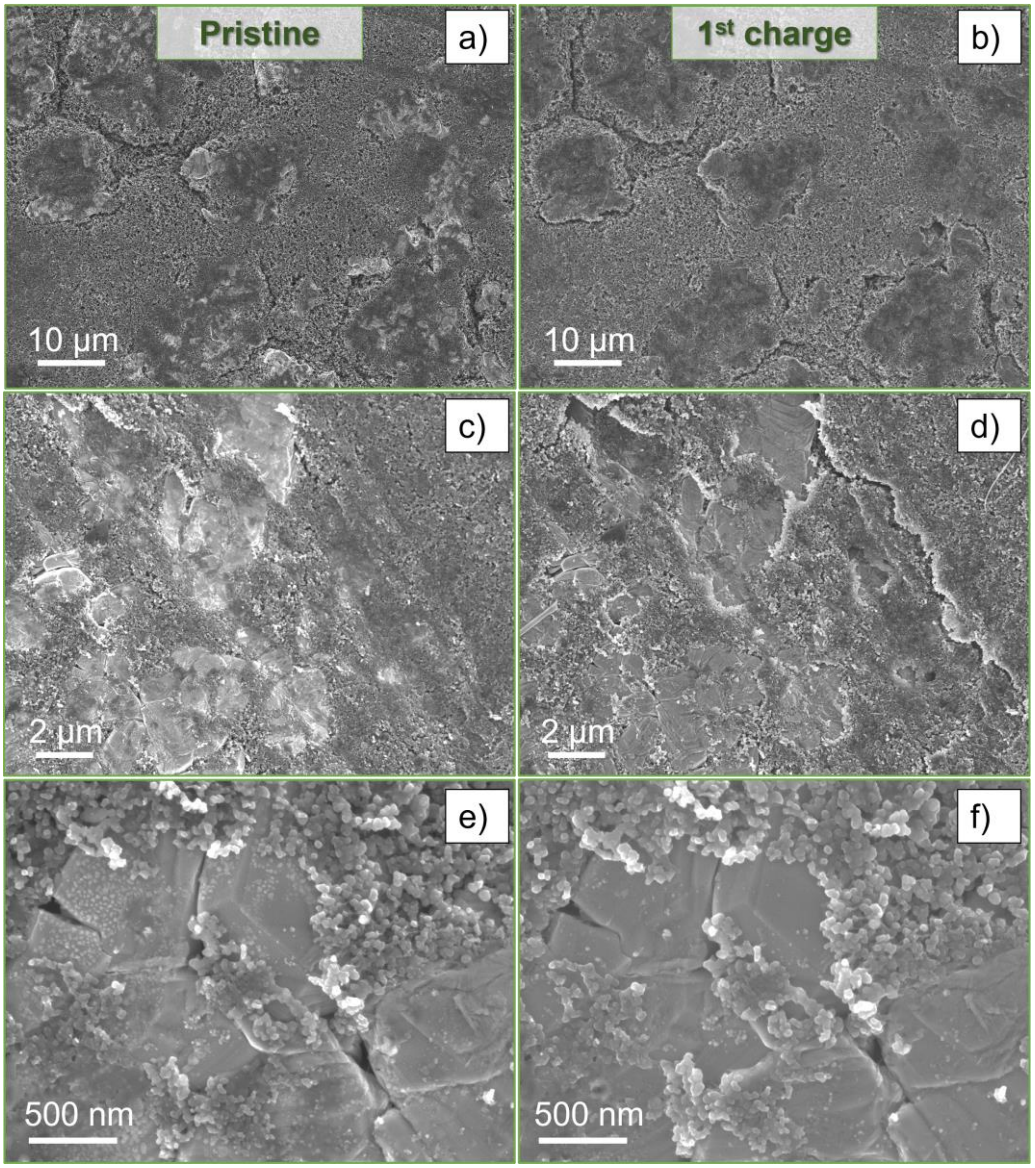

Figure 3-14. SEM micrographs of NaMNMO electrode at different magnifications and in different spots: a), c), e) pristine electrode before cycling and b), d), f) same sampling zones after the first charge in full cell configuration.

From the micrographs obtained for NaMNMO electrode, it is possible to observe that for all the spots considered, no substantial differences can be distinguished between the pristine electrode (**Figure 3-14a,c,e**) and the charged one (**Figure 3-14b,d,f**) even at higher magnifications, with the surface morphology remaining basically the same. It is worth noting that, despite most of the electrode surface is unchanged, a small difference can be observed between **Figure 3-14c** and **Figure 3-14d**, where a surface crack is formed after the charge process.

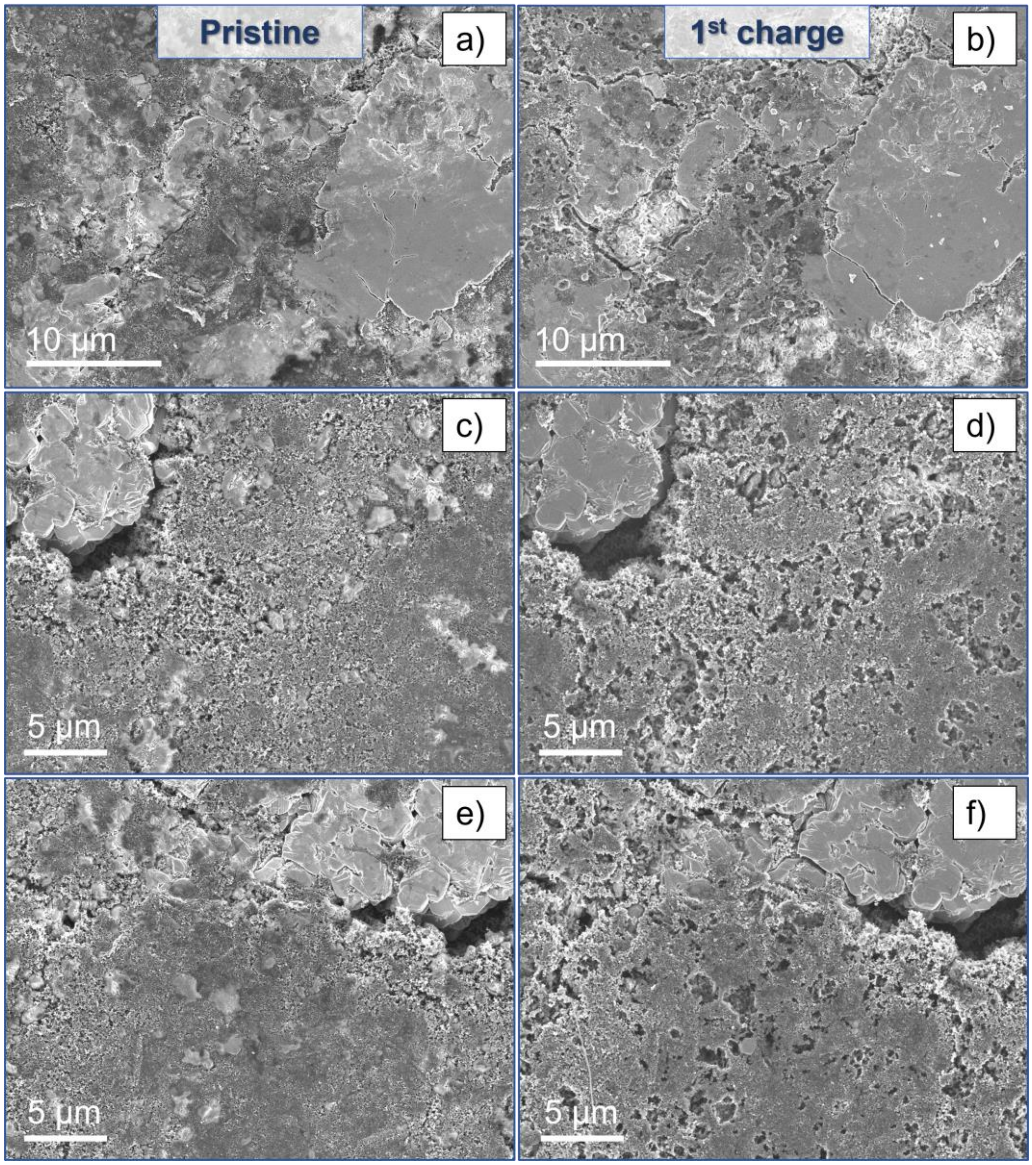

Figure 3-15. SEM micrographs of NaMNMO/$Na_2C_4O_4$ electrode at different magnifications and in different spots: a), c), e) pristine electrode before cycling and b), d), f) same sampling zones after the first charge in full cell configuration.

When considering the NaMNMO/$Na_2C_4O_4$ electrode, all the spots considered display several differences between the surface morphology before cycling (**Figure 3-15a,c,e**) and after the first charge with presodiation via sacrificial additive (**Figure 3-15b,d,f**). In particular, the surface morphology of the electrode after the first charge shows the formation of several holes, likely due to CO_2 evolution upon the irreversible oxidation of $Na_2C_4O_4$. On one hand, this gas release might favor

an increase in the electrode porosity, resulting in a better wetting of the active material by the electrolyte solution and in an improved ion diffusion; however, on the other hand, the formation or enlargement of some surface cracks is also observed, hence resulting in the loss of electrical contact between the particles composing the electrode, which in turn could cause a faster decrease in the long-term performance.

To better understand the different electrochemical behavior upon presodiation, the structural evolution of NaMNMO and NaMNMO/$Na_2C_4O_4$ upon cycling was evaluated by means of operando XRD performed during the first two cycles of each cathode half-cell, as shown in **Figure 3-16**. The obtained voltage profiles upon cycling are reported with the associated diffraction patterns.

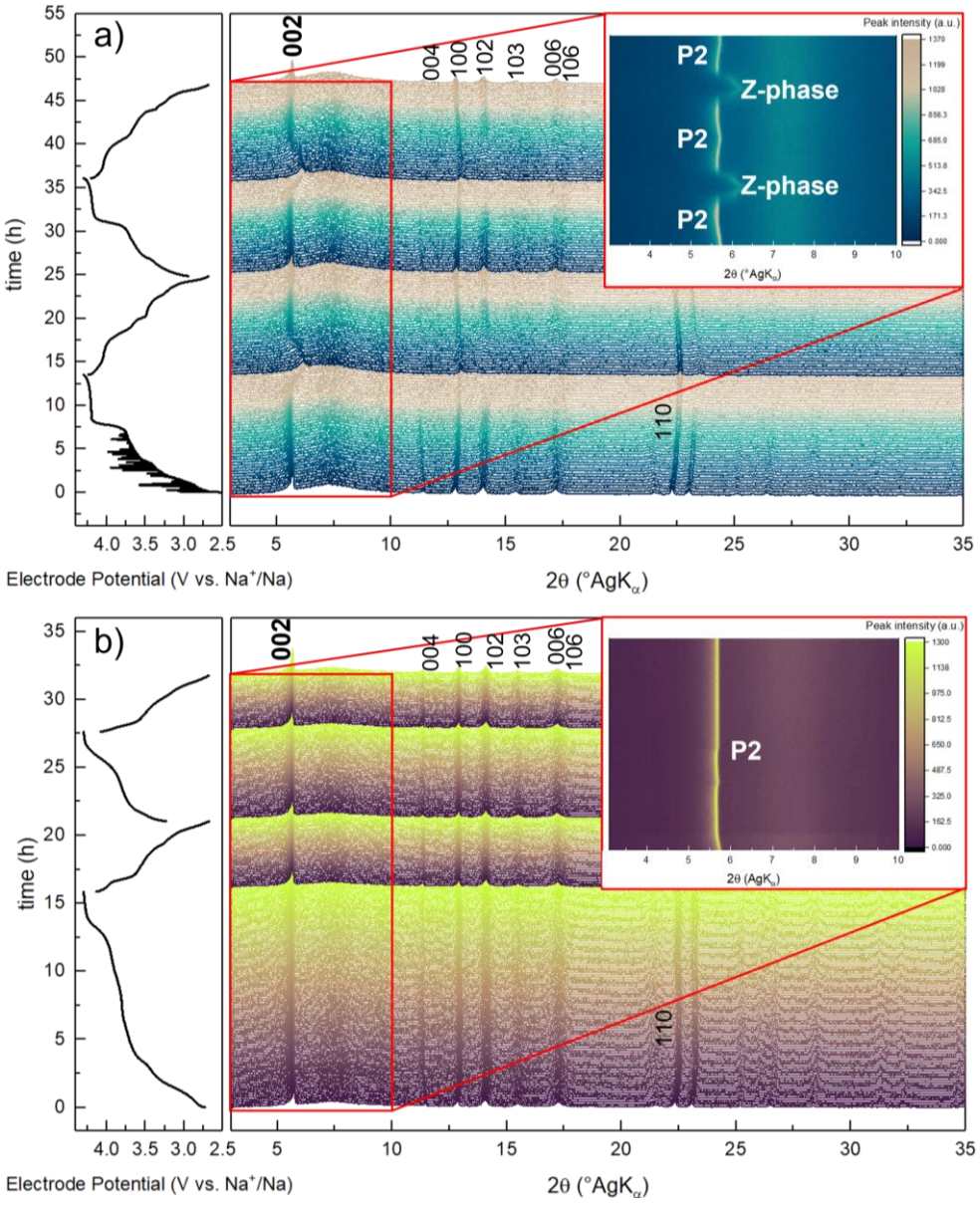

Figure 3-16. Operando XRD performed upon the first two cycles at 10 mA g^{-1} for a) NaMNMO and b) NaMNMO/$Na_2C_4O_4$ half cells. The insets show a contour map highlighting the 002-reflection region associated to the P2 phase.

At the initial stage of the charging process, all reflections in the operando diffraction patterns for NaMNMO perfectly match those obtained from the pristine powder in **Figure 3-1a**, and are consistent with works reported in literature. When charging in the 2.7 V < E < 4.00 V, several structural changes upon cycling can be observed. In particular, during the initial charge in **Figure 3-16a**, the 100, 102, 103 and 110 peaks are shifted to higher diffraction angles, which indicates a contraction of the *a*-parameter. The subsequent discharge leads to a shift in the opposite direction, indicating an expansion of the *a*-parameter, and this trend is repeated during the following cycle, indicating a reversibility of this process. The trend for the *a*-parameter upon cycling can be tentatively rationalized by considering the radius of the Ni-active metal ion being reversibly oxidized during desodiation to provide charge compensation within a solid solution regime [388]. Considering the same voltage window upon charge, the 002 and 004 peaks are instead shifted to lower diffraction angles, indicating an expansion in the *c*-parameter. the trend of this parameter can be rationalized by considering that upon charge, sodium ions are extracted from the structure of the cathode, resulting in a decreased positive charge stored between oxygen ions; hence, the repulsion between neighboring MO_2 slabs becomes stronger, and the interlayer distance (d = *c*/2) increases accordingly. Upon further charging to 4.3 V, the 002-reflection assigned to the P2 phase first remains at a constant position when entering the high-voltage plateau region (about 4.2 V), and then starts decreasing until almost disappearing, indicating an almost complete phase transition. As the P2-related reflection starts to decrease, a new broadened reflection starts to appear at higher diffraction angle, which has been reported to belong to the so-called OP4 phase for Mg-doped Ni-, Mn-based layered oxides [389,390]. This reflection becomes broader and keeps shifting to higher angles when approaching the 4.3 V cut-off, as a result of the increasing number of O2-type layers. The continuous shifting would suggest the presence of several intermediate structures rather than only one specific OP4 structure, and the extensive peak broadening of the reflection is consistent with these intermediate structures existing at the same time. Overall, the phase transition in the high-voltage region appears as a continuous process, already described in literature as the "Z-phase" [391]. Upon discharge, the P2-related reflection rises back with progressive disappearing of the Z-phase, following the opposite trend as compared to the charge process, with a contraction of the *c*-parameter due to the shielding effect of the inserted sodium ions for the repulsion between neighboring MO_2 slabs. This behavior is also repeated during the second cycle, indicating a high reversibility. Interestingly, the lattice parameter of the P2-related reflection (i.e. 002) stops changing at about 3.7 V, which is before the P2 → Z-phase transition takes place, possibly giving rise to a pseudocapacitive region with Na^+/vacancy ordering, which is reported to occur for similar doped layered oxides, and indicated by a flat high-voltage plateau [392].

As for the NaMNMO/$Na_2C_4O_4$ half-cell (**Figure 3-16b**), the structural evolution upon cycling displays a rather different behavior, with both the *a* and *c* lattice parameters only changing at the

beginning of the first charge until the decomposition of squarate starts, after which they remain basically constant. The 002 reflection only has a slight shift back to higher angles when reaching 3.9 V, after which it goes back to lower diffraction angles and remains constant throughout the whole cycling. This trend in the *c*-parameter indicates that the structure does not change largely during the first charge, in particular during the $Na_2C_4O_4$ decomposition. Moreover, the Z-phase is never reached, indicating a delay or polarization of the phase transition. Indeed, the presence of a smooth plateau in the high-voltage region as compared to the flatter plateau of NaMNMO may indicate that the Na^+/vacancy ordering is prevented for NaMNMO/$Na_2C_4O_4$; in general, the lack of ordering should result in alleviated oxygen layer gliding and increased Na^+ diffusion coefficient, while delaying the phase transformation [351,392]. In this case, the phase transformation is either polarized or delayed beyond the upper cut-off employed, resulting in the loss of capacity from the high-voltage region. However, when considering the specific capacity, the presodiated material still displays better initial performance, possibly as a result of the Na^+/vacancy disordering providing a better diffusion, although the stabilization effect of Mg-doping might be affected, as the capacity retention in the long cycling is worsened.

The evolution of the electronic structure and variations in the Mn (**Figure 3-17**) and Ni (**Figure 3-18**) local environments during the first cycle of NaMNMO and NaMNMO/$Na_2C_4O_4$ half-cells were monitored by means of synchrotron X-ray absorption spectroscopy (XAS). The galvanostatic profiles are presented in **Figure 3-17a-b** and **Figure 3-18a-b** for Mn and Ni, respectively, highlighting the acquisition points for both transition metals.

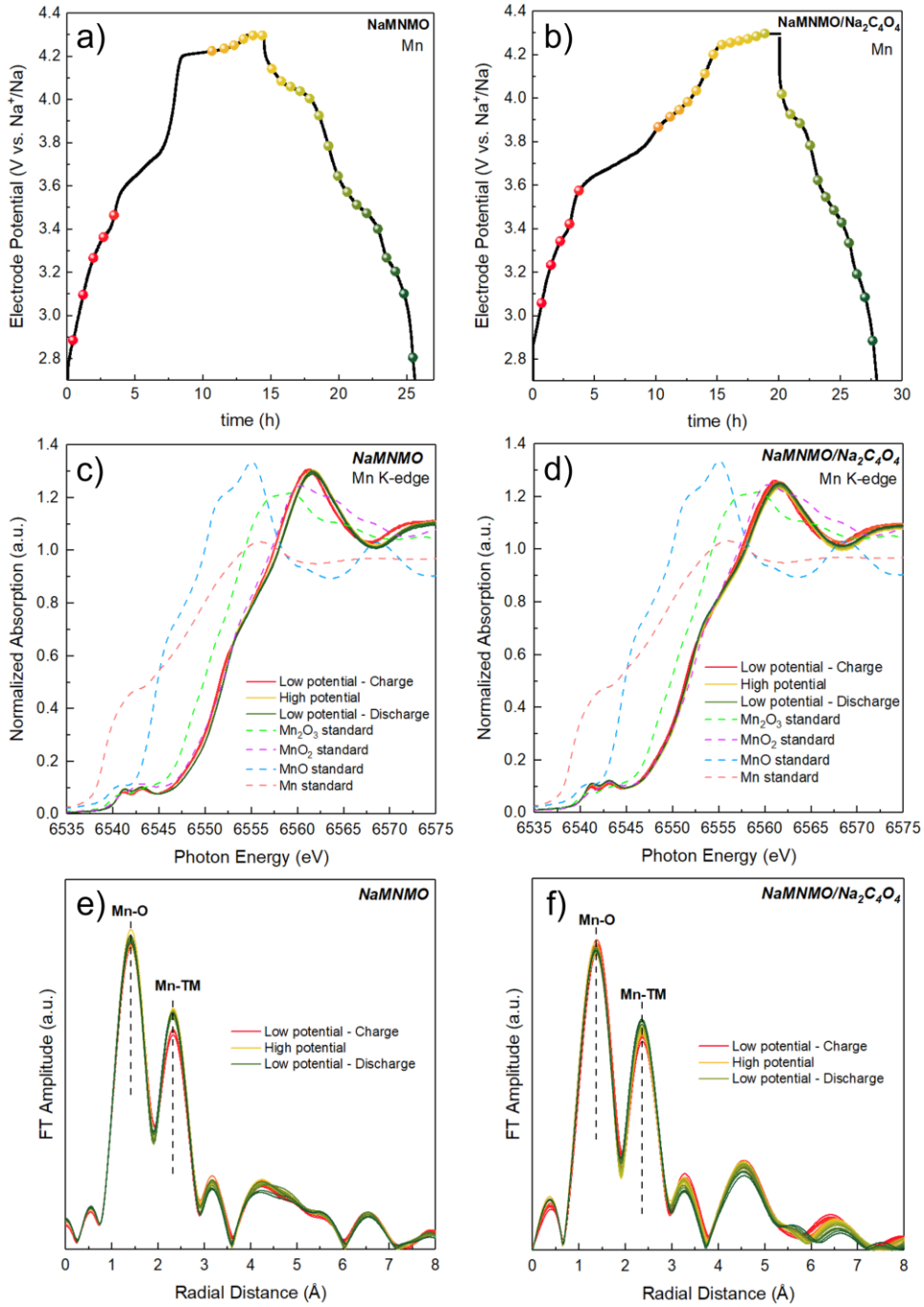

Figure 3-17. Galvanostatic profiles for a) NaMNMO and b) NaMNMO/$Na_2C_4O_4$, indicating the different acquisition points during the cycle; XANES spectra at Mn K-edge for c) NaMNMO and d) NaMNMO/$Na_2C_4O_4$; corresponding EXAFS spectra for e) NaMNMO and f) NaMNMO/$Na_2C_4O_4$. The colors for the spectra at different potentials correspond to those indicated in the galvanostatic profiles.

When comparing the standard references Mn_2O_3, MnO_2 and MnO to the XAS data obtained for NaMNMO and NaMNMO/$Na_2C_4O_4$, the X-ray absorption near edge structure (XANES) spectra in **Figure 3-17c-d** evidently show that the pristine electrodes are consistent with Mn being in +4 oxidation state. As the Mn^{4+}/Mn^{3+} redox couple is cut out of the chosen voltage window, the electronic structure of Mn is not expected to change upon cycling, and this is confirmed by the Mn K-edge never shifting at all potentials considered, for both the half-cells. This is further confirmed by

the extended X-ray absorption fine structure (EXAFS) spectra in **Figure 3-17e-f**, where the shells at 1.4 Å and 2.3 Å represent the Mn-O and Mn-TM interactions, respectively. Indeed, the interatomic distances never change upon cycling in both systems, indicating no changes in the fine structure of Mn. Overall, the tetravalent Mn ions are confirmed to be electrochemically inactive and only provide stabilization to the layered structure. Moreover, they are found to be not affected by the decomposition of the sacrificial salt.

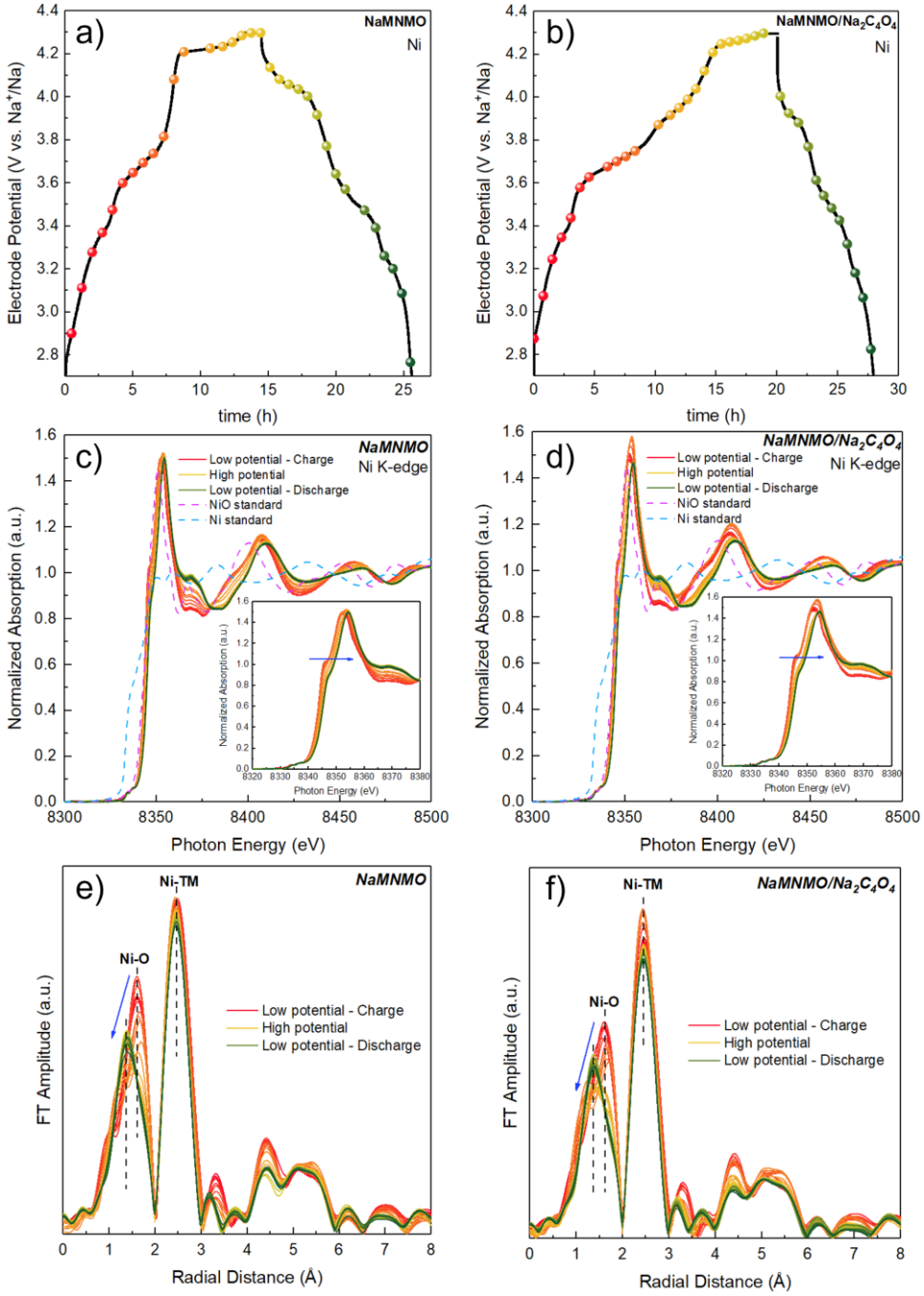

Figure 3-18. Galvanostatic profiles for a) NaMNMO and b) NaMNMO/$Na_2C_4O_4$, indicating the different acquisition points during the cycle; XANES spectra at Ni K-edge for c) NaMNMO and d) NaMNMO/$Na_2C_4O_4$; corresponding EXAFS spectra for e) NaMNMO and f) NaMNMO/$Na_2C_4O_4$. The colors for the spectra at different potentials correspond to those indicated in the galvanostatic profiles.

As for the Ni ions, when comparing the NiO standard to the obtained measurements, the XANES spectra in **Figure 3-18c-d** evidently show that the pristine electrodes are consistent with Ni being in +2 oxidation state. As the only redox-active species, the Ni K-edge shifts to higher energy regions upon charge, indicating oxidation of the Ni^{2+} species. For both half-cells, the energy shift from the pristine state to the charged state up to 4.3 V is about 4 eV, which is consistent with Ni being oxidized up to +4 oxidation state [393,394]. By calculating the theoretical capacity considering only Ni^{2+}/Ni^{4+} as the redox-active couple in NaMNMO, accounting for the extraction of 0.4 Na^+ equivalents, a value of 105 mAh g^{-1} is obtained, which is in good agreement with the practical capacity of the cathode from **Figure 3-4b**. The capacity at first cycle being higher might account for some irreversible oxygen activity. Interestingly, the energy shift in NaMNMO occurs gradually through the whole charge, while NaMNMO/$Na_2C_4O_4$ displays a more sudden shift to higher energies when squarate is decomposing (E > 3.7 V). This result indicates that the Ni charge transfer reaction for NaMNMO spans throughout the whole charge, whereas in NaMNMO/$Na_2C_4O_4$ there is a jump in the Ni redox activity taking place in the high-voltage region, in correspondence of squarate decomposition. From the Ni EXAFS results in **Figure 3-18e-f**, the characteristic shells at 1.6 Å and 2.6 Å, related to the Ni-O and Ni-TM interactions, are also displayed. In particular, it is possible to observe that the Ni-O interatomic distance decreases as a result of the oxidation to Ni^{4+}, accounting for the *a*-parameter decreasing upon charge observed in **Figure 3-16a-b**. The Ni-TM interatomic distances are comparable to those of Mn-TM from **Figure 3-17e-f**, indicating that Ni and Mn ions are randomly and uniformly distributed in the TM layer [395].

Interestingly, for both NaMNMO and NaMNMO/$Na_2C_4O_4$ upon discharge, the XANES and EXAFS results indicate that the Ni K-edge and Ni-O interatomic distance do not completely go back to the initial stage. Given the complexity of the system, it is rather hard to fully understand the mechanism of reaction or failure of the materials, but the evidence of these signals not being completely reversible during the first cycle may account for the irreversible capacity of the cathode at the first cycle, due to the possibility of lattice oxygen contributing to the capacity in the high-voltage region [396,397].

In order to obtain more detailed information of the different reaction behavior between the two full cells, the composition of the passivation layers at the cathode and anode after the first cycle was observed. Indeed, a hint of possible differences in the electrolyte decomposition products was already observed when opening the cycled cells, as the separators employed in the presodiated full cell displayed a much brownish color from the anode side, possibly indicating a more severe electrolyte decomposition as displayed in **Figure 3-19a**. Hence, the composition of surface layers formed by electrolyte decomposition products was examined in detail by means of ex-situ XPS. **Figure 3-19b-c**

shows the C1s spectra of NaMNMO and CCDHC electrodes analyzed in pristine conditions as well as after 1 cycle with and without the squarate additive.

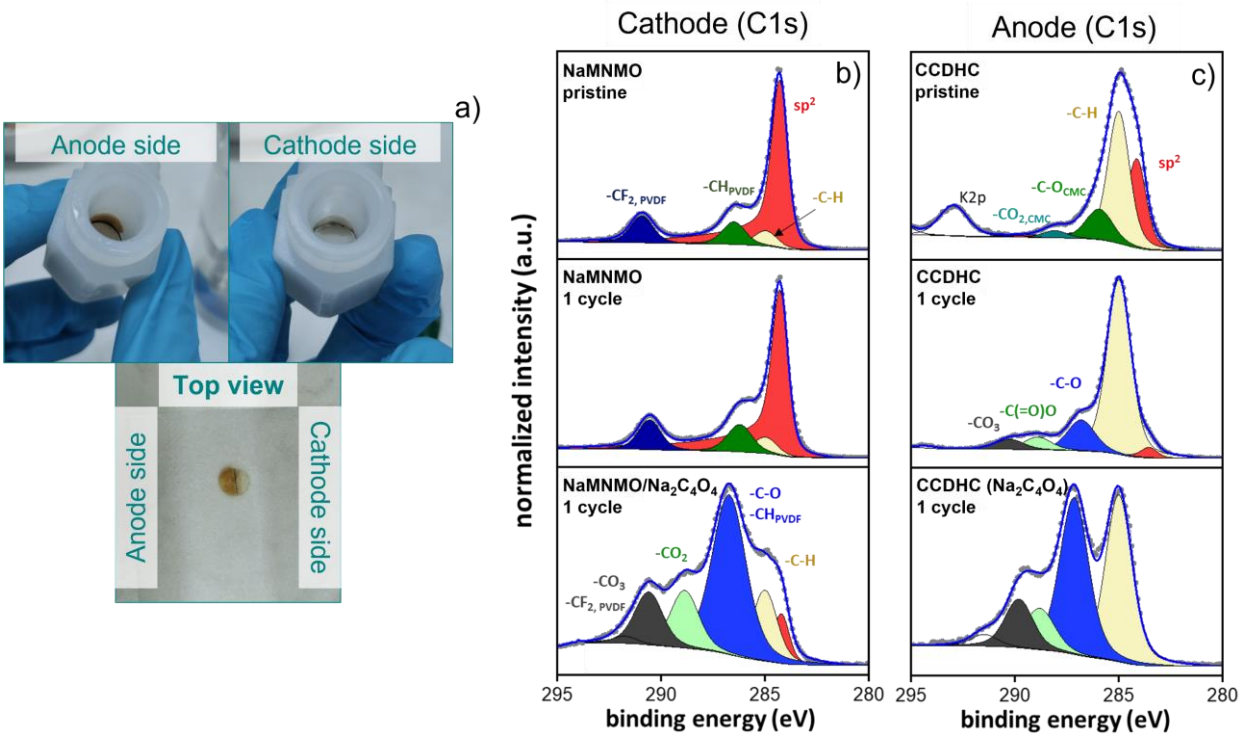

Figure 3-19. a) Picture of the top-side separator after cycling of $NaMNMO/Na_2C_4O_4$||CCDHC full cell; C1s spectra of b) NaMNMO and c) CCDHC electrodes in pristine conditions as well as after one cycle, with and without the presence of squarate.

When considering the cathode (**Figure 3-19b**), the pristine NaMNMO electrode basically shows four peaks, which are related to the sp^2 hybridized carbon of the Super C-65 conductive additive at ~284.4 eV, -C-H from air-borne carbonaceous contamination (so-called "adventitious carbon") at 285 eV [398], and the two chemical environments of the polyvinylidene fluoride (PVdF) binder -C-H at 286.5 eV, and -C-F at 290.9 eV, respectively. After one cycle, the electrode without squarate is displaying a very similar composition. This indicates a low electrolyte decomposition as would be expected of EC:PC-containing electrolytes cycled in a potential window of $1.2\ V < E < 4.29\ V$. By contrast, the addition of squarate to the electrode composition yields intensive peaks corresponding to the formation of -C-O (286.8 eV), $-CO_2$ (288.8 eV), and $-CO_3$ (290.5 eV) species composing the Cathode Electrolyte Interphase (CEI). In addition, the intensity of the sp^2 peak strongly decreases, thus suggesting that the presence of the squarate additive is resulting in a stronger decomposition of the electrolyte and in a formation of a thicker electrode-electrolyte interphase.

As for the anode side (**Figure 3-19c**), the pristine CCDHC electrode also displays four main peaks, related to the sp^2 hybridized hard carbon at ~284.2 eV, -C-H from adventitious carbon at 285 eV [398], and the two chemical environments of the carboxymethyl cellulose (CMC) binder -C-O-C- at 286.5

eV, and -CO_2 at 288.3 eV, respectively. After one cycle in the full cell without presodiation, a strong decrease in sp^2 hard carbon is observed, while the intensity of hydrocarbons increased. Carbonate species -C-O (286.7 eV), -CO_2 (288.9 eV), and -CO_3 (290.1 eV) species are emerging, resulting from EC and PC decomposition products to form the SEI layer. The addition of squarate leads to further thickening of the SEI layer as no sp^2 peak is observed, and all three SEI components (i.e., -C-O, -CO_2, and -CO_3) are increasing in intensity. Similar to the observation made on the NaMNMO cathode, the presence of squarate seems to favor the formation of carbonate species on the electrodes' surface upon charge, resulting in a thickening of both passivation layers.

To further investigate the interfacial properties of the material, impedance spectra were recorded in full cell configuration at the bias potential of 4.0 V during the 1st and 2nd cycle, and then every 10 cycles upon sodiation (**Figure 3-20**), using a three-electrode cell configuration with Na metal ring reference (EL-CELL). All the Nyquist plots obtained (**Figure 3-20a-b**) are characterized by five main features: (I) an intercept with the real axis in the high frequency region; (II) a small semicircle at high frequencies; (III) a semicircle in the medium frequency region; (IV) a bigger semicircle in the medium-to-low frequency region; (V) a straight line in the low frequency region. The obtained Nyquist plots have been modeled by the Equivalent Circuit method [327], and the related parameters have been calculated through a NLLS fitting protocol by using the RelaxIS3 software (rhd instruments). The intercept (I) at high frequencies represents the migration of Na^+ ions through the electrolyte solution, hence it was modeled as a pure resistive element (R_{el}). The first small semicircle (II) at high frequencies is attributed to the contact resistance between the current collector and the electrode particles, thus it was modeled as a resistive element (R_{cont}) in parallel with a double layer capacitive element (C_{cont}). The semicircle (III) at medium frequencies is related to the migration of Na^+ ions through the passivation layers of the anode and cathode with charges accumulating onto their surface, and was modeled as a resistive element ($R_{SEI/CEI}$) in parallel with a capacitor element ($C_{SEI/CEI}$). The bigger semicircle (IV) at medium-to-low frequencies can be ascribed to the faradaic charge transfer process with double layer formation onto the surface of the active material particles, modeled as a resistive element (R_{ct}) in parallel with a capacitor element (C_{dl}). Finally, the line (V) at low frequency describes a semi-infinite diffusion to a blocking electrode, which was modeled with a Warburg impedance (W) in series with a capacitor element (C_i) indicating intercalation capacitance. The resulting equivalent circuit, written according to Boukamp's notation [328,329], is $R_{el}(R_{cont}C_{cont})(R_{SEI/CEI}C_{SEI/CEI})(R_{ct}C_{dl})WC_i$. For the fitting procedure, the pure capacitive elements were substituted by constant phase elements (Q), in order to consider the non-ideal, capacitive behavior given by electrode inhomogeneity and surface roughness [327]. To better visualize and deconvolute all the impedance contributions, the DRT analysis method was applied, by calculating the DRT function γ according to Tikhonov regularization [331] (**Figure**

3-20e-f). The low frequency points, as simulated by WC_i elements, were subtracted from the overall impedance (Figure 3-20c-d).

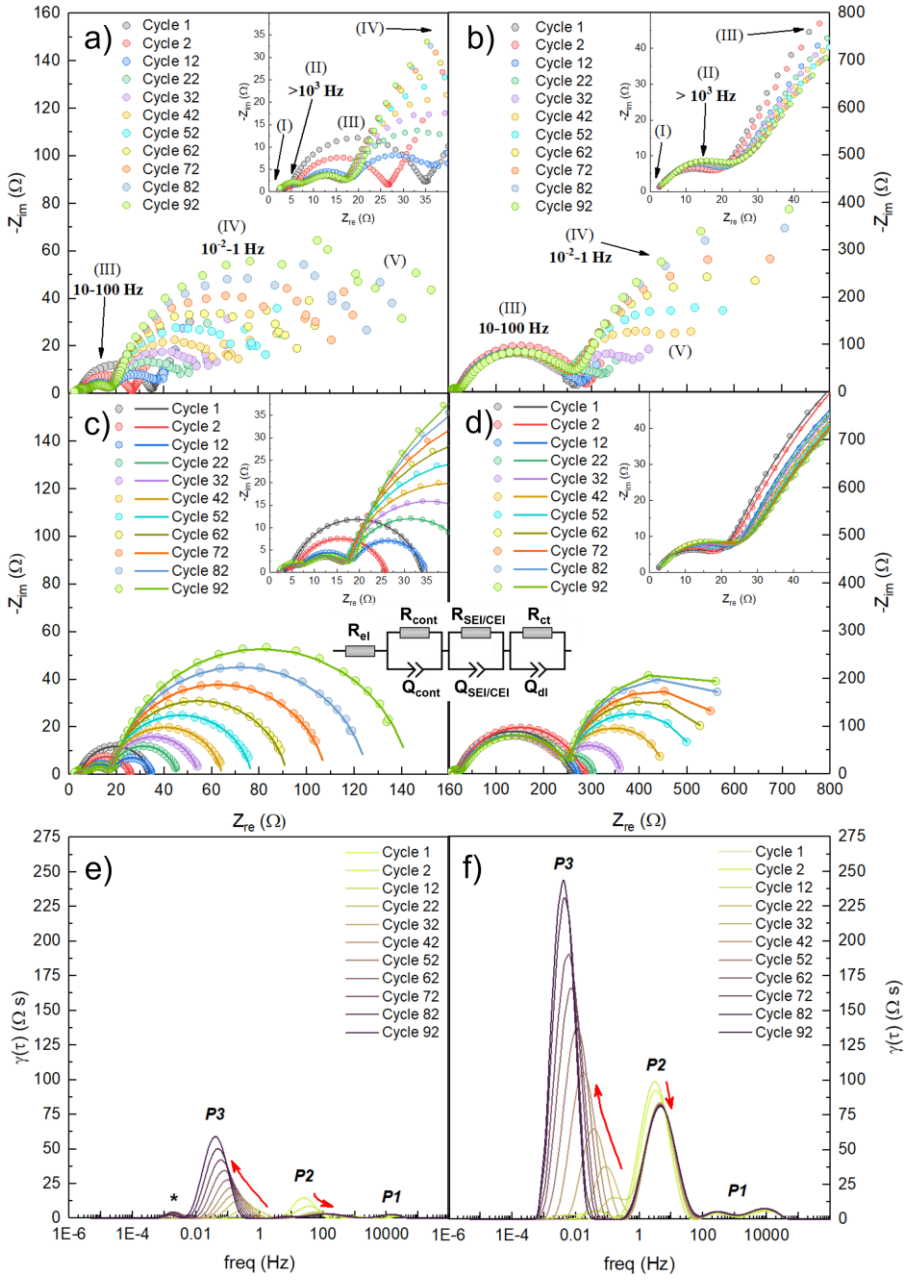

Figure 3-20. Electrochemical impedance spectroscopy analysis of NaMNMO||CCDHC and $NaMNMO/Na_2C_4O_4$||CCDHC full cells, performed at the 1st, 2nd and every 10 cycles in the frequency range 3 mHz < f < 199 kHz: Nyquist plots obtained for a) NaMNMO||CCDHC and b) $NaMNMO/Na_2C_4O_4$||CCDHC; Nyquist plots after subtraction of the diffusive part displayed for c) NaMNMO||CCDHC and d) $NaMNMO/Na_2C_4O_4$||CCDHC, with related fits and equivalent circuit employed; Distribution of relaxation times for e) NaMNMO||CCDHC and f) $NaMNMO/Na_2C_4O_4$||CCDHC.

The Nyquist plots obtained after Warburg subtraction for the two full cells upon cycling are shown in Figure 3-20c-d, and the fitting has been performed by using the equivalent circuit $R_{el}(R_{cont}C_{cont})(R_{SEI/CEI}C_{SEI/CEI})(R_{ct}C_{dl})$. By observing the resulting diagrams, all semicircles and their

evolution are now better visible for both cells, especially the low-frequency semicircle. In particular, it is possible to notice a quite big difference in the magnitude of the resistances between the cells, as the NaMNMO||CCDHC system displays much lower polarizations with respect to the presodiated NaMNMO/$Na_2C_4O_4$||CCDHC system. From the calculation of the DRT (**Figure 3-20e-f**), the different polarizations associated to each semicircle in the Nyquist plot can be better deconvoluted according to their time constants, resulting in different characteristic frequencies. Although it was not possible to discriminate between the separate anode and cathode contributions due to their time constants being too similar, by plotting the DRT as a function of cycle number, it was possible to define three main contributions for both cells (the small hump at low frequencies, labeled as *, is an artifact due to the removal of the Warburg diffusion), each having a different behavior: P1 in the high frequency range is small and constant throughout cycling, hence it is consistent with the contribution of the contact resistance (R_{cont}); P2 in the high-to-medium frequency range can be related to the sum of the resistances of the passivation layers for both electrodes ($R_{SEI/CEI}$), with the R_{SEI} generally being the dominant polarization; finally, P3 at low frequencies has a stronger dependency on the number of cycles, and is increasing in both cases, hence it is associated with the resistance of charge-transfer (R_{ct}) of both electrodes upon cycling. Interestingly, the trend of the polarizations is the same in both cells, with P3 always increasing and P2 remaining constant after the first cycles. However, the intensity of the peaks for NaMNMO/$Na_2C_4O_4$||CCDHC is much higher, indicating a very high polarization for both the passivation layer and the charge transfer resistance, as observed from the Nyquist plots.

Based on the reported data, the calculated values of the circuital elements, obtained by fitting the Nyquist plots, are plotted as a function of cycle number for NaMNMO||CCDHC and NaMNMO/$Na_2C_4O_4$||CCDHC (**Figure 3-21**), to evidence the behavior of the cells upon cycling.

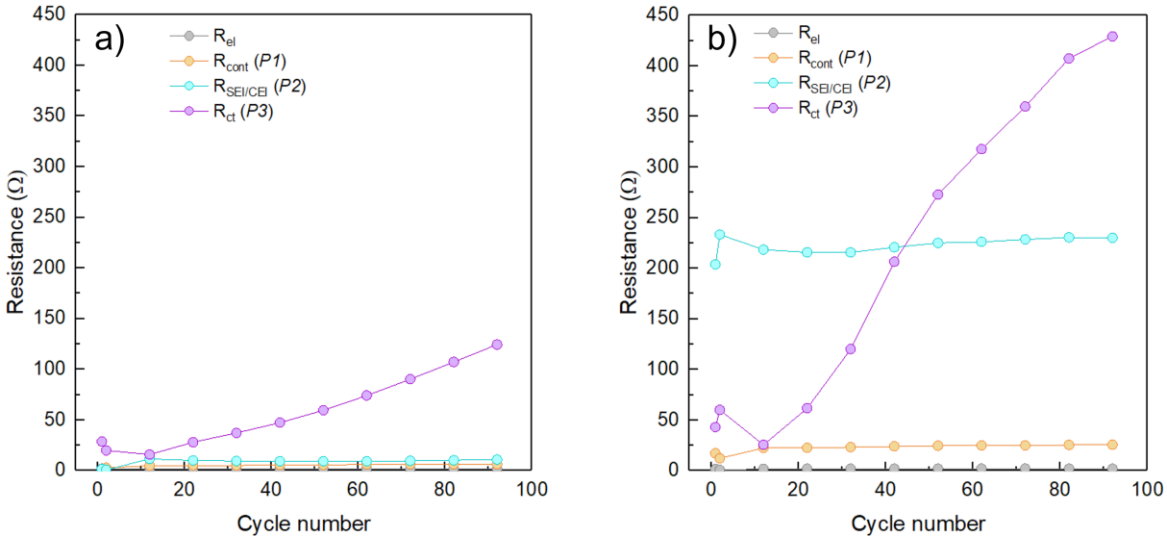

Figure 3-21. Trend of R_{el}, R_{cont}, $R_{SEI/CEI}$ and R_{ct} as a function of cycle number for a) NaMNMO||CCDHC and b) NaMNMO/$Na_2C_4O_4$||CCDHC full cells.

In **Figure 3-21a**, the resistance of the electrolyte, R_{el}, basically remains constant upon cycling until the 92 cycles observed. The resistance of the passivation layer, $R_{SEI/CEI}$, displays a lower value in the first cycle due to the SEI/CEI not yet completely formed (E_{cell} = 4.00 V), and then increases in the second cycle due to the complete formation of SEI and CEI; after the second cycle, it remains low and constant. These results suggest the formation of thin passivation layers during the first charge, which then remain stable in the subsequent cycles, hence preventing further electrolyte decomposition. As for the resistance to charge transfer, R_{ct}, an initial decrease is observed from the 1st to the 10th cycle, after which the resistance values start increasing almost at a constant rate, probably due to the sodium irreversible depletion from the SEI formation causing an unbalancing in the charges between anode and cathode, eventually resulting in the loss of performance. When considering the presodiated cell in **Figure 3-21b**, the resistance of the electrolyte, R_{el}, is basically the same as the NaMNMO||CCDHC cell, remaining constant upon cycling. The resistance of the passivation layers, $R_{SEI/CEI}$, displays a very similar trend, increasing after the first cycle and then remaining constant upon cycling; however, the order of magnitude of the associated impedance is more than 20 times higher. This result is consistent with the results obtained from the XPS measurements (**Figure 3-19b-c**), indicating the formation of thicker and more insulating SEI/CEI upon squarate decomposition. The effects of such passivation layers are therefore reflected on the charge transfer resistance, R_{ct}, which starts at similar values as in **Figure 3-21a**, but it increases at a much faster rate, as a result of a more sluggish kinetics of the redox processes, hence leading to a faster loss of performance.

3.3 Conclusions

The use of $Na_2C_4O_4$ as a green and cheap presodiation source in sodium-ion full cells was evaluated for a layered oxide-hard carbon system, namely $Na_{0.66}Mn_{0.75}Ni_{0.2}Mg_{0.05}O_2$ as the cathode and CCDHC as the anode. The standard galvanostatic cycling of the single electrodes tested in half cells displayed quite good performance and stability upon cycling. From the rate capability tests, both electrodes showed high capacity retention and relatively low polarization at low-medium current, with the cathode being able to sustain current densities as high as 2000 mA g^{-1}. When tested in full cell configuration, the charge/discharge performance was quite good, but it decayed upon cycling due to the irreversible formation of SEI which was not balanced, as expected. When the presodiation additive was employed, a higher initial charge capacity was achieved as a result of additional sodium provided to address SEI formation. However, a lower capacity retention upon long cycling was observed. When comparing the NaMNMO||CCDHC and the NaMNMO/$Na_2C_4O_4$||CCDHC systems, SEM micrographs on pristine and charged cathodes revealed the formation of holes and crack enlargement on the electrode surface after squarate decomposition leading to CO_2 evolution. Moreover, operando XRD measurements allowed to observe differences in the structural evolution of the two cells,

confirming the polarization of the high-voltage plateau related to P2/Z-phase transition, which accounts for a large portion of the capacity. Operando XAS measurement confirmed that the redox activity of Ni is affected by the squarate decomposition, although the electronic evolution of Ni in the two systems is quite similar upon the first cycle. Ex-situ XPS after squarate decomposition revealed the presence of insulating carbonate species in the passivation layer of both electrodes possibly due to reaction of the produced CO_2 with Na, contributing to the formation of thicker SEI/CEI. This was confirmed by means of EIS measurements, revealing a much higher $R_{SEI/CEI}$ when squarate is employed, resulting in a faster increase of R_{ct} and performance decay. Overall, the combination of the chosen anode and cathode materials is found to be compatible for full cell applications, also considering the high loadings employed. The sacrificial salt $Na_2C_4O_4$ is indeed able to provide additional sodium to address the SEI formation at the anode side, resulting in a cheaper and greener alternative as compared to using higher amounts of cathode, part of which would remain as a dead weight. Further studies are however needed for practical applications, focusing on optimizing the presodiation process and the stability at the interfaces in order to achieve longer cycle life with slower capacity fade.

4 General conclusions

In this thesis work, the structural and interfacial properties, their evolution upon cycling and within the single cycle, and the performance of two electrochemical energy storage systems have been studied.

Regarding the first system, a Silicon/Hard Carbon composite, combined to a crosslinked Chitosan-based binder, has been evaluated as a possible anode for Li-ion batteries. The synthesized hard carbon derived from waste biomass (CCDHC) and the final composite have been characterized in terms of structure, morphology and electrochemical performance. Then, the structural and interfacial evolutions and the reversibility of the alloying reaction have been studied by means of ex-situ Raman spectroscopy and potentiostatic electrochemical impedance spectroscopy (PEIS).
The superiority of CCDHC as the buffering matrix was demonstrated by comparing the electrochemical performance of the Si/CCDHC composite with those of a Si/Gr composite, fabricated employing the same electrode compositions in terms of mass ratio of the components, and the same CS/CA binder. The electrochemical performance over 100 cycles at 1.0 A g^{-1} for Si/CCDHC highlighted a stable specific capacity of about 800 mAh g^{-1} with coulombic efficiencies quickly stabilizing at 99.4 %. Moreover, no indication of breakage and reformation of the SEI upon cycling was observed. These results proved the effective buffering activity of CCDHC as compared to commercial graphite. The performance of a bare Si anode without any buffering matrix was also evaluated, showing the characteristic decay due to repeated and unbuffered volume changes upon cycling. The superiority of the CS/CA binder was also demonstrated by comparing the electrochemical performance of the Si/CCDHC composite with different binders, with the same electrode compositions and cycling conditions. The electrochemical performance over 100 cycles showed an improved and more stable capacity when CS/CA binder is used as compared to PAA, CMC and Alg. Moreover, by means of SEM and PEIS performed on pristine and cycled electrodes with different binders, a higher integrity and lower increase in polarization upon cycling was observed when employing CS/CA, proving the beneficial effect of the crosslinked binder. The rate capability of the composite up to 4.0 A g^{-1} displayed a very good capacity retention at high rates and a good capacity recovery after the faster rate, with low polarization effects up to 1.0 A g^{-1}. Ex-situ Raman spectroscopy at chosen degrees of (de)lithiation was used to evaluate the structural evolution upon the first cycle, demonstrating the irreversible amorphization of Si upon the first lithiation through the progressive disappearance of the characteristic 1TO peak. The lithiation of the CCDHC matrix was also observed by the intensity decrease of the characteristic D and G bands, demonstrating a partial reversibility due to some Li-ion trapping in the hard carbon. The partially lithiated state of the carbon matrix is believed to act as Li scaffold, increasing the conductivity of the composite. Irreversible

formation of Li_2O is also detected due to lithium reacting with the partially oxidized Si surface. The interfacial evolution upon cycling was evaluated by means of PEIS performed at the 1st and every 10th cycle. The fits obtained by the equivalent circuit method revealed a high stability of the electrolyte and SEI resistances, which were very low and stable upon cycling, indicating the formation of a thin and stable passivation layer. The resistance associated to the charge transfer displayed an increasing trend up to 90 cycles, after which it showed a tendency towards stabilization. An initial sharper increase of R_{ct} is consistent with the formation of insulating Li_2O at the surface of the active material after the first lithiation. The Warburg coefficient displayed an initially increasing trend upon cycling, indicating a hindered solid-state diffusion and a decreasing diffusion coefficient, with a progressive stabilization upon cycling. The interfacial evolution was also evaluated within the single cycle by means of SPEIS and calculation of the DRT function to deconvolute the different contributions. The resistance of the electrolyte was found to be stable throughout the whole cycle. The resistance associated to SEI decreased in the first lithiation steps until it becomes stable, following the opposite trend upon de-lithiation, suggesting a stretching of the SEI upon volume expansion but without cracking. The R_{ct} was found to decrease at increasing lithiation degree, and it reversibly increased upon de-lithiation, displaying resistance minima being consistent with the starting and ending of redox activities, respectively, hence confirming the reversibility of the alloying reaction. Given the stability of the material, a proof-of-concept full cell was built by using LFP as the cathode material, resulting in a high reversible capacity of 600 mAh g^{-1}_{an}, a low potential hysteresis and an energy efficiency of about 87.7 %, hence demonstrating the applicability in a full cell configuration.

Concerning the second system, an extended study on the effect of presodiation via $Na_2C_4O_4$ in a Na-ion battery has been performed, focusing on the use of P2 $Na_{0.66}Mn_{0.75}Ni_{0.2}Mg_{0.05}O_2$ layered oxide (NaMNMO) serving as the cathode, and CCDHC serving as the anode. The electrochemical performance of each material was first assessed singularly, and then in combination to build a full cell, either with or without the presodiation additive. The NaMNMO cathode in half-cell configuration exhibited a stable specific capacity of 105 mAh g^{-1} over 100 cycles at 20 mA g^{-1} current density, and an initial coulombic efficiency of 84 % rapidly reaching and stabilizing at 99.5 %. The rate performance of the cathode material revealed the ability to sustain high specific currents up to 2000 mA g^{-1}, with a low polarization and a high capacity retention displayed up to 100 mA g^{-1}. The CCDHC anode in half-cell configuration displayed a stable specific capacity of 165 mAh g^{-1} over 100 cycles at 20 mA g^{-1} current density, but a high irreversible capacity of 116 mAh g^{-1} at the first cycle resulting in an initial coulombic efficiency of 61 %, rising to values close to 100 % in the following cycles. The rate performance of the anode material revealed a lower tolerance to high specific currents as compared to the cathode, with a low polarization and a high capacity retention up to 40 mA g^{-1}. After singularly testing the two electrode materials, their compatibility in full cell configuration for 120 cycles at 20

mA g^{-1} was evaluated, without accounting for the SEI formation when considering the charge balancing. During the first cycle, a 60 % coulombic efficiency resulting from the irreversible SEI formation is observed as expected from the half-cell measurements. In the following cycles, a coulombic efficiency of 99.5 % is reached, with an average specific capacity of 80 mAh g^{-1} at the second cycle, slowly fading upon cycling. Half-cells with only $Na_2C_4O_4$ as the active material were electrochemically tested, providing confirmation of the irreversible decomposition of the salt and of the specific capacity it is able to provide, which was observed to be about 315 mAh g^{-1}. Subsequently, electrodes containing an appropriate NaMNMO/$Na_2C_4O_4$ ratio were fabricated and tested in half-cell. The CV revealed a high polarization of all processes upon squarate decomposition, with the high voltage phase transition being the most affected process, indicating a change in the redox activity of the material. The galvanostatic cycling revealed the effective decomposition of $Na_2C_4O_4$ providing additional sodium upon charge, resulting in an initial specific capacity of 181 mAh g^{-1}. However, the subsequent cycles display a capacity drop to 60 mAh g^{-1} and a low capacity retention. When tested in a full cell for 120 cycles at 20 mA g^{-1}, the presodiated full cell displays an initial charge capacity of 200 mAh g^{-1}, with stabilization at 90-95 mAh g^{-1} in the first 15 cycles, but a rapid decrease in the following cycles. The change in the surface morphology of the cathode was investigated by SEM performed at the pristine and charged state during the first cycle, revealing the formation of holes and enlargement of cracks in the NaMNMO/$Na_2C_4O_4$ electrode upon CO_2 evolution from squarate decomposition, probably causing a lower integrity upon cycling. Operando XRD was performed during the first two cycles in order to assess the effect of presodiation in the structural evolution, confirming that the P2 → Z-phase transition is not observed and polarized to higher potential upon squarate decomposition, which could also possibly cause a lack in the Na^+/vacancy ordering. The evolution of the electronic structure was investigated by means of operando XAS during the first cycle, revealing that the Ni redox activity was also affected, with a more intense energy shift in the high-voltage region after the squarate decomposition has occurred. Moreover, in both NaMNMO and NaMNMO/$Na_2C_4O_4$ electrodes, the Ni-Kedge and Ni-O interatomic distances upon discharge do not go back to the initial stage, indicating a possible contribution of lattice oxygen to capacity, accounting for the first cycle irreversible capacity of the cathode. The electrodes' surface composition after the first cycle was also evaluated by means of ex-situ XPS performed on pristine and cycled electrodes. The measurements on anode and cathode from the NaMNMO||CCDHC system after one cycle revealed the presence of carbonate species on the anode surface as a result of SEI formation, while almost no changes were found for the cathode as compared to the pristine state. As for the NaMNMO/Na_2C_4O4||CCDHC system after one cycle, the presence of carbonate species was detected for both electrodes as compared to the pristine state, also revealing a much thicker SEI and CEI formation upon squarate decomposition, contributing to hindered performance upon cycling. These observations were further

confirmed by performing PEIS measurements at 1st, 2nd and every 10 cycles on the two systems, with calculation of the DRT function to better deconvolute all the processes. Indeed, when considering the different polarizations, the trend between the two full cells is very similar, but $R_{SEI/CEI}$ when the sacrificial salt is used for presodiation has much higher values, confirming the formation of thicker and more insulating passivation layers ultimately leading to a hindered charge transfer, as indicated by the faster increase of R_{ct} as compared to the NaMNMO||CCDHC cell.

In conclusion, for application in LIBs, the Si/CCDHC composite anode employing the CS/CA binder outperforms the state-of-the-art graphite anode and is found to be compatible for use with LFP. Indeed, the possibility to use abundant and environmentally friendly Si as the main electroactive species, the production of carbon from waste biomass, the use of a greener binder as compared to commercial PVdF, and the feasibility of building a full cell with the low-cost LFP cathode, make this system suitable for further optimization and use in high-energy density applications and fast charging devices, while keeping the environmental footprint of the employed materials as sustainable as possible.

The aim of sustainability for practical applications is successfully pursued also for the studied SIB configuration, thus hinting at the possibility to reduce the production costs because of the higher natural abundance of raw materials. The use of a Co-free cathode and a biowaste-derived carbon anode make the studied system also suitable for further optimization and eventual scalability on a larger scale. The use of a green and cheap presodiation additive would allow to overcome the cathode excess otherwise necessary to address the SEI formation, hence avoiding the resulting "dead" weight of inactive cathode, also contributing to a cost reduction of the battery.

Overall, both proposed works yielded good results towards practical applications in a perspective of circular economy and sustainability of materials.

5 References

(1) Masson-Delmotte, V.; Zhai, P.; Pörtner, H.-O.; Roberts, D.; Skea, J.; Shukla, P.R.; Pirani, A.; Moufouma-Okia, W.; Péan, C.; Pidcock, R.; Connors, S.; Matthews, J.B.R.; Chen, Y.; Zhou, X.; Gomis, M.I.; Lonnoy, E.; Maycock, T.; Tignor, M.; Waterfield, T.; *IPCC, 2018: Global Warming of 1.5°C. An IPCC Special Report on the Impacts of Global Warming of 1.5°C above Pre-Industrial Levels and Related Global Greenhouse Gas Emission Pathways, in the Context of Strengthening the Global Response to the Threat of Climate Change, Sustainable Development, and Efforts to Eradicate Poverty*; Cambridge University Press, Cambridge, UK and New York, NY, USA, 2018.

(2) NOAA National Centers for Environmental information, *Climate at a Glance: Global Time Series*, December 2022 https://www.ncei.noaa.gov/access/monitoring/climate-at-a-glance/global/time-series.

(3) NOAA National Centers for Environmental Information, *Monthly Global Climate Report for Annual 2021*, January 2022 https://www.ncei.noaa.gov/access/monitoring/monthly-report/global/202113.

(4) Pörtner, H.-O.; Roberts, D.C.; Tignor, M.; Poloczanska, E.S.; Mintenbeck, K.; Alegría, A.; Craig, M.; Langsdorf, S.; Löschke, S.; Möller, V.; Okem, A.; Rama, B.; *IPCC, 2022: Climate Change 2022: Impacts, Adaptation and Vulnerability. Contribution of Working Group II to the Sixth Assessment Report of the Intergovernmental Panel on Climate Change*; Cambridge University Press. Cambridge University Press, Cambridge, UK and New York, NY, USA, 2022.

(5) *United Nations / Framework Convention on Climate Change (2015) Adoption of the Paris Agreement, 21st Conference of the Parties, Paris: United Nations;* 2015.

(6) *IEA (2022), Energy System Overview*; IEA, Paris, 2022.

(7) *Climate Watch Historical GHG Emissions*. Washington, DC: World Resources Institute https://www.climatewatchdata.org/ghg-emissions.

(8) Core Writing Team, Pachauri, R.K.; Meyer, L.A.; *IPCC, 2014: Climate Change 2014: Synthesis Report. Contribution of Working Groups I, II and III to the Fifth Assessment Report of the Intergovernmental Panel on Climate Change*; IPCC, Geneva, Switzerland, 2014.

(9) Baumert, K.A.; Herzog, T.; Pershing, J.; *Navigating the Numbers: Greenhouse Gas Data and International Climate Policy*; 2005.

(10) *IEA (2022), Electricity Sector*; IEA, Paris, 2022.

(11) *IEA (2022), Transport*; IEA, Paris, 2022.

(12) Garche, J.; Moseley, P.T.; *Electrochemical Energy Storage for Renewable Sources and Grid Balancing*; 2015.

(13) Dunn, B.; Kamath, H.; Tarascon, J.M.; Electrical Energy Storage for the Grid: A Battery of Choices. *Science* **2011**, 334 (6058), 928–935. https://doi.org/10.1126/science.1212741.

(14) Khalid, M.; Arshid, N.; Grace, N.; *Advances in Supercapacitor and Supercapattery: Innovations in Energy Storage Devices*; Elsevier, 2021.

(15) Nagaura, T.; Tozawa, K.; *Progress in Batteries and Solar Cells*; 1990.

(16) Rudola, A.; Rennie, A.J.R.; Heap, R.; Meysami, S.S.; Lowbridge, A.; Mazzali, F.; Sayers, R.; Wright, C.J.; Barker, J; Commercialisation of High Energy Density Sodium-Ion Batteries: Faradion's Journey and Outlook. *J. Mater. Chem. A* **2021**, 9, 8279–8302. https://doi.org/10.1039/d1ta00376c.

(17) The First-generation Sodium-ion Battery Launch Event https://www.catl.com/en/news/685.html.

(18) He, M.; Davis, R.; Chartouni, D.; Johnson, M.; Abplanalp, M.; Troendle, P.; Suetterlin, R.P.; Assessment of the First Commercial Prussian Blue Based Sodium-Ion Battery. *J. Power Sources* **2022**, 548, 232036. https://doi.org/10.1016/j.jpowsour.2022.232036.

(19) Meyers, W.F.; Bell, B.; Simmon, J.W.; Electric Current-Producing Cell with Anydrous Organic Liquid Electrolyte. *United States Pat.* **1969**, 28 (2), 131–134.

(20) Goodenough, J.B.; *Batteries for Sustainability: Selected Entries from the Encyclopedia of Sustainability Science and Technology*; Springer, 2013.

(21) Armand, M.B.; Whittingham, M.S.; Huggins, R.A.; The Iron Cyanide Bronzes. *Mater. Res. Bull.* **1972**, 7 (2), 101–107. https://doi.org/10.1016/0025-5408(72)90266-8.

(22) Steele, B.C.H.; *Fast Ion Transport in Solids: Solid State Batteries and Devices*; North Holland Publ., 1973.

(23) Mauger, A.; Julien, C.M.; Goodenough, J.B.; Zaghib, K.; Tribute to Michel Armand: From Rocking Chair – Li-Ion to Solid-State Lithium Batteries. *J. Electrochem. Soc.* **2020**, 167 (7), 070507. https://doi.org/10.1149/2.0072007jes.

(24) Lazzari, M.; Scrosati, B.; A Cyclable Lithium Organic Electrolyte Cell Based on Two Intercalation Electrodes. *J. Electrochem. Soc.* **1980**, 127 (3), 773–774. https://doi.org/10.1149/1.2129753.

(25) Whittingham, M.S.; Gamble, F.R.; The Lithium Intercalates of the Transition Metal Dichalcogenides. *Mater. Res. Bull.* **1975**, 10 (5), 363–371. https://doi.org/10.1016/0025-5408(75)90006-9.

(26) Whittingham, M.S.; Electrical Energy Storage and Intercalation Chemistry. *Science* **1976**, 192 (4244), 1126–1127. https://doi.org/10.1126/science.192.4244.1126.

(27) Whittingham, M.S.; Fanwood; N.J.; Chalcogenide Battery. *United States Pat.* **1977**, 1–5.

(28) Peled, E.; The Electrochemical Behavior of Alkali and Alkaline Earth Metals in Nonaqueous Battery Systems - The Solid Electrolyte Interphase Model. *J. Electrochem. Soc.* **1979**, 126 (12), 2047–2051. https://doi.org/10.1149/1.2128859.

(29) Besenhard, J.O.; Eichinger, G.; High Energy Density Lithium Cells. Part I. Electrolytes and Anodes. *J. Electroanal. Chem.* **1976**, 68 (1), 1–18. https://doi.org/10.1016/S0022-0728(76)80298-7.

(30) Francis, R.W.; Christopher, H.A.; Lithium-Aluminum Electrode. *J. Electrochem. Soc.* **1977**, 124, 1490–1492. https://doi.org/10.1149/1.2133098

(31) Nicholson, M.M.; Lithium-Magnesium Electrodes in Propylene Carbonate. *J. Electrochem. Soc.* **1974**, 121 (6), 734. https://doi.org/10.1149/1.2401900.

(32) Besenhard, J.O.; Fritz, H.P.; Cathodic Reduction of Graphite in Organic Solutions of Alkali and NR_4^+ Salts. *J. Electroanal. Chem.* **1974**, 53 (2), 329–333. https://doi.org/10.1016/S0022-0728(74)80146-4.

(33) Eichinger, G.; Besenhard, J.O.; High Energy Density Lithium Cells. Part II. Cathodes and Complete Cells. *J. Electroanal. Chem.* **1976**, 72, 1–31. https://doi.org/10.1016/S0022-0728(76)80072-1.

(34) Besenhard, J.O.; The Electrochemical Preparation and Properties of Ionic Alkali Metal and NR_4-Graphite Intercalation Compounds in Organic Electrolytes. *Carbon* **1976**, 14 (2), 111–115. https://doi.org/10.1016/0008-6223(76)90119-6.

(35) Dunning, J.S.; Tiedemann, W.H.; Hsueh, L.; Bennion, D.N.; A Secondary, Nonaqueous Solvent Battery. *J. Electrochem. Soc.* **1971**, 118 (12), 1886. https://doi.org/10.1149/1.2407861.

(36) Schipper, F.; Aurbach, D.; A Brief Review: Past, Present and Future of Lithium Ion Batteries. *Russ. J. Electrochem.* **2016**, 52 (12), 1095–1121. https://doi.org/10.1134/S1023193516120120.

(37) Armand, M.B.; Duclot, M.; Electrochemical Generators for Producing Current and New Materials for Their Manufacture. *United States Pat.* **1981**, 45 (19).

(38) Reddy, M.V.; Mauger, A.; Julien, C.M.; Paolella, A.; Zaghib, K.; Brief History of Early Lithium-Battery Development. *Materials* **2020**, 13 (1884). https://doi.org/10.1016/j.coelec.2021.100858.

(39) Basu, S.; Zeller, C.; Flanders, P.J.; Fuerst, C.D.; Johnson, W.D.; Fischer, J.E.; Synthesis and Properties of Lithium-Graphite Intercalation Compounds. *Mater. Sci. Eng.* **1979**, 38 (3), 275–283. https://doi.org/10.1016/0025-5416(79)90132-0.

(40) Mizushima, K.; Jones, P.C.; Wiseman, P.J.; Goodenough, J.B.; Li_xCoO_2 ($0 < x \leq 1$): A New Cathode Material for Batteries of High Energy Density. *Solid State Ion.* **1981**, 3-4, 171-174. https://doi.org/10.1016/0167-2738(81)90077-1.

(41) Fong, R.; von Sacken, U.; Dahn, J.R.; Studies of Lithium Intercalation into Carbons Using Nonaqueous Electrochemical Cells. *J. Electrochem. Soc.* **1990**, 137 (7), 2009–2013. https://doi.org/10.1149/1.2086855.

(42) Verma, P.; Maire, P.; Novák, P.; A Review of the Features and Analyses of the Solid Electrolyte Interphase in Li-Ion Batteries. *Electrochim. Acta* **2010**, 55 (22), 6332–6341. https://doi.org/10.1016/j.electacta.2010.05.072.

(43) Aurbach, D.; Levi, M.D.; Levi, E.; Schechter, A.; Failure and Stabilization Mechanisms of Graphite Electrodes. *J. Phys. Chem. B* **1997**, 101 (12), 2195–2206. https://doi.org/10.1021/jp962815t.

(44) Sleigh, A.K.; von Sacken, U.; Unusual Cycling Behaviour of Disordered Carbons in Li/C Cells. *Solid State Ion.* **1992**, 57 (1–2), 99–102. https://doi.org/10.1016/0167-2738(92)90069-2.

(45) Zhang, J.; Zhang, L.; Sun, F.; Wang, Z.; An Overview on Thermal Safety Issues of Lithium-Ion Batteries for Electric Vehicle Application. *IEEE Access* **2018**, 6, 23848–23863. https://doi.org/10.1109/ACCESS.2018.2824838.

(46) Scrosati, B.; van Schalkwijk, W.A.; *Advances in Lithium-Ion Batteries*; 2002.

(47) Nazri, G.-A.; Pistoia, G.; *Lithium Batteries - Science and Technology*; 2009.

(48) Philippe, B.; Hahlin, M.; Edström, K.; Gustafsson, T.; Siegbahn, H.; Rensmo, H.; Photoelectron Spectroscopy for Lithium Battery Interface Studies. *J. Electrochem. Soc.* **2016**, 163 (2), A178–A191. https://doi.org/10.1149/2.0051602jes.

(49) Schmuch, R.; Wagner, R.; Hörpel, G.; Placke, T.; Winter, M.; Performance and Cost of Materials for Lithium-Based Rechargeable Automotive Batteries. *Nat. Energy* **2018**, 3 (4), 267–278. https://doi.org/10.1038/s41560-018-0107-2.

(50) Johnson, W.B.; Worrell, W.L. Lithium and Sodium Intercalated Dichalcogenides: Properties and Electrode Applications. *Synth. Met.* **1982**, 4 (3), 225–248. https://doi.org/10.1016/0379-6779(82)90015-7.

(51) Delmas, C.; Braconnier, J.-J.; Fouassier, C.; Hagenmuller, P.; Electrochemical Intercalation of Sodium in Na_xCoO_2 Bronzes. *Solid State Ion.* **1981**, 3–4, 165–169. https://doi.org/10.1016/0167-2738(81)90076-X.

(52) Braconnier, J.-J.; Delmas, C.; Hagenmuller, P.; Etude Par Desintercalation Electrochimique Des Systemes Na_xCrO_2 et Na_xNiO_2. *Mater. Res. Bull.* **1982**, 17 (8), 993–1000. https://doi.org/10.1016/0025-5408(82)90124-6.

(53) Yazami, R.; Touzain, P.; A Reversible Graphite-Lithium Negative Electrode for Electrochemical Generators. *J. Power Sources* **1983**, 9 (3), 365–371. https://doi.org/10.1016/0378-7753(83)87040-2.

(54) Ge, P.; Fouletier, M.; Electrochemical Intercalation of Sodium in Graphite. *Solid State Ionics* **1988**, 28–30, 1172–1175.

(55) Han, M.H.; Gonzalo, E.; Singh, G.; Rojo, T.; A Comprehensive Review of Sodium Layered Oxides: Powerful Cathodes for Na-Ion Batteries. *Energy Environ. Sci.* **2015**, 8 (1), 81–102. https://doi.org/10.1039/c4ee03192j.

(56) Oshima, T.; Kajita, M.; Okuno, A.; Development of Sodium-Sulfur Batteries. *Int. J. Appl. Ceram. Technol.* **2004**, 1, 269–276. https://doi.org/10.1111/j.1744-7402.2004.tb00179.x.

(57) Sudworth, J.L.; Zebra Batteries. *J. Power Sources* **1994**, 51 (1–2), 105–114. https://doi.org/10.1016/0378-7753(94)01967-3.

(58) Benato, R.; Cosciani, N.; Crugnola, G.; Dambone Sessa, S.; Lodi, G.; Parmeggiani, C.; Todeschini, M.; Sodium Nickel Chloride Battery Technology for Large-Scale Stationary Storage in the High Voltage Network. *J. Power Sources* **2015**, 293, 127–136. https://doi.org/10.1016/j.jpowsour.2015.05.037.

(59) Stevens, D.A.; Dahn, J.R.; High Capacity Anode Materials for Rechargeable Sodium-Ion Batteries. *J. Electrochem. Soc.* **2000**, 147 (4), 1271. https://doi.org/10.1149/1.1393348.

(60) Stevens, D.A.; Dahn, J.R.; The Mechanisms of Lithium and Sodium Insertion in Carbon Materials. *J. Electrochem. Soc.* **2001**, 148 (8), A803. https://doi.org/10.1149/1.1379565.

(61) Delmas, C.; Sodium and Sodium-Ion Batteries: 50 Years of Research. *Adv. Energy Mater.* **2018**, 8 (17), 1–9. https://doi.org/10.1002/aenm.201703137.

(62) Olivetti, E.A.; Ceder, G.; Gaustad, G.G.; Fu, X.; Lithium-Ion Battery Supply Chain Considerations : Analysis of Potential Bottlenecks in Critical Metals. *Joule* **2017**, 1 (2), 229–243. https://doi.org/10.1016/j.joule.2017.08.019.

(63) Zubi, G.; Dufo-López, R.; Carvalho, M.; Pasaoglu, G.; The Lithium-Ion Battery: State of the Art and Future Perspectives. *Renew. Sustain. Energy Rev.* **2018**, 89, 292–308. https://doi.org/10.1016/j.rser.2018.03.002.

(64) Chen, T.; Jin, Y.; Lv, H.; Yang, A.; Liu, M.; Chen, B.; Xie, Y.; Chen, Q.; Applications of Lithium-Ion Batteries in Grid-Scale Energy Storage Systems. *Trans. Tianjin Univ.* **2020**, 26 (3), 208–217. https://doi.org/10.1007/s12209-020-00236-w.

(65) Ponrouch, A.; Palacín, M.R.; Post-Li Batteries : Promises and Challenges. *Philos. Transitions A* **2019**, 377, 2152. https://doi.org/10.1098/rsta.2018.0297.

(66) Mogensen, R.; Brandell, D.; Younesi, R.; Solubility of the Solid Electrolyte Interphase (SEI) in Sodium Ion Batteries. *ACS Energy Lett.* **2016**, 1 (6), 1173–1178. https://doi.org/10.1021/acsenergylett.6b00491.

(67) Kundu, D.; Talaie, E.; Duffort, V.; Nazar, L.F.; The Emerging Chemistry of Sodium Ion Batteries for Electrochemical Energy Storage. *Angew. Chemie - Int. Ed.* **2015**, 54 (11), 3432–3448. https://doi.org/10.1002/anie.201410376.

(68) Sawicki, M.; Shaw, L.L.; Advances and Challenges of Sodium Ion Batteries as Post Lithium Ion Batteries. *RSC Adv.* **2015**, 5 (65), 53129–53154. https://doi.org/10.1039/c5ra08321d.

(69) Hwang, J.Y.; Myung, S.T.; Sun, Y.K.; Sodium-Ion Batteries: Present and Future. *Chem. Soc. Rev.* **2017**, 46 (12), 3529–3614. https://doi.org/10.1039/c6cs00776g.

(70) Palacín, M.R.; Recent Advances in Rechargeable Battery Materials: A Chemist's Perspective. *Chem. Soc. Rev.* **2009**, 38 (9), 2565–2575. https://doi.org/10.1039/b820555h.

(71) Chung, D.D.L.; Review: Graphite. *J. Mater. Sci.* **2002**, 37 (8), 1475–1489. https://doi.org/10.1023/A:1014915307738.

(72) Shi, H.; Barker, J.; Saïdi, M.Y.; Koksbang, R.; Structure and Lithium Intercalation Properties of Synthetic and Natural Graphite. *J. Electrochem. Soc.* **1996**, 143 (11), 3466–3472. https://doi.org/10.1149/1.1837238.

(73) Tran, T.; Kinoshita, K.; Lithium Intercalation/Deintercalation Behavior of Basal and Edge Planes of Highly Oriented Pyrolytic Graphite and Graphite Powder. *J. Electroanal. Chem.* **1995**, 386 (1–2), 221–224. https://doi.org/10.1016/0022-0728(95)03907-X.

(74) Asenbauer, J.; Eisenmann, T.; Kuenzel, M.; Kazzazi, A.; Chen, Z.; Bresser, D.; The Success Story of Graphite as a Lithium-Ion Anode Material - Fundamentals, Remaining Challenges, and Recent Developments Including Silicon (Oxide) Composites. *Sustain. Energy Fuels* **2020**, 4 (11), 5387–5416. https://doi.org/10.1039/d0se00175a.

(75) Hofmann, U.; Rudorff, W.; The Formation of Salts from Graphite by Strong Acids. *Trans. Faraday Soc.* **1938**, 34, 1017–1021. https://doi.org/10.1039/TF9383401017.

(76) Rüdorff, W.; Hofmann, U. Über Graphitsalze. *Zeitschrift für Anorg. und Allg. Chemie* **1938**, 238 (1), 1–50. https://doi.org/10.1002/zaac.19382380102.

(77) Dahn, J.R.; Phase Diagram of Li_xC_6. *Phys. Rev. B* **1991**, *44* (17), 9170–9177.

https://doi.org/10.1103/PhysRevB.44.9170.

(78) Senyshyn, A.; Dolotko, O.; Mühlbauer, M.J.; Nikolowski, K.; Fuess, H.; Ehrenberg, H.; Lithium Intercalation into Graphitic Carbons Revisited: Experimental Evidence for Twisted Bilayer Behavior. *J. Electrochem. Soc.* **2013**, 160 (5), A3198–A3205. https://doi.org/10.1149/2.031305jes.

(79) Heß, M.; Novák, P.; Shrinking Annuli Mechanism and Stage-Dependent Rate Capability of Thin-Layer Graphite Electrodes for Lithium-Ion Batteries. *Electrochim. Acta* **2013**, 106, 149–158. https://doi.org/10.1016/j.electacta.2013.05.056.

(80) Song, X.Y.; Kinoshita, K.;Tran, T.D.; Microstructural Characterization of Lithiated Graphite. *J. Electrochem. Soc.* **1996**, 143 (6), L120. https://doi.org/10.1149/1.1836896.

(81) Nobuhara, K.; Nakayama, H.; Nose, M.; Nakanishi, S.; Iba, H.; First-Principles Study of Alkali Metal-Graphite Intercalation Compounds. *J. Power Sources* **2013**, 243, 585–587. https://doi.org/10.1016/j.jpowsour.2013.06.057.

(82) Fredenhagen, K.; Cadenbach, G.; Die Bindung von Kalium Durch Kohlenstoff. *Zeitschrift für Anorg. und Allg. Chemie* **1926**, 158 (1), 249–263. https://doi.org/10.1002/zaac.19261580122.

(83) Rüdorff, W.; Schulze, E.; Über Alkaligraphitverbindungen. *ZAAC - J. Inorg. Gen. Chem.* **1954**, 277 (3–4), 156–171. https://doi.org/10.1002/zaac.19542770307.

(84) Wan, W.; Wang, H.; Study on the First-Principles Calculations of Graphite Intercalated by Alkali Metal (Li, Na, K). *Int. J. Electrochem. Sci.* **2015**, 10 (4), 3177–3184.

(85) Liu, Y.; Merinov, B.V.; Goddard, W.A.; Origin of Low Sodium Capacity in Graphite and Generally Weak Substrate Binding of Na and Mg among Alkali and Alkaline Earth Metals. *Proc. Natl. Acad. Sci. U.S.A.* **2016**, 113 (14), 3735–3739. https://doi.org/10.1073/pnas.1602473113.

(86) Hasa, I.; Dou, X.; Buchholz, D.; Shao-Horn, Y.; Hassoun, J.; Passerini, S.; Scrosati, B.; A Sodium-Ion Battery Exploiting Layered Oxide Cathode, Graphite Anode and Glyme-Based Electrolyte. *J. Power Sources* **2016**, 310, 26–31. https://doi.org/10.1016/j.jpowsour.2016.01.082.

(87) Kim, H.; Hong, J.; Yoon, G.; Kim, H.; Park, K.Y.; Park, M.S.; Yoon, W.S.; Kang, K.; Sodium Intercalation Chemistry in Graphite. *Energy Environ. Sci.* **2015**, 8 (10), 2963–2969. https://doi.org/10.1039/c5ee02051d.

(88) Dahbi, M.; Yabuuchi, N.; Kubota, K.; Tokiwa, K.; Komaba, S.; Negative Electrodes for Na-Ion Batteries. *Phys. Chem. Chem. Phys.* **2014**, 16 (29), 15007–15028. https://doi.org/10.1039/c4cp00826j.

(89) Yabuuchi, N.; Kubota, K.; Dahbi, M.; Komaba, S.; Research Development on Sodium-Ion Batteries. *Chem. Rev.* **2014**, 114 (23), 11636–11682. https://doi.org/10.1021/cr500192f.

(90) Dou, X.; Hasa, I.; Hekmatfar, M.; Diemant, T.; Behm, R.J.; Buchholz, D.; Passerini, S.; Pectin, Hemicellulose, or Lignin? Impact of the Biowaste Source on the Performance of Hard Carbons for Sodium-Ion Batteries. *ChemSusChem* **2017**, 10 (12), 2668–2676. https://doi.org/10.1002/cssc.201700628.

(91) Lotfabad, E.M.; Ding, J.; Cui, K.; Kohandehghan, A.; Kalisvaart, W.P.; Hazelton, M.; Mitlin, D.; High-Density Sodium and Lithium Ion Battery Anodes from Banana Peels. *ACS Nano* **2014**, 8 (7), 7115–7129. https://doi.org/10.1021/nn502045y.

(92) Hou, H.; Qiu, X.; Wei, W.; Zhang, Y.; Ji, X.; Carbon Anode Materials for Advanced Sodium-Ion Batteries. *Adv. Energy Mater.* **2017**, *7 (*24), 1–30. https://doi.org/10.1002/aenm.201602898.

(93) Marsh, H.; Rodrìguez-Reinoso, F.; *Activated Carbon*; 2006.

(94) Montoya, V.H.; Bonilla-Petriciolet, A.; *Lignocellulosic Precursors Used in the Synthesis of Activated Carbon*; InTech, 2012.

(95) Qiu, S.; Xiao, L.; Sushko, M.L.; Han, K.S.; Shao, Y.; Yan, M.; Liang, X.; Mai, L.; Feng, J.; Cao, Y.; Ai, X.; Yang, H.; Liu, J.; Manipulating Adsorption–Insertion Mechanisms in Nanostructured Carbon Materials for High-Efficiency Sodium Ion Storage. *Adv. Energy Mater.* **2017**, 7 (17), 1–11.

https://doi.org/10.1002/aenm.201700403.

(96) Tsai, P.C.; Chung, S.C.; Lin, S.K.; Yamada, A.; Ab Initio Study of Sodium Intercalation into Disordered Carbon. *J. Mater. Chem. A* **2015**, 3 (18), 9763–9768. https://doi.org/10.1039/c5ta01443c.

(97) Li, Z.; Bommier, C.; Chong, Z. Sen; Jian, Z.; Surta, T.W.; Wang, X.; Xing, Z.; Neuefeind, J.C.; Stickle, W.F.; Dolgos, M.; Greaney, P.A.; Ji, X.; Mechanism of Na-Ion Storage in Hard Carbon Anodes Revealed by Heteroatom Doping. *Adv. Energy Mater.* **2017**, 7 (18), 1–10. https://doi.org/10.1002/aenm.201602894.

(98) Franklin, R.E.; Crystallite Growth in Graphitizing and Non-Graphitizing Carbons. *Proc. R. Soc. London. Ser. A. Math. Phys. Sci.* **1951**, 209 (1097), 196–218. https://doi.org/10.1098/rspa.1951.0197.

(99) Harris, P.J.F.; New Perspectives on the Structure of Graphitic Carbons. *Crit. Rev. Solid State Mater. Sci.* **2005**, 30 (4), 235–253. https://doi.org/10.1080/10408430500406265.

(100) Robinson, J.T.; Zalalutdinov, M.K.; Cress, C.D.; Culbertson, J.C.; Friedman, A.L.; Merrill, A.; Landi, B.J.; Graphene Strained by Defects. *ACS Nano* **2017**, 11 (5), 4745–4752. https://doi.org/10.1021/acsnano.7b00923.

(101) Wang, H.M.; Wang, H.X.; Chen, Y.; Liu, Y.J.; Zhao, J.X.; Cai, Q.H.; Wang, X.Z.; Phosphorus-Doped Graphene and (8, 0) Carbon Nanotube: Structural, Electronic, Magnetic Properties, and Chemical Reactivity. *Appl. Surf. Sci.* **2013**, 273 (2), 302–309. https://doi.org/10.1016/j.apsusc.2013.02.035.

(102) Ban, L.L.; Crawford, D.; Marsh, H.; Lattice-Resolution Electron Microscopy in Structural Studies of Non-Graphitizing Carbons from Polyvinylidene Chloride (PVDC). *J. Appl. Crystallogr.* **1975**, *8 (*4), 415–420. https://doi.org/10.1107/s0021889875010904.

(103) Townsend, S.J.; Lenosky, T.J.; Muller, D.A.; Nichols, C.S.; Elser, V.; Negatively Curved Graphitic Sheet Model of Amorphous Carbon. *Phys. Rev. Lett.* **1992**, 69 (6), 921–924. https://doi.org/10.1103/PhysRevLett.69.921.

(104) Terzyk, A.P.; Furmaniak, S.; Harris, P.J.F.; Gauden, P.A.; Włoch, J.; Kowalczyk, P.; Rychlicki, G.; How Realistic Is the Pore Size Distribution Calculated from Adsorption Isotherms If Activated Carbon Is Composed of Fullerene-like Fragments? *Phys. Chem. Chem. Phys.* **2007**, 9 (44), 5919–5927. https://doi.org/10.1039/b710552e.

(105) Xu, D.; Chen, C.; Xie, J.; Zhang, B.; Miao, L.; Cai, J.; Huang, Y.; Zhang, L.; A Hierarchical N/S-Codoped Carbon Anode Fabricated Facilely from Cellulose/Polyaniline Microspheres for High-Performance Sodium-Ion Batteries. *Adv. Energy Mater.* **2016**, 6 (6), 1–7. https://doi.org/10.1002/aenm.201501929.

(106) Reddy, M.A.; Helen, M.; Groß, A.; Fichtner, M.; Euchner, H.; Insight into Sodium Insertion and the Storage Mechanism in Hard Carbon. *ACS Energy Lett.* **2018**, 3 (12), 2851–2857. https://doi.org/10.1021/acsenergylett.8b01761.

(107) Bommier, C.; Surta, T.W.; Dolgos, M.; Ji, X.; New Mechanistic Insights on Na-Ion Storage in Nongraphitizable Carbon. *Nano Lett.* **2015**, 15 (9), 5888–5892. https://doi.org/10.1021/acs.nanolett.5b01969.

(108) Stratford, J.M.; Allan, P.K.; Pecher, O.; Chater, P.A.; Grey, C.P.; Mechanistic Insights into Sodium Storage in Hard Carbon Anodes Using Local Structure Probes. *Chem. Commun.* **2016**, 52 (84), 12430–12433. https://doi.org/10.1039/c6cc06990h.

(109) Dou, X.; Geng, C.; Buchholz, D.; Passerini, S.; Research Update: Hard Carbon with Closed Pores from Pectin-Free Apple Pomace Waste for Na-Ion Batteries. *APL Mater.* **2018**, 6 (4), 0–5. https://doi.org/10.1063/1.5013132.

(110) Bommier, C.; Luo, W.; Gao, W.Y.; Greaney, A.; Ma, S.; Ji, X.; Predicting Capacity of Hard Carbon Anodes in Sodium-Ion Batteries Using Porosity Measurements. *Carbon* **2014**, 76, 165–174. https://doi.org/10.1016/j.carbon.2014.04.064.

(111) Xie, F.; Xu, Z.; Guo, Z.; Titirici, M.M.; Hard Carbons for Sodium-Ion Batteries and Beyond. *Prog. Energy*

2020, 2 (4). https://doi.org/10.1088/2516-1083/aba5f5.

(112) Cao, Y.; Xiao, L.; Sushko, M.L.; Wang, W.; Schwenzer, B.; Xiao, J.; Nie, Z.; Saraf, L.V.; Yang, Z.; Liu, J.; Sodium Ion Insertion in Hollow Carbon Nanowires for Battery Applications. *Nano Lett.* **2012**, 12 (7), 3783–3787. https://doi.org/https://doi.org/10.1021/nl3016957.

(113) Ding, J.; Wang, H.; Li, Z.; Kohandehghan, A.; Cui, K.; Xu, Z.; Zahiri, B.; Tan, X.; Lotfabad, E.M.; Olsen, B.C.; Mitlin, D.; Carbon Nanosheet Frameworks Derived from Peat Moss as High Performance Sodium Ion Battery Anodes. *ACS Nano* **2013**, 7 (12), 11004–11015. https://doi.org/10.1021/nn404640c.

(114) Zhang, B.; Ghimbeu, C.M.; Laberty, C.; Vix-Guterl, C.; Tarascon, J.M.; Correlation between Microstructure and Na Storage Behavior in Hard Carbon. *Adv. Energy Mater.* **2016**, 6 (1), 1–9. https://doi.org/10.1002/aenm.201501588.

(115) Li, Y.; Hu, Y.S.; Titirici, M.M.; Chen, L.; Huang, X.; Hard Carbon Microtubes Made from Renewable Cotton as High-Performance Anode Material for Sodium-Ion Batteries. *Adv. Energy Mater.* **2016**, 6 (18). https://doi.org/10.1002/aenm.201600659.

(116) Yuan, C.; Wu, H. Bin; Xie, Y.; Lou, X.W.; Mixed Transition-Metal Oxides: Design, Synthesis, and Energy-Related Applications. *Angew. Chemie - Int. Ed.* **2014**, 53 (6), 1488–1504. https://doi.org/10.1002/anie.201303971.

(117) Xu, X.; Liu, W.; Kim, Y.; Cho, J.; Nanostructured Transition Metal Sulfides for Lithium Ion Batteries: Progress and Challenges. *Nano Today* **2014**, 9 (5), 604–630. https://doi.org/10.1016/j.nantod.2014.09.005.

(118) Dong, S.; Chen, X.; Zhang, X.; Cui, G.; Nanostructured Transition Metal Nitrides for Energy Storage and Fuel Cells. *Coord. Chem. Rev.* **2013**, 257 (13–14), 1946–1956. https://doi.org/10.1016/j.ccr.2012.12.012.

(119) Park, D.Y.; Sun, Y.K.; Myung, S.T.; Carbothermal Synthesis of Molybdenum(IV) Oxide as a High Rate Anode for Rechargeable Lithium Batteries. *J. Power Sources* **2015**, 280, 1–4. https://doi.org/10.1016/j.jpowsour.2015.01.042.

(120) Carbonari, G.; Maroni, F.; Gabrielli, S.; Staffolani, A.; Tossici, R.; Palmieri, A.; Nobili, F.; Synthesis and Characterization of Vanillin-Templated Fe_2O_3 Nanoparticles as a Sustainable Anode Material for Li-Ion Batteries. *ChemElectroChem* **2019**, 6 (6), 1915–1920. https://doi.org/10.1002/celc.201900189.

(121) Staffolani, A.; Darjazi, H.; Carbonari, G.; Maroni, F.; Gabrielli, S.; Nobili, F.; Fe_3O_4/Graphene Composite Anode Material for Fast-Charging Li-Ion Batteries. *Molecules* **2021**, 26 (14), 4316.

(122) Aricò, A.S.; Bruce, P.; Scrosati, B.; Tarascon, J.M.; van Schalkwijk, W.A.; Nanostructured Materials for Advanced Energy Conversion and Storage Devices. *Nat. Mater.* **2005**, 4, 366–377. https://doi.org/https://doi.org/10.1038/nmat1368.

(123) Yu, X.Y.; Yu, L.; Lou, X.W.; Metal Sulfide Hollow Nanostructures for Electrochemical Energy Storage. *Adv. Energy Mater.* **2016**, 6 (3), 1–14. https://doi.org/10.1002/aenm.201501333.

(124) Zhu, G.N.; Wang, Y.G.; Xia, Y.Y.; Ti-Based Compounds as Anode Materials for Li-Ion Batteries. *Energy Environ. Sci.* **2012**, 5 (5), 6652–6667. https://doi.org/10.1039/c2ee03410g.

(125) Zhang, L.; Wu, H.B.; Lou, X.W.; Iron-Oxide-Based Advanced Anode Materials for Lithium-Ion Batteries. *Adv. Energy Mater.* **2014**, 4 (4), 1–11. https://doi.org/10.1002/aenm.201300958.

(126) Cabana, J.; Monconduit, L.; Larcher, D.; Palacín, M.R.; Beyond Intercalation-Based Li-Ion Batteries: The State of the Art and Challenges of Electrode Materials Reacting through Conversion Reactions. *Adv. Mater.* **2010**, 22 (35), 170–192. https://doi.org/10.1002/adma.201000717.

(127) Puthusseri, D.; Wahid, M.; Ogale, S.; Conversion-Type Anode Materials for Alkali-Ion Batteries: State of the Art and Possible Research Directions. *ACS Omega* **2018**, 3 (4), 4591–4601. https://doi.org/10.1021/acsomega.8b00188.

(128) Lowe, M.A.; Gao, J.; Abruña, H.D.; In Operando X-Ray Studies of the Conversion Reaction in Mn_3O_4 Lithium Battery Anodes. *J. Mater. Chem. A* **2013**, 1 (6), 2094–2103. https://doi.org/10.1039/c2ta01270g.

(129) Zhang, L.; Sun, D.; Kang, J.; Feng, J.; Bechtel, H.A.; Wang, L.W.; Cairns, E.J.; Guo, J.; Electrochemical Reaction Mechanism of the MoS_2 Electrode in a Lithium-Ion Cell Revealed by in Situ and Operando X-Ray Absorption Spectroscopy. *Nano Lett.* **2018**, 18 (2), 1466–1475. https://doi.org/10.1021/acs.nanolett.7b05246.

(130) Zhao, Z.W.; Wen, T.; Liang, K.; Jiang, Y.F.; Zhou, X.; Shen, C.C.; Xu, A.W.; Carbon-Coated Fe_3O_4/VO_x Hollow Microboxes Derived from Metal-Organic Frameworks As a High-Performance Anode Material for Lithium-Ion Batteries. *ACS Appl. Mater. Interfaces* **2017**, 9 (4), 3757–3765. https://doi.org/10.1021/acsami.6b15110.

(131) Lu, J.; Chen, Z.; Pan, F.; Cui, Y.; Amine, K.; High-Performance Anode Materials for Rechargeable Lithium-Ion Batteries. *Electrochem. Energy Rev.* **2018**, 1 (1), 35–53. https://doi.org/10.1007/s41918-018-0001-4.

(132) Poizot, P.; Laruelle, S.; Grugeon, S.; Dupont, L.; Tarascon, J.M.; Nano-Sized Transition-Metal Oxides as Negative-Electrode Materials for Lithium-Ion Batteries. *Nature* **2000**, 407 (6803), 496–499. https://doi.org/10.1038/35035045.

(133) Bresser, D.; Passerini, S.; Scrosati, B.; Leveraging Valuable Synergies by Combining Alloying and Conversion for Lithium-Ion Anodes. *Energy Environ. Sci.* **2016**, 9 (11), 3348–3367. https://doi.org/10.1039/c6ee02346k.

(134) Kitaura, H.; Takahashi, K.; Mizuno, F.; Hayashi, A.; Tadanaga, K.; Tatsumisago, M.; Mechanochemical Synthesis of α-Fe_2O_3 Nanoparticles and Their Application to All-Solid-State Lithium Batteries. *J. Power Sources* **2008**, 183 (1), 418–421. https://doi.org/10.1016/j.jpowsour.2008.05.032.

(135) Butala, M.M.; Danks, K.R.; Lumley, M.A.; Zhou, S.; Melot, B.C.; Seshadri, R.; MnO Conversion in Li-Ion Batteries: In Situ Studies and the Role of Mesostructuring. *ACS Appl. Mater. Interfaces* **2016**, *8 (*10), 6496–6503. https://doi.org/10.1021/acsami.5b12840.

(136) Chen, G.; Yan, L.; Luo, H.; Guo, S.; Nanoscale Engineering of Heterostructured Anode Materials for Boosting Lithium-Ion Storage. *Adv. Mater.* **2016**, 28 (35), 7580–7602. https://doi.org/10.1002/adma.201600164.

(137) Li, L.; Jacobs, R.; Gao, P.; Gan, L.; Wang, F.; Morgan, D.; Jin, S.; Origins of Large Voltage Hysteresis in High-Energy-Density Metal Fluoride Lithium-Ion Battery Conversion Electrodes. *J. Am. Chem. Soc.* **2016**, 138 (8), 2838–2848. https://doi.org/10.1021/jacs.6b00061.

(138) Kim, H.; Kim, H.; Kim, H.; Kim, J.; Yoon, G.; Lim, K.; Yoon, W.S.; Kang, K.; Understanding Origin of Voltage Hysteresis in Conversion Reaction for Na Rechargeable Batteries: The Case of Cobalt Oxides. *Adv. Funct. Mater.* **2016**, 26 (28), 5042–5050. https://doi.org/10.1002/adfm.201601357.

(139) Larcher, D.; Masquelier, C.; Bonnin, D.; Chabre, Y.; Masson, V.; Leriche, J.B.; Tarascon, J.M.; Effect of Particle Size on Lithium Intercalation into α-Fe_2O_3. *J. Electrochem. Soc.* **2003**, 150 (1), A133. https://doi.org/10.1149/1.1528941.

(140) Wang, X.; Chen, X.; Gao, L.; Zheng, H.; Zhang, Z.; Qian, Y.; One-Dimensional Arrays of Co_3O_4 Nanoparticles: Synthesis, Characterization, and Optical and Electrochemical Properties.; *J. Phys. Chem. B* **2004**, 108 (42), 16401–16404. https://doi.org/10.1021/jp048016p.

(141) Zhao, Y.; Wang, L.P.; Sougrati, M.T.; Feng, Z.; Leconte, Y.; Fisher, A.; Srinivasan, M.; Xu, Z.; A Review on Design Strategies for Carbon Based Metal Oxides and Sulfides Nanocomposites for High Performance Li and Na Ion Battery Anodes. *Adv. Energy Mater.* **2017**, 7 (9). https://doi.org/10.1002/aenm.201601424.

(142) Liu, H.; Liu, X.; Li, W.; Guo, X.; Wang, Y.; Wang, G.; Zhao, D.; Porous Carbon Composites for Next Generation Rechargeable Lithium Batteries. *Adv. Energy Mater.* **2017**, 7 (24), 1–24. https://doi.org/10.1002/aenm.201700283.

(143) Choi, S.H.; Lee, J.H.; Kang, Y.C.; Perforated Metal Oxide-Carbon Nanotube Composite Microspheres with Enhanced Lithium-Ion Storage Properties. *ACS Nano* **2015**, 9 (10), 10173–10185. https://doi.org/10.1021/acsnano.5b03822.

(144) Wu, D.; Shen, R.; Yang, R.; Ji, W.; Jiang, M.; Ding, W.; Peng, L.; Mixed Molybdenum Oxides with Superior Performances as an Advanced Anode Material for Lithium-Ion Batteries. *Sci. Rep.* **2017**, 7, 1–9. https://doi.org/10.1038/srep44697.

(145) Klein, F.; Jache, B.; Bhide, A.; Adelhelm, P.; Conversion Reactions for Sodium-Ion Batteries. *Phys. Chem. Chem. Phys.* **2013**, 15 (38), 15876–15887. https://doi.org/10.1039/c3cp52125g.

(146) Zheng, X.; Li, J.; A Review of Research on Hematite as Anode Material for Lithium-Ion Batteries. *Ionics* **2014**, 20 (12), 1651–1663. https://doi.org/10.1007/s11581-014-1262-5.

(147) Akhlaghi, N.; Najafpour-Darzi, G.; Manganese Ferrite ($MnFe_2O_4$) Nanoparticles: From Synthesis to Application - A Review. *J. Ind. Eng. Chem.* **2021**, 103, 292–304. https://doi.org/10.1016/j.jiec.2021.07.043.

(148) Liu, Y.; Zhang, N.; Yu, C.; Jiao, L.; Chen, J.; $MnFe_2O_4$@C Nanofibers as High-Performance Anode for Sodium-Ion Batteries. *Nano Lett.* **2016**, 16 (5), 3321–3328. https://doi.org/10.1021/acs.nanolett.6b00942.

(149) Bhattacharjya, D.; Sinhamahapatra, A.; Ko, J.J.; Yu, J.S.; High Capacity and Exceptional Cycling Stability of Ternary Metal Sulfide Nanorods as Li Ion Battery Anodes. *Chem. Commun.* **2015**, 51 (69), 13350–13353. https://doi.org/10.1039/c5cc04289e.

(150) Wang, X.; Kim, H.M.; Xiao, Y.; Sun, Y.K.; Nanostructured Metal Phosphide-Based Materials for Electrochemical Energy Storage. *J. Mater. Chem. A* **2016**, 4 (39), 14915–14931. https://doi.org/10.1039/c6ta06705k.

(151) Wang, Q.; Zhao, C.; Lu, Y.; Li, Y.; Zheng, Y.; Qi, Y.; Rong, X.; Jiang, L.; Qi, X.; Shao, Y.; Pan, D.; Li, B.; Hu, Y.S.; Chen, L. Advanced Nanostructured Anode Materials for Sodium-Ion Batteries. *Small* **2017**, 13 (42), 1–32. https://doi.org/10.1002/smll.201701835.

(152) Zhang, W.J.; A Review of the Electrochemical Performance of Alloy Anodes for Lithium-Ion Batteries. *J. Power Sources* **2011**, 196 (1), 13–24. https://doi.org/10.1016/j.jpowsour.2010.07.020.

(153) Obrovac, M.N.; Chevrier, V.L.; Alloy Negative Electrodes for Li-Ion Batteries. *Chem. Rev.* **2014**, 114 (23), 11444–11502. https://doi.org/10.1021/cr500207g.

(154) Ding, Y.L.; Wu, C.; Kopold, P.; Van Aken, P.A.; Maier, J.; Yu, Y.; Graphene-Protected 3D Sb-Based Anodes Fabricated via Electrostatic Assembly and Confinement Replacement for Enhanced Lithium and Sodium Storage. *Small* **2015**, 11 (45), 6026–6035. https://doi.org/10.1002/smll.201502000.

(155) Loeffler, B.N.; Bresser, D.; Passerini, S.; Copley, M.; Secondary Lithium-Ion Battery Anodes: From First Commercial Batteries to Recent Research Activities. *Johnson Matthey Technol. Rev.* **2015**, 59 (1), 34–44. https://doi.org/10.1595/205651314x685824.

(156) Li, J.Y.; Xu, Q.; Li, G.; Yin, Y.X.; Wan, L.J.; Guo, Y.G.; Research Progress Regarding Si-Based Anode Materials towards Practical Application in High Energy Density Li-Ion Batteries. *Mater. Chem. Front.* **2017**, 1 (9), 1691–1708. https://doi.org/10.1039/c6qm00302h.

(157) Ji, L.; Lin, Z.; Alcoutlabi, M.; Zhang, X.; Recent Developments in Nanostructured Anode Materials for Rechargeable Lithium-Ion Batteries. *Energy Environ. Sci.* **2011**, 4 (8), 2682–2689. https://doi.org/10.1039/c0ee00699h.

(158) Winter, M.; Besenhard, J.O.; Electrochemical Lithiation of Tin and Tin-Based Intermetallics and Composites. *Electrochim. Acta* **1999**, 45 (1), 31–50. https://doi.org/10.1016/S0013-4686(99)00191-7.

(159) Wang, J.W.; Liu, X.H.; Mao, S.X.; Huang, J.Y.; Microstructural Evolution of Tin Nanoparticles during in Situ Sodium Insertion and Extraction. *Nano Lett.* **2012**, 12 (11), 5897–5902. https://doi.org/10.1021/nl303305c.

(160) Chevrier, V.L.; Ceder, G.; Challenges for Na-Ion Negative Electrodes. *J. Electrochem. Soc.* **2011**, 158 (9), A1011. https://doi.org/10.1149/1.3607983.

(161) Darwiche, A.; Marino, C.; Sougrati, M.T.; Fraisse, B.; Stievano, L.; Monconduit, L.; Better Cycling Performances of Bulk Sb in Na-Ion Batteries Compared to Li-Ion Systems: An Unexpected Electrochemical Mechanism. *J. Am. Chem. Soc.* **2013**, 135 (27), 10179. https://doi.org/10.1021/ja4056195.

(162) Su, X.; Wu, Q.; Li, J.; Xiao, X.; Lott, A.; Lu, W.; Sheldon, B.W.; Wu, J.; Silicon-Based Nanomaterials for Lithium-Ion Batteries: A Review. *Adv. Energy Mater.* **2014**, 4 (1), 1–23. https://doi.org/10.1002/aenm.201300882.

(163) Kang, K.; Lee, H.S.; Han, D.W.; Kim, G.S.; Lee, D.; Lee, G.; Kang, Y.M.; Jo, M.H.; Maximum Li Storage in Si Nanowires for the High Capacity Three-Dimensional Li-Ion Battery. *Appl. Phys. Lett.* **2010**, 96 (5). https://doi.org/10.1063/1.3299006.

(164) Zhang, L.; Liu, X.; Zhao, Q.; Dou, S.; Liu, H.; Si-Containing Precursors for Si-Based Anode Materials of Li-Ion Batteries : A Review. *Energy Storage Mater.* **2016**, 4, 92–102. https://doi.org/10.1016/j.ensm.2016.01.011.

(165) Tian, H.; Xin, F.; Wang, X.; He, W.; Han, W.; High Capacity Group-IV Elements (Si, Ge, Sn) Based Anodes for Lithium-Ion Batteries. *J. Mater.* **2015**, 1 (3), 153–169. https://doi.org/10.1016/j.jmat.2015.06.002.

(166) Ellis, L.D.; Wilkes, B.N.; Hatchard, T.D.; Obrovac, M.N.; In Situ XRD Study of Silicon, Lead and Bismuth Negative Electrodes in Nonaqueous Sodium Cells. *J. Electrochem. Soc.* **2014**, 161 (3), 416–421. https://doi.org/10.1149/2.080403jes.

(167) Liang, S.; Cheng, Y.J.; Zhu, J.; Xia, Y.; Müller-Buschbaum, P.; A Chronicle Review of Nonsilicon (Sn, Sb, Ge)-Based Lithium/Sodium-Ion Battery Alloying Anodes. *Small Methods* **2020**, *4* (8). https://doi.org/10.1002/smtd.202000218.

(168) Wu, X. L.; Guo, Y. G.; Wan, L. J. Rational Design of Anode Materials Based on Group IVA Elements (Si, Ge, and Sn) for Lithium-Ion Batteries. *Chem. - An Asian J.* **2013**, 8 (9), 1948–1958. https://doi.org/10.1002/asia.201300279.

(169) Julien, C.M.; Mauger, A.; Zaghib, K.; Groult, H.; Comparative Issues of Cathode Materials for Li-Ion Batteries. *Inorganics* **2014**, 2 (1), 132–154. https://doi.org/10.3390/inorganics2010132.

(170) Slater, M.D.; Kim, D.; Lee, E.; Johnson, C.S.; Sodium-Ion Batteries. *Adv. Funct. Mater.* **2013**, 23 (8), 947–958. https://doi.org/10.1002/adfm.201200691.

(171) You, Y.; Manthiram, A.; Progress in High-Voltage Cathode Materials for Rechargeable Sodium-Ion Batteries. *Adv. Energy Mater.* **2018**, 8 (2), 1–11. https://doi.org/10.1002/aenm.201701785.

(172) Laubach, S.; Laubach, S.; Schmidt, P.C.; Ensling, D.; Schmid, S.; Jaegermann, W.; Thissen, A.; Nikolowski, K.; Ehrenberg, H.; Changes in the Crystal and Electronic Structure of $LiCoO_2$ and $LiNiO_2$ upon Li Intercalation and De-Intercalation. *Phys. Chem. Chem. Phys.* **2009**, 11, 3278–3289. https://doi.org/10.1039/B901200A.

(173) Arroyo y de Dompablo, M.E.; Marianetti, C.; Van der Ven, A.; Ceder, G.; Jahn-Teller Mediated Ordering in Layered Li_xMO_2 Compounds. *Phys. Rev. B - Condens. Matter Mater. Phys.* **2001**, 63 (14), 1–9. https://doi.org/10.1103/PhysRevB.63.144107.

(174) Reimers, J.N.; Dahn, J.R.; Electrochemical and In Situ X-Ray Diffraction Studies of Lithium Intercalation in Li_xCoO_2. *J. Electrochem. Soc.* **1992**, 139 (8), 2091–2097. https://doi.org/10.1149/1.2221184.

(175) Van der Ven, A.; Aydinol, M.K.; Ceder, G.; Kresse, G.; Hafner, J.; First-Principles Investigation of Phase Stability in Li_xCoO_2. *Phys. Rev. B* **1998**, 58 (6), 2975–2987. https://doi.org/10.1103/PhysRevB.58.2975.

(176) Li, X.; Liu, J.; Meng, X.; Tang, Y.; Banis, M.N.; Yang, J.; Hu, Y.; Li, R.; Cai, M.; Sun, X.; Significant

Impact on Cathode Performance of Lithium-Ion Batteries by Precisely Controlled Metal Oxide Nanocoatings via Atomic Layer Deposition. *J. Power Sources* **2014**, 247, 57–69. https://doi.org/10.1016/j.jpowsour.2013.08.042.

(177) Li, X.; Liu, J.; Banis, M.N.; Lushington, A.; Li, R.; Cai, M.; Sun, X.; Atomic Layer Deposition of Solid-State Electrolyte Coated Cathode Materials with Superior High-Voltage Cycling Behavior for Lithium Ion Battery Application. *Energy Environ. Sci.* **2014**, 7 (2), 768–778. https://doi.org/10.1039/c3ee42704h.

(178) Yabuuchi, N.; Ohzuku, T.; Novel Lithium Insertion Material of $LiCo_{1/3}Ni_{1/3}Mn_{1/3}O_2$ for Advanced Lithium-Ion Batteries. *J. Power Sources* **2003**, 119–121, 171–174. https://doi.org/10.1016/S0378-7753(03)00173-3.

(179) Zhang, X.; Jiang, W.J.; Mauger, A.; Qilu; Gendron, F.; Julien, C.M.; Minimization of the Cation Mixing in $Li_{1+x}(NMC)_{1-x}O_2$ as Cathode Material. *J. Power Sources* **2010**, 195 (5), 1292–1301. https://doi.org/10.1016/j.jpowsour.2009.09.029.

(180) Delmas, C.; Fouassier, C.; Hagenmuller, P.; Structural Classification and Properties of the Layered Oxides. *Phys. B+C* **1980**, 99 (1–4), 81–85. https://doi.org/https://doi.org/10.1016/0378-4363(80)90214-4.

(181) Paulsen, J.M.; Dahn, J.R.; O2-Type $Li_{2/3}[Ni_{1/3}Mn_{2/3}]O_2$: A New Layered Cathode Material for Rechargeable Lithium Batteries II. Structure, Composition and Properties. *J. Electrochem. Soc.* **2000**, 147 (7), 2478. https://doi.org/10.1149/1.1393556.

(182) Lu, Z.; Dahn, J.R.; Can All the Lithium Be Removed from P2-$Li_{2/3}[Ni_{1/3}Mn_{2/3}]O_2$? *J. Electrochem. Soc.* **2001**, 148 (7), A710. https://doi.org/10.1149/1.1376116.

(183) Lu, Z.; Dahn, J.R.; In Situ X-Ray Diffraction Study of P2-$Na_{2/3}[Ni_{1/3}Mn_{2/3}]O_2$. *J. Electrochem. Soc.* **2001**, 148 (11), A1225. https://doi.org/10.1149/1.1407247.

(184) Wang, H.; Yang, B.; Liao, X.Z.; Xu, J.; Yang, D.; He, Y.S.; Ma, Z.F.; Electrochemical Properties of P2-$Na_{2/3}[Ni_{1/3}Mn_{2/3}]O_2$ Cathode Material for Sodium Ion Batteries When Cycled in Different Voltage Ranges. *Electrochim. Acta* **2013**, 113, 200–204. https://doi.org/10.1016/j.electacta.2013.09.098.

(185) Yabuuchi, N.; Yano, M.; Yoshida, H.; Kuze, S.; Komaba, S.; Synthesis and Electrode Performance of O3-Type $NaFeO_2$-$NaNi_{1/2}Mn_{1/2}O_2$ Solid Solution for Rechargeable Sodium Batteries . *J. Electrochem. Soc.* **2013**, 160 (5), A3131–A3137. https://doi.org/10.1149/2.018305jes.

(186) Xu, J.; Chou, S.L.; Wang, J.L.; Liu, H.K.; Dou, S.X.; Layered P2-$Na_{0.66}Fe_{0.5}Mn_{0.5}O_2$ Cathode Material for Rechargeable Sodium-Ion Batteries. *ChemElectroChem* **2014**, 1 (2), 371–374. https://doi.org/10.1002/celc.201300026.

(187) Dahbi, M.; Yoshida, H.; Kubota, K.; Komaba, S.; Yabuuchi, N.; Layered Oxides as Positive Electrode Materials for Na-Ion Batteries. *MRS Bull.* **2014**, 39 (05), 416–422. https://doi.org/10.1557/mrs.2014.85.

(188) Mendiboure, A.; Delmas, C.; Hagenmuller, P.; Electrochemical Intercalation and Deintercalation of Na_xMnO_2 Bronzes. *J. Solid State Chem.* **1985**, 57 (3), 323–331. https://doi.org/10.1016/0022-4596(85)90194-X.

(189) Saadoune, I.; Maazaz, A.; Menetrier, M.; Delmas, C.; On the $Na_xNi_{0.6}Co_{0.4}O_2$ System: Physical and Electrochemical Studies. *J. Solid State Chem.* **1996**, 117 (122), 111–117. https://doi.org/10.1006/jssc.1996.0090.

(190) Singh, G.; Acebedo, B.; Cabanas, M.C.; Shanmukaraj, D.; Armand, M.; Rojo, T.; An Approach to Overcome First Cycle Irreversible Capacity in P2-$Na_{2/3}[Fe_{1/2}Mn_{1/2}]O_2$. *Electrochem. commun.* **2013**, 37, 61–63. https://doi.org/10.1016/j.elecom.2013.10.008.

(191) Martínez De Ilarduya, J.; Otaegui, L.; Galcerán, M.; Acebo, L.; Shanmukaraj, D.; Rojo, T.; Armand, M.; Towards High Energy Density, Low Cost and Safe Na-Ion Full-Cell Using P2–$Na_{0.67}[Fe_{0.5}Mn_{0.5}]O_2$ and $Na_2C_4O_4$ Sacrificial Salt. *Electrochim. Acta* **2019**, 321, 1–9. https://doi.org/10.1016/j.electacta.2019.134693.

(192) Ohzuku, T.; Kitagawa, M.; Hirai, T.; Electrochemistry of Manganese Dioxide in Lithium Nonaqueous Cell: III. X-Ray Diffractional Study on the Reduction of Spinel-Related Manganese Dioxide. *J. Electrochem. Soc.* **1990**, 137 (3), 3–9. https://doi.org/10.1149/1.2086552.

(193) Thackeray, M.M.; David, W.I.F.; Bruce, P.G.; Goodenough, J.B.; Lithium Insertion into Manganese Spinels. *Mater. Res. Bull.* **1983**, 18 (4), 461–472. https://doi.org/10.1016/0025-5408(83)90138-1.

(194) Thackeray, M.M.; Johnson, P.J.; de Picciotto, L.A.; Bruce, P.G.; Goodenough, J.B.; Electrochemical Extraction of Lithium from $LiMn_2O_4$. *Mater. Res. Bull.* **1984**, 19 (2), 179–187. https://doi.org/10.1016/0025-5408(84)90088-6.

(195) Amatucci, G.G.; Schmutz, C.N.; Blyr, A.; Sigala, C.; Gozdz, A.S.; Larcher, D.; Tarascon, J.M.; Materials' Effects on the Elevated and Room Temperature Performance of C/$LiMn_2O_4$ Li-Ion Batteries. *J. Power Sources* **1997**, 69 (1–2), 11–25. https://doi.org/10.1016/S0378-7753(97)02542-1.

(196) Thackeray, M.M.; Manganese Oxides for Lithium Batteries. *Prog. Solid State Chem.* **1997**, 25 (1–2), 1–71. https://doi.org/10.1016/S0079-6786(97)81003-5.

(197) Gummow, R.J.; de Kock, A.; Thackeray, M.M.; Improved Capacity Retention in Rechargeable 4V Lithium/Lithium-Manganese Oxide (Spinel) Cells. *Solid State Ionics* **1994**, 69 (1), 59–67. https://doi.org/10.1016/0167-2738(94)90450-2.

(198) Park, O.K.; Cho, Y.; Lee, S.; Yoo, H.C.; Song, H.K.; Cho, J.; Who Will Drive Electric Vehicles, Olivine or Spinel? *Energy Environ. Sci.* **2011**, 4 (5), 1621–1633. https://doi.org/10.1039/c0ee00559b.

(199) Xia, Y.; Zhou, Y.; Yoshiot, M.; Capacily Fading on Cycling of 4V Li/$LiMn_2O_4$ Cells. *Electrochem. Soc.* **1997**, 144 (8), 2593–2600. https://doi.org/10.1149/1.1837870.

(200) Jang, D.H.; Oh, S.M.; Electrolyte Effects on Spinel Dissolution and Cathodic Capacity Losses in 4V Li/$Li_xMn_2O_4$ Rechargeable Cells. *J. Electrochem. Soc.* **1997**, 144 (10), 3342–3348. https://doi.org/10.1149/1.1838016.

(201) Julien, C.M.; Mauger, A.; Review of 5-V Electrodes for Li-Ion Batteries: Status and Trends. *Ionics* **2013**, 19, 951-988. https://doi.org/10.1007/s11581-013-0913-2.

(202) Zhong, Q.; Bonakdarpour, A.; Zhang, M.; Gao, Y.; Dahn, J.R.; Synthesis and Electrochemistry of $LiNi_xMn_{2-X}O_4$. *J. Electrochem. Soc.* **1997**, 144 (1), 205–213. https://doi.org/10.1149/1.1837386.

(203) Yabuuchi, N.; Yano, M.; Kuze, S.; Komaba, S.; Electrochemical Behavior and Structural Change of Spinel-Type $Li[Li_xMn_{2-x}]O_4$ (x = 0 and 0.2) in Sodium Cells. *Electrochim. Acta* **2012**, 82, 296–301. https://doi.org/10.1016/j.electacta.2012.06.123.

(204) Geller, S.; Durand, J.L.; Refinement of the Structure of $LiMnPO_4$. *Acta Crystallogr.* **1960**, 13 (4), 325–331. https://doi.org/10.1107/s0365110x60002521.

(205) Santoro, R.P.; Newnham, R.E.; Antiferromagnetism in $LiFePO_4$. *Acta Crystallogr.* **1967**, 22 (3), 344–347. https://doi.org/10.1107/s0365110x67000672.

(206) Malik, R.; Zhou, F.; Ceder, G.; Phase Diagram and Electrochemical Properties of Mixed Olivines from First-Principles Calculations. *Phys. Rev. B - Condens. Matter Mater. Phys.* **2009**, 79 (21), 1–7. https://doi.org/10.1103/PhysRevB.79.214201.

(207) Scrosati, B.; Garche, J.; Lithium Batteries: Status, Prospects and Future. *J. Power Sources* **2010**, 195 (9), 2419–2430. https://doi.org/10.1016/j.jpowsour.2009.11.048.

(208) Di Lecce, D.; Verrelli, R.; Hassoun, J.; Lithium-Ion Batteries for Sustainable Energy Storage: Recent Advances Towards New Cell Configurations. *Green Chem.* **2017**, 19 (15), 3442–3467. https://doi.org/10.1039/c7gc01328k.

(209) Ben Mayza, A.; Ramanathan, M.; Radhakrishnan, R.; Ha, S.; Ramani, V.; Prakash, J.; Zaghib, K.; Thermal Characterization of $LiFePO_4$ Cathode in Lithium-Ion Cells. *ECS Trans.* **2011**, 35 (34), 177–183. https://doi.org/10.1149/1.3654216.

(210) Yuan, L.X.; Wang, Z.H.; Zhang, W.X.; Hu, X.L.; Chen, J.T.; Huang, Y.H.; Goodenough, J.B.;

Development and Challenges of $LiFePO_4$ Cathode Material for Lithium-Ion Batteries. *Energy Environ. Sci.* **2011**, 4 (2), 269–284. https://doi.org/10.1039/c0ee00029a.

(211) Padhi, A.K.; Phospho-Olivine as Positive-Electrode Materials for Rechargeable Lithium Batteries. *J. Electrochem. Soc.* **1997**, 144 (4), 1188. https://doi.org/https://doi.org/10.1149/1.1837571.

(212) Oh, S.W.; Myung, S.T.; Oh, S.M.; Oh, K.H.; Amine, K.; Scrosati, B.; Sun, Y.K.; Double Carbon Coating of $LiFePO_4$ as High Rate Electrode for Rechargeable Lithium Batteries. *Adv. Mater.* **2010**, 22 (43), 4842–4845. https://doi.org/10.1002/adma.200904027.

(213) Aravindan, V.; Gnanaraj, J.; Lee, Y.S.; Madhavi, S.; $LiMnPO_4$ - A next Generation Cathode Material for Lithium-Ion Batteries. *J. Mater. Chem. A* **2013**, 1 (11), 3518–3539. https://doi.org/10.1039/c2ta01393b.

(214) Wolfenstine, J.; Allen, J.; Ni^{3+}/Ni^{2+} Redox Potential in $LiNiPO_4$. *J. Power Sources* **2005**, 142 (1–2), 389–390. https://doi.org/10.1016/j.jpowsour.2004.11.024.

(215) Amine, K.; Yasuda, H.; Yamachi, M.; Olivine $LiCoPO_4$ as 4.8V Electrode Material for Lithium Batteries. *Electrochem. Solid-State Lett.* **2000**, 3 (4), 178–179. https://doi.org/10.1149/1.1390994.

(216) Di Lecce, D.; Gancitano, V.; Hassoun, J.; Investigation of Mn and Fe Substitution Effects on the Characteristics of High-Voltage $LiCo_{1-x}M_xPO_4$ (x = 0.1, 0.4) Cathodes Prepared by Sol-Gel Route. *ACS Sustain. Chem. Eng.* **2020**, 8 (1), 278–289. https://doi.org/10.1021/acssuschemeng.9b05325.

(217) Jiang, J.; Dahn, J.R.; ARC Studies of the Thermal Stability of Three Different Cathode Materials: $LiCoO_2$; $Li[Ni_{0.1}Co_{0.8}Mn_{0.1}]O_2$; and $LiFePO_4$, in $LiPF_6$ and LiBoB EC/DEC Electrolytes. *Electrochem. commun.* **2004**, 6 (1), 39–43. https://doi.org/10.1016/j.elecom.2003.10.011.

(218) Bramnik, N.N.; Nikolowski, K.; Baehtz, G.; Bramnik, K.G.; Ehrenberg, H.; Phase Transitions Occurring upon Lithium Insertion-Extraction of $LiCoPO_4$. *Chem. Mater.* **2007**, 19 (4), 908–915. https://doi.org/10.1021/cm062246u.

(219) Li, G.; Azuma, H.; Tohda, M.; LiMnPO4 as the Cathode for Lithium Batteries. *Electrochem. Solid-State Lett.* **2002**, 5 (6), 135–138. https://doi.org/10.1149/1.1475195.

(220) Di Lecce, D.; Brescia, R.; Scarpellini, A.; Prato, M.; Hassoun, J.; A High Voltage Olivine Cathode for Application in Lithium-Ion Batteries. *ChemSusChem* **2016**, 9 (2), 223–230. https://doi.org/10.1002/cssc.201501330.

(221) Hong, Y.; Tang, Z.; Hong, Z.; Zhang, Z.; $LiMn_{1-x}Fe_xPO_4$ (x = 0, 0.1, 0.2) Nanorods Synthesized by a Facile Solvothermal Approach as High Performance Cathode Materials for Lithium-Ion Batteries. *J. Power Sources* **2014**, 248, 655–659. https://doi.org/10.1016/j.jpowsour.2013.09.123.

(222) Zhang, B.; Wang, X.; Li, H.; Huang, X.; Electrochemical Performances of $LiFe_{1-x}Mn_xPO_4$ with High Mn Content. *J. Power Sources* **2011**, 196 (16), 6992–6996. https://doi.org/10.1016/j.jpowsour.2010.10.051.

(223) Moreau, P.; Guyomard, D.; Gaubicher, J.; Boucher, F.; Structure and Stability of Sodium Intercalated Phases in Olivine $FePO_4$. *Chem. Mater.* **2010**, 22 (14), 4126–4128. https://doi.org/10.1021/cm101377h.

(224) Jian, Z.; Hu, Y.S.; Ji, X.; Chen, W.; NASICON-Structured Materials for Energy Storage. *Adv. Mater.* **2017**, 29 (20). https://doi.org/10.1002/adma.201601925.

(225) Chen, S.; Wu, C.; Shen, L.; Zhu, C.; Huang, Y.; Xi, K.; Maier, J.; Yu, Y.; Challenges and Perspectives for NASICON-Type Electrode Materials for Advanced Sodium-Ion Batteries. *Adv. Mater.* **2017**, 29 (48), 1–21. https://doi.org/10.1002/adma.201700431.

(226) Jin, T.; Li, H.; Zhu, K.; Wang, P.F.; Liu, P.; Jiao, L.; Polyanion-Type Cathode Materials for Sodium-Ion Batteries. *Chem. Soc. Rev.* **2020**, 49 (8), 2342–2377. https://doi.org/10.1039/c9cs00846b.

(227) Jian, Z.; Zhao, L.; Pan, H.; Hu, Y.S.; Li, H.; Chen, W.; Chen, L.; Carbon Coated $Na_3V_2(PO_4)_3$ as Novel Electrode Material for Sodium Ion Batteries. *Electrochem. commun.* **2012**, 14 (1), 86–89. https://doi.org/10.1016/j.elecom.2011.11.009.

(228) Kajiyama, S.; Kai, K.; Okubo, M.; Yamada, A.; Potentiometric Study to Reveal Reaction Entropy

Behavior of Biphasic $Na_{1+2x}V_2(PO_4)_3$ Electrodes. *Electrochemistry* **2016**, 84 (4), 234–237. https://doi.org/10.5796/electrochemistry.84.234.

(229) Jian, Z.; Yuan, C.; Han, W.; Lu, X.; Gu, L.; Xi, X.; Hu, Y.S.; Li, H.; Chen, W.; Chen, D.; Ikuhara, Y.; Chen, L.; Atomic Structure and Kinetics of NASICON $Na_xV_2(PO_4)_3$ Cathode for Sodium-Ion Batteries. *Adv. Funct. Mater.* **2014**, 24 (27), 4265–4272. https://doi.org/10.1002/adfm.201400173.

(230) Jian, Z.; Han, W.; Lu, X.; Yang, H.; Hu, Y.S.; Zhou, J.; Zhou, Z.; Li, J.; Chen, W.; Chen, D.; Chen, L.; Superior Electrochemical Performance and Storage Mechanism of $Na_3V_2(PO_4)_3$ Cathode for Room-Temperature Sodium-Ion Batteries. *Adv. Energy Mater.* **2013**, 3 (2), 156–160. https://doi.org/10.1002/aenm.201200558.

(231) Bianchini, M.; Brisset, N.; Fauth, F.; Weill, F.; Elkaim, E.; Suard, E.; Masquelier, C.; Croguennec, L.; $Na_3V_2(PO_4)_2F_3$ Revisited : A High-Resolution Diffraction Study. *Chem. Mater.* **2014**, 26 (14), 4238-4247. https://doi.org/10.1021/cm501644g.

(232) Peng, J.; Zhang, W.; Liu, Q.; Wang, J.; Chou, S.; Liu, H.; Dou, S.; Prussian Blue Analogues for Sodium-Ion Batteries: Past, Present, and Future. *Adv. Mater.* **2022**, 34 (15), 1–20. https://doi.org/10.1002/adma.202108384.

(233) Xu, Y.; Wan, J.; Huang, L.; Ou, M.; Fan, C.; Wei, P.; Peng, J.; Liu, Y.; Qiu, Y.; Sun, X.; Fang, C.; Li, Q.; Han, J.; Huang, Y.; Alonso, J.A.; Zhao, Y.; Structure Distortion Induced Monoclinic Nickel Hexacyanoferrate as High-Performance Cathode for Na-Ion Batteries. *Adv. Energy Mater.* **2019**, 9 (4), 1–10. https://doi.org/10.1002/aenm.201803158.

(234) Wang, W.; Gang, Y.; Hu, Z.; Yan, Z.; Li, W.; Li, Y.; Gu, Q.F.; Wang, Z.; Chou, S.L.; Liu, H.K.; Dou, S.X.; Reversible Structural Evolution of Sodium-Rich Rhombohedral Prussian Blue for Sodium-Ion Batteries. *Nat. Commun.* **2020**, 11 (1), 1–9. https://doi.org/10.1038/s41467-020-14444-4.

(235) Rehman, R.; Peng, J.; Yi, H.; Shen, Y.; Yin, J.; Li, C.; Fang, C.; Li, Q.; Han, J.; Highly Crystalline Nickel Hexacyanoferrate as a Long-Life Cathode Material for Sodium-Ion Batteries. *RSC Adv.* **2020**, 10 (45), 27033–27041. https://doi.org/10.1039/d0ra03490h.

(236) Kosaka, W.; Ishihara, T.; Yashiro, H.; Taniguchi, Y.; Hashimoto, K.; Ohkoshi, S.I.; Synthesis of Ferromagnetic CsCuCr Prussian Blue Analogue with a Tetragonal Structure. *Chem. Lett.* **2005**, 34 (9), 1278–1279. https://doi.org/10.1246/cl.2005.1278.

(237) Peng, J.; Li, C.; Yin, J.; Wang, J.; Yu, Y.; Shen, Y.; Fang, J.; Chen, A.; Xu, Y.; Rehman, R.; Fang, C.; Miao, L.; Jiang, R.; Li, Q.; Han, J.; Huang, Y.; Novel Cerium Hexacyanoferrate(II) as Cathode Material for Sodium-Ion Batteries. *ACS Appl. Energy Mater.* **2019**, 2 (1), 187–191. https://doi.org/10.1021/acsaem.8b01686.

(238) He, G.; Nazar, L.F.; Crystallite Size Control of Prussian White Analogues for Nonaqueous Potassium-Ion Batteries. *ACS Energy Lett.* **2017**, 2 (5), 1122–1127. https://doi.org/10.1021/acsenergylett.7b00179.

(239) Xiang, X.; Zhang, K.; Chen, J.; Recent Advances and Prospects of Cathode Materials for Sodium-Ion Batteries. *Adv. Mater.* **2015**, 27 (36), 5343–5364. https://doi.org/10.1002/adma.201501527.

(240) Ren, W.; Qin, M.; Zhu, Z.; Yan, M.; Li, Q.; Zhang, L.; Liu, D.; Mai, L.; Activation of Sodium Storage Sites in Prussian Blue Analogues via Surface Etching. *Nano Lett.* **2017**, 17 (8), 4713–4718. https://doi.org/10.1021/acs.nanolett.7b01366.

(241) Peng, J.; Ou, M.; Yi, H.; Sun, X.; Zhang, Y.; Zhang, B.; Ding, Y.; Wang, F.; Gu, S.; López, C.A.; Zhang, W.; Liu, Y.; Fang, J.; Wei, P.; Li, Y.; Miao, L.; Jiang, J.; Fang, C.; Li, Q.; Fernández-Díaz, M.T.; Alonso, J.A.; Chou, S.; Han, J.; Defect-Free-Induced Na^+ disordering in Electrode Materials. *Energy Environ. Sci.* **2021**, 14 (5), 3130–3140. https://doi.org/10.1039/d1ee00087j.

(242) Simonov, A.; De Baerdemaeker, T.; Boström, H.L. B.; Ríos Gómez, M.L.; Gray, H.J.; Chernyshov, D.; Bosak, A.; Bürgi, H.B.; Goodwin, A.L.; Hidden Diversity of Vacancy Networks in Prussian Blue Analogues. *Nature* **2020**, 578 (7794), 256–260. https://doi.org/10.1038/s41586-020-1980-y.

(243) Wu, X.; Wu, C.; Wei, C.; Hu, L.; Qian, J.; Cao, Y.; Ai, X.; Wang, J.; Yang, H.; Highly Crystallized

$Na_2CoFe(CN)_6$ with Suppressed Lattice Defects as Superior Cathode Material for Sodium-Ion Batteries. *ACS Appl. Mater. Interfaces* **2016**, 8 (8), 5393–5399. https://doi.org/10.1021/acsami.5b12620.

(244) Song, J.; Wang, L.; Lu, Y.; Liu, J.; Guo, B.; Xiao, P.; Lee, J.J.; Yang, X.Q.; Henkelman, G.; Goodenough, J.B.; Removal of Interstitial H_2O in Hexacyanometallates for a Superior Cathode of a Sodium-Ion Battery. *J. Am. Chem. Soc.* **2015**, 137 (7), 2658–2664. https://doi.org/10.1021/ja512383b.

(245) Yan, C.; Zhao, A.; Zhong, F.; Feng, X.; Chen, W.; Qian, J.; Ai, X.; Yang, H.; Cao, Y.; A Low-Defect and Na-Enriched Prussian Blue Lattice with Ultralong Cycle Life for Sodium-Ion Battery Cathode. *Electrochim. Acta* **2020**, 332, 135533. https://doi.org/10.1016/j.electacta.2019.135533.

(246) Shang, Y.; Li, X.; Song, J.; Huang, S.; Yang, Z.; Xu, Z.J.; Yang, H.Y.; Unconventional Mn Vacancies in Mn–Fe Prussian Blue Analogs: Suppressing Jahn-Teller Distortion for Ultrastable Sodium Storage. *Chem* **2020**, 6 (7), 1804–1818. https://doi.org/10.1016/j.chempr.2020.05.004.

(247) Yin, J.; Shen, Y.; Li, C.; Fan, C.; Sun, S.; Liu, Y.; Peng, J.; Qing, L.; Han, J.; In Situ Self-Assembly of Core–Shell Multimetal Prussian Blue Analogues for High-Performance Sodium-Ion Batteries. *ChemSusChem* **2019**, 12 (21), 4786–4790. https://doi.org/10.1002/cssc.201902013.

(248) Chou, S.L.; Pan, Y.; Wang, J.Z.; Liu, H.K.; Dou, S.X.; Small Things Make a Big Difference: Binder Effects on the Performance of Li and Na Batteries. *Phys. Chem. Chem. Phys.* **2014**, 16 (38), 20347–20359. https://doi.org/10.1039/c4cp02475c.

(249) Li, J.T.; Wu, Z.Y.; Lu, Y.Q.; Zhou, Y.; Huang, Q.S.; Huang, L.; Sun, S.G.; Water Soluble Binder, an Electrochemical Performance Booster for Electrode Materials with High Energy Density. *Adv. Energy Mater.* **2017**, 7 (24), 1–30. https://doi.org/10.1002/aenm.201701185.

(250) Schappacher, F.; Winter, M.; Passerini, S.; Balducci, A.; Lux, S.F.; Low Cost, Environmentally Benign Binders for Lithium-Ion Batteries. *J. Electrochem. Soc.* **2010**, 157 (3), A320. https://doi.org/10.1149/1.3291976.

(251) Dou, S.X.; Xu, J.; Liu, H.K.; Chou, S.L.; Gu, Q.; The Effect of Different Binders on Electrochemical Properties of $LiNi_{1/3}Mn_{1/3}Co_{1/3}O_2$ Cathode Material in Lithium Ion Batteries. *J. Power Sources* **2012**, 225, 172–178. https://doi.org/10.1016/j.jpowsour.2012.10.033.

(252) Li, J.; Lewis, R.B.; Dahn, J.R.; Sodium Carboxymethylcellulose - A Potential Binder for Si Negative Electrodes for Li-Ion Batteries. *Electrochem. Solid-State Lett.* **2007**, 10 (2), 17–20. https://doi.org/10.1021/ac60078a026.

(253) Magasinski, A.; Zdyrko, B.; Kovalenko, I.; Hertzberg, B.; Burtovyy, R.; Huebner, C.F.; Fuller, T.F.; Luzinov, I.; Yushin, G.; Toward Efficient Binders for Li-Ion Battery Si-Based Anodes: Polyacrylic Acid. *ACS Appl. Mater. Interfaces* **2010**, 2 (11), 3004–3010. https://doi.org/10.1021/am100871y.

(254) Bigoni, F.; De Giorgio, F.; Soavi, F.; Arbizzani, C.; Sodium Alginate: A Water-Processable Binder in High-Voltage Cathode Formulations. *J. Electrochem. Soc.* **2017**, 164 (1), A6171–A6177. https://doi.org/10.1149/2.0281701jes.

(255) Kovalenko, I.; Zdyrko, B.; Magasinski, A.; Hertzberg, B.; Milicev, Z.; Burtovyy, R.; Luzinov, I.; Yushin, G.; A Major Constituent of Brown Algae for Use in High-Capacity Li-Ion Batteries. *Science* **2011**, 334 (6052), 75–79. https://doi.org/10.1126/science.1209150.

(256) Kuenzel, M.; Porhiel, R.; Bresser, D.; Asenbauer, J.; Axmann, P.; Wohlfahrt-Mehrens, M.; Passerini, S.; Deriving Structure-Performance Relations of Chemically Modified Chitosan Binders for Sustainable High-Voltage $LiNi_{0.5}Mn_{1.5}O_4$ Cathodes. *Batter. Supercaps* **2020**, 3 (2), 155–164. https://doi.org/10.1002/batt.201900140.

(257) Chen, C.; Lee, S.H.; Cho, M.; Kim, J.; Lee, Y.; Cross-Linked Chitosan as an Efficient Binder for Si Anode of Li-Ion Batteries. *ACS Appl. Mater. Interfaces* **2016**, 8 (4), 2658–2665. https://doi.org/10.1021/acsami.5b10673.

(258) Morales, D.; Ruther, R.E.; Nanda, J.; Greenbaum, S.; Ion Transport and Association Study of Glyme-Based Electrolytes with Lithium and Sodium Salts. *Electrochim. Acta* **2019**, 304, 239–245.

https://doi.org/10.1016/j.electacta.2019.02.110.

(259) Khani, H.; Kalami, S.; Goodenough, J.B.; Micropores-in-Macroporous Gel Polymer Electrolytes for Alkali Metal Batteries. *Sustain. Energy Fuels* **2019**, 4 (1), 177–189. https://doi.org/10.1039/c9se00690g.

(260) Kim, J.I.; Choi, Y.G.; Ahn, Y.; Kim, D.; Park, J.H.; Optimized Ion-Conductive Pathway in UV-Cured Solid Polymer Electrolytes for All-Solid Lithium/Sodium Ion Batteries. *J. Memb. Sci.* **2021**, 619, 118771. https://doi.org/10.1016/j.memsci.2020.118771.

(261) Tatsumisago, M.; Hayashi, A.; Sulfide Glass-Ceramic Electrolytes for All-Solid-State Lithium and Sodium Batteries. *Int. J. Appl. Glas. Sci.* **2014**, 5 (3), 226–235. https://doi.org/10.1111/ijag.12084.

(262) Arbizzani, C.; Gabrielli, G.; Mastragostino, M.; Thermal Stability and Flammability of Electrolytes for Lithium-Ion Batteries. *J. Power Sources* **2011**, 196 (10), 4801–4805. https://doi.org/10.1016/j.jpowsour.2011.01.068.

(263) Tarascon, J.M.; Armand, M.; Issues and Challenges Facing Rechargeable Lithium Batteries. *Nature* **2001**, 414 (6861), 359–367. https://doi.org/10.1038/35104644.

(264) Palomares, V.; Casas-Cabanas, M.; Castillo-Martínez, E.; Han, M.H.; Rojo, T.; Update on Na-Based Battery Materials. A Growing Research Path. *Energy Environ. Sci.* **2013**, 6 (8), 2312–2337. https://doi.org/10.1039/c3ee41031e.

(265) Eshetu, G.G.; Grugeon, S.; Kim, H.; Jeong, S.; Wu, L.; Gachot, G.; Laruelle, S.; Armand, M.; Passerini, S.; Comprehensive Insights into the Reactivity of Electrolytes Based on Sodium Ions. *ChemSusChem* **2016**, 9 (5), 462–471. https://doi.org/10.1002/cssc.201501605.

(266) Bommier, C.; Ji, X.; Electrolytes, SEI Formation, and Binders: A Review of Nonelectrode Factors for Sodium-Ion Battery Anodes. *Small* **2018**, 14 (16), 1–20. https://doi.org/10.1002/smll.201703576.

(267) Ma, L.A.; Naylor, A.J.; Nyholm, L.; Younesi, R.; Strategies for Mitigating Dissolution of Solid Electrolyte Interphases in Sodium-Ion Batteries. *Angew. Chemie - Int. Ed.* **2021**, 60 (9), 4855–4863. https://doi.org/10.1002/anie.202013803.

(268) Zhang, S.S.; A Review on Electrolyte Additives for Lithium-Ion Batteries. *J. Power Sources* **2006**, 162 (2), 1379–1394. https://doi.org/10.1016/j.jpowsour.2006.07.074.

(269) Dahbi, M.; Nakano, T.; Yabuuchi, N.; Fujimura, S.; Chihara, K.; Kubota, K.; Son, J.Y.; Cui, Y.T.; Oji, H.; Komaba, S.; Effect of Hexafluorophosphate and Fluoroethylene Carbonate on Electrochemical Performance and the Surface Layer of Hard Carbon for Sodium-Ion Batteries. *ChemElectroChem* **2016**, 3 (11), 1856–1867. https://doi.org/10.1002/celc.201600365.

(270) Knobloch, F.; Hanssen, S.V.; Lam, A.; Pollitt, H.; Salas, P.; Chewpreecha, U.; Huijbregts, M.A.J.; Mercure, J.F.; Net Emission Reductions from Electric Cars and Heat Pumps in 59 World Regions over Time. *Nat. Sustain.* **2020**, 3 (6), 437–447. https://doi.org/10.1038/s41893-020-0488-7.

(271) Hannan, M.A.; Hoque, M.M.; Hussain, A.; Yusof, Y.; Ker, P.J.; State-of-the-Art and Energy Management System of Lithium-Ion Batteries in Electric Vehicle Applications: Issues and Recommendations. *IEEE Access* **2018**, 6, 19362–19378. https://doi.org/10.1109/ACCESS.2018.2817655.

(272) Andre, D.; Kim, S.J.; Lamp, P.; Lux, S.F.; Maglia, F.; Paschos, O.; Stiaszny, B.; Future Generations of Cathode Materials: An Automotive Industry Perspective. *J. Mater. Chem. A* **2015**, 3 (13), 6709–6732. https://doi.org/10.1039/c5ta00361j.

(273) Iqbal, A.; Chen, L.; Chen, Y.; Gao, Y.; Chen, F.; Li, D.; Lithium-Ion Full Cell with High Energy Density Using Nickel-Rich $LiNi_{0.8}Co_{0.1}Mn_{0.1}O_2$ Cathode and SiO-C Composite Anode. *Int. J. Miner. Metall. Mater.* **2018**, 25 (12), 1473–1481. https://doi.org/10.1007/s12613-018-1702-8.

(274) Gaines, L.; Richa, K.; Spangenberger, J.; Key Issues for Li-Ion Battery Recycling. *MRS Energy Sustain.* **2018**, 5 (1), 1–14. https://doi.org/10.1557/mre.2018.13.

(275) Mossali, E.; Picone, N.; Gentilini, L.; Rodrìguez, O.; Pérez, J.M.; Colledani, M.; Lithium-Ion Batteries

towards Circular Economy: A Literature Review of Opportunities and Issues of Recycling Treatments. *J. Environ. Manage.* **2020**, 264. https://doi.org/10.1016/j.jenvman.2020.110500.

(276) Wang, J.; Nie, P.; Ding, B.; Dong, S.; Hao, X.; Dou, H.; Zhang, X.; Biomass Derived Carbon for Energy Storage Devices. *J. Mater. Chem. A* **2017**, 5 (6), 2411–2428. https://doi.org/10.1039/c6ta08742f.

(277) Franco Gonzalez, A.; Yang, N.H.; Liu, R.S.; Silicon Anode Design for Lithium-Ion Batteries: Progress and Perspectives. *J. Phys. Chem. C* **2017**, 121 (50), 27775–27787. https://doi.org/10.1021/acs.jpcc.7b07793.

(278) Shen, X.; Zhang, X.Q.; Ding, F.; Huang, J.Q.; Xu, R.; Chen, X.; Yan, C.; Su, F.Y.; Chen, C.M.; Liu, X.; Zhang, Q.; Advanced Electrode Materials in Lithium Batteries: Retrospect and Prospect. *Energy Mater. Adv.* **2021**, 2021, 1–15. https://doi.org/10.34133/2021/1205324.

(279) Zhou, X.; Yin, Y.; Wan, L.; Guo, Y.; Self-Assembled Nanocomposite of Silicon Nanoparticles Encapsulated in Graphene through Electrostatic Attraction for Lithium-Ion Batteries. *Adv. Energy Mater.* **2012**, 2 (9), 1086-1090. https://doi.org/10.1002/aenm.201200158.

(280) Zhou, X.; Wan, L.; Guo, Y.; Binding SnO_2 Nanocrystals in Nitrogen-Doped Graphene Sheets as Anode Materials for Lithium-Ion Batteries. *Adv. Mater.* **2013**, 25 (15), 2152-2157. https://doi.org/10.1002/adma.201300071.

(281) Dou, F.; Shi, L.; Chen, G.; Zhang, D.; Silicon/Carbon Composite Anode Materials for Lithium-Ion Batteries. *Electrochem. Energ. Rev.* **2019**, 2, 149-198. https://doi.org/10.1007/s41918-018-00028-w.

(282) Wang, J.; Zhao, H.; Liu, X.; Wang, J.; Wang, C.; Electrochemical Properties of SnO_2/Carbon Composite Materials as Anode Material for Lithium-Ion Batteries. *Electrochim. Acta* **2011**, 56 (18), 6441–6447. https://doi.org/10.1016/j.electacta.2011.04.134.

(283) Baldinelli, A.; Dou, X.; Buchholz, D.; Marinaro, M.; Passerini, S.; Barelli, L.; Addressing the Energy Sustainability of Biowaste-Derived Hard Carbon Materials for Battery Electrodes. *Green Chem.* **2018**, 20 (7), 1527–1537. https://doi.org/10.1039/c8gc00085a.

(284) Erk, C.; Brezesinski, T.; Sommer, H.; Schneider, R.; Janek, J.; Toward Silicon Anodes for Next-Generation Lithium Ion Batteries: A Comparative Performance Study of Various Polymer Binders and Silicon Nanopowders. *ACS Appl. Mater. Interfaces* **2013**, 5 (15), 7299–7307. https://doi.org/10.1021/am401642c.

(285) Hu, S.; Cai, Z.; Huang, T.; Zhang, H.; Yu, A.; A Modified Natural Polysaccharide as a High-Performance Binder for Silicon Anodes in Lithium-Ion Batteries. *ACS Appl. Mater. Interfaces* **2019**, 11 (4), 4311–4317. https://doi.org/10.1021/acsami.8b15695.

(286) Shen, L.; Shen, L.; Wang, Z.; Chen, L.; In Situ Thermally Cross-Linked Polyacrylonitrile as Binder for High-Performance Silicon as Lithium Ion Battery Anode. *ChemSusChem* **2014**, 7 (7), 1951–1956. https://doi.org/10.1002/cssc.201400030.

(287) Espinosa-Villatoro, E.; Nelson Weker, J.; Ko, J.S.; Quiroga-González, E.; Tracking the Evolution of Processes Occurring in Silicon Anodes in Lithium Ion Batteries by 3D Visualization of Relaxation Times. *J. Electroanal. Chem.* **2021**, 892, 115309. https://doi.org/10.1016/j.jelechem.2021.115309.

(288) Guo, J.; Sun, A.; Chen, X.; Wang, C.; Manivannan, A.; Cyclability Study of Silicon-Carbon Composite Anodes for Lithium-Ion Batteries Using Electrochemical Impedance Spectroscopy. *Electrochim. Acta* **2011**, 56 (11), 3981–3987. https://doi.org/10.1016/j.electacta.2011.02.014.

(289) Ciucci, F.; Chen, C.; Analysis of Electrochemical Impedance Spectroscopy Data Using the Distribution of Relaxation Times: A Bayesian and Hierarchical Bayesian Approach. *Electrochim. Acta* **2015**, 167, 439–454. https://doi.org/10.1016/j.electacta.2015.03.123.

(290) Venkateswara Rao, C.; Soler, J.; Katiyar, R.; Shojan, J.; West, W.C.; Katiyar, R.S.; Investigations on Electrochemical Behavior and Structural Stability of $Li_{1.2}Mn_{0.54}Ni_{0.13}Co_{0.13}O_2$ Lithium-Ion Cathodes via in-Situ and Ex-Situ Raman Spectroscopy. *J. Phys. Chem. C* **2014**, 118 (26), 14133–14141. https://doi.org/10.1021/jp501777v.

(291) Zhang, C.; Wang, F.; Han, J.; Bai, S.; Tan, J.; Liu, J.; Li, F.; Challenges and Recent Progress on Silicon-Based Anode Materials for Next-Generation Lithium-Ion Batteries. *Small Struct.* **2021**, 2 (6), 2100009. https://doi.org/10.1002/sstr.202100009.

(292) Moyassari, E.; Streck, L.; Paul, N.; Trunk, M.; Neagu, R.; Chang, C.C.; Hou, S.C.; Märkisch, B.; Gilles, R.; Jossen, A.; Impact of Silicon Content within Silicon-Graphite Anodes on Performance and Li Concentration Profiles of Li-Ion Cells Using Neutron Depth Profiling. *J. Electrochem. Soc.* **2021**, 168 (2), 020519. https://doi.org/10.1149/1945-7111/abe1db.

(293) Ferrari, A. C.; Robertson, J.; Interpretation of Raman Spectra of Disordered and Amorphous Carbon. *Phys. Rev. B* **2000**, 61 (20). https://doi.org/10.1007/BF02543692.

(294) Darjazi, H.; Staffolani, A.; Sbrascini, L.; Bottoni, L.; Tossici, R.; Nobili, F.; Sustainable Anodes for Lithium- and Sodium-Ion Batteries Based on Coffee Ground-Derived Hard Carbon and Green Binders. *Energies* **2020**, 13 (23), 6216. https://doi.org/10.3390/en13236216.

(295) Beda, A.; Taberna, P.L.; Simon, P.; Matei Ghimbeu, C.; Hard Carbons Derived from Green Phenolic Resins for Na-Ion Batteries. *Carbon* **2018**, 139, 248–257. https://doi.org/10.1016/j.carbon.2018.06.036.

(296) Velez, V.; Ramos-Sánchez, G.; Lopez, B.; Lartundo-Rojas, L.; González, I.; Sierra, L.; Synthesis of Novel Hard Mesoporous Carbons and Their Application as Anodes for Li and Na Ion Batteries. *Carbon* **2019**, 147, 214–226. https://doi.org/10.1016/j.carbon.2019.02.083.

(297) Spizzirri, P.G.; Fang, J.H.; Rubanov, S.; Gauja, E.; Prawer, S.; Nano-Raman Spectroscopy of Silicon Surfaces. *Mater. Forum* **2008**, 34, 161–166. https://doi.org/10.48550/arXiv.1002.2692

(298) Zwick, A.; Carles, R.; Multiple-Order Raman Scattering in Crystalline and Amorphous Silicon. *Phys. Rev. B* **1993**, 48 (9), 6024–6032. https://doi.org/10.1103/PhysRevB.48.6024.

(299) Mishra, P.; Jain, K.P.; First- and Second-Order Raman Scattering in Nanocrystalline Silicon. *Phys. Rev. B - Condens. Matter Mater. Phys.* **2001**, 64 (7), 733041–733044. https://doi.org/10.1103/PhysRevB.64.073304.

(300) Kravets, V.G.; Kolmykova, V.Y.; Raman Scattering of Light in Silicon Nanostructures: First- and Second-Order Spectra. *Opt. Spectrosc.* **2005**, 99 (1), 68–73. https://doi.org/10.1134/1.1999895.

(301) Newbury, D.E.; Ritchie, N.W.M.; Is Scanning Electron Microscopy/Energy Dispersive X-Ray Spectrometry (SEM/EDS) Quantitative? *Scanning* **2013**, 35 (3), 141–168. https://doi.org/10.1002/sca.21041.

(302) Wang, N.; Liu, Q.; Sun, B.; Gu, J.; Yu, B.; Zhang, W.; Zhang, D.; N-Doped Catalytic Graphitized Hard Carbon for High-Performance Lithium/Sodium-Ion Batteries. *Sci. Rep.* **2018**, 8 (1), 1–8. https://doi.org/10.1038/s41598-018-28310-3.

(303) Wu, J.J.; Bennett, W.R.; Fundamental Investigation of Si Anode in Li-Ion Cells. *IEEE Energytech.* **2012**, 1–5. https://doi.org/10.1109/EnergyTech.2012.6304667.

(304) Maroni, F.; Carbonari, G.; Croce, F.; Tossici, R.; Nobili, F.; Anatase TiO_2 as a Cheap and Sustainable Buffering Filler for Silicon Nanoparticles in Lithium-Ion Battery Anodes. *ChemSusChem* **2017**, 10 (23), 4771–4777. https://doi.org/10.1002/cssc.201701431.

(305) Yu, X.; Xue, F.; Huang, H.; Liu, C.; Yu, J.; Sun, Y.; Dong, X.; Cao, G.; Jung, Y.; Synthesis and Electrochemical Properties of Silicon Nanosheets by DC Arc Discharge for Lithium-Ion Batteries. *Nanoscale* **2014**, 6 (12), 6860–6865. https://doi.org/10.1039/c3nr06418b.

(306) Levi, M.D.; Aurbach, D.; The Mechanism of Lithium Intercalation in Graphite Film Electrodes in Aprotic Media. Part 1. High Resolution Slow Scan Rate Cyclic Voltammetric Studies and Modeling. *J. Electroanal. Chem.* **1997**, 421 (1–2), 79–88. https://doi.org/10.1016/S0022-0728(96)04832-2.

(307) Saha, P.; Mohanta, T.R.; Kumar, A.; SEI Layer and Impact on Si-Anodes for Li-Ion Batteries. *Silicon Anode Syst. Lithium-Ion Batter.* **2022**, 183–263. https://doi.org/10.1016/B978-0-12-819660-1.00001-3.

(308) Shen, C.; Fang, X.; Ge, M.; Zhang, A.; Liu, Y.; Ma, Y.; Mecklenburg, M.; Nie, X.; Zhou, C.; Hierarchical

Carbon-Coated Ball-Milled Silicon: Synthesis and Applications in Free-Standing Electrodes and High-Voltage Full Lithium-Ion Batteries. *ACS Nano* **2018**, 12 (6), 6280–6291. https://doi.org/10.1021/acsnano.8b03312.

(309) Cheng, X.W.; Zhao, D.L.; Wu, L.L.; Ding, Z.W.; Hu, T.; Meng, S.; Core-Shell Structured Si@Ni Nanoparticles Encapsulated in Graphene Nanosheet for Lithium Ion Battery Anodes with Enhanced Reversible Capacity and Cyclic Performance. *Electrochim. Acta* **2018**, 265, 348–354. https://doi.org/10.1016/j.electacta.2018.01.198.

(310) Nzabahimana, J.; Guo, S.; Hu, X. Facile Synthesis of Si@void@C Nanocomposites from Low-Cost Microsized Si as Anode Materials for Lithium-Ion Batteries. *Appl. Surf. Sci.* **2019**, 479, 287–295. https://doi.org/10.1016/j.apsusc.2019.01.215.

(311) Fan, P.; Mu, T.; Lou, S.; Cheng, X.; Gao, Y.; Du, C.; Zuo, P.; Ma, Y.; Yin, G.; Amorphous Carbon-Encapsulated Si Nanoparticles Loading on MCMB with Sandwich Structure for Lithium Ion Batteries. *Electrochim. Acta* **2019**, 306, 590–598. https://doi.org/10.1016/j.electacta.2019.03.154.

(312) Wang, Z.; Zheng, B.; Liu, H.; Zhang, C.; Wu, F.; Luo, H.; Yu, P.; One-Step Synthesis of Nanoporous Silicon@Graphitized Carbon Composite and Its Superior Lithium Storage Properties. *J. Alloys Compd.* **2021**, 861, 157955. https://doi.org/10.1016/j.jallcom.2020.157955.

(313) Yu, C.; Tian, X.; Xiong, Z.; Zhang, Z.; Sun, Z.; Piao, X.; High Stability of Sub-Micro-Sized Silicon/Carbon Composites Using Recycling Silicon Waste for Lithium-Ion Battery Anode. *J. Alloys Compd.* **2021**, 869, 159124. https://doi.org/10.1016/j.jallcom.2021.159124.

(314) Liu, W.; Wang, J.; Wang, J.; Guo, X.; Yang, H.; Three-Dimensional Nitrogen-Doped Carbon Coated Hierarchically Porous Silicon Composite as Lithium-Ion Battery Anode. *J. Alloys Compd.* **2021**, 874, 159921. https://doi.org/10.1016/j.jallcom.2021.159921.

(315) Liu, Z.; Du, J.; Jia, H.; Wang, W.; Zhang, M.; Ma, J.; Nie, Y.; Liu, T.; Song, K.; Design of Hierarchical Buffer Structure for Silicon/Carbon Composite as a High-Performance Li-Ion Batteries Anode. *J. Mater. Sci. Mater. Electron.* **2022**, 33 (6), 3002–3015. https://doi.org/10.1007/s10854-021-07500-2.

(316) Qi, C.; Li, S.; Yang, Z.; Xiao, Z.; Zhao, L.; Yang, F.; Ning, G.; Ma, X.; Wang, C.; Xu, J.; Gao, J.; Suitable Thickness of Carbon Coating Layers for Silicon Anode. *Carbon* **2022**, 186, 530–538. https://doi.org/10.1016/j.carbon.2021.10.062.

(317) Zhao, J.; Rui, B.; Wei, W.; Nie, P.; Chang, L.; Xue, X.; Wang, L.; Jiang, J.; Encapsulating Silicon Particles by Graphitic Carbon Enables High-Performance Lithium-Ion Batteries. *J. Colloid Interface Sci.* **2022**, 607, 1562–1570. https://doi.org/10.1016/j.jcis.2021.09.005.

(318) Nanda, J.; Datta, M.K.; Remillard, J.T.; O'Neill, A.; Kumta, P.N.; In Situ Raman Microscopy during Discharge of a High Capacity Silicon-Carbon Composite Li-Ion Battery Negative Electrode. *Electrochem. commun.* **2009**, 11 (1), 235–237. https://doi.org/10.1016/j.elecom.2008.11.006.

(319) Krause, A.; Tkacheva, O.; Omar, A.; Langklotz, U.; Giebeler, L.; Dörfler, S.; Fauth, F.; Mikolajick, T.; Weber, W.M.; In Situ Raman Spectroscopy on Silicon Nanowire Anodes Integrated in Lithium Ion Batteries. *J. Electrochem. Soc.* **2019**, 166 (3), A5378–A5385. https://doi.org/10.1149/2.0541903jes.

(320) Sifuentes, A.; Stowe, A.C.; Smyrl, N.; Determination of the Role of Li_2O on the Corrosion of Lithium Hydride. *J. Alloys Compd.* **2013**, 580, 271–273. https://doi.org/10.1016/j.jallcom.2013.02.046.

(321) Zając, A.; Hanuza, J.; Wandas, M.; Dymińska, L.; Determination of N-Acetylation Degree in Chitosan Using Raman Spectroscopy. *Spectrochim. Acta - Part A Mol. Biomol. Spectrosc.* **2015**, 134, 114–120. https://doi.org/10.1016/j.saa.2014.06.071.

(322) Hy, S.; Felix; Chen, Y.H.; Liu, J.Y.; Rick, J.; Hwang, B.J.; In Situ Surface Enhanced Raman Spectroscopic Studies of Solid Electrolyte Interphase Formation in Lithium Ion Battery Electrodes. *J. Power Sources* **2014**, 256, 324–328. https://doi.org/10.1016/j.jpowsour.2014.01.092.

(323) Domi, Y.; Doi, T.; Nakagawa, H.; Yamanaka, T.; Abe, T.; Ogumi, Z.; In Situ Raman Study on Reversible Structural Changes of Graphite Negative-Electrodes at High Potentials in $LiPF_6$-Based

Electrolyte Solution. *J. Electrochem. Soc.* **2016**, 163 (10), A2435–A2440. https://doi.org/10.1149/2.1301610jes.

(324) Sole, C.; Drewett, N.E.; Hardwick, L.J.; In Situ Raman Study of Lithium-Ion Intercalation into Microcrystalline Graphite. *Faraday Discuss.* **2014**, 172, 223–237. https://doi.org/10.1039/c4fd00079j.

(325) Cheng, X.Q.; Li, H.J.; Zhao, Z.X.; Wang, Y.Z.; Wang, X.M.; The Use of In-Situ Raman Spectroscopy in Investigating Carbon Materials as Anodes of Alkali Metal-Ion Batteries. *New Carbon Mater.* **2021**, 36 (1), 93–105. https://doi.org/10.1016/S1872-5805(21)60007-0.

(326) Huang, S.; Li, Z.; Wang, B.; Zhang, J.; Peng, Z.; Qi, R.; Wang, J.; Zhao, Y.; N-Doping and Defective Nanographitic Domain Coupled Hard Carbon Nanoshells for High Performance Lithium/Sodium Storage. *Adv. Funct. Mater.* **2018**, 28 (10), 1–10. https://doi.org/10.1002/adfm.201706294.

(327) Barsoukov, E.; Macdonald, J.R.; *Impedance Spectroscopy - Theory, Experiment and Applications*; 2005.

(328) Boukamp, B.A.; A Nonlinear Least Squares Fit Procedure for Analysis of Immittance Data of Electrochemical Systems. *Solid State Ionics* **1986**, 20, 31–44.

(329) Boukamp, B.A.; A Package for Impedance/Admittance Data Analysis. *Solid State Ionics* **1986**, 18–19 (PART 1), 136–140. https://doi.org/10.1016/0167-2738(86)90100-1.

(330) Tröltzsch, U.; Kanoun, O.; Tränkler, H.R.; Characterizing Aging Effects of Lithium Ion Batteries by Impedance Spectroscopy. *Electrochim. Acta* **2006**, 51 (8–9), 1664–1672. https://doi.org/10.1016/j.electacta.2005.02.148.

(331) Gavrilyuk, A.L.; Osinkin, D.A.; Bronin, D.I.; The Use of Tikhonov Regularization Method for Calculating the Distribution Function of Relaxation Times in Impedance Spectroscopy. *Russ. J. Electrochem.* **2017**, 53 (6), 575–588. https://doi.org/10.1134/S1023193517060040.

(332) Illig, J.; Ender, M.; Chrobak, T.; Schmidt, J.P.; Klotz, D.; Ivers-Tiffée, E.; Separation of Charge Transfer and Contact Resistance in $LiFePO_4$-Cathodes by Impedance Modeling . *J. Electrochem. Soc.* **2012**, 159 (7), A952–A960. https://doi.org/10.1149/2.030207jes.

(333) Pan, K.; Zou, F.; Canova, M.; Zhu, Y.; Kim, J.H.; Comprehensive Electrochemical Impedance Spectroscopy Study of Si-Based Anodes Using Distribution of Relaxation Times Analysis. *J. Power Sources* **2020**, 479, 229083. https://doi.org/10.1016/j.jpowsour.2020.229083.

(334) Reuter, F.; Baasner, A.; Pampel, J.; Piwko, M.; Dörfler, S.; Althues, H.; Kaskel, S.; Importance of Capacity Balancing on The Electrochemical Performance of $Li[Ni_{0.8}Co_{0.1}Mn_{0.1}]O_2$ (NCM811)/Silicon Full Cells . *J. Electrochem. Soc.* **2019**, 166 (14), A3265–A3271. https://doi.org/10.1149/2.0431914jes.

(335) Asenbauer, J.; Varzi, A.; Passerini, S.; Bresser, D.; Revisiting the Energy Efficiency and (Potential) Full-Cell Performance of Lithium-Ion Batteries Employing Conversion/Alloying-Type Negative Electrodes. *J. Power Sources* **2020**, 473, 228583. https://doi.org/10.1016/j.jpowsour.2020.228583.

(336) Lee, J.T.; Callaway, D.S.; The Cost of Reliability in Decentralized Solar Power Systems in Sub-Saharan Africa. *Nat. Energy* **2018**, 3 (11), 960–968. https://doi.org/10.1038/s41560-018-0240-y.

(337) Chu, S.; Majumdar, A.; Opportunities and Challenges for a Sustainable Energy Future. *Nature* **2012**, 488 (7411), 294–303. https://doi.org/10.1038/nature11475.

(338) Fares, R.L.; Webber, M.E.; The Impacts Of Storing Solar Energy in the Home to Reduce Reliance on the Utility. *Nat. Energy* **2017**, 2, 17001. https://doi.org/10.1038/nenergy.2017.1.

(339) Palomares, V.; Serras, P.; Villaluenga, I.; Hueso, K.B.; Carretero-González, J.; Rojo, T.; Na-Ion Batteries, Recent Advances and Present Challenges to Become Low Cost Energy Storage Systems. *Energy Environ. Sci.* **2012**, 5 (3), 5884–5901. https://doi.org/10.1039/c2ee02781j.

(340) Pan, H.; Hu, Y.S.; Chen, L.; Room-Temperature Stationary Sodium-Ion Batteries for Large-Scale Electric Energy Storage. *Energy Environ. Sci.* **2013**, 6 (8), 2338–2360. https://doi.org/10.1039/c3ee40847g.

(341) Nithya, C.; Gopukumar, S.; Sodium Ion Batteries: A Newer Electrochemical Storage. *Wiley Interdiscip.*

Rev. Energy Environ. **2015**, 4 (3), 253–278. https://doi.org/10.1002/wene.136.

(342) Chen, H.; Cong, T.N.; Yang, W.; Tan, C.; Li, Y.; Ding, Y.; Progress in Electrical Energy Storage System: A Critical Review. *Prog. Nat. Sci.* **2009**, 19 (3), 291–312. https://doi.org/10.1016/j.pnsc.2008.07.014.

(343) Etacheri, V.; Marom, R.; Elazari, R.; Salitra, G.; Aurbach, D.; Challenges in the Development of Advanced Li-Ion Batteries: A Review. *Energy Environ. Sci.* **2011**, 4 (9), 3243–3262. https://doi.org/10.1039/c1ee01598b.

(344) Dresselhaus, M.S.; Thomas, I.L.; Alternative Energy Technologies. *Nature* **2001**, 414, 332–337. https://doi.org/10.1038/35104599.

(345) Perrin, M.; Saint-Drenan, Y.M.; Mattera, F.; Malbranche, P.; Lead-Acid Batteries in Stationary Applications: Competitors and New Markets for Large Penetration of Renewable Energies. *J. Power Sources* **2005**, 144 (2), 402–410. https://doi.org/10.1016/j.jpowsour.2004.10.026.

(346) Eftekhari, A.; Kim, D.W.; Sodium-Ion Batteries: New Opportunities beyond Energy Storage by Lithium. *J. Power Sources* **2018**, 395, 336–348. https://doi.org/10.1016/j.jpowsour.2018.05.089.

(347) Liu, C.; Li, F.; Lai-Peng, M.; Cheng, H.M.; Advanced Materials for Energy Storage. *Adv. Mater.* **2010**, 22 (8), 28–62. https://doi.org/10.1002/adma.200903328.

(348) Usiskin, R.; Lu, Y.; Popovic, J.; Law, M.; Balaya, P.; Hu, Y.S.; Maier, J.; Fundamentals, Status and Promise of Sodium-Based Batteries. *Nat. Rev. Mater.* **2021**, 6 (11), 1020–1035. https://doi.org/10.1038/s41578-021-00324-w.

(349) Zuo, W.; Yang, Y.; Synthesis, Structure, Electrochemical Mechanisms, and Atmospheric Stability of Mn-Based Layered Oxide Cathodes for Sodium Ion Batteries. *Accounts Mater. Res.* **2022**, 3 (7), 709–720. https://doi.org/10.1021/accountsmr.2c00058.

(350) Ramesh, A.; Tripathi, A.; Balaya, P.; A Mini Review on Cathode Materials for Sodium-Ion Batteries. *Int. J. Appl. Ceram. Technol.* **2022**, 19 (2), 913–923. https://doi.org/10.1111/ijac.13920.

(351) Wang, P.F.; Yao, H.R.; Liu, X.Y.; Yin, Y.X.; Zhang, J.N.; Wen, Y.; Yu, X.; Gu, L.; Guo, Y.G. Na^+/Vacancy Disordering Promises High-Rate Na-Ion Batteries. *Sci. Advaces* **2018**, 4 (3). https://doi.org/DOI: 10.1126/sciadv.aar6018.

(352) Zuo, W.; Innocenti, A.; Zarrabeitia, M.; Bresser, D.; Yang, Y.; Passerini, S.; Layered Oxide Cathodes for Sodium-Ion Batteries: Storage Mechanism, Electrochemistry, and Techno-Economics. *Acc. Chem. Res.* **2023**, 56 (3), 284-296. https://doi.org/10.1021/acs.accounts.2c00690.

(353) Liu, X.; Zuo, W.; Zheng, B.; Xiang, Y.; Zhou, K.; Xiao, Z.; Shan, P.; Shi, J.; Li, Q.; Zhong, G.; Fu, R.; Yang, Y.; P2-$Na_{0.67}Al_xMn_{1-x}O_2$: Cost-Effective, Stable and High-Rate Sodium Electrodes by Suppressing Phase Transitions and Enhancing Sodium Cation Mobility. *Angew. Chemie - Int. Ed.* **2019**, 58 (50), 18086–18095. https://doi.org/10.1002/anie.201911698.

(354) Yabuuchi, N.; Yoshida, H.; Komaba, S.; Crystal Structures and Electrode Performance of Alpha-$NaFeO_2$ for Rechargeable Sodium Batteries. *Electrochemistry* **2012**, 80 (10), 716–719. https://doi.org/10.5796/electrochemistry.80.716.

(355) Lee, E.; Brown, D.E.; Alp, E.E.; Ren, Y.; Lu, J.; Woo, J.J.; Johnson, C.S.; New Insights into the Performance Degradation of Fe-Based Layered Oxides in Sodium-Ion Batteries: Instability of Fe^{3+}/Fe^{4+} Redox in α-$NaFeO_2$. *Chem. Mater.* **2015**, 27 (19), 6755–6764. https://doi.org/10.1021/acs.chemmater.5b02918.

(356) Zuo, W.; Liu, X.; Qiu, J.; Zhang, D.; Xiao, Z.; Xie, J.; Ren, F.; Wang, J.; Li, Y.; Ortiz, G.F.; Wen, W.; Wu, S.; Wang, M.S.; Fu, R.; Yang, Y.; Engineering Na^+-Layer Spacings to Stabilize Mn-Based Layered Cathodes for Sodium-Ion Batteries. *Nat. Commun.* **2021**, 12 (1), 1–11. https://doi.org/10.1038/s41467-021-25074-9.

(357) Zhang, R.; Yang, S.; Li, H.; Zhai, T.; Li, H.; Air Sensitivity of Electrode Materials in Li/Na Ion Batteries: Issues and Strategies. *InfoMat* **2022**, 4 (6), 1–26. https://doi.org/10.1002/inf2.12305.

(358) Wu, X.; Guo, J.; Wang, D.; Zhong, G.; McDonald, M.J.; Yang, Y.; P2-Type $Na_{0.66}Ni_{0.33-x}Zn_xMn_{0.67}O_2$ as New High-Voltage Cathode Materials for Sodium-Ion Batteries. *J. Power Sources* **2015**, 281, 18–26. https://doi.org/10.1016/j.jpowsour.2014.12.083.

(359) Guo, Y.J.; Wang, P.F.; Niu, Y. Bin; Zhang, X.D.; Li, Q.; Yu, X.; Fan, M.; Chen, W.P.; Yu, Y.; Liu, X.; Meng, Q.; Xin, S.; Yin, Y.X.; Guo, Y.G.; Boron-Doped Sodium Layered Oxide for Reversible Oxygen Redox Reaction in Na-Ion Battery Cathodes. *Nat. Commun.* **2021**, 12 (1), 1–11. https://doi.org/10.1038/s41467-021-25610-7.

(360) Di Lecce, D.; Campanella, D.; Hassoun, J. Insight on the Enhanced Reversibility of a Multimetal Layered Oxide for Sodium-Ion Battery. *J. Phys. Chem. C* **2018**, 122 (42), 23925–23933. https://doi.org/10.1021/acs.jpcc.8b07596.

(361) Darjazi, H.; Bottoni, L.; Moazami, H.R.; Rezvani, S.J.; Balducci, L.; Sbrascini, L.; Staffolani, A.; Tombesi, A.; Nobili, F.; From Waste to Resources: Transforming Olive Leaves to Hard Carbon as Sustainable and Versatile Electrode Material for Li/Na-Ion Batteries and Supercapacitors. *Mater. Today Sustain.* **2023**, 100313. https://doi.org/10.1016/J.MTSUST.2022.100313.

(362) Bottoni, L.; Darjazi, H.; Sbrascini, L.; Staffolani, A.; Gabrielli, S.; Pastore, G.; Tombesi, A.; Nobili, F. Electrochemical Characterization of Charge Storage at Anodes for Sodium-Ion Batteries Based on Corncob Waste-Derived Hard Carbon and Binder. *ChemElectroChem* **2023**, 202201117, 1–12. https://doi.org/10.1002/celc.202201117.

(363) Winter, M.; Besenhard, J.O.; *Handbook of Battery Materials*; 2015.

(364) Nakayama, T.; Komaba, S.; Ozeki, T.; Murata, W.; Ogata, A.; Gotoh, K.; Ishikawa, T.; Yabuuchi, N.; Fujiwara, K.; Electrochemical Na Insertion and Solid Electrolyte Interphase for Hard-Carbon Electrodes and Application to Na-Ion Batteries. *Adv. Funct. Mater.* **2011**, 21 (20), 3859–3867. https://doi.org/10.1002/adfm.201100854.

(365) Zhao, J.; Zhao, L.; Chihara, K.; Okada, S.; Yamaki, J.I.; Matsumoto, S.; Kuze, S.; Nakane, K. Electrochemical and Thermal Properties of Hard Carbon-Type Anodes for Na-Ion Batteries. *J. Power Sources* **2013**, 244, 752–757. https://doi.org/10.1016/j.jpowsour.2013.06.109.

(366) Song, Z.; Zou, K.; Xiao, X.; Deng, X.; Li, S.; Hou, H.; Lou, X.; Zou, G.; Ji, X.; Presodiation Strategies for the Promotion of Sodium-Based Energy Storage Systems. *Chem. - A Eur. J.* **2021**, 27 (65), 16082–16092. https://doi.org/10.1002/chem.202102433.

(367) Martinez De Ilarduya, J.; Otaegui, L.; López del Amo, J.M.; Armand, M.; Singh, G.; NaN_3 Addition, a Strategy to Overcome the Problem of Sodium Deficiency in P2-$Na_{0.67}[Fe_{0.5}Mn_{0.5}]O_2$ Cathode for Sodium-Ion Battery. *J. Power Sources* **2017**, 337, 197–203. https://doi.org/10.1016/j.jpowsour.2016.10.084.

(368) Park, K.; Yu, B.C.; Goodenough, J.B.; Electrochemical and Chemical Properties of Na_2NiO_2 as a Cathode Additive for a Rechargeable Sodium Battery. *Chem. Mater.* **2015**, 27 (19), 6682–6688. https://doi.org/10.1021/acs.chemmater.5b02684.

(369) Guo, Y.J.; Niu, Y. Bin; Wei, Z.; Zhang, S.Y.; Meng, Q.; Li, H.; Yin, Y.X.; Guo, Y.G. Insights on Electrochemical Behaviors of Sodium Peroxide as a Sacrificial Cathode Additive for Boosting Energy Density of Na-Ion Battery. *ACS Appl. Mater. Interfaces* **2021**, 13 (2), 2772–2778. https://doi.org/10.1021/acsami.0c20870.

(370) Liu, X.; Tan, Y.; Wang, W.; Wei, P.; Seh, Z.W.; Sun, Y.; Ultrafine Sodium Sulfide Clusters Confined in Carbon Nano-Polyhedrons as High-Efficiency Presodiation Reagents for Sodium-Ion Batteries. *ACS Appl. Mater. Interfaces* **2021**, 13 (23), 27057–27065. https://doi.org/10.1021/acsami.1c05144.

(371) Jezowski, P.; Crosnier, O.; Brousse, T.; Sodium Borohydride ($NaBH_4$) as a High-Capacity Material for Next-Generation Sodium-Ion Capacitors. *Open Chem.* **2021**, 19 (1), 432–441. https://doi.org/10.1515/chem-2021-0040.

(372) Jeżowski, P.; Chojnacka, A.; Pan, X.; Béguin, F.; Sodium Amide as a "Zero Dead Mass" Sacrificial Material for the Pre-Sodiation of the Negative Electrode in Sodium-Ion Capacitors. *Electrochim. Acta*

2021, 375. https://doi.org/10.1016/j.electacta.2021.137980.

(373) Shanmukaraj, D.; Kretschmer, K.; Sahu, T.; Bao, W.; Rojo, T.; Wang, G.; Armand, M.; Highly Efficient, Cost Effective, and Safe Sodiation Agent for High-Performance Sodium-Ion Batteries. *ChemSusChem* **2018**, 11 (18), 3286–3291. https://doi.org/10.1002/cssc.201801099.

(374) Pan, X.; Chojnacka, A.; Béguin, F.; Advantageous Carbon Deposition during the Irreversible Electrochemical Oxidation of $Na_2C_4O_4$ Used as a Presodiation Source for the Anode of Sodium-Ion Systems. *Energy Storage Mater.* **2021**, 40, 22–30. https://doi.org/10.1016/j.ensm.2021.04.048.

(375) Arnaiz, M.; Shanmukaraj, D.; Carriazo, D.; Bhattacharjya, D.; Villaverde, A.; Armand, M.; Ajuria, J.; A Transversal Low-Cost Pre-Metallation Strategy Enabling Ultrafast and Stable Metal Ion Capacitor Technologies. *Energy Environ. Sci.* **2020**, 13 (8), 2441–2449. https://doi.org/10.1039/d0ee00351d.

(376) Gauckler, C.; Dillenz, M.; Maroni, F.; Pfeiffer, L.F.; Biskupek, J.; Sotoudeh, M.; Fu, Q.; Kaiser, U.; Dsoke, S.; Euchner, H.; Axmann, P.; Wohlfahrt-Mehrens, M.; Groß, A.; Marinaro, M.; Detailed Structural and Electrochemical Comparison between High Potential Layered P2-NaMnNi and Doped P2-NaMnNiMg Oxides. *ACS Appl. Energy Mater.* **2022**, 5 (11), 13735–13750. https://doi.org/10.1021/acsaem.2c02402.

(377) Han, M.; Zhu, C.; Ma, T.; Pan, Z.; Tao, Z.; Chen, J.; In Situ Atomic Force Microscopy Study of Nano-Micro Sodium Deposition in Ester-Based Electrolytes. *Chem. Commun.* **2018**, 54 (19), 2381–2384. https://doi.org/10.1039/c7cc09751d.

(378) Parry, K.L.; Shard, A.G.; Short, R.D.; White, R.G.; Whittle, J.D.; Wright, A.; ARXPS Characterisation of Plasma Polmerised Surface Chemical Gradients. *Surf. Interface Anal.* **2006**, 38 (11), 1497–1504. https://doi.org/10.1002/sia.2400.

(379) Herklotz, M.; Weiß, J.; Ahrens, E.; Yavuz, M.; Mereacre, L.; Kiziltas-Yavuz, N.; Drager, C.; Ehrenberg, H.; Eckert, J.; Fauth, F.; Giebeler, L.; Knapp, M.; A Novel High-Throughput Setup for in Situ Powder Diffraction on Coin Cell Batteries. *J. Appl. Crystallogr.* **2016**, 49, 340–345. https://doi.org/10.1107/S1600576715022165.

(380) Ravel, B.; Newville, M.; ATHENA, ARTEMIS, HEPHAESTUS: Data Analysis for X-Ray Absorption Spectroscopy Using IFEFFIT. *J. Synchrotron Radiat.* **2005**, 12 (4), 537–541. https://doi.org/10.1107/S0909049505012719.

(381) Pfeiffer, L.F.; Jobst, N.; Gauckler, C.; Lindén, M.; Marinaro, M.; Passerini, S.; Wohlfahrt-Mehrens, M.; Axmann, P.; Layered P2-$Na_xMn_{3/4}Ni_{1/4}O_2$ Cathode Materials For Sodium-Ion Batteries: Synthesis, Electrochemistry and Influence of Ambient Storage. *Front. Energy Res.* **2022**, 10, 1–17. https://doi.org/10.3389/fenrg.2022.910842.

(382) Dinnebier, R.E.; Nuss, H.; Jansen, M.; The Crystal Structures of Solvent-Free Alkali-Metal Squarates from Powder Diffraction Data. *Zeitschrift fur Krist.* **2005**, 220 (11), 954–961. https://doi.org/10.1524/zkri.2005.220.11_2005.954.

(383) Zhang, L.; Wang, C.; Liu, Y.; Ren, M.; Du, J.; Chen, A.; Li, F.; Suppressing Interlayer-Gliding and Jahn-Teller Effect in P2-Type Layered Manganese Oxide Cathode via Mo Doping for Sodium-Ion Batteries. *Chem. Eng. J.* **2021**, 426, 130813. https://doi.org/10.1016/j.cej.2021.130813.

(384) Hasa, I.; Buchholz, D.; Passerini, S.; Hassoun, J.; A Comparative Study of Layered Transition Metal Oxide Cathodes for Application in Sodium-Ion Battery. *ACS Appl. Mater. Interfaces* **2015**, 7 (9), 5206–5212. https://doi.org/10.1021/am5080437.

(385) Luo, R.; Wu, F.; Xie, M.; Ying, Y.; Zhou, J.; Huang, Y.; Ye, Y.; Li, L.; Chen, R.J.; Habit Plane-Driven P2-Type Manganese-Based Layered Oxide as Long Cycling Cathode for Na-Ion Batteries. *J. Power Sources* **2018**, 383, 80–86. https://doi.org/10.1016/j.jpowsour.2018.02.053.

(386) Wang, K.; Yan, P.; Sui, M.; Phase Transition Induced Cracking Plaguing Layered Cathode for Sodium-Ion Battery. *Nano Energy* **2018**, 54, 148–155. https://doi.org/10.1016/j.nanoen.2018.09.073.

(387) Gutierrez, A.; Dose, W.M.; Borkiewicz, O.; Guo, F.; Avdeev, M.; Kim, S.; Fister, T.T.; Ren, Y.; Bareño, J.; Johnson, C.S.; On Disrupting the Na^+-Ion/Vacancy Ordering in P2-Type Sodium-Manganese-

Nickel Oxide Cathodes for Na^+-Ion Batteries. *J. Phys. Chem. C* **2018**, 122 (41), 23251–23260. https://doi.org/10.1021/acs.jpcc.8b05537.

(388) Kubota, K.; Kumakura, S.; Yoda, Y.; Kuroki, K.; Komaba, S.; Electrochemistry and Solid-State Chemistry of $NaMeO_2$ (Me = 3d Transition Metals). *Adv. Energy Mater.* **2018**, 8 (17), 1–30. https://doi.org/10.1002/aenm.201703415.

(389) Singh, G.; Tapia-Ruiz, N.; Lopez Del Amo, J.M.; Maitra, U.; Somerville, J.W.; Armstrong, A.R.; Martinez De Ilarduya, J.; Rojo, T.; Bruce, P.G.; High Voltage Mg-Doped $Na_{0.67}Ni_{0.3-x}Mg_xMn_{0.7}O_2$ (x = 0.05, 0.1) Na-Ion Cathodes with Enhanced Stability and Rate Capability. *Chem. Mater.* **2016**, 28 (14), 5087–5094. https://doi.org/10.1021/acs.chemmater.6b01935.

(390) Tapia-Ruiz, N.; Dose, W.M.; Sharma, N.; Chen, H.; Heath, J.; Somerville, J.W.; Maitra, U.; Islam, M.S.; Bruce, P.G.; High Voltage Structural Evolution and Enhanced Na-Ion Diffusion in P2-$Na_{2/3}Ni_{1/3-x}Mg_xMn_{2/3}O_2$ ($0 \leq x \leq 0.2$) Cathodes from Diffraction, Electrochemical and Ab Initio Studies. *Energy Environ. Sci.* **2018**, 11 (6), 1470–1479. https://doi.org/10.1039/c7ee02995k.

(391) Somerville, J.W.; Sobkowiak, A.; Tapia-Ruiz, N.; Billaud, J.; Lozano, J.G.; House, R.A.; Gallington, L.C.; Ericsson, T.; Haggstrom, L.; Roberts, M.R.; Maitra, U.; Bruce, P.G.; Nature of the "Z"-Phase in Layered Na-Ion Battery Cathodes. *Energy Environ. Sci.* **2019**, 12, 2223–2232. https://doi.org/10.1039/C8EE02991A.

(392) Zuo, W.; Qiu, J.; Hong, C.; Liu, X.; Li, J.; Ortiz, G.F.; Li, Q.; Zheng, S.; Zheng, G.R.; Yang, Y.; Structure-Performance Relationship of Zn^{2+} Substitution in P2-$Na_{0.66}Ni_{0.33}Mn_{0.67}O_2$ with Different Ni/Mn Ratios for High-Energy Sodium-Ion Batteries. *ACS Appl. Energy Mater.* **2019**, 2 (7), 4914–4924. https://doi.org/10.1021/acsaem.9b00614.

(393) Clément, R.J.; Xu, J.; Middlemiss, D.S.; Alvarado, J.; Ma, C.; Meng, Y.S.; Grey, C.P.; Direct Evidence for High Na^+ Mobility and High Voltage Structural Processes in P2-$Na_x[Li_yNi_zMn_{1-y-z}]O_2$ (x, y, $z \leq 1$) Cathodes from Solid-State NMR and DFT Calculations. *J. Mater. Chem. A* **2017**, 5 (8), 4129–4143. https://doi.org/10.1039/c6ta09601h.

(394) Yabuuchi, N.; Yoshii, K.; Myung, S.T.; Nakai, I.; Komaba, S.; Detailed Studies of a High-Capacity Electrode Material for Rechargeable Batteries, Li_2MnO_3–$LiCo_{1/3}Ni_{1/3}Mn_{1/3}O_2$. *J. Am. Chem. Soc.* **2011**, 133 (12), 4404–4419. https://doi.org/10.1021/ja108588y.

(395) Cheng, Z.; Zhao, B.; Guo, Y.J.; Yu, L.; Yuan, B.; Hua, W.; Yin, Y.X.; Xu, S.; Xiao, B.; Han, X.; Wang, P.F.; Guo, Y.G.; Mitigating the Large-Volume Phase Transition of P2-Type Cathodes by Synergetic Effect of Multiple Ions for Improved Sodium-Ion Batteries. *Adv. Energy Mater.* **2022**, 12 (14), 1–9. https://doi.org/10.1002/aenm.202103461.

(396) Hy, S.; Liu, H.; Zhang, M.; Qian, D.; Hwang, B.J.; Meng, Y.S.; Performance and Design Considerations for Lithium Excess Layered Oxide Positive Electrode Materials for Lithium Ion Batteries. *Energy Environ. Sci.* **2016**, 9 (6), 1931–1954. https://doi.org/10.1039/c5ee03573b.

(397) Yu, H.; Zhou, H.; High-Energy Cathode Materials (Li_2MnO_3-$LiMO_2$) for Lithium-Ion Batteries. *J. Phys. Chem. Lett.* **2013**, 4 (8), 1268–1280. https://doi.org/10.1021/jz400032v.

(398) Swift, P.; Adventitious Carbon — The Panacea for Energy Referencing? *Surf. Interface Anal.* **1982**, 4 (2), 47–51. https://doi.org/10.1002/sia.740040204.

ACKNOWLEDGMENTS

At the end of this three-year path, I believe I have collected quite a number of people who deserve a mention in this thesis at the very least.

First of all, I would like to thank my supervisor Prof. Francesco Nobili for giving me the chance to pursue this path, for the advice and the teachings contributing to my education in the field of electrochemistry; Dr. Sonia Dsoke, for hosting me during my five-month visiting period in the IAM-ESS laboratories at KIT, Karlsruhe, Germany, and for giving me the opportunity to learn new things and improve my knowledge; Angelina Sarapulova, Lydia Gehrlein, Fabian Jeschull, Tolga Akcay and Dennis Triller for helping me carry on the research at KIT and contributing to some of the measurements in this thesis; Dr. Mario Marinaro and Cornelius Gauckler from ZSW, Ulm, Germany, for also contributing to the work carried out during my visiting period in collaboration with KIT by providing some of the materials tested.

Secondly, I would like to thank my family who supported me during these years and, despite the ups and downs, always encouraged me to follow my own path and achieve my goals. I want to express my gratitude in particular to my brother Gabriel, for always being my strength.

Last but not least, I want to thank all the people who stood by my side and put up with me in this adventure. A very special mention goes to Sonila, Noemi and Patrizio, for being there every day and helping me carry on despite all the bad moments, you have been the shoulders I could cry on when I needed the most and the lights shedding the way in my darkest times; Federico, for your kindness and support, for always being a good friend since high school, and most of all for finally showing me the meaning of Stonehenge; Andrea, for your stubbornness, for being a pain in the ass, and for always pushing me to do better at work and in life; Giorgio, for always cheering me up with your jokes, especially in the last months of our PhD, and making things a bit lighter; Luca, for being a good friend, colleague and drinking partner, and for agreeing to all the silly things coming to my mind, even the dumbest ones; Antunes, for being a friend, colleague, teacher and one of the most brilliant people I know, your contribution to this thesis was fundamental. And of course, all the people I met and hung out with during these three years, each one of you somehow left me something that helped me going forward one step at a time.